High-contrast, ultra-intense laser-solid interaction physics with engineered targets

Leonard Nikolas Konstantin Döhl

Doctor of Philosophy

University of York

Physics

November 2019

Abstract

The key objectives of this thesis are to understand how to efficiently couple a high power laser to a target and produce bright X-ray and energetic ion sources. The approaches taken are to use plasma mirrors to improve the laser contrast, structure the target surface to increase the laser absorption and the use of ultra thin targets for ion acceleration. The experimental work is combined with computational calculations to further develop an understanding of the laser-target physics.

The suppression of the early interaction is investigated using a double plasma mirror setup. This is studied by developing a model using geometric optics and ionisation thresholds of plasma mirrors. By using these calculations in Helios simulations it is inferred that the laser interaction with the target is delayed closer to the peak of the pulse. As a result, the target expansion is reduced to sub-micron lengths by the time the main laser peak interacts with the target.

On an experiment using silicon targets with micro-structured surfaces we observe an enhancement in the X-ray emission. A conical crystal spectrometer is used for recording the emission centralised on K_α. The enhancement is interpreted from comparing the emission between micro-structured and flat surfaced targets. By combining the micro-structured targets with a double plasma mirror setup, a method for engineering plasma density scale length is achieved.

By laser irradiating graphene we observe the generation of protons and carbon ions using radiochromic film and CR-39. The measurements are linked to EPOCH particle-in-cell simulations. From simulations it is inferred that the onset of relativistically induced transparency is important for producing energetic ions. The ion motion is determined by the emerging electric fields in experiment and simulations.

Contents

List of Tables

List of Figures

Acknowledgments

I would like to thank my supervisor, Nigel Woolsey, who I have known and worked with since my undergraduate studies in York. Throughout the years I have valued his support, engagement and approach of challenging my learning experience in a constructive way I would have not done otherwise. With him the PhD had been an exciting adventure and feel fortunate for his guidance.

I want to acknowledge everyone who provided me support outside of the PhD that kept me fighting until the end. My friend at YPI, Koki Imada, kept me sane and provided me a place to stay when I was forced to vacate my last accommodation. We had many great memories that reminded to enjoy life to survive the write up of the thesis. I value our friendship and will remain forever grateful for having him as a friend.

I like to thank Scott Doyle for not only the initial version of this thesis template, but having been a great colleague in the office. My other colleagues that I appreciate for having on this journey, both currently and formerly at York, are Luca Antonelli, Steven Biggs, David Blackman, Philip Bradford, Philip Durey, Martin Read and Eleanor Tubman.

The YPI administration team, Donna Cook, Kathryn Harvey, Ruth Lowman, Hillary Marshall and Jenni Prestley, provided opportunities and support during the course of my PhD that made the work in this thesis possible and advanced my experience. They were the best administration team one could ask for, and I highly appreciated their ongoing help.

In Chapter 4 I presented details about the Vulcan petawatt laser. I want to acknowledge the helpful information provided by Ian Musgrave at Central Laser Facility (CLF). Furthermore, the design of the 3D-printed compact double plasma mirror holder I developed received feedback from Robert Clarke and Christopher Spindloe at CLF, as well as Wayne Robinson and Jason Flatt. They have supported me in making it possible for the holder to be made.

Chapter 5 presented my spectral measurements on an experiment I joined as part of my PhD objective. I want to thank Nico Neumann, who led the experiment for his completed PhD, as the results are of great interest. I value his friendship that helped me advance on the work and enjoy my time. I also want to thank Tina Ebert, Markus Hesse, Jonathan

Jarrett, Dean Rusby and Alexandra Tebartz who were part of the experimental team and we have worked as a team successfully.

Thanks to the collaboratory that I did at National Central University (NCU, Taiwan), I investigated the use of graphene for ion acceleration with Yasuhiro Kuramitsu (now at Osaka University). Our journey together led to learning very exciting facts about our results that became part of my PhD. As the work progressed we have been supported of Nicola Booth at CLF, Yuji Fukuda at KPSI, Masato Kanasaki at Kobe University, Wei-Yen Woon at NCU, Christopher Ridgers at University of York, Youichi Sakawa at Osaka University and Yasuhiro's students. I want to particularly acknowledge for their expertise and contribution to my work. The experimental measurements shown in Chapter 6 were achieved by myself, Nicola, Robert Heathcote at CLF, and Christopher Baird, Damon Farley and William Trickey at University of York.

My Japanese drumming group and family, Tengu Taiko Drummers, have kept me standing tall during the hardest of times. The three-and-a-bit years motivated me over the course working on the PhD and brought much more meaning to my life. They are like my family from a different world. I thank you all for being part of my life, Natalie-Clare Brimicombe, Steven Crabb, Wayne Grainger, Anja Hardwick-Plews, Anna Hardwick-Plews, Jared Hardwick, Javan Hardwick-Plews, Sue Hine, John Hughes, Vanessa Kettlestring, Caroline Montgomery, Jez Stretch, Sarah Tilston, Lisa Wilson and Cat Wagstaff. "*Ichi Ni Sore!*"

Finally, my family are core of the reason to keep on waking up every day. They will also make me pursue a life which I continue supporting theirs and back. My parents Osbert and Ulrike, siblings Frederic, Johannes, Elisabeth, Maximilian, Katharina and Clara, grandparents Hans, Ruth and Ruth Koch (you will always be remembered), aunt Barbara and her husband Thomas Simmel, in-laws Anke Myrrhe, Aline Arakaki, Torben Rytter, Michelle Nørmark, and nieces and nephews, Caroline Døhl-Rytter, Victoria Døhl-Rytter, Christiane Døhl-Rytter, Victor Nørmark, and Bruno Myrrhe, as well as the two newcomers to witness our world, made me who I am today and motivated me one way or the other to complete my PhD. Nothing beats the love of family. I love you all!

Declaration

This thesis has not previously been accepted for any degree and is not being concurrently submitted in candidature for any degree other than Doctor of Philosophy of the University of York. This thesis is the result of my own investigations, except where otherwise stated. All other sources are acknowledged by explicit references.

I declare that this thesis is a presentation of original work and I am the sole author. This work has not previously been presented for an award at this, or any other, University. All sources are acknowledged as References.

Much of the work has been presented at international conferences and internal seminars with a full list provided in Appendix 1. Part of the work has been published in:

- L. N. K. Döhl, R. Alraddadi, N. Booth, Y. Fukuda, Y. Kuramitsu, C. Ridgers and N. Woolsey, *Modeling ion acceleration from ultra-thin graphene using the Vulcan petawatt laser*, SCARF Annual Report 2017-2018, 47-48 (2019).

All Helios and PrismSPECT calculations were conducted and analyzed by the author and discussed between the author and Prof Nigel Woolsey. Access to these codes on the Prism server at Central Laser Facility (CLF, UK) was provided by Dr Raoul Trines. Extended Particle-in-cell Open Collaboration (EPOCH) simulations were conducted by the author, where additional simulations supporting the results in Table 6.2 and Figure 6.16 were provided by Dr Reem Alraddadi at King Saud University (Saudi Arabia). The results were analysed by the author and discussed with Dr Alraddadi, Dr Christopher Ridgers and Prof Woolsey. For these simulations, I would like to acknowledge the use of the SCARF cluster provided by STFC Scientific Computing Department and the Viking cluster provided by the University of York.

CR-39 data processing and analysis presented in Chapter 3 was based on research training conducted at Kansai Photon Science Institute (KSPI, Japan) and Kobe University (Japan), which was provided by Dr Yuji Fukuda and Dr Masato Kanasaki.

The temporal profile of the Vulcan petawatt laser and details about the facility was provided by Dr Ian Musgrave. All calculations using the temporal profile were conducted by the author, which used data taken from Ref.[5,8] and provided by Thorlabs Ltd. Technical Support. The double plasma mirror (DPM) used on the Vulcan petawatt laser experiments was designed by Dr Nico Neumann and CLF engineers. The compact 3D-printed DPM holder was designed using Autodesk Inventor by the author. The author received feedback and suggestions on the final design from Dr Robert Clarke and Dr Christopher Spindloe at CLF, and Mr Jason Flatt and Mr Wayne Robinson at University of York. The holder was 3D printed by Dr Spindloe at CLF. Measurements from using the DPM holder were taken on an

experiment using the LFEX at Institute of Laser Engineering (ILE, Japan). The investigation was led by Prof Yasuhiro Kuramitsu at Osaka University (Japan), and was conducted by the author, Dr Yasunobu Arikawa at ILE, Mr Takamasa Hihara, Prof Yasuhiro Kuramitsu, Mr Takumi Minami and Mr Kentaro Sakai at Osaka University, and Ms Yu-Zhu Liao and Dr Wei-Yen Woon at National Central University (NCU, Taiwan). Further support during the experiment was provided by Dr Yuji Fukuda at KPSI, Dr Masato Kanasaki at Kobe University, and Dr Alessio Morace, Mr Masato Ota and Prof Youichi Sakawa at ILE. The interpretation of the results is from the author and discussed with Prof Woolsey.

Experiments were carried out using the Vulcan petawatt laser at CLF (UK). The experimental campaign using targets with microstructured surfaces was led by Prof Markus Roth at Technische Universität Darmstadt (Germany) and conducted by the author, Ms Tina Ebert, Mr Markus Hesse, Dr Neumann and Dr Alexandra Tebartz at Darmstadt, Mr Jonathan Jarrett at University of Strathclyde (UK), and Mr Robert Heathcote and Dr Dean Rusby at CLF. Ongoing support by Ms Aasia Hughes, Dr David Neely and Dr Spindloe at CLF and Dr Paul McKenna at University of Strathclyde was provided on the experiment. The targets were fabricated by Ms Ebert, Dr Neumann and Dr Gabriel Schaumann in Darmstadt using the method in Subsection 5.1.1, as described by Ebert et al. [7]. Scanning electron microscope image of the target surface was provided by Ms Ebert and Dr Neumann. All the data acquisition, processing and analysis associated with the X-ray spectroscopy is done by the author, where part of the data reduction approach uses data taken from Ref. [2,9,10] and PrismSPECT. The results were discussed between the author, Prof Woolsey and Dr Sergey Pikuz at Russian Academy of Sciences (Russia).

The experimental campaign led by Dr Nicola Booth using large-area suspended graphene was conducted by the author, Dr Booth and Mr Heathcote at CLF, Mr Christopher Baird, Mr Damon Farley and Mr William Trickey from University of York, and Prof Kuramitsu at Osaka University. Ongoing support during the experiment was provided by Dr Kate Lancaster, Dr Christopher Murphy and Prof Nigel Woolsey at University of York. The targets were fabricated by Dr Woon at NCU and delivered by Mr Shih-Ming He from NCU, which is described in Subsection 6.1.1 and published by Khasanah et al. [11] Images of graphene targets were taken using the scanning electron microscope at the Nanocenter (York) and provided by Dr Barat Kuerbanjiang and Dr Vlado Lazarov. Calculations and analysis of RCF data was done by the author, where the energy deposition curves and ion energies were calculated using a MATLAB code provided by Dr David Carroll at CLF. Data from the SRIM code [12] were used for these calculations. Analysis of CR-39 data was done by the author, Dr Fukuda and Dr Kanasaki with discussions between the author, Dr Fukuda, Dr Kanasaki, Prof Kuramitsu and Prof Woolsey. CR-39 calibration measurements were conducted by Dr Fukuda using the Heavy Ion Medical Accelerator in Chiba (HIMAC, Japan).

The work presented herein was funded by the Engineering and Physical Sciences Research

Council (EPSRC) and Science and Technology Facilities Council (STFC), grant reference number: EP/L01663X/1.

Chapter 1

Introduction

The 2018 Nobel Prize in Physics celebrates the technology called the chirped pulse amplifier (CPA) by Strickland and Mourou [13] that since 1985 has revolutionized the development of high power laser (HPL) systems. A number of exciting areas emerged using the CPA such as the generation of laser-driven radiation and particle sources. When a high intensity laser pulse interacts with a micron-thin solid material the strong electromagnetic fields due to the laser produce bright X-rays, [14,15] relativistic electrons [16] and many-MeV ions. [17,18] These sources are of particular interest for applications in astrophysics, [19,20] diagnostic development, [21,22] material studies, [23] oncology [24–26] and fusion energy. [27–29] To realise these potentials it is important to optimize and control the properties of the laser-driven radiation and particle sources. In order to do this, extensive research and development using HPL technology and advanced engineering capabilities focus on understanding the physics that underpins the generation of these sources.

1.1 X-ray radiation sources

The interaction of a high-intensity laser with a solid surface drives the generation of an energetic, high-flux electron beam. Electrons propagate into the solid material and produce X-rays via bremsstrahlung [14,30] and electron collisions with atoms. [31] The latter leads to the generation of spectral line emission. The laser interaction with a material, such as aluminium and silicon, which drives the electrons bombardment produces a characteristic X-ray spectrum. The spectral lines are characteristic of K-shell line emission from many ionisation states of the atoms in the target. [15,32] K-shell emission is of great importance for understanding the relativistic electron interaction and transport in matter. This also provides an insight to the behaviour of astronomical phenomena emitting spectral high energy radiation, such as solar flares. [19]

The K-shell spectrum includes a characteristic K_α line emission. K_α is the most probable emission to occur in matter [33,34] for most experimental studies and applications. This results

in K_α being the brightest emission line in the K-shell spectrum and, hence, most studied line emission. The emitted energy is well-known for the majority of all elements.[35] For materials, such as aluminium and silicon, the emission also has a high monochromaticity. High intensity and monochromatic emission is advantageous to a number of applications such as spectral calibration[21] and X-ray photoelectron spectroscopy.[23]

If optimised, HPL can generate short duration K_α pulses with intensities about four orders of magnitude brighter than conventional sources.[36] This could provide measurements with high temporal resolution and details of the fundamental physics of matter.

1.2 Compact ion accelerators

In the mid-1980s Gitomer et al.[37] observed the first MeV ions by irradiating a high-intensity laser on a solid foil, which was before the use of the CPA technology. Once high power laser facilities were developed using this technology, multi-MeV ions were produced through a strong electrostatic field in 2000.[17] This was later described by Wilks et al.[38] with the laser driving electrons ponderomotively to high energies. The ion acceleration mechanism became known as target normal sheath acceleration (TNSA). Since these early studies, experimental investigations linked to theory and simulations have advanced laser-driven ion acceleration concepts to generate hundreds of MeV ions. Recently, Higginson et al.[18] reported proton energies close to 100 MeV using nano-thin foils. These studies, amongst other works, motivated researchers on developing laser-driven high energy ion sources for future applications.

1.2.1 Fast ion ignition approach to inertial confinement fusion

One application for energetic ions is in fusion research. Fusion research focuses on developing ways for producing energy as an alternative to fossil fuels addressing the rising global energy consumption and climate crisis. The two main approaches are magnetic[39] and inertial confinement fusion[40] (MCF and ICF respectively). Both use deuterium and tritium as the fuel because of their high reaction probability at conditions achievable in MCF and ICF. The fusion reaction is

$$\mathrm{D} + \mathrm{T} \rightarrow {}^4\mathrm{He}\ [3.5\ \mathrm{MeV}] + \mathrm{n}\ [14.1\ \mathrm{MeV}] \tag{1.1}$$

Fast ignition is an advanced scheme to accomplish ICF. The approach separates the processes that compress the fuel and thereafter heat a fraction of the fuel to thermonuclear temperatures using a fast pulse of charged particles. The capsule containing the fuel is compressed for longer than a nanosecond to an areal density of $\rho r \approx 0.3$ g/cm^2 in the hot spot region while the fuel reaches $\rho r \approx 3$ g/cm^2. The latter ρr is required for achieving a fuel burn fraction of at least 30%. $\rho r \approx 0.3$ g/cm^2 is necessary in order to heat the surrounding cool and dense fuel via α capture.[40]

In the original fast ignition approach the fast pulse for heating the compressed fuel are electrons. The relativistic electrons of energies exceeding 0.5 MeV propagate rapidly through the capsule. These electrons generate a return current that opposes the current that the relativistic electrons induce. This return current consists of thermal electrons with a high density that heats the compressed fuel (see sub-section 2.2.7 for details on the return current). The main challenge using electrons is the beam divergence to achieve a high coupling efficiency of electrons to the fuel.[41]

An alternative to circumvent the electron divergence is by using a pulse of fast ions. In this approach a high flux of ions are deposited in the volume of the compressed fuel. In order to achieve this a specific ion energy and energy spread is necessary for depositing the ions after propagating a certain depth into the capsule. Studies suggest that a a high flux proton beam between 15 and 23 MeV can be used for heating the fuel to thermonuclear temperatures.[27,28]

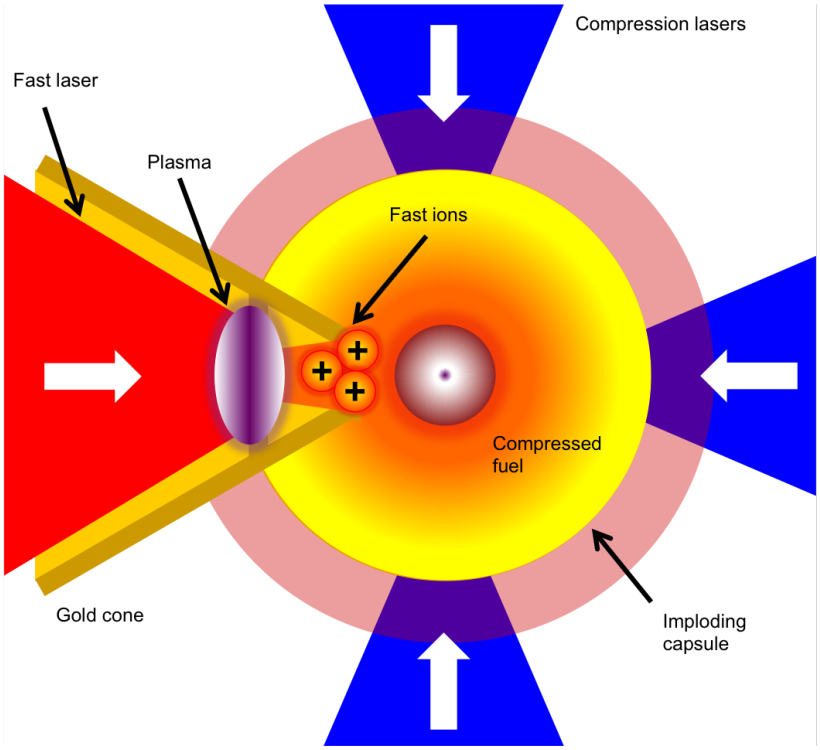

Figure 1.1: Illustration of ion fast ignition in ICF.

1.2.2 Hadron therapy

Another promising application of high energy ion sources is hadron therapy. Inside matter ions have a linear energy transfer (LET), which is the amount of energy deposited by the ions. For ions of a specific energy there is a depth, called the stopping range, the ion moves into matter where most of the ion energy is absorbed. The impact of the deposited ions in human tissues is measured by the relative biological effectiveness. If this effectiveness is

high, the ions damage the DNA molecule such the biological system cannot repair the induced damage. For carbon ions the LET and relative biological effectively spatially coincide closely, resulting in an efficient approach for killing cancer cells. Hence, carbon ions are preferably used for deep-seated tumour therapy.[25,42] Carbon ions of energies up to 4.8 GeV are used for an ion stopping range beneficial to tumour treatment.[25,43]

The most powerful conventional accelerator used for hadron therapy is the Heavy-Ion Medical Accelerator in Chiba (HIMAC, Japan) commissioned in 1994. The 120×65 m^2 accelerator uses electric fields of the order of 10^7 V/m to drive carbon ions of 4.8 GeV (400 MeV/n) nominal energy.[42,43] In comparison, when a high intensity laser pulse interacts with solid matter the electric fields generated exceed 10^{13} V/m within a space of tens of microns. Therefore, high power laser technologies and microengineering capabilities have the potential of generating ion sources comparable to large-scale conventional accelerators. The compact size may even reduce the complexity of running the accelerator and, as a result, reduce operation and maintenance costs.

1.3 Outline

The focus of this thesis is understanding how to efficiently couple an ultra-intense laser pulse to a solid target and, in turn, generate bright X-ray and energetic ion sources. The thesis is structured in the following way:

A theoretical overview of the relevant physics is provided to aid the understanding of the presented work. This will specifically describe the details of the laser interaction with a overdense plasma, including the generation of K_α line emission and ion acceleration mechanisms.

After introducing the theory, an overview of the key diagnostics used in this work is provided. Spectrally-resolved X-ray spectroscopy is described for recording and analysing K_α emission in Chapter 5. A ion energy spectrometer that spatially resolves a laser-driven ion beam is described for the measurements in Chapter 6.

The results are split into three chapters. Chapter 4 presents the use of a double plasma mirror (DPM) for improving the laser contrast. A basic model using geometric optics and ionization thresholds is developed. The model calculations are used in Helios simulations for the suppression of early laser interaction with a solid target. Simulation results also show that the interaction delays the target expansion closer to the main peak of the laser, reducing the plasma scale length as a result. Work on implementing the DPM on two different high power laser facilities will be presented. The DPM enables high intensity laser experiments with high density targets studied in Chapters 5 and 6.

Chapter 5 presents results of using silicon targets with microstructured surfaces. Measurements taken with a conical crystal spectrometer show that these targets increase the

brightness of K_α emission significantly. Spectral analysis of the K_α using the PrismSPECT code provide a basic insight to the physical conditions during the laser-target interaction. In addition, the DPM setup used on the experiments with the targets show an improvement in shot-to-shot reproducibility. By combining the DPM and targets with microstructured surfaces, a method for controlling the plasma density scale length is achieved.

Chapter 6 describes the initial observations of energetic proton and carbon ions by laser irradiating large-area suspended graphene (LSG) targets. The measurements are linked to EPOCH particle-in-cell simulations. From the simulation results it is inferred that the onset of relativistic induced transparency is important for producing highly energetic ions. The ion acceleration mechanisms generating these ions are inferred from comparing the simulations to theory. In addition, the simulations show similarities and differences in the divergence of the ions seen in experiment, which are discussed.

Finally, a summary of the key results is given in the conclusion of this thesis. From this, the current challenges unanswered in the presented work with recommendations on how prospective investigations may continue will be discussed.

Chapter 2

High intensity laser interaction physics with overdense matter

This Chapter introduces the state of matter called a plasma and the conditions that define a plasma. A high intensity laser irradiating a solid target creates a plasma of high density, where the interaction can lead to the generation of relativistic electrons, which drive the generation of K-shell line and energetic ion emission. This includes the K_α emission studied in Chapter 5 and a number of mechanisms that can drive ions to high energy in relation to the results in Chapter 6.

The equations are written in Système International (SI) units. Where needed, the equations are rewritten in units conventional to laser-plasma physics and relevant to this thesis.

2.1 A basic plasma

A simple plasma is a quasineutral gas consisting of charged (and neutral) particles. The particles exhibit collective behaviour when subject to an electric or magnetic field[39].

2.1.1 Debye length

There are three conditions that define a plasma. The physical dimensions of a plasma must be much larger than the distance that charged particles screen out the effect of a nearby electric field. This distance is the Debye length, λ_D,

$$\lambda_D = \sqrt{\frac{k_B \varepsilon_0}{e^2}\left(\frac{1}{n_e/T_E + Z^2 n_i/T_i}\right)} \tag{2.1}$$

$$\lambda_D[\mathrm{nm}] \approx 7.43 \times 10^9 \sqrt{\frac{1}{n_e[\mathrm{cm}^{-3}]/T_e[\mathrm{eV}] + Z^2 n_i[\mathrm{cm}^{-3}]/T_i[\mathrm{eV}]}} \tag{2.2}$$

ε_0 is the permittivity of free space, e is the elementary charge, k_B is the Boltzmann constant, T_e and n_e are the electron temperature and density, and Z, T_i and n_i are the ion charge number, temperature and density. Eqn. 2.2 is a simplified form to Eqn. 2.1, where the units of λ_D, T_e, n_e, T_i and n_i are specified in the squared brackets.[39,40,44]

The second condition emerges from the plasma screening external fields. This phenomenon is only possible if the number of particles within a "Debye sphere", N_D – a spherical volume of radius λ_D – is much greater than one. N_D is defined as[39,40,44]

$$N_D = \frac{4}{3}\pi n_e \lambda_D^3 \tag{2.3}$$

$$N_D \approx 1.72 \times 10^9 \sqrt{\frac{T_e^3[\mathrm{eV}]}{n_e[\mathrm{cm}^{-3}]}} \tag{2.4}$$

2.1.2 Plasma frequency

The third condition that defines a plasma is that the electrostatic interaction between the particles dominates over collisions with a collision rate, ν. The plasma frequency, ω_{pe}, characterises the electrostatic interaction, which is greater than ν to satisfy the condition. ω_{pe} is defined as[30,39,45]

$$\omega_{pe} = \sqrt{\frac{n_e e^2}{\varepsilon_0 m_e}} \tag{2.5}$$

$$\omega_{pe}[\mathrm{Hz}] \approx 5.64 \times 10^4 \sqrt{n_e[\mathrm{cm}^{-3}]} \tag{2.6}$$

where m_e is the mass of an electron.

Eqns. 2.1-2.6 are given in terms of the electrons. The equations can be rewritten to include the positively charged ions. However, m_e is a factor of ~1840 smaller than the mass of a proton, m_p. This implies that electrons move faster than ions. Therefore, the response of a plasma to electromagnetic fields is mainly determined by the electrons.

2.2 Laser interaction with overdense matter

Throughout this thesis the focus is on understanding the interaction of a short-duration, high-intensity laser pulse with overdense matter, which is described in this section.

2.2.1 Lorentz force

In the single particle picture a charged particle moves according to the external electric and magnetic fields, $\mathbf{E}$ and $\mathbf{B}$, acting on it. The change of motion is described by the Lorentz force, $\mathbf{F}$, as[30,46]

$$\mathbf{F} = q(\mathbf{E} + \mathbf{v} \times \mathbf{B}) \tag{2.7}$$

where q and $\mathbf{v}$ are the particle charge and velocity. For an electron, $q = -e$ and $\mathbf{v} = \mathbf{v}_e$, and for an ion of charge Z, $q = Ze$ and $\mathbf{v} = \mathbf{v}_i$.

A laser exerts fields $\mathbf{E}_0$ and $\mathbf{B}_0$ on electrons. The fields are perpendicular to the direction the laser propagates and to each other. As the laser moves $\mathbf{E}_0$ oscillates the electrons back and forth with time. If assuming that the laser was a simple plane wave, $\mathbf{B}_0$ does not exert a significant force unless the electrons are moving close to speed of light, c, which are then called relativistic electrons. Otherwise the particle motion can be characterized by $\mathbf{E}_0$ alone.

2.2.2 Critical density

In the following explanation it is assumed that the laser is a plane wave and approaches a plasma density ramp. The laser oscillates the electrons at the start of the density ramp, which results in the electrons re-radiating the laser as dipole radiation. As the density increases, more electrons are driven. The dipole radiation results in a constructive interference that refracts the laser. This refraction continues up to the turning point that the laser propagation into the plasma reverses. This is shown in Figure 2.1. The density at the turning point is determined by the laser incidence angle relative to the density gradient, θ_0, and the critical density, n_{cr}, as $n_{cr}\cos^2\theta_0$. n_{cr} is determined by the laser angular frequency, ω_0, which by substitution into Eqn. 2.5 gives n_{cr} as[30]

$$n_{cr} = \frac{\varepsilon_0 m_e \omega_0^2}{e^2} \tag{2.8}$$

$$n_{cr}[\mathrm{cm}^{-3}] \approx \frac{1.1 \times 10^{21}}{\lambda_0^2[\mu\mathrm{m}]} \tag{2.9}$$

If $n_e < n_{cr}$ then the laser propagates through an underdense plasma. On the other hand, if $n_e > n_{cr}$ then the plasma is overdense and the laser cannot propagate past the turning point.

Part of the laser propagates as an evanescent wave past the turning point along the density ramp until the density reaches n_{cr}. The depth that this wave moves between the turning point and n_{cr} is the skin depth,[30]

$$\delta_s = \frac{c}{\omega_{pe}\sqrt{1 - (\omega_0^2/\omega_{pe}^2)\cos^2\theta_0}} \tag{2.10}$$

Consider the following example: An infrared laser of wavelength $\lambda_0 = 1.054$ μm and frequency $\omega_0 = 2\pi c/\lambda_0$ results in $n_{cr} \approx 1 \times 10^{21}$ cm^{-3}. The laser irradiates a silicon target of density $n_e = ZN_A\rho/A$. N_A is Avogadro's number, ρ is the mass density and A is the mass number of the material. Assuming the target is fully ionised and at solid density ($\rho = 2.33$ g cm^{-3} and $A = 28.09$), $n_e \approx 7 \times 10^{23}$ cm^{-3}. Hence, $n_e > n_{cr}$. This results in the possibility of a high contrast infrared laser interacting with overdense matter.

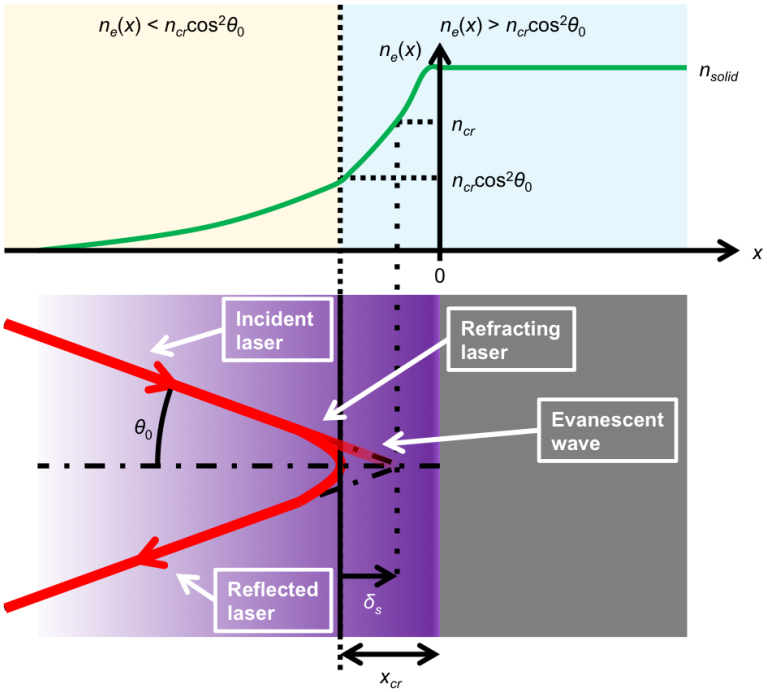

Figure 2.1: Laser propagation at an incidence angle, θ_0, into a overdense plasma. At the surface of position x_{cr} the laser reflects when the plasma density reaches $n_{cr}\cos^2\theta_0$. The evanescent laser field moves a skin depth, δ_s, from the surface.

2.2.3 Ionisation

Matter is ionised by a laser to form a plasma. One way this occurs is via photoelectron ionisation.[30] A laser photon of energy $\mathcal{E}_0$ encounters an electron bound to an atom. The electron is confined in an energy level. The electron absorbs a photon and is liberated from the atom if $\mathcal{E}_0$ exceeds the ionisation energy, $\mathcal{E}_n$. The free electron has an energy of $\mathcal{E}_e = \mathcal{E}_0 - \mathcal{E}_n$.

The photon energy is determined by the laser by $\mathcal{E}_0 = hc/\lambda_0$, where h is Planck's constant. Most lasers do not operate at wavelengths satisfying $\mathcal{E}_0 > \mathcal{E}_n$ for photoelectron ionisation. An alternative photoionisation process is possible with increasing laser intensity, I_0. A high-intensity laser releases a bound electron when the number of absorbed photons, N_0, provide an energy $N_0 hc/\lambda_0$ exceeding $\mathcal{E}_n$. The electron is released with an energy of

$$\mathcal{E}_e = N_0 hc/\lambda_0 - \mathcal{E}_n \tag{2.11}$$

This process is called multiphoton ionisation, which starts to occur when $I_0 > 10^{10}$ W/cm^2.[30]

A high-intensity laser also photoionises atoms via tunneling or barrier-suppression ionisation.[30] In both cases the electric field of the laser suppresses the electrostatic potential that binds the electron to the atom. For tunneling ionisation the potential is suppressed to an energy comparable but greater than $\mathcal{E}_n$. The electron has a probability of tunneling through the potential barrier and escape the atom. As for barrier suppression ionisation, the

potential is decreased below $\mathcal{E}_n$ such that the electron spontaneously escape the atom. For barrier-suppression to become important to ionisation,

$$I_0 > \frac{c\mathcal{E}_n^4}{128\pi Z^2 e^6} \tag{2.12}$$

$$I_0[\mathrm{W/cm^2}] \gtrapprox 4\times 10^9 \frac{\mathcal{E}_n^4[\mathrm{eV}]}{Z^2} \tag{2.13}$$

2.2.4 Collisional absorption

The initial photoionisation by the laser on solid matter forms a overdense plasma. At the surface of this plasma the free electrons are driven directly by the laser and gain energy. Thereafter the electrons transfer the energy to ions (and atoms) via inverse bremsstrahlung. This is a collisional absorption process. Electron-ion collisions dampen the electron motion with a collision rate, ν_{ei}, which is

$$\nu_{ei} = \frac{4\sqrt{2\pi}}{3}\frac{Zn_e e^4}{m_e^2 v_e^3}\ln(\Lambda) \tag{2.14}$$

$$\nu_{ei}[\mathrm{Hz}] = 2.91\times 10^{-6} Z n_e[\mathrm{cm^{-3}}](T_e[\mathrm{eV}])^{-3/2}\ln(\Lambda) \tag{2.15}$$

$\ln(\Lambda)$ is the Coulomb logarithm accounting for the largest and smallest electron-ion separation that an electron scatters off an ion. Eqn. 2.15 shows that collisions are important in dense and cold matter and, in turn, influence the laser-to-matter absorption efficiency.[30,45]

2.2.5 Resonance absorption

As laser intensity and wavelength increase such that $I_0\lambda_0^2 \geq 10^{15}$ W μm^2/cm^2, collisional absorption becomes inefficient. This occurs once the electron-ion collision rate, ν_{ei}, is less than the laser frequency, $\omega_0 = 2\pi c/\lambda_0$. A high I_0 increases the electron temperature, which in turn reduces ν_{ei}. As a result, collisionless absorption processes, such as resonance absorption,[30,45] may dominate over collisions.

At the surface $n_{cr}\cos^2\theta_0$ that the laser reflects, the evanescent laser field propagates a skin depth into the overdense plasma. The laser couples to a Langmuir wave at the critical density surface, defined at n_{cr}. The wave in turn drives the electrons to high energies through resonance absorption. Electrons are resonantly driven with a frequency of $\omega_{pe} = \omega_0$. This relation is rewritten using Eqns. 2.5 and 2.8 to $n_e = n_{cr}$. Therefore, resonance absorption is most effective at the critical density of the overdense plasma. Resonance absorption is a collisionless absorption process because the energy coupling occurs between the laser and Langmuir waves.[29,30,45]

If the evanescent laser penetrating a skin depth into the plasma has an electric field component along surface normal, the laser couples to the Langmuir wave at n_{cr}. Otherwise, to a linear approximation, there is no such coupling. Therefore, a p-polarised laser pulse is

needed for resonance absorption. This polarity has an electric field component parallel to surface normal, whereas the field from an s-polarised laser is always perpendicular. Assuming that the field is perfectly transverse, the s-polarised laser does not generate a resonance wave.[30,40]

A key parameter that determines the absorption efficiency is the plasma density scale length, L. L is a length derived from to the plasma density, n_e, and density gradient, $|\nabla n_e|$, as[30,45]

$$L = \frac{n_e}{|\nabla n_e|} \tag{2.16}$$

$|\nabla n_e| \approx dn_e/dx$ when assuming that the laser-plasma interaction is along the normal of the plasma surface. Resonance absorption occurs where $n_e = n_{cr}$ and, therefore, L is rewritten to $L_{cr} = n_{cr}/|\nabla n_{cr}|$ for specifying the density scale length at the density n_{cr} in this thesis.

The absorption efficiency due to resonance absorption depends on the laser polarity, plasma density scale length, L_{cr}, and laser incidence angle, θ_0. A p-polarised laser has a component of $\mathbf{E}_0$ parallel to the normal of the plasma surface normal, and an s-polarised laser is purely perpendicular to the normal. Assuming that the surface is assumed to be flat, absorption by an s-polarised laser is purely via collisions, whereas the p-polarised laser include resonance absorption (see Gibbon[30] for details). Resonance absorption results in an optimum absorption efficiency for certain values of L_{cr} and θ_0. The larger L_{cr} is in relation to the laser wavelength, λ_0, the smaller θ_0 is for maximum absorption. This is a key motivation for irradiating a p-polarised laser at an oblique incidence angle on solid targets. At $\theta_0 = 0°$ the polarisations have the same absorption efficiency because both are perpendicular to the plasma surface normal.[30,45]

On high power laser experiments λ_0 and θ_0 are determined by the setup. L_{cr} is difficult to define because it depends on the laser interaction with the overdense target. Experiments can benefit from a method for controlling the interaction in order to optimise and reproduce L_{cr}. In turn this can improve the laser-to-plasma absorption efficiency. Further details and corresponding results are discussed in Chapters 4 and 5.

2.2.6 Ponderomotive force

A tightly-focused, short pulse duration laser exhibits high intensities and steep intensity gradients in its electric component. This causes the electrons to oscillate to relativistic velocities in the direction of the electric field component with a frequency of $2\omega_0$. The driving force is called the ponderomotive force, which is derived by time-averaging I_0 over a laser period as[16,30,47]

$$f_p = -\frac{\gamma_e e^2}{4 m_e \omega_0^2} \nabla E_0^2 \tag{2.17}$$

$$= -\nabla(\gamma_e - 1) m_e c^2 \tag{2.18}$$

∇E_0^2 denotes the intensity gradient, and γ_e is the Lorentz factor of the electrons. The ponderomotive force acts in the direction of high intensity fluctuation. As electrons attain relativistic velocities the magnetic component of the laser becomes important and, as a result, accelerates the relativistic electrons in the propagation direction of the laser. This acceleration is often referred to as $\mathbf{J} \times \mathbf{B}$ heating.[16,30,47,48]

At $I_0\lambda_0^2 \gtrapprox 10^{18}$ W μm^2/cm^2, the ponderomotive force is important for generating relativistic electrons. If assuming that ponderomotive heating is the main driving process, the electron temperature, T_{rel}, can be estimated using Wilks' scaling,[16]

$$T_{rel} = m_e c^2(\gamma_e - 1) \tag{2.19}$$

$$T_{rel}[\text{eV}] \approx 5.11 \times 10^5 \left(\left(1 + \frac{I_0[\text{W/cm}^2]\lambda_0^2[\mu\text{m}]}{1.37 \times 10^{18}} \right)^{1/2} - 1 \right) \tag{2.20}$$

2.2.7 Relativistic electrons

Relativistic electrons are mostly generated by the laser approaching $I_0\lambda_0^2 \gtrapprox 10^{18}$ W μm^2/cm^2. One role of these electrons is for transporting energy into the overdense plasma. Typically the laser only penetrates a depth δ_s into the plasma. This restricts the volumetric heating to near the critical density surface. The electrons carry the energy from the laser into the region of the overdense plasma and solid matter otherwise inaccessible by the laser.[30,40]

Relativistic electrons with density n_f and velocity $\mathbf{v}_f$ transport through the plasma with a forward current density

$$\mathbf{J}_f = -en_f\mathbf{v}_f \tag{2.21}$$

The electrons induce a current that produces magnetic fields unless a self-generating current inside the plasma opposes the electron motion. This is known as the return current density, $\mathbf{J}_r = -en_r\mathbf{v}_r$. In the limit that magnetic field formation is very small, $\mathbf{J}_r$ balances with the forward-moving relativistic electron current density, $\mathbf{J}_f$, as[49,50]

$$\mathbf{J}_f + \mathbf{J}_r \approx 0 \tag{2.22}$$

The relativistic electrons have a high velocity and low density. For a overdense plasma, n_r is larger than n_f. As the current densities are balanced, this implies that $\mathbf{v}_r$ is small. Therefore, the relativistic electrons generate thermal electrons inside the plasma. The thermal electrons are important for producing spectral line emission described in Section 2.3.

Relativistic electrons that propagate out of the target rear side generate strong electric fields. The fields accelerate the ions from the target and on target surface above MeV energies. The different mechanisms that accelerate ions to these energies are described in Section 2.4.

2.2.8 Relativistically induced transparency

Laser propagation depends on the refractive index, n, of the plasma. n is equal to the square root of the dielectric constant, $n = \sqrt{\epsilon}$. Assuming collision rates are much smaller than ω_0 the non-relativistic refractive index is[30]

$$n = \sqrt{1 - \frac{\omega_{pe}^2}{\omega_0^2}} \tag{2.23}$$

$$= \sqrt{1 - \frac{n_e}{n_{cr}}} \tag{2.24}$$

Eqn. 2.24 is derived from Eqn. 2.23 by substituting for the frequencies with Eqns. 2.5 and 2.8. If $n_e > n_{cr}$, the refractive index is imaginary. As a result, the laser reflects at the surface and is stopped from moving into the overdense plasma. On the other hand, in a underdense plasma where $n_e \leq n_{cr}$ the refractive index is real and, therefore, the plasma is transparent. The laser propagation inside the plasma depends on n.

A overdense plasma is subject to hydrodynamic processes and laser heating. Hydrodynamics expands the overdense plasma which decreases the electron density, n_e. Laser heating leads to relativistic motion of the electrons, increasing the electron Lorentz factor, γ_e. Both processes change the refractive index of the plasma, n. Accounting for the relativistic correction to the refractive index, n, in Eqn. 2.24 gives

$$n = \sqrt{1 - \frac{n_e}{\gamma_e n_{cr}}} \tag{2.25}$$

n is imaginary as long as $n_e > \gamma_e n_{cr}$ and the plasma reflects the laser at the surface. However, as n_e decreases and γ_e increases, the imaginary value of n reduces. n becomes real once $n_e \leq \gamma_e n_{cr}$. This means that the laser propagates through the plasma which behaves like a underdense plasma. The phenomenon is known as relativistically induced transparency (RIT)[29]. This is important for understanding the ion acceleration results in Chapter 6.

2.2.9 Hydrodynamics

The laser interaction forms and heats a plasma which then expands. The expansion is collective plasma motion, which is characterised by hydrodynamics. Hydrodynamic processes are important when intense laser interaction occurs over durations of picoseconds and nanoseconds. The interaction determines the plasma density scale length, L_{cr}.[30,45] This affects the laser-to-target coupling efficiency and is important for understanding any laser-target interaction.

The collective motion exhibited by the electrons and ions in a plasma are described as two separate fluids for these particles. Each fluid is characterised by a set of conservation

equations:[30,45,51]

$$\frac{\partial \rho}{\partial t} + \nabla \cdot (\rho \mathbf{u}) = 0 \tag{2.26}$$

$$\rho \frac{\partial \mathbf{u}}{\partial t} + \rho(\mathbf{u} \cdot \nabla)\mathbf{u} = \frac{\rho}{m}\mathbf{F}_{net} \tag{2.27}$$

$$\frac{\partial}{\partial t}\left(\rho\varepsilon + \frac{\rho u^2}{2}\right) + \nabla \cdot \left(\rho \mathbf{u}\left(\varepsilon + \frac{u^2}{2}\right) + P\mathbf{u}\right) = \frac{\rho}{m}\mathcal{E}_{net} \tag{2.28}$$

Eqn. 2.26 is mass continuity, which ensures that mass is conserved for a fluid of mass density, ρ, and velocity, $\mathbf{u}$.

Conservation of momentum is defined by Eqn. 2.27 for the fluid of mass m. The right-hand side of the equation gives the forces changing the fluid momentum. This includes terms such as the Lorentz force due to the laser, pressure gradient moving the fluid between regions of pressure imbalance, and collisions.

Eqn. 2.28 is the conservation of energy. The internal energy of the fluid is given by the specific energy, ε. Energy transfer into and out of the fluid is described by the net energy source and loss term, $\mathcal{E}_{net}$. Processes transferring energy include thermal conduction, collisions and volumetric heating due to the laser.

Eqns. 2.26-2.28 are solved using an equation of state (EOS). An EOS describes the relation between the fluid parameters according to an assumed hydrodynamic model.[45,51]

2.3 K-shell line radiation

In this section the atomic physics associated with characteristic K_α emission will be described. Throughout this section silicon will be used because the results in Chapter 5 used silicon as the laser-irradiated target.

2.3.1 Inner-shell ionisation

Laser-driven relativistic electrons propagate into the plasma region partially or not ionised by the laser-target interaction. If the electron energy exceeds the ionisation energy of a silicon atom in its ground state, $\mathcal{E}_n = 2.438$ keV,[52] then an electron in the K-shell can be liberated. This creates a K-shell vacancy in the ionised atom as shown in Figures 2.2 (a) and (b). K-shell ionisation can also occur when a photon of energy exceeding 2.438 keV is absorbed.[45,53,54] Whether collisional or radiative ionisation dominates is complicated to determine. Studies have shown that X-rays have a higher probability of producing K-shell vacancies over relativistic electrons in thin Al targets.[15,55] In buried Al targets, where the target density is higher, K-shell vacancies from collisional ionisation becomes important.[55,56]

Afterwards, an electron from an excited state de-excites to fill the vacancy via spontaneous or stimulated emission. If the electron transitions from the L-shell to the K-shell then

the this processes is known as a KL-transition. Upon de-excitation one of two processes can happen. The energy released during the de-excitation is absorbed by another bound electron, resulting in a non-radiative KLL Auger emission[53] (see Figure 2.2 (c)). The alternative process is the emission of a K_α photon, which is depicted in Figure 2.2 (d). For silicon the emitted photon energy is 1.739 keV.[15,53,55]

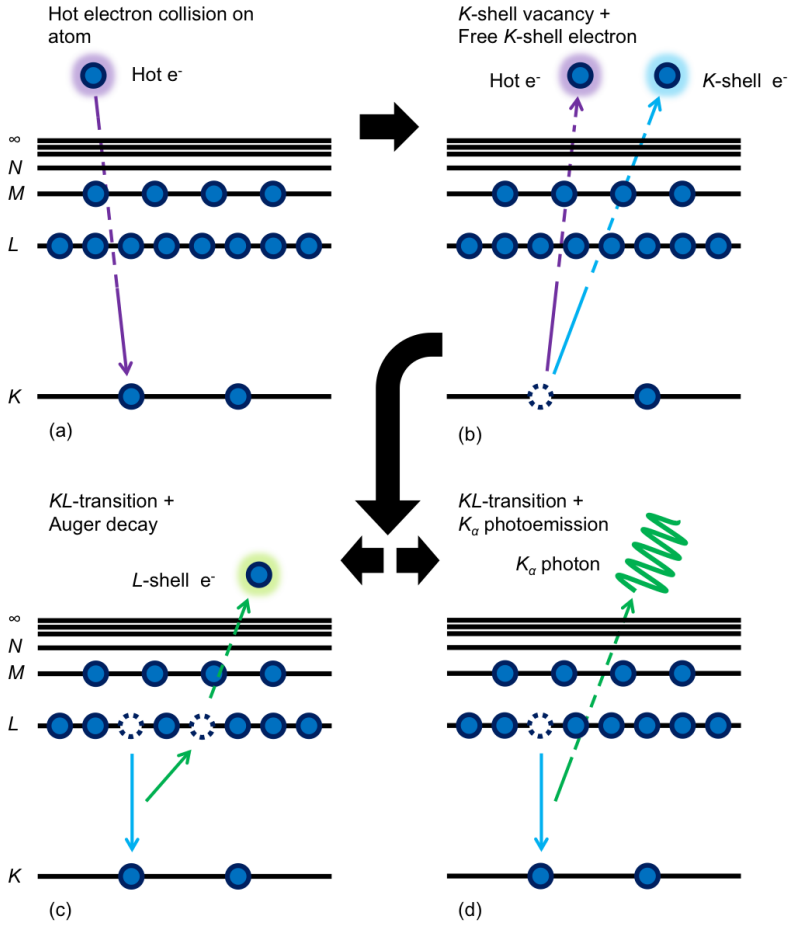

Figure 2.2: (a) Ground state silicon is ionised by a hot electron whose energy exceeds the ground state ionisation energy. The K-, L-, M- and N-shells are labeled. (b) After collision a K-shell electron is ejected from the atom. An electron from the excited L-shell de-excites to fill the K-shell vacancy. The energy from the KL-transition leads to either (c) electron emission via Auger decay or (d) emitting a K_α photon.

The time-integrated K_α emission depends on the number of K-shell vacancies generated and the branching ratio between Auger decay and photoemission. The rate of forming K-shell vacancies depends on the exciting flux of electrons (and photons) producing these vacancies and decay rate of inner-shell vacancies. The decay rate is a few femtoseconds.[33,55] If the exciting flux is sufficiently high then K-shell vacancies are continuously formed producing bright K_α signals. Recombination rates for de-exciting electrons scales roughly with the density product of ions and free electrons, $n_i n_e$.[57] Hence, for KL-transition in overdense matter, such as a solid target, the time-dependent recombination rate of the K_α emission is

highest. In turn, the time-integrated intensity of the emission is optimised.

The photon produced from the transitions illustrated in Figures 2.2 (a)-(d) is referred to as K_α line emission of photon energy $\mathcal{E}_x = 1.739$ keV.[35]. The energy of the KL-transition changes upon sequential ionisation of the outer shells. Thermal free electrons of a few eV in a plasma ionise the M-shell in Figures 2.2 (a)-(d). Removing bound electrons reduces the shielding of the electrostatic potential from the nucleus due to the electrons, which leads to a larger separation between energy states. Therefore, the K_α line emission shifts to higher photon energies following successive ionisation.[15,55,57] The lines are labeled using numerical notation for identifying ionisation state.[54] For Si I ($\mathcal{E}_x = 1.739$ keV) the M-shell is not ionised, Si II (1.742 keV) one electron is removed, Si III (1.743 keV) two electrons removed, and Si IV (1.745 keV) has three electrons removed. $\mathcal{E}_x$ are taken from the spectral calculations presented in Chapter 5. The notation does not account for inner-shell vacancies, which becomes complicated after removing all M-shell electrons. Thermal electrons open and ionise the L-shell as energies reach tens of eV. Consequently, the ionisation state of the initial and final states are different. For identifying line emission with an open L-shell, isoelectronic notation[54] is used, which is based on the total number of bound electrons. These include emission from F-like to Li-like states of silicon. If the electron temperature starts approaching 100 eV and leave only one L-shell electron, the KL-transitions produces K-shell emission, which is conventionally referred to He-like and Ly-like ion with emission following described as He_α and Ly_α lines.[15,54,55] The Si I-IV, Li-like and He_α line emission that result from successive outer-shell ionisation are depicted in Figure 2.3. In this thesis the lines of interest are from Si I-IV states where the L-shell is closed. The relative spectral intensities between these states depends on the thermal electron energies shown in Chapter 5.

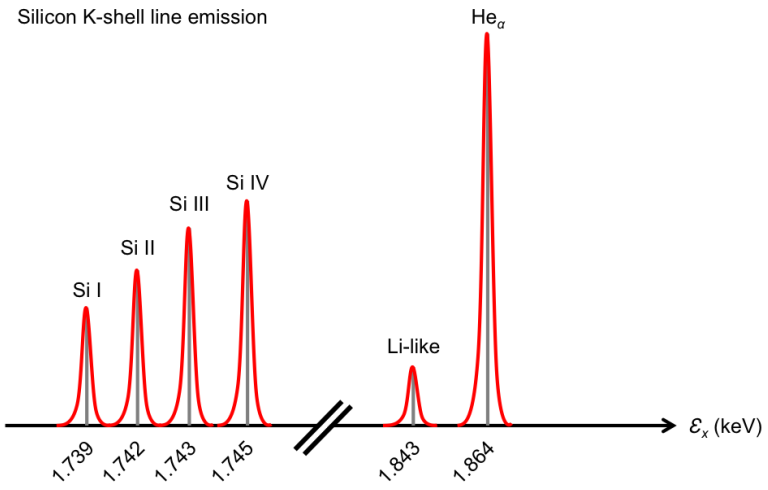

Figure 2.3: Illustration of silicon K_α line emission from different ionisation states from Si I to He_α. The lines are labeled using conventional notations. Relative spectral intensities are arbitrary in the drawing.

2.3.2 Atomic rate equation

Atomic rates determine the time-scales that an energy state j is populated and depopulated with electrons from state k. The number of electrons occupying states j and k are defined by the population densities, n_j and n_k. The rate equation for populating and depopulating state j is

$$\frac{dn_j}{dt} = \sum_{k \neq j}^{N} n_k W_{kj} - \sum_{k \neq j}^{N} n_j W_{jk} \tag{2.29}$$

The number of participating states, N, are accounted in the summation. W_{kj} and W_{jk} are the rates of the processes populating and depopulating state j.[58,59]

The number of K_α photons produced are determined by the collisional ionisation, de-excitation and photoabsorption rates.[15,36,45,53–55] Collisional ionisation is determined by the thermal electron energy distributions and corresponding ionisation cross section. Thermal electrons are generated by the laser interaction and from the return current balancing the relativistic electrons moving through the plasma (see Subsection 2.2.7). Thermal electrons ionise outer shells as well as inner shells, for example for the K-shell in silicon when the energies exceed ionisation energy $\mathcal{E}_n = 2.438$ keV.[52] The ionisation rates also depend on the densities of thermal electrons and energy states available.[36]

The de-excitation rate determines how rapid an L-shell electron de-excites to the K-shell vacancy. For silicon this rate can be as high as 10^{15} Hz.[55]

The intensity of a radiation source, such as K_α emission, is reduced by the absorption and scattering of photons in the plasma. The optical depth, τ, determines the intensity lost. There are two limits to τ, which are optically thick (with a high optical depth, $\tau >> 1$) and optically thin (with a low optical depth, $\tau << 1$). $\tau = \kappa \rho s$ where κ is the opacity, which is a specific cross section, and s is the length the radiation propagates in to the plasma.[45,51] Reabsorption of a K_α photon via photoabsorption is possible only if a vacancy in the L-shell exists. This is unlikely in cold matter and, therefore, the opacity is determined by scattering. The optical depth for scattering is low if the material is sufficiently thin. The scenario changes, and becomes complex, in hot plasmas where the atomic system have L-shell vacancies. For clarity, a hypothetical zero-width plasma, which has no opacity, is considered in this work because this removes the photoabsorption term in the rate equation. Experiments use materials of finite thickness, which reintroduces additional challenges on assuming a zero-width plasma.

When the processes populating and depopulating state j are balanced, the population in state j does not change with time. Hence, the rate equation in Eqn. 2.29 becomes zero, as in, $dn_j/dt = 0$. This scenario is known as steady-state balance. An excited state in a overdense plasma can achieve steady-state balance as the lifetime of electrons in the state can be comparable to the time scales populating the state.[58]

2.3.3 Local thermodynamic equilibrium

Thermodynamic equilibrium describes the rate equation of a closed atomic system at a fixed temperature. The closed system means that the rates for populating and depopulating atomic states are in steady-state balance. The ratio of population between states is determined by a Boltzmann distribution. Thermodynamic equilibrium is satisfied when the time for achieving steady-state balance is faster than the changes in the plasma dynamics. This condition is satisfied for large plasma such as the core of stars.[51,58]

A plasma generated in the laboratory cannot achieve complete thermodynamic equilibrium because the exterior of the plasma is not in balance with excitation processes. This is because the mean free path for collisional and photoabsorption are larger than the scale length of the temperature gradient. However, the laboratory plasma can achieve local thermodynamic equilibrium (LTE). This requires the mean free path of the absorption processes to be smaller than the plasma scale lengths in a small region of the plasma. A localised volume of overdense plasma can satisfy LTE. The population distribution of the states is given by the Boltzmann relation and Saha equation.[51,58]

Energetic electrons and photons drive the generation of inner-shell vacancies, which is an inherently non-LTE process. The cross section for inner-shell ionisation is significantly higher for photons than by electrons.[15,55] Modelling a plasma in non-LTE involves solving a set of rate equations with all absorption and emission processes included. The calculations may be time consuming depending on the atomic system and complexity of the atomic physics model used. Non-LTE is necessary for producing K_α emission from a overdense plasma and is used for the spectral calculations provided in Chapter 5.

2.3.4 K_α line broadening

K_α line emission is hypothetically a single energy at 1.739 keV with a line shape and width determined by natural broadening. When spectrally resolving K_α line from a dense plasma, the observed emission is typically a broad asymmetric peak rather than a single line. There are a number of processes that broaden K_α line emission. Line emission naturally broadens because of the lifetime of an electron in the excited state before de-exciting to the K-shell vacancy. The uncertainty in measuring the lifetime, Δt, is related to the de-excitation rate. Therefore, the natural width, $\Delta\mathcal{E}$, is determined by the Heisenberg uncertainty principle,

$$\Delta\mathcal{E} = \frac{h}{2\pi\Delta t} \tag{2.30}$$

This broadens the line to a Lorentzian peak with a full-width-half-maximum (FWHM) of $\Delta\mathcal{E}$.[53,57,58]

K_α line emission is split in two components, $K_{\alpha 1}$ and $K_{\alpha 2}$, due to spin-orbit coupling. Relativistic effects couple electron orbital angular momentum and spin, which splits the

energy levels according to the total angular momentum from the coupling. The total angular momentum quantum number, j, takes a list of values for an orbital state of quantum number, l, and spin s,[54]

$$|l - s| \leq j \leq l + s \tag{2.31}$$

In the case of a K-shell vacancy in silicon, the electron moves from the L-shell to the vacant K-shell state. The orbital state is $1s$ for the K-shell. Hence, by allowed transitions rules, the electron is initially in the $2p$ orbital state. The p-orbital state has $l = 1$ and $s = 1/2$, which give $j = 1/2, 3/2$. As a result, the energy level splits into the $P_{1/2}$ and $P_{3/2}$ levels (using spectroscopic notation, L_j, where L is the orbital angular momentum), which have an energy separation of $\sim$0.7 eV. Electrons transition from both levels to the K-shell. Therefore, K_α emission is seen as two distinct lines close to each other.

K_α emission is spectrally asymmetric when observed. The line is broader towards lower energies than towards higher energies. Asymmetric broadening occurs in the presence of external electric fields. This Stark broadening includes the Coulomb interaction between charged particles and electric component of a laser. The fields couple to the electric moment of electrons to separate the energy levels within each shell. This widens the emission, where the broadening is greater towards the lower energies of the K_α line.[57,58]

In experiments the diagnostic has a limited resolution for resolving spectral emission. This results in instrumental broadening, which is discussed in detail in Chapter 3.

As explained in Subsection 2.3.1, the K_α line emission shifts towards higher photon energies as thermal electrons ionise the outer-shells. In this thesis the lines studied are from the ionisation states Si I (1.740 keV), Si II (1.742 keV), Si III (1.743 keV) and Si IV (1.745 keV). These span a spectral range of 5 eV. The lines are subject to the same line broadening given above. If the broadening is of a few eV, the lines superpose and form a wide peak. Individual lines are indistinguishable and require spectral calculations given in Chapter 5 for identification.

2.4 Laser driven ion acceleration using solid targets

As described in Subsection 2.2.7, the laser drives relativistic electrons at the surface of the irradiated solid target. The electrons can propagate out of the target rear side and generate strong electric fields. The fields accelerate the ions from the target and the target surface to energies well above MeV. The ion energies achieved depend on the acceleration mechanism driving the ions. This section describes the mechanisms that produce energetic ions, which includes an explanation on how the onset of RIT can aid the acceleration.

2.4.1 Target normal sheath acceleration

Relativistic electrons from the laser irradiated front surface of the target can move to the rear target side. As they eject from the target a charge imbalance forms. This creates an electrostatic sheath field, E_{TNSA}, normal to the rear surface, as shown in Figure 2.4. The field causes electrons whose energies are insufficient to overcome the field to reflux back into the target. Assuming the mean energy of refluxing electrons is T_{rel} and the sheath field to be continuous over a length L_{sh}, E_{TNSA} is estimated from Poisson's equation as[29]

$$E_{TNSA} \approx T_{rel}[\text{eV}]/L_{sh} \tag{2.32}$$

Eqn. 2.32 suggests that electrons of energies less than T_{rel} reflux back to the target. This leads to ionisation of atoms at the target rear surface. The ions produced are accelerated by the sheath field to energy $\mathcal{E}_i$. This acceleration mechanism is called target normal sheath acceleration (TNSA).[29,60] Assuming that the ions are initially at rest and driven normal to the surface then by energy conservation,

$$\mathcal{E}_i \approx ZeE_{TNSA}L_{sh} \tag{2.33}$$

$$\mathcal{E}_i \approx ZT_{rel} \tag{2.34}$$

Using Wilks' scaling (Eqn. 2.20) for T_H in Eqn. 2.34 when $I_0\lambda_0^2 \gtrapprox 10^{20}$ W μm^2/cm^2, a calculation suggests that $\mathcal{E}_i \gtrapprox 4Z$ MeV. This estimate assumes that electrons are driven by the ponderomotive force. The calculation is a crude estimate suggesting that MeV ions can be generated via TNSA. Experimental studies have shown that ions can achieve higher energies than predicted by the given calculations (see for examples Ref.[17,18,37,61,62]).

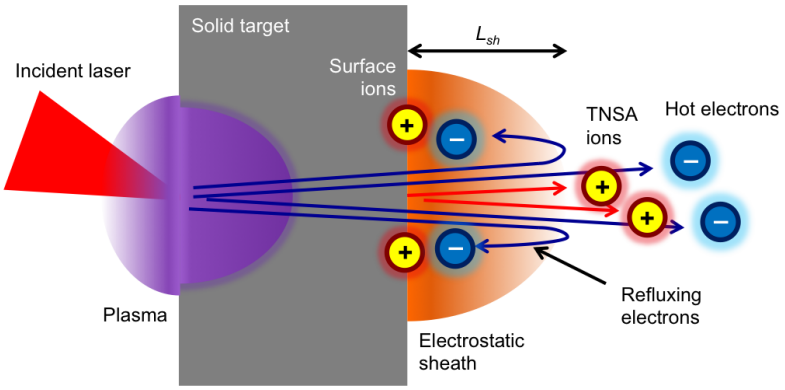

Figure 2.4: Illustration depicting target normal sheath acceleration.

In experiments the laser-irradiated target has surface contamination containing hydrogen. The refluxing electrons ionise hydrogen to produce protons at the rear surface. The protons are within the sheath field and, hence, preferentially driven to high energies via TNSA. Consequently, protons screen the sheath field for heavy ion acceleration reducing the coupling

of the sheath field to the heavy ions.[29] Hence, removing the hydrogen contamination will increase $\mathcal{E}_i$ for heavy ions, as reported in other studies.[61]

2.4.2 Enhanced target normal sheath acceleration

Enhanced TNSA (ETNSA) is where the sheath field for TNSA is amplified. In turn ions driven by TNSA gain energy by a laser field penetrating through the target to the rear surface. This results in the laser driving electrons to high energies across the irradiated target volume and differs from the case for TNSA where the laser drives electron from the front surface up to a skin depth into the target. For ETNSA the target thickness must be comparable to the skin depth, and as a result, all electrons in the target are accelerated. Hence, more electrons move out of target rear, amplifying the sheath field.[63]

2.4.3 Radiation pressure acceleration

At the irradiated target surface the steady component of the ponderomotive force due the laser exerts high radiation pressures. This drives an overdense region of relativistic electrons into the target. In turn a strong charge separation field forms between the electrons and ions. This drags the ions alongside the dense hot electrons. This process is referred to as radiation pressure acceleration (RPA).[29] This differs from TNSA and ETNSA in that the ion acceleration occurs at the irradiated front surface rather than the rear. In order to maximise the acceleration due to RPA it is important to preserve the overdense plasma by minimising the electron heating due to the oscillating component of the ponderomotive force.

There are two regimes for RPA: hole-boring[16] and light-sail.[29] The impact of the regimes to ion acceleration is determined by the target thickness. Hole-boring pushes a dense electron surface into a target much thicker than the plasma skin depth. This bores a hole into the target. Hole-boring transitions to light-sail when the dense electron surface moves out through the target rear side. This displaces the whole irradiated target by radiation pressure. Figure 2.5 illustrates light-sail RPA. For light-sail to occur the target thickness must be comparable to or slightly thicker than the skin depth.

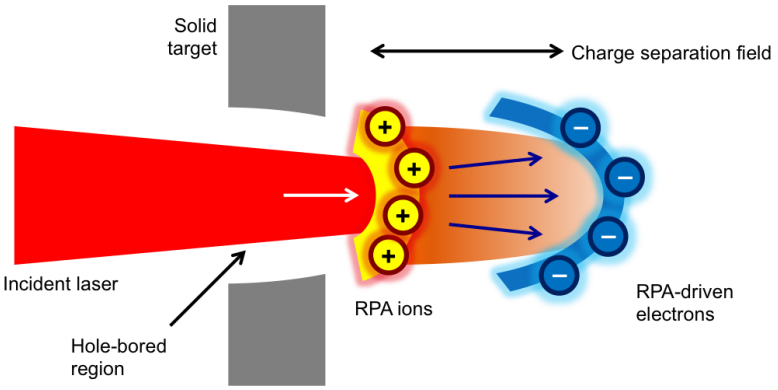

Figure 2.5: Illustration depicting radiation pressure acceleration in the light-sail regime.

In Chapter 6 the targets used are of a few nanometers thin and comparable to the skin depth. Therefore, ion acceleration due the radiation pressure will be discussed in terms of light-sail RPA. The ion energies, $\mathcal{E}_i$, are estimated from the dimensionless laser fluence, $\mathcal{F}$,[29]

$$\mathcal{E}_i = m_i c^2 \frac{\mathcal{F}}{2(\mathcal{F}+1)} \tag{2.35}$$

$$\mathcal{F} = \frac{2}{\rho_i x_0 c^2} \int_0^{t_{ret}} I_0(t) dt \tag{2.36}$$

ρ_i is the mass density of the ions and x_0 is the initial target thickness. The time integral determines the time over which the laser of intensity, I_0, pushes the target. Here the interaction extends up to the time t_f that the target remains of overdense. Once the target is transparent to the laser, RPA is no longer driving the ions. The retarded time is $t_{ret} = t_f - x_f/c$, where x_f is the final target position before the target turns transparent.

2.4.4 Coulomb explosion

Another laser-driven acceleration mechanism studied using nano-thin targets is Coulomb explosion (CE). The laser volumetrically ionises the target and heats the electrons. Electrons vacate the plasma rapidly, leaving a positively charged region in the target. If the ion density within the plasma remains high, a strong Coulomb field is produced. This field explodes the ion density and accelerates ions to high energies. In order to achieve many-MeV ions the Coulomb field needs to grow over a time faster than the target requires to disintegrate. Hence, maximizing the Coulomb field strength requires target thicknesses comparable to or thinner than the skin depth, which is a few nanometers for solid-density plasma.[64–66]

The Coulomb field, E_{CE}, depends on the net charge density, ρ_q, enclosed by the overdense plasma of thickness Δx. Assuming for a laser-irradiated flat foil of solid-density that CE is a planar explosion, E_{CE} is derived from Gauss's Flux Law,[67]

$$E_{CE} = \frac{1}{\varepsilon_0} \int_0^{\Delta x} \rho_q(x) dx \tag{2.37}$$

where ε_0 is the permittivity of free space. Dielectric effects in the nano-thin plasma attenuating the electric fields is assumed negligible.

2.4.5 Relativistically induced transparency for ion acceleration

Laser irradiating solid targets restricts the ion acceleration near the overdense plasma. This means that ions gain energy from the electrostatic fields near the target. After the ions are driven away from the plasma, the main acceleration process providing the highest ion energies ceases because the strongest electric fields are confined to the target. This limits the highest ion energies achievable. On the other hand, if the solid targets are of thicknesses comparable

to the skin depth, it is possible for the laser to heat the electrons in the overdense plasma to relativistic energies. This leads to the onset of RIT as the plasma become relativistically transparent to electric fields. The relativistic electrons propagate forward, which causes the acceleration fields to move with the electrons. As a result the fields catch up with the energetic ions ahead continuing the acceleration. The ions gain more energy during their co-motion with the acceleration fields. This suggests that the onset of RIT can boost the ion energies to higher energies achievable in the case without the overdense plasma turning relativistically transparent. Previous work inferred the onset of RIT to be important for justifying the high ion energies.[18,64,68]

2.4.6 Breakout afterburner

Initially the electrons are subject to faster changes in motion than ions when driven by electric fields. This can result in a drift velocity between electrons and ions for nano-thick targets. During laser-solid interaction the plasma becomes relativistically transparent to the laser. This results in plasma behaviour akin to a underdense system. Consequently, the relative velocity drift and onset of RIT lead to the formation of a two-stream electron-ion instability known as a Buneman instability. The instability grows an electric field that rapidly accelerates the ions. This process is called the breakout afterburner (BOA).[69]

Studies infer BOA from linking the dispersion relation of the instability to particle-in-cell simulations.[63,69,70] In simulations, the impact of BOA is inferred from a steep energy gradient in the ion phase-space immediately after the onset of RIT.[71] The gradient spatially coincides with a strong electric field that increases in amplitude due to BOA. By inferring the energy gradient in ion space-phase and co-motion of a growing and strong electric field with the ions, it can be interpreted if ion acceleration through the BOA mechanism is plausible in high power laser experiments.

In contrast to studies on the above acceleration mechanisms there are limited experiments suggesting that BOA drives the ions to high energies.[61,68] Data analysis is linked with simulations predicting the emergence of the Buneman instability in order to explain how BOA accelerates the ions to the observed energies.

Chapter 3

Diagnostic methods for studying laser-driven radiation and ion sources

This chapter focuses on the two key diagnostics used in experiments. These are a conical crystal spectrometer for X-ray emission spectroscopy and spatially-resolved ion energy detector for recording the spatial distribution and energy of a laser-driven ion beam. The sections for each diagnostic describe how the instruments work, which includes details on the main components, practical concerns addressed in setup and limitations. The data processing and analysis approach are discussed in relation to achieving the experimental results presented in Chapters 5 and 6.

3.1 X-ray emission spectroscopy

Spectroscopy is a method for dispersing electromagnetic radiation to a continuum of wavelengths. The spectrum can provide information about the radiative and atomic processes of the source. In this work a conical crystal spectrometer is used for spectrally-resolving X-ray emission from the laser interaction with a solid silicon target. Measurements centred on K_α emission are the focus for the setup and results in Chapter 5. Advantages of the spectrometer over other designs are the high spectral brightness and spectral resolution.[72]

3.1.1 Conical crystal spectrometer

A conical crystal spectrometer has two planes: a spectral dispersion plane and a focusing plane. These are illustrated in Figure 3.1. In the spectral dispersion plane the source at vertical and horizontal positions s and h emits X-rays of energy $\mathcal{E}_x$ onto the crystal surface from the origin. The origin is located at the apex of the conical crystal geometry with a

cone angle, θ_c. Subscripts 1, 2 and 3 indicate the lowest, central and highest $\mathcal{E}_x$ dispersed in Figure 3.1. The crystal diffracts the X-rays at Bragg angle θ_B onto the image plane at position g. The focusing plane of the spectrometer (not shown) ensures that the crystal focuses the X-rays to a narrow spectral image along the image plane. For this image to be at best focus, $\alpha + \beta = 90°$.[72]

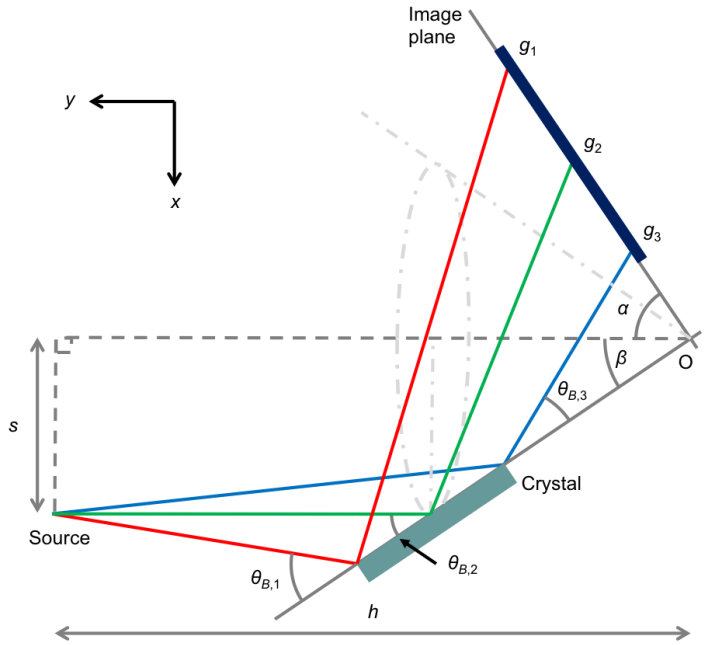

Figure 3.1: Illustration to the spectral dispersion plane of a conical crystal spectrometer. The crystal disperses X-rays from the source at position (h,s) by a crystal at angle β to the image plane at angle α and position g. The origin coincides with the apex of the conical crystal. For the conical geometry $\alpha + \beta = 90°$.

The crystal acts as a multi-layer diffraction grating, where the uniform separation between the crystal planes is d. Hence, X-rays incident at angle θ_B diffract by the crystal as a wave with wavelength $\lambda_x = hc/\mathcal{E}_x$, where h is Planck's constant and c is the speed of light. The diffraction obeys Bragg's law,[73,74]

$$2d\sin(\theta_B) = n\lambda_x = \frac{nhc}{\mathcal{E}_x} \tag{3.1}$$

For the conical crystal spectrometer used in Chapter 5 the diffraction order, n, is unity.

The spectral dispersion of the conical crystal spectrometer is an adaptation from the Von Hamos spectrometer.[72] In the Von Hamos geometry the crystal plane (along the horizontal axis, x, in Figure 3.1) and image plane are tilted by angles β and α relative to the horizontal axis. The spectral dispersion for image position, g, for the Von Hamos geometry is[74]

$$g = \frac{h\sin(\theta_B - \beta) + s\cos(\theta_B - \beta)}{\sin(\theta_B + \alpha + \beta)} \tag{3.2}$$

θ_B is calculated from $\mathcal{E}_x$ using Eqn. 3.1. For the special case of a conical crystal spectrometer, $\alpha + \beta = 90°$ and $\alpha = 90°$ and $\beta = 0°$, Eqn. 3.2 simplifies to

$$g = h \tan(\theta_B) + s \tag{3.3}$$

The cone angle of the crystal determines the optimum X-ray wavelength for which the spectrometer is designed. For this the Bragg angle of the optimum wavelength is equal to the cone angle. This corresponds to the X-ray diffracting a distance $h/2$ from the origin − apex of the conical crystal − on the crystal surface. This results in the spectral image to be at best focus in the image plane. In order to optimise the setup such that the optimum wavelength is centred in the spectrum, the centre of the crystal surface must be at $h/2$.

For the experimental results in Chapter 5 a potassium acid phthalate (KAP) crystal with a plane spacing of $d = 13.317$ Å (often noted as $2d = 26.634$ Å) and cone angle of 15.234° is used. Because of the position of the origin, the setup is optimised for a source at position $s = -41.8$ mm and $h = 306.8$ mm. The spectrum is centred to a wavelength of 6.984 Å, which corresponds to a 1.775 keV photon. Hence, K_α emission (1.739 keV) from laser-irradiated silicon is close to the centre of the spectral image. The crystal length is 48 mm, which set the spectral range between 8.0 and 6.0 Å, or 1.55 and 2.07 keV in terms of photon energy. In the experimental setup the source position is $s = -60$ and $h = 405$ mm because of limited diagnostic space. This results in a smaller solid angle projected from the source on the crystal surface. Hence, the spectral range is reduced to 7.5 and 6.7 Å, or 1.65 and 1.85 keV. This is confirmed by measurement. The setup ensured a highly focused spectral image centred on Si K_α and the spectral range prevents measuring higher K-shell emission such as Si He_α at 1.864 keV.

Figure 3.2 shows the spectral dispersion curve for the conical crystal spectrometer. The curve is calculated using Eqns. 3.1 and 3.3 with $s = -60$ and $h = 405$. Si K_α at photon energy $\mathcal{E}_x = 1.739$ keV is marked by the green dashed line, which by the curve corresponds to the image plane position $g = 52.5$ mm. As shown by the fitted straight line (red dashed line) the curve is almost linear within the spectral range from 1.65 to 1.85 keV. The gradient of this line gives the spectral dispersion relation,

$$\frac{d\mathcal{E}_x}{dg} = -(1.45 \pm 0.01) \times 10^{-2} \text{ [keV/mm]} \tag{3.4}$$

The error in Eqn. 3.4 is based on linear regression analysis.

The spectral dispersion of the spectrometer setup used is mainly sensitive to the crystal angle relative to the horizontal axis, β. This is shown in Figures 3.3 (a)-(d) for β, image plane angle, α and source positions s and h. The blue profile corresponds to using $s = -60$ and $h = 405$ mm in Eqn. 3.3. The dashed red and green profiles show the change in the spectral dispersion when increasing or decreasing β, α, s or h to the values given in the legends.

Modifying α, s or h leads to insignificant changes to the spectral dispersion. On the other hand, a small change in β results in a large change. For $\beta \neq 0°$ the conical spectrometer is out of focus as $\alpha + \beta \neq 90°$. Focusing the spectrometer with an alignment laser helps ensuring that $\beta = 0°$ and $\alpha + \beta = 90°$. Therefore, the spectral dispersion can be determined by purely knowing s and h.

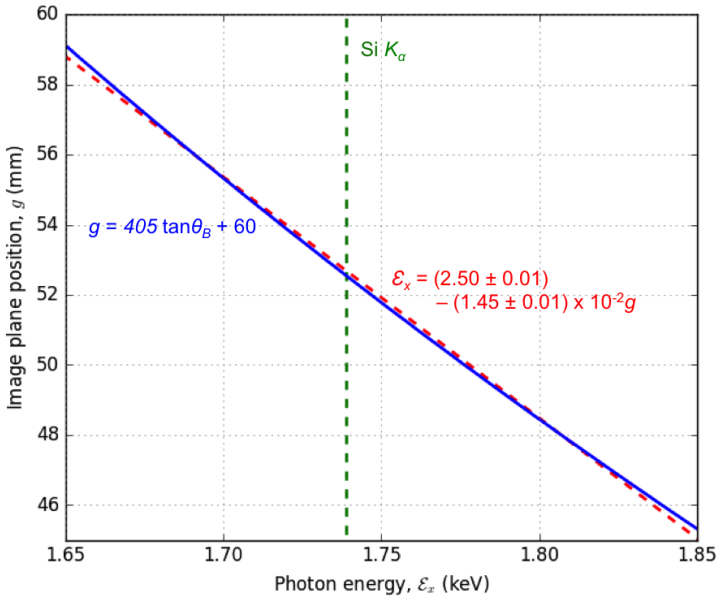

Figure 3.2: Spectral dispersion curve (blue) for the conical crystal spectrometer, where $s = -60$ and $h = 405$. Spectral dispersion relation, which is the absolute gradient of the red dashed line fitted to the curve, is $-(1.45 \pm 0.01) \times 10^{-2}$ keV/mm. The vertical green dashed line corresponds to Si K_α at 1.739 keV.

3.1.2 Crystal reflectivity

In the kinematical approximation diffraction occurs as photons scatter off the atoms in crystal planes. The crystal is a multi-layer system of static crystal planes, which ideally are assumed to be parallel and equally spaced by a distance d. The direction of scattered photons depends on the wavelength for constructive interference (as implied by Eqn. 3.1) and polarity of the photon relative to the crystal plane. For a flux of X-rays incident at angle θ_B the optimum scattering is a 'reflected' projection of the X-rays at the plane surface with a scattering angle $\phi = 2\theta_B$. Scattering of s-polarised X-rays is independent of the incident angle whereas p-polarised X-rays increases in scattering as the angle reduces to $\theta_B = 45°$. Therefore, the ratio of diffracted over incident intensity, otherwise called the crystal integrated reflectivity, R_c, is lower for p-polarised radiation. For incoherent X-rays the reflectivity is the root-mean-squared summation of the s- and p-polarised X-rays.[9]

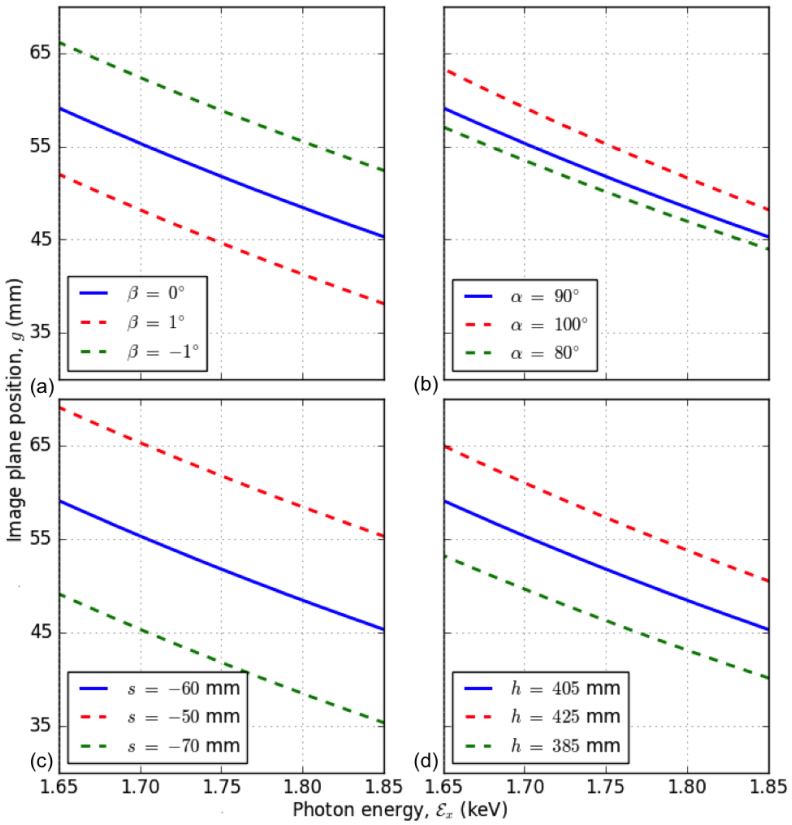

Figure 3.3: Spectral dispersion curves for photons of energies E_x using eqns. 3.1 and 3.2. The parameters are changed between (a) $\pm 10°$ for α, (b) $\pm 1°$ for β, (c) ± 100 mm for h and (d) ± 20 mm for s.

The intensity broadens by a full-width-half-maximum (FWHM) width of $\Delta\theta$ in the scattering direction defined by the angle $\Delta\phi = \phi - 2\theta_B$. $\Delta\phi = 0°$ is in the direction of optimum scattering. R_c is related to the broadened diffracted intensity, $I(\Delta\phi)$, and the incident intensity, I_o, by[9]

$$R_c(\Delta\phi) = \frac{\pi\Delta\theta}{2}\frac{I(\Delta\phi)}{I_o} \tag{3.5}$$

The curve described by $I(\Delta\phi)/I_o$ as a function of $\Delta\phi$ is known as the rocking curve. Note that $R_c < 1$ because the crystal absorbs a small fraction of the radiation.

Broadening depends on the number of crystal planes diffracting radiation, imperfections in the uniformity and periodicity of the crystal structure, sometimes referred to as mosaic structure, and other diagnostic components, such as a slit and pixelation of a detector. Hence, the broadening width, $\Delta\theta$, varies by width due to diffraction, $\Delta\theta_d$, imperfection, $\Delta\theta_m$, and instrumental broadening, $\Delta\theta_i$. Assuming that all broadening widths are described by a Lorentzian function, $\Delta\theta = \Delta\theta_d + \Delta\theta_m + \Delta\theta_i$. These reduce the spectral resolution of the instrument and as a result diffracted peak intensity. $\Delta\theta$ is usually small.[9]

Henke et al.[9] determined the peak and integrated ratios of diffracted intensity at peak over incident intensity, $I(0)/I_o$, as a function of photon energy, $\mathcal{E}_x$, and polarity for different

crystals. These ratios for s- and p-polarised photons are squared and then averaged to obtain $I(0)/I_o$ for unpolarised radiation. The ratios preclude the crystal broadening that reduces the intensity at peak. Therefore, in this work it is assumed that $R_c \approx I(0)/I_o$ and directly obtained from Henke et al.[9].

3.1.3 Imaging plate

In the experiments the spectral X-ray emission is recorded using image plates (IPs). An IP is a multi-layer film composed of a protective, phosphor, support and magnetic layer from front to back. Layouts of IPs by Fujifilm© with atomic composition, densities and thicknesses are shown in Figure 3.4. The information is taken from Bonnet et al.[1]. The plastic protective layer on SR- and MS-type IPs attenuates radiation below 20 keV according to X-ray attenuation data from the NIST database.[2] Therefore, Fujifilm© BAS-TR 2040, which has the same structure as BAS2500 TR in Figure 3.4, without the protective layer is used as IP.

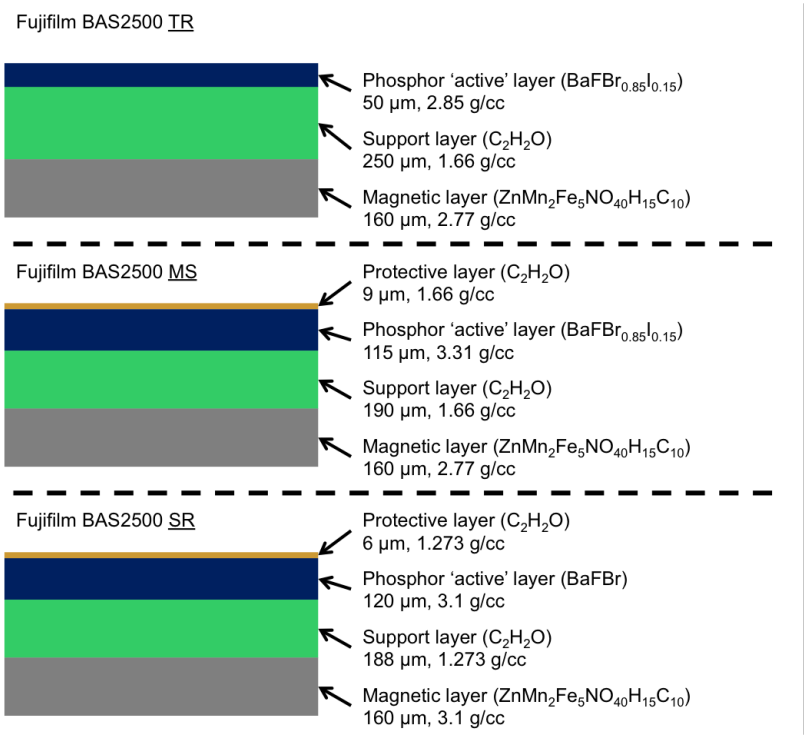

Figure 3.4: Structural layout of TR, MS and SR IPs by Fujifilm©. Details taken from Bonnet et al.[1].

The phosphor layer is the photo-absorbing layer for detecting X-rays. It is composed of alkaline earth metals and halogens, such as BaFBr or BaFBrI, with Eu^{2+} dopants. When an ionizing particle, either a photon or charged particle, of energy $\geq$24.8 eV[52] falls on the IP an Eu^{2+} dopant is ionized to Eu^{3+}. The electron excited to the conduction band of the film is captured by the halogens, forming a metastable state in the halogens. By irradiating the halogens with a photon of at least 2 eV (620 nm) the captured electron is liberated and

recombines with the Eu^{3+} to Eu^{2+}. The recombination produces a characteristic photon of ~3 eV (about 400 nm). This process is called photo-stimulated luminescence (PSL).[1,75]

PSL is commonly used by laser-based scanners for digitising IP data.[75] The experimental data is digitised with a Fujifilm© FLA-5000 scanner. An s-polarized, 635 nm red laser scans the IP and records the stimulated emission with a photomultiplier tube. The data is saved as a 16-bit TIFF image file. The PSL is converted to quantum level, QL, which is the signal in the TIFF file as base-ten values. The scanning settings are for the resolution $Res = 25$ μm, sensitivity $S = 2000$, latitude $L = 5$ and 16-bit gradation $G = 2^{16}$ - 1 = 65535. The conversion from QL to PSL, where PSL corresponds to the measured spectral intensity, I_m, is[10,76]

$$I_m = \left(\frac{Res}{100}\right)^2 \frac{4000}{S} 10^{L\left(\frac{QL}{G} - 0.5\right)} \tag{3.6}$$

Scanning is conducted in a dark room to minimize background light during scanning. Thereafter the IP is irradiated by a bright white light source to recombine all electrons back to the Eu^{2+} dopants. This erases the data so the IP can be reused.

The IP response to X-rays of different energies, $\mathcal{E}_x$, depends linearly on $\mathcal{E}_x$. This suggests that Eu^{2+} dopants are more sensitive to photons of increasing energy. In addition, according to Iwabuchi et al.[75] the measured intensity, I_m, from PSL during scanning is directly proportional to the concentration of Eu^{3+} dopants produced. This assumption is appropriate for X-rays below 6 keV.[77] Hence, it is assumed that the X-ray intensity irradiated on the IP is derived from I_m by dividing I_m by the IP response function, $R_r = a\mathcal{E}_x$. The constant of proportionality is assumed to be $a = 4.85 \times 10^{-4}$ PSL/keV.[1]

IPs have advantages and disadvantages over electronic imaging detectors. An IP is simple to use and enables installing the diagnostic in the vicinity of the target without the electromagnetic pulse from the laser-target interaction causing the diagnostic to fail on shot.[1,77,78] This is important because the conical crystal spectrometer is designed to be placed near the target. The main drawbacks of using IPs are that measurements are time-integrated and have relatively poor spatial resolution.

3.1.4 X-ray filtering

Filtering electromagnetic radiation is important for the conical crystal spectrometer. In the laser-solid interaction high fluxes of photons and electrons emit from the target. The IP is directly shielded from this radiation by a thick lead sheet. On the other hand, photons and electrons irradiate and scatter inside the crystal, producing a high radiation fluorescence. This directly irradiates the IP and is observed as background emission. Further fluorescence is also produced from the spectrometer casing made of metallic materials. Filters attenuate the radiation, ensuring the spectrally-unresolved background signal is suppressed and spectrally-resolved measurements are reduced below saturation. In addition, filters are used before

the crystal because they are important for avoiding the crystal to overheat from absorbing radiation.[9]

A filter of mass density ρ and thickness l attenuates the incident radiation of intensity I_o to a transmission intensity of I. The attenuation ratio, $R_a = I/I_o$, is described by the Beer-Lambert Law,[35]

$$R_a = \frac{I}{I_o} = \exp(-\mu_m \rho l) \tag{3.7}$$

μ_m is the total attenuation coefficient in units of cm^2/g. This is a specific cross section accounting for absorption, scattering and reflection of radiation in the filter. μ_m is a function of photon energy, $\mathcal{E}_x$, and varies between different types of materials.

In the experiment the filters are composed of aluminium (Al), beryllium (Be), mylar and polyethylene terephthalate (PET). Mass densities are $\rho = 2.70$, 1.85, 1.38 and 1.38 $\mathrm{g/cm}^3$ respectively. Aluminium is coated to about 40 nm on 5 μm thick mylar, and PET is 6 μm thick. These filters are placed between the X-ray source and crystal. 25 μm thick beryllium is placed between the crystal and IP.

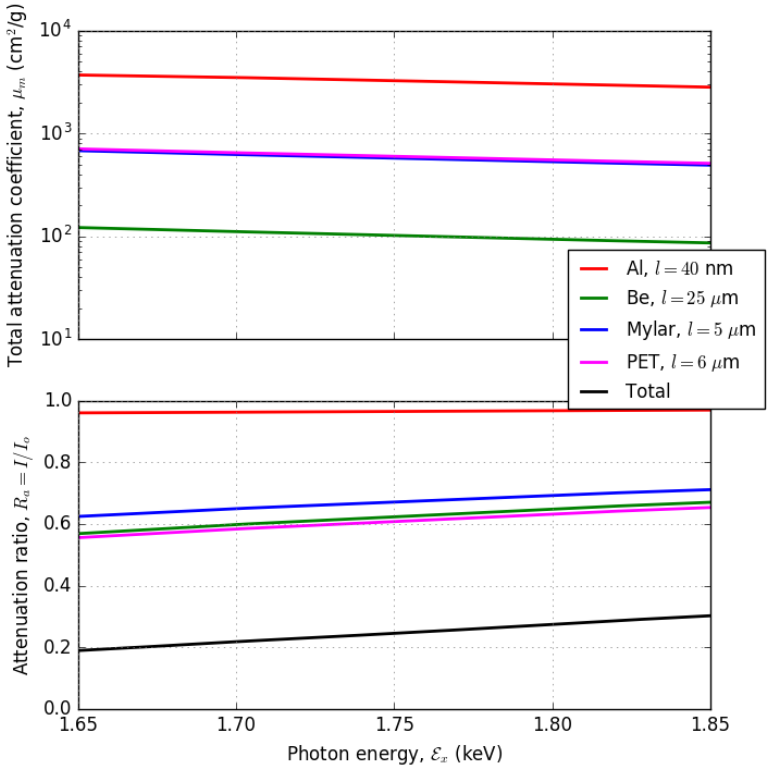

Figure 3.5: (a) Total attenuation coefficients with photon energy of aluminium (red), beryllium (green), mylar (blue) and PET (magenta) obtained from the NIST database.[2] (b) Attenuation ratio calculated with Eqn. 3.7 and the data shown in (a), where the black line shows the total attenuated signal from the individual coloured profiles.

The total mass attenuation, μ_m, for photon energies between $\mathcal{E}_x = 1.65$ and 1.85 keV is

shown in Figure 3.5 (a) for the filters used in experiment. The data is obtained from the NIST database.[2] Figure 3.5 (a) shows that aluminium has the highest μ_m, which means that aluminium attenuates radiation more than the other filters. Therefore, only a small amount of aluminium is used for filtering. Using Eqn. 3.7 with the plotted μ_m, mass densities and thicknesses used, the attenuation ratios, $R_a = I/I_o$, are calculated and shown in Figure 3.5 (b). The black line shows the total attenuation ratio, which is a product of the individual ratios. Between $\mathcal{E}_x = 1.65$ and 1.85 keV the spectral signal is attenuated almost linearly between 20 and 30%.

3.1.5 Spectral data processing and reduction

Figure 3.6 (a) shows a digitised spectral image recorded on the experiment. The spectral and spatial axes, g and w, are indicated on the image. The minimum and maximum spectral range and position of Si K_α are shown. Regions used to estimate the background in the spectral data are highlighted. The image widens slightly towards lower g (higher photon energies) compared to K_α. Figure 3.6 (b) shows an average spatial profile of K_α along the w-axis on the image. The vertical axis is quantum level, QL, with the average taken from a number of data shots with similar target and shot parameters. By taking the lineout along the spectrum in the g-axis, the blue spectral profile shown in Figure 3.6 (c) is obtained. The central peak corresponds to K_α. The g-axis is reversed to avoid confusion about the orientation of the spectrum in terms of photon energy later. The corresponding average background spectrum in magenta is extracted from the regions next to the spectral image.

As indicated by Figure 3.6 (b), the spectrum has a spatial width over which radiation spreads. The width determines the spatial resolution of the spectrometer. As inferred from Figure 3.6 (b) the width is (0.101 ± 0.005) mm, which corresponds to roughly 4 pixels on the image. In ImageJ the lineout tool is used to extract the profiles shown in Figure 3.6 (c) (blue). The lineout width over which pixels adjacent to the line are averaged over is set to 9 pixels. This corresponds closely to the width at fifth maximum is (0.208 ± 0.005), which is 8 pixels. The reason for this choice is to include more detail of the spectral signal in the data extrapolation.

Three spectra are extracted from the digitised spectral image: the raw and two background spectra. The raw spectrum is taken with the lineout along the spectral image, giving the spectrum shown in Figure 3.6 (c). The lineout is translated to the two adjacent regions next to the spectrum. These regions correspond to the background spectra consisting of scanning noise and spectrally unresolved emission. The background spectra are averaged to obtain the average background signal recorded over the raw spectrum.

The QL signal of the raw and background spectra are converted to PSL using Eqn. 3.6. The background signal is then subtracted from the raw spectrum. This provides the corrected spectrum with measured intensity, I_m.

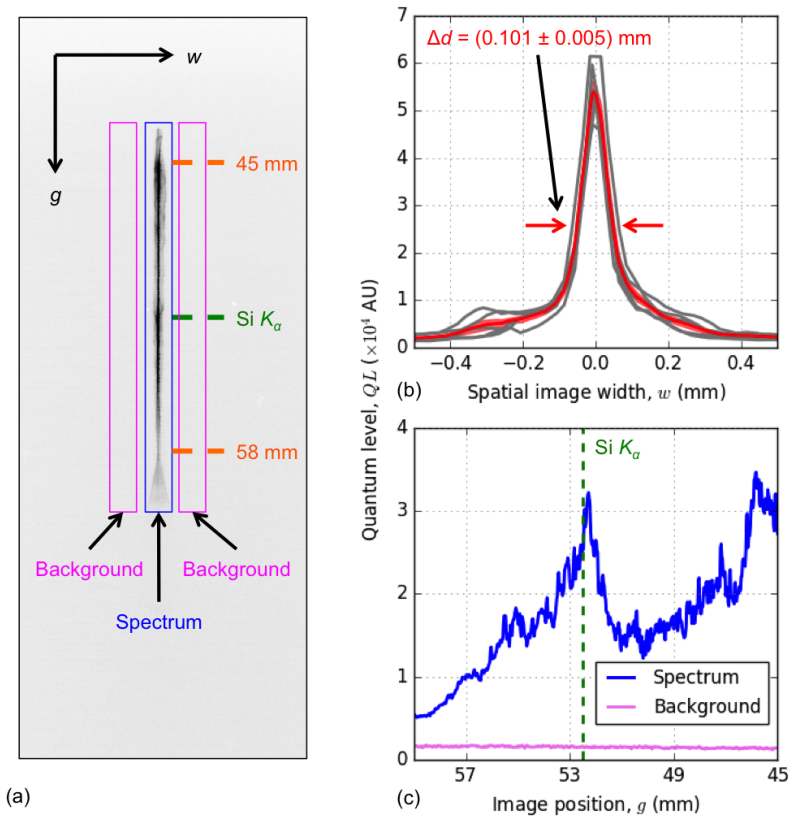

Figure 3.6: (a) Spectral image acquired on-shot with the conical crystal spectrometer. Position of spectral range (orange), Si K_α (green), spectrum (blue) and background (magenta) regions are indicated. (b) Spatial profiles extracted along w-axis over similar shots at K_α (gray) are averaged (red), providing a spectral FWHM of (0.101 ± 0.005) mm. (c) Spectral profiles extracted along g-axis of spectrum and background region.

The corrected spectrum is calibrated by translating the image position, g, to the expected position of the K_α peak. The K_α position is calculated using the spectral dispersion profile shown in Figure 3.2 for the experimental setup. For a K_α photon of 1.739 keV, $g = 52.5$ mm. Ideally, two well-known spectral peaks are needed to accurately calibrate the spectrum. Using only one spectral peak for calibration results in some uncertainty in the dispersion. After spectral calibration the spectral dispersion is applied to the spectrum to convert the image position g to photon energy, $\mathcal{E}_x$.

The measured spectral intensity, I_m, is converted to the actual intensity irradiated from the X-ray source, I_s, by using three correction terms. These corrections are the crystal reflectivity, R_c, IP response function, R_r, and total attenuation ratio of the filters, R_a. All correction terms are functions of $\mathcal{E}_x$. The conversion relation is

$$I_s = \frac{I_m}{R_c R_r R_a} \tag{3.8}$$

After this correction, the final spectrum with spectral intensity against $\mathcal{E}_x$ is obtained for

analysis. Data for R_c is taken from Henke et al.[9] and R_r from Haugh et al.[10] R_a is calculated using Eqn. 3.7 and using data for total mass attenuation from the NIST database.[2]

There are limitations to this data processing approach. There is no absolute intensity calibration performed for the spectrometer. Therefore, the spectral intensity is in arbitrary units and only provide qualitative measurements. Secondly, it is seen in Figure 3.6 (a) that the spectral image is wider towards higher photon energies. The resolution is measured at the K_α peak and, therefore, the accuracy of the analysis is limited to K_α. When applying the spectral dispersion to the spectrum, it is assumed that the photon energies are determined by the dispersion. It is shown in Chapter 5 that this assumption breaks down for identifying the spectral peaks at higher energies.

3.2 Spatially-resolved ion energy detector

The laser-target interaction produces radiation, electrons and ions with spatial and energy distributions determined by the electromagnetic fields driving them. When incident on a solid material the radiation and particles induce a change in the material structure, which depends on the radiative source fluxes and energy. As a result the material records information on the spatial and energy distributions of the radiation and particle sources. In this section the use of a detector stack composed of radiochromic film (RCF) and CR-39 is described for detecting protons and carbon ions. RCF and CR-39 are described separately to explain how they work and are used in connection to the measurements presented in Chapter 6.

3.2.1 Stopping power of materials

When an ion of energy $\mathcal{E}_i$ moves through matter with a depth x it deposits a fraction of its energy via Coulomb interaction with the electrons. The energy loss rate is determined by the stopping power, $S = -d\mathcal{E}_i/dx$, which is commonly assumed to be linear and describe a continuous energy loss.[25,26,79,80] Once the ion energy has decreased sufficiently energy straggling exhibited by the electrons becomes important, which results in the ion depositing its energy rapidly and stoping at a depth of $x \approx R$. R is known as the stopping range and it is rewritten to the penetration depth, ρR, by multiplying R by the density of matter, ρ.

For a near monoenergetic ion beam irradiated on a detector plate, the ions deposit a proportion of their energy at depth $x < R$. As the ions reach a depth R the majority of ions are stopped and deposit nearly all of their energy. This results in the Bragg response curve depicted in Figure 3.7 (a). This curve features a low energy deposition continuum called the sub-peak region and a peak at R known as the Bragg peak. The peak has a finite width because of the stochastic nature of the ion-matter interaction in the detector plate.[26,42]

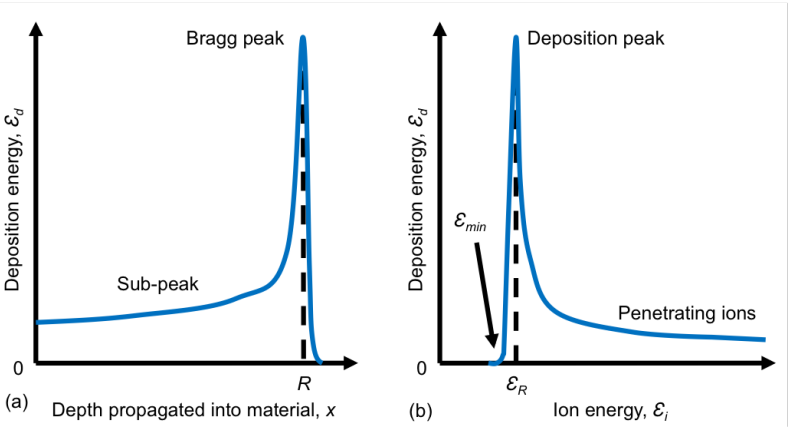

Figure 3.7: (a) Bragg response curve with the peak at ion stopping range R. (b) Energy deposition curve with the peak at ion energy $\mathcal{E}_R$ and minimum threshold energy for absorption $\mathcal{E}_{min}$.

The Bragg peak results in the deposition energy profile as a function of ion energy, $\mathcal{E}_i$, illustrated in Figure 3.7 (b). Ions of energy $\mathcal{E}_R$ deposit nearly all their energy and stop in the detector plate, which spatially coincides with the Bragg peak at R. The high deposition continuum at energies $\mathcal{E}_i > \mathcal{E}_R$ corresponds to ions that penetrate the detector and, hence, deposit a fraction of their energy. The value of $\mathcal{E}_R$ is shifted to higher ion energies by placing another material before the detector that stops ions whose energy is below the threshold energy, $\mathcal{E}_{min}$, from reaching the detector. This provides a method for designing a stack of detector plates and attenuating materials to record a selected range of ion energies.[79,80]

The response function of the detector plate is assumed to be directly proportional to the energy deposition curve (see Figure 3.7 (b)). The constant of proportionality, a, is the sensitivity of the detector plate. This relation assumes that the energy deposition is independent of the detector thickness and depth the ion propagates into the material[1]. A similar assumption is used for the response function of the detector plate to X-rays in Subsection 3.1.3.

The higher the ion stopping power, S, the shorter the stopping range, R. S depends on the mass density, ρ, and atomic charge, Z, of the detector plate and incident ion charge, Z_i, energy, $\mathcal{E}_i$ and mass, m_i, by the Bethe-Bloch equation,[26]

$$S \propto \rho Z Z_i^2 \left(\frac{1}{\beta_i^2} \ln \left(\frac{\beta_i^2}{1-\beta_i^2} \right) - 1 \right) \tag{3.9}$$

$$\beta_i^2 = 1 - \left(1 + \frac{\mathcal{E}_i}{m_i c^2} \right)^{-2} \tag{3.10}$$

Eqn. 3.9 indicates that the stopping power rises as ρ, Z and Z_i increase. This suggests that a material with a high density, high ion charge and incident ions with a high positive charge are stopped over a short stopping range. Furthermore, the bracket term in Eqn. 3.9 is a function of $\mathcal{E}_i$ and m_i (see Eqn. 3.10). This term increases S when the ion energy is low and using heavy ions.

3.2.2 Radiochromic film

A radiochromic film (RCF) is a detector plate containing a colourless radiation-sensitive material within a multi-layer plastic structure. This sensitive layer turns blue upon absorption of energetic radiation, such as photons and particles, when used at room temperature. For experiments using high power lasers RCF are commonly used for spatially- and energy-resolving the laser-driven ion beam[18,81,82] and perturbing the ion beam with laser-produced electromagnetic fields.[83,84]

There are a number of RCFs available for radiation measurements. For this work the two types of RCF used are HDV2[3] and EBT2.[4] Differences in their layout are shown in Figure 3.8. HDV2 has a 8 μm sensitive layer supported on a 97 μm polyester base. EBT2 is a five-layer RCF with a 30 μm sensitive layer, which is thicker than the layer in HDV2. Hence, EBT2 is more sensitive for absorbing radiation than HDV2.[80]

After absorbing radiation the discoloured RCF is digitised by scanning the film with a Nikon photographic scanner. Images are stored as 8-bit RGB-scale values in a TIFF file. RGB values per pixel determine the absorbed radiation dose and, hence, provide information about the spatial ion beam distribution.

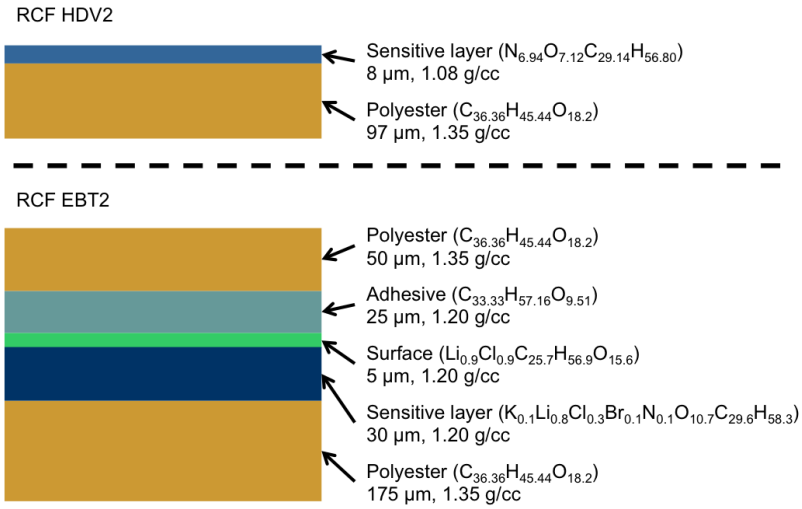

Figure 3.8: Structure and compositions of the layers in RCF-type HDV2[3] (top) and EBT2[4] (bottom). The thickness and composition of the sensitive layers define the low and high sensitivities respectively.

3.2.3 Columbia Resin #39 (CR-39)

RCF absorb all types of radiation – photons, electrons and ions. Placing 13 μm Al before the RCF reduces the signal of photons below 1 keV to less than 1% via attenuation (see Subsection 3.1.4). This optimises the detected radiation mainly to electrons and ions. Distinguishing between electrons and ions requires a method to separate the particles. In this work the spatially-resolved ion energy detector containing RCF is placed 5 cm from the

target. This makes it challenging to install a magnet before the detector for deflecting electrons away without perturbing the laser-target interaction or ion measurements. To separate electrons and ions the simple approach taken is to place CR-39 plates in the detector. CR-39 is insensitive to photons and electrons, which restricts the detection to ions. In addition, CR-39 are used to identify protons and carbon ions in the ion beam.[85]

CR-39 (Columbia Resin #39 or allyl diglycol carbonate) is a plastic polymer of density 1.31 g/cm^3 and monomer formula $C_{12}H_{18}O_7$. Initial motivation for using CR-39 dates back to manufacturing optics for the bombers in World War II, and today it is used as lightweight eyeglass lenses.[86] CR-39 is highly insensitive to photons and electrons. Therefore it is suitable to use as a secondary diagnostic to spatially-resolved ion energy spectrometry measurements.[87]

There are various types of CR-39 used for identifying ions. For the experimental measurements TASTRAK[88] from Track Analysis Systems Ltd (UK) is used. TASTRAK is 1 mm thick and records protons with an energy range of 3 MeV. Other types of CR-39 available include BARYOTRAK[89] and HARZLAS TD-1[85] from Japan Fukuvi Chemical Industry Co. Ltd, which are suitable for protons with a 20 MeV and 3 MeV energy range respectively. BARYOTRAK has a smoother surface structure compared to HARZLAS TD-1 and TASTRAK, which reduces the formation of granules when etching the CR-39. Furthermore, polyethylene terephthalate (PET) and polycarbonate (PC) are plastics that are insensitive to protons. These can be used as a method for separating heavier ions from protons.[90] Due to availability during experiment, TASTRAK is used for the results presented in Chapter 6. BARYOTRAK and HARZLAS TD-1 are used in the chemical etching analysis described in the next subsection.

3.2.3.1 Multi-step chemical etching method

Ions moving through CR-39 undergo Coulomb interaction and nuclear reaction (see Subsection 3.2.1). The Coulomb interaction break the molecular bonds, which weakens the material structure. Nuclear reaction stops the ion at a stopping range, R. R provides an estimate for the ion energy. By chemically etching the CR-39, R can be measured.

The following description on processing and analysing CR-39 is based on research training conducted at Kansai Photon Science Institute and Kobe University. BARYOTRAK and HARZLAS TD-1 samples of size $40 \times 20 \times 1$ mm^3 are laser imprinted with 7×7 mm^2 area, which are marked by numbers 1 to 5 and Cf. The marked squares $1-5$ are irradiated by the radioactive decay products from ^{241}Am, and the Cf square is irradiated by the products from ^{252}Cf. Both radioactive nuclei decay with a high probability via alpha emission,

$$^{241}_{95}Am \rightarrow {}^{237}_{93}Np + {}^{4}_{2}He\ [5.486\ \text{MeV}] + \gamma \tag{3.11}$$

$$^{252}_{98}Cf \rightarrow {}^{248}_{96}Cm + {}^{4}_{2}He\ [6.217\ \text{MeV}] + \gamma \tag{3.12}$$

A smaller number of nuclei decay via spontaneous fission, which produces ion fragments heavier than helium. For regions $1-4$ collimator tubes of 50, 20, 10 and 1 mm length place the ^{241}Am source at different distances from the CR-39 (see Figure 3.9 (a) for the setup). A 3×3 hole array is used at the source entrance and placed 1 mm from the CR-39 over region 5. The areas are irradiated by the decay and fission products for 10 minutes in ambient air. Over the Cf region the products from ^{252}Cf irradiate the CR-39 at a 1 mm separation for 15 minutes in vacuum because of the short travel range of the decay nuclei.

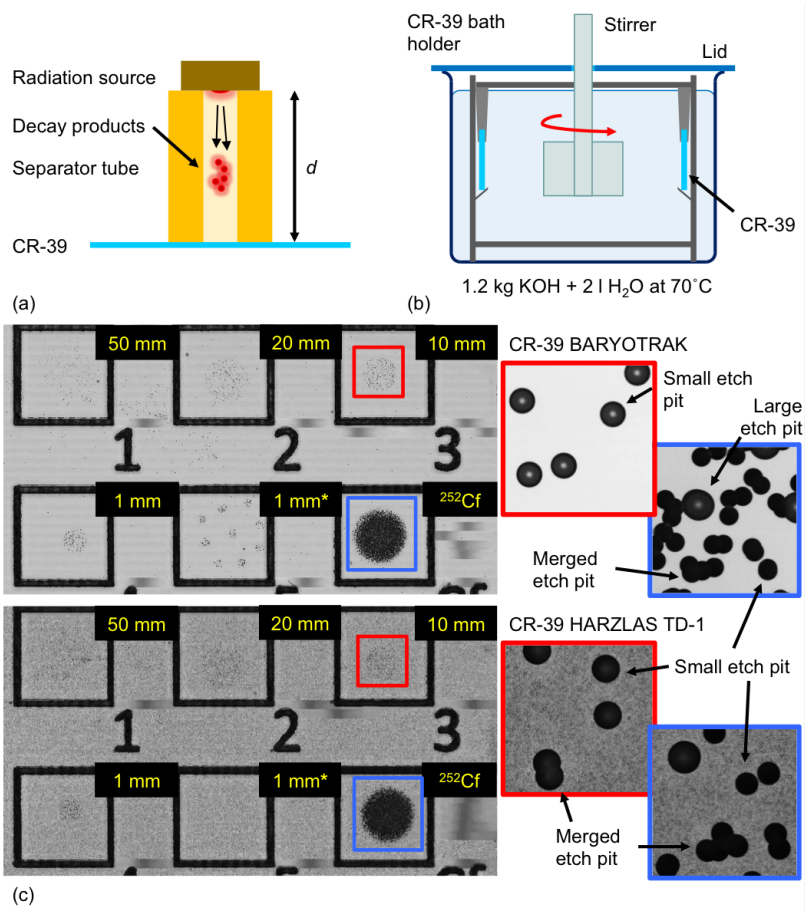

Figure 3.9: Basic method for detecting ions with CR-39. (a) A radioactive source emits alpha particles through a collimator of length d to the CR-39. (b) By chemically etching the CR-39 in a hot KOH and water solution etch pits emerge at the ion-irradiated regions shown in (c). The two types of CR-39 – BARYOTRAK and HARZLAS TD-1 – show individual and merged etch pits after 12 hours of etching time.

Figure 3.9 (b) illustrates the chemical etching method on CR-39. In a large glass beaker 1.2 kg of potassium hydroxide (KOH) is dissolved in 2 l of water. The solution is heated to 70 °C by a hot plate. An automated revolving stirrer distributes the heat across the solution. A plastic lid is placed on the beaker to trap the evaporating water because a decrease in the relative water-to-KOH concentration slightly increases the etching rate. The concentration also changes as etched CR-39 molecules contaminate the solution and modifies the etching

rate. Therefore the solution needs replacement every six hours of total etching time for a consistent etching rate and analysis.

After etching, the CR-39 samples are cleaned with running tap water and then air dried. Shaded areas corresponding to the etch pits on the samples are observable. The samples are imaged using a HSP-1000 fully automated optical microscope (FAOM).[91] The FAOM uses a monochrome line sensor to digitize the CR-39 to a 8-bit JPEG image with a spatial resolution of 7 μm per pixel. Using a magnification up to 200$\times$ the etch pits are resolved with a 0.35×0.35 μm^2 resolution. The autofocus system identifies the clearest features on the CR-39 to record sharp images with the integrated CCD camera. To ensure the autofocus focuses on the front surface of the CR-39 during data recording rather than the backside, the sample is displaced 3 μm away from the FAOM and out of focus beforehand. The FAOM scans across the surface and digitises 350×350 μm^2 images of the sample surface. The images are automatically constructed to larger image sizes with the largest image recorded being 40×20 mm^2. Images of the scanned BARYOTRAK and HARZLAS TD-1 are shown in Figure 3.9 (c). Etch pits are clearly seen in region Cf, whereas the number of etch pits from region 5 to 1 decreases as the ^{241}Am distance from the CR-39 increases. The small inserted images show etch pits in regions 3 and Cf. FAOM can distinguish individual etch pits from merged pits if the irradiated ion flux is below 10^5 cm^{-2}. Otherwise an atomic force microscope can be used to separate etch pits from ion fluxes exceeding 10^9 cm^{-2}.[87]

The HspFit analysis software accompanying the FAOM provides rapid data acquisition of etch pit positions, circular to elliptical shape and algorithm for separating etch pits from dust and granules. Ellipses are drawn over the etch pits automatically identified. The ellipses are adjusted in size and aspect ratio between major and minor diameters. A threshold determining the permitted spacing between etch pits is used to separate single etch pits from merged pits and dust. These parameters are used to record the number and radii of etch pits.

The above procedure is for etching the CR-39 samples for one hour in the solution. After analysing the scanned images, the samples are again etched for one hour, cleaned, digitised and analysed. This approach is repeated in succession to record the etch pit radii with etching time. The method is referred to as multi-step chemical etching.

3.2.3.2 Etch pit analysis

The evaluation of the CR-39 damage is determined from the shape and depth of the etch pits using the multi-step chemical etching method illustrated in Figures 3.10 (a)-(c). The black dashed line indicate etched surfaces and the solid line shows the surface etched to. The etched surface position, G, extends from the initial surface before etching, which grows with an etch rate, v_{et}. The depth and radius of the etch pit are L and r_s. The stopping range is R. The energy and size of ions interacting with the material determine the shape of the

etch pits. Figures 3.10 (a)-(c) are recreated from Kanasaki et al.[85,87]

As shown in Figure 3.10 (a), a high energy ion propagates through the material without stopping because the stopping range is greater than the material thickness, $R > l$. Etching the CR-39 shows a trumpet-shaped etch pit emerge on the front surface and a bell-shaped pit on the back surface. The shapes form because of the narrow volume damaged in the material and the etching geometry. This type of etch pit provides a measure of the ion energy exceeded.[87]

A low-energy heavy ion damages a large volume of material. Etching the material produces a cylindrically-shaped etch pit (see Figure 3.10 (b)). Pit shape is approximately unchanging. The pit radius, r_s, grows with the same etch rate, v_{et}, removing a thickness G at the surface. As a result, $r_s \approx G$. This fixes v_{et} and, in turn, gives a measure for G. Irradiating an unused CR-39 sample from the experiment with low energy, heavy ions and etching the sample with those used in experiment simultaneously gives an estimate of G. This also provides a calibration method for the etching rate.[87]

A light ion of low energy moves a distance $R < l$ into the material. The ion continuously damages the material nearly uniformly along the ion trajectory. When etching with an etch rate, v_{et}, the etch pit forms with a conical geometry of radius, r_s. This geometry is preserved as long as the depth of material removed along the etch pit is less than R, as in, $G - L \leq R$. L is the depth of the etch pit, which increases with etch time while the pit shape is conical. As $G - L > R$ with continuous etching, a phase transition in the etch pit geometry occurs. At this point L does not change with etch time. The transition changes the geometry to a spherical shape after etching a depth $G - (R - L))$ from the end of the conical phase. At the point the spherical phase starts, r_s is related to G, R and L by[85,87]

$$r_s^2 = 2LG - 2LR + L^2 \tag{3.13}$$

From Eqn. 3.13, the etching gradient is $dr_s^2/dG = 2L$. r_s and G are estimated from the growing etch pit radii of the light and heavy ions. The spherical phase at which Eqn. 3.13 applies occurs when r_s^2 increases linearly with G. Hence, dr_s^2/dG is interpolated at this phase. Hence, R is determined from r_s and G by rewriting Eqn. 3.13 as[85,87]

$$R = G + \frac{1}{4}\left(\frac{dr_s^2}{dG}\right) - r_s^2 \Big/ \left(\frac{dr_s^2}{dG}\right) \tag{3.14}$$

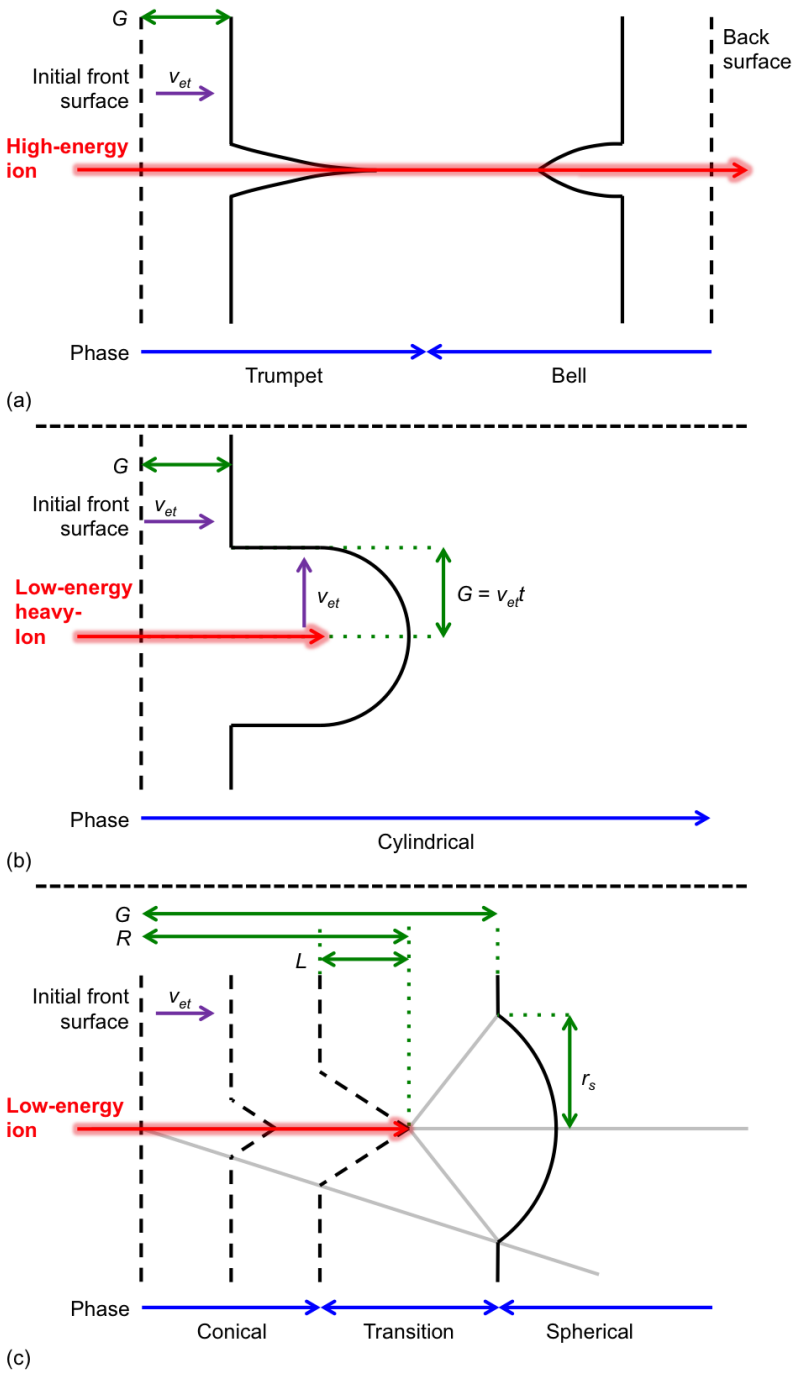

Figure 3.10: Etch pit phases for different types and energies of ions. Dashed lines indicate etched surfaces and solid lines is the current surface after etching. (a) A high-energy ion penetrates the CR-39 without stopping. A trumpet- and bell-shaped etch pit form at the front and back surface. (b) A low-energy, heavy ion damages a wide region, forming a cylindrical etch pit whose radius is related to the etch rate. (c) A low-energy, light ion creates a conical etch pit of depth L up to removing $R - L$ from the surface. Further etching changes the pit geometry to a spherical shape. Measuring the etch pit radius r_s at the spherical phase provides a measure of R.

Sample measurements of etch pit radii due to alpha, r_s, and heavy fission fragments,

G, from ^{252}Cf growing with time are shown in Figure 3.11 (a). The error bars indicate the standard error in r_s and G. Notice that G is growing at a slightly decreasing rate towards later etching time. This is because the etching rate slows down with a change in the potassium hydroxide concentration. For accuracy, the solution should be replaced every six hours of etching time.

The measurements are plotted in Figure 3.11 (b) as r_s^2 against G. During the conical phase of the etch pit geometry, r_s^2 is continuously growing with G. The spherical phase starts as r_s^2 changes linearly with G, which begins when $G = (51.1 \pm 0.3)$ and $r_s = (38.9 \pm 0.1)$ μm. A straight line is fitted to the data to interpolate the gradient as $dr_s^2/dG = (127 \pm 3)$ μm. Hence, using Eqn. 3.14 at $G = (51.1 \pm 0.3)$ and $r_s = (38.9 \pm 0.1)$ μm results in the stopping range of the alpha particle to be $R = (71 \pm 1)$ μm.

The estimated stopping range, R, is compared to expected stopping power calculated using the Stopping and Range of Ions in Matter (SRIM) code.[12] In the setup the ion projectiles are alpha particles and the irradiated material is given as CR-39. The calculations provide stopping powers and ranges for different ion energies, $\mathcal{E}_i$, used. For the estimated R above, $\mathcal{E}_i = (8.83 \pm 0.01)$ MeV. This is greater than the expected 6.217 MeV. The discrepancy may arise from the potassium hydroxide concentration changing with time.

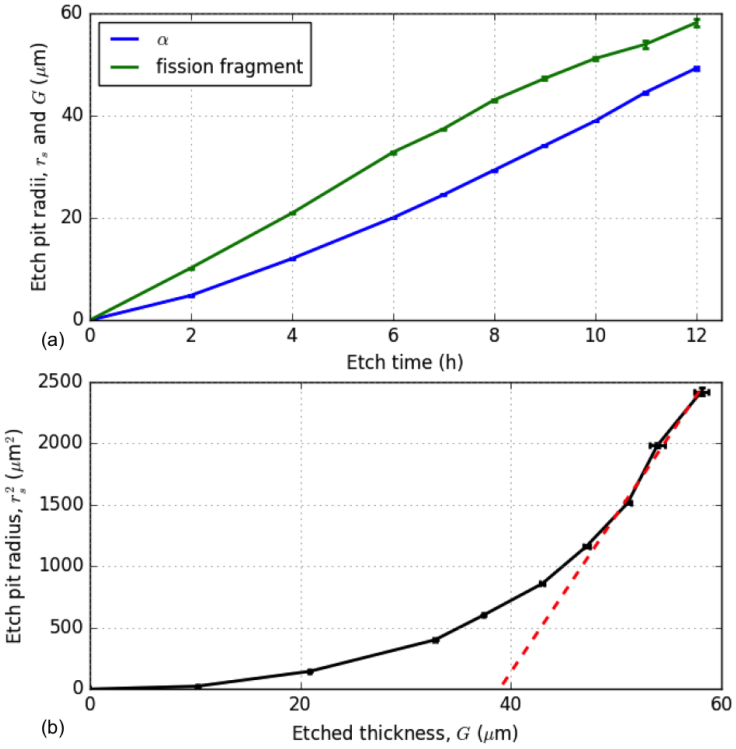

Figure 3.11: Example measurements of etch pit radii produced by the ^{4}He and fission fragments, r_s and G, from ^{252}Cf with (a) etch time and (b) comparing r_s^2 and G.

Furthermore, the sensitivity of CR-39 to interact with incident ions is estimated from the etch pit radius, r_s, and etched material thickness, G,[87]

$$S = \frac{1 + \left(r_s/G\right)^2}{1 - \left(r_s/G\right)^2} \tag{3.15}$$

If r_s is large then S will be large. The sensitivity depends on the concentration of dioxide (O_2) molecules in the CR-39. O_2 oxidises to hydroxide (OH) when reacting with an energetic ion. The reaction enhances the damaged region, which in turn results in a larger r_s when etching. As a result, the accuracy of measuring the stopping range depends on the concentration of O_2 before the CR-39 is irradiated by energetic ions. Minimizing the outgassing of O_2 requires storing CR-39 in a freezer under atmospheric pressure. Therefore, CR-39 should not be kept under vacuum. Kanasaki et al.[87] shows that the expected r_s reduces to 90% after 1 hour and 25% after 10 hours in vacuum.

Care must be taken when handling CR-39. If the material is subject to external pressure, the surface is damaged. This changes the etch rate uniformity across the surface, leading to the formation of artefacts when etching which affects the accuracy of measuring r_s. Therefore it is best practice to handle CR-39 on the frame and minimize handling time.

3.2.4 Diagnostic description

For the results in Chapter 6 the spatially-resolved ion energy detector is used. This detector is a stack composed of attenuating plates, RCFs and CR-39. The detector used RCF for spatially resolving the ion (and electron) beam distributions. Plates made of aluminium, mylar and iron are placed between RCFs to attenuate the ions. This results in measuring increasing ion energies on the RCFs into the detector stack. The identification of protons and carbon ions is achieved by including CR-39 inside the stack. The stack designs used in this work are described in the experimental setup in Chapter 6. For calculating the ion energies detected by each RCF and CR-39, the stopping powers of all materials used in the stack designs are obtained from the SRIM code.[12] These are imported to a MATLAB® code for calculating energy deposition curves. The peak deposition is assumed to be the ion energy detected.

Chapter 4

Double plasma mirror systems for enhancing the contrast of high power laser pulses

Much research using high power laser facilities focus on optimising the laser-to-target coupling for generating particle and radiation sources efficiently. This motivates the development of advanced and sophisticated target technology. These include the fabrication of targets with micro-structured surfaces[7] and down to one atom thickness.[11] The main challenge of using such targets is ensuring that the near-solid density target integrity is preserved during the early interaction with the laser pulse. If significantly intense, the pedestal and prepulses ahead of the main peak cause hydrodynamic processes that expand the target to a large plasma with densities lower than near-solid. In addition, these temporal intensity structures, such as amplified spontaneous emission (ASE) seeded from noise, fluctuate in time and intensity. These can change the plasma scale length shot-by-shot. A solution for a high intensity laser interaction on solid targets is to suppress the pedestal and prepulses using a double plasma mirror (DPM).

This chapter outlines the use and performance of a DPM assembly. These assemblies are designed to the requirements of high power laser experiments. Discussions on physical and mechanical constraints are addressed for two designs: a four-shot cycle DPM system on the Vulcan petawatt laser, and a compact 3D-printed DPM holder on the LFEX laser. This work supports the development of methods for mitigating the interaction early in the laser by using the DPM as a tool for controlling this interaction.[92]

4.1 Temporal intensity structure of a high power laser

The Vulcan petawatt laser based at the Central Laser Facility, Rutherford Appleton Laboratory, UK, uses the optical parametric chirped pulse amplification (OPCPA) technology[93]

for a high-contrast, high-intensity laser pulse. This approach is common to high power laser facilities worldwide.[92,94–96] The key stages in an OPCPA are shown in Figure 4.1 - for details see Danson et al.[93] In summary, the main Nd:glass oscillator (stage 1 in Figure 4.1) injects a low-energy laser pulse through the optical parametric amplifier (OPA)[97] to pre-amplify the pulse by at least three orders of magnitude (stage 2). Next, the laser is amplified to high energies and compressed to short pulse duration using the chirped pulse amplifier (CPA).[13] This was the subject of the 2018 Nobel Prize in Physics awarded to Strickland[98] and Mourou[99]. The CPA first stretches the laser pulse using an optical system consisting of two large telescopes and a pair of reflective gratings (stage 3). This ensures that the optical components will not be damaged during and after the amplification stage that follows the stretching.[30] The amplifier boosts the laser energy by more than four orders of magnitude (stage 4). Thereafter, a pair of large reflection gratings removes the optical chirp to re-compress the pulse to picosecond duration and shorter (stage 5). Finally, an off-axis parabolic mirror focuses the laser to a micron-sized spot (stage 6), delivering a highly intense laser pulse on target (stage 7).

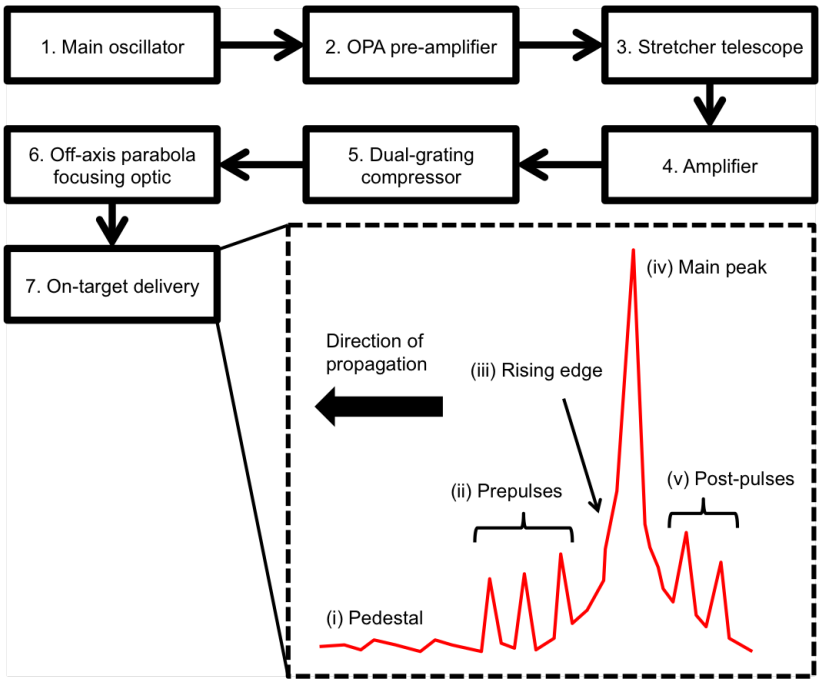

Figure 4.1: Flow diagram showing the key stages of delivering a high power laser pulse on target using the Vulcan petawatt laser. A drawing of the delivered on-target laser pulse shows five features in the temporal intensity profile: (i) pedestal, (ii) prepulses, (iii) rising edge, (iv) main peak and (v) postpulses.

Ideally, the highly intense laser pulse should be a single sharp peak. In reality, as depicted in Figure 4.1, the laser has a temporal intensity structure comprising of: (i) a pedestal arising from ASE that can occur many nanoseconds before the main peak; (ii) prepulses from microscopic imperfections in the optics of the laser system; (iii) rising edge which

may arise from, for example, the amplification of parametric fluorescence in the OPA and scattering in the gratings; (iv) main peak; and (v) postpulses. Features (i)-(iii) will interact with the target ahead of the main peak. If the laser irradiates a overdense target, these early interactions heat [30,40] and, when sufficiently intense, ionize [5,100] the target. In turn, the target expands hydrodynamically. In addition, these temporal features fluctuate in intensity and time between shots. This is undesired for experiments that require a reliable intense laser pulse and targets with high densities. Therefore it is desired, and in many cases necessary, to suppress any early interaction in the laser. Before discussing a method for achieving this, the origin of the features in the laser pulse due to the OPCPA and the concept of "laser contrast" will be described to understand the challenge of controlling the temporal shape of the laser pulse.

4.1.1 The pedestal and rising edge

The CPA is the key component generating the high energy and intense laser pulse. The drawback of this technology is that it produces two inherent temporal intensity structures in the pulse: the pedestal and rising edge. These are indicated in Figure 4.1 as (i) and (iii).

The pedestal is a result of amplified spontaneous emission (ASE) occurring in the CPA amplifier.[5] The amplifier consists of disks operating at a high gain over a few milliseconds before injecting the main laser pulse into the system.[101] The high gain nature leads to the disks losing energy by spontaneously emitting photons. Consequently, both the main laser pulse and this spontaneous emission will be amplified during operation. The ASE is incoherent and has a bandwidth, which results in the compressor smearing the signal instead of compressing. This in turn produces an intensity continuum spanning at least a nanosecond ahead of the main peak, as depicted by (i) in Figure 4.1.

The rising edge is a region of increasing laser intensity a few picoseconds ahead of the main peak. The large reflection gratings in the stretcher of the CPA extend the pulse duration by spectrally chirping the laser pulse. The laser has a bandwidth, which is a spectral range typically in orders of nanometers for a pico- to sub-picosecond laser pulse.[93,102] The broader the bandwidth, the shorter the compressed pulse duration. The stretched laser is then amplified. Thereafter, the reflection gratings in the compressor spectrally de-chirps the laser in order to re-compress the pulse duration to a sharp intensity peak. The interaction of the laser with the gratings results in spectral phase modulation that broadens the pulse duration. This phase error in the stretcher is also amplified by the amplifier. The interaction produce the rising edge depicted by (iii) in Figure 4.1.

4.1.2 Prepulses

Illustrated by feature (ii) in Figure 4.1, prepulses are rapid sharp intensity bursts that interact with the target hundreds of picoseconds before the main peak. Prepulses can be created

from microscopic defects in the optics.[97] On the Vulcan petawatt laser system, the multi-pass amplifiers and unwanted reflections from the optics between these amplifiers generate prepulses, which are challenging to correct. The high-gain amplifier increases the prepulse intensities, which can fluctuate between shots. To minimise amplifying the prepulses the OPA is included to pre-amplify the main peak[97,103] (see stage 2 in Figure 4.1).

The prepulses are of greater concern as they can cause short and rapid hydrodynamic disruptions at the target surface early in the laser-target interaction. Without probing the laser pulse on-shot or predicting their occurrence the details of the laser-matter interaction are difficult to study.

The postpulses emerging hundreds of picoseconds after the main peak in the laser (see feature (v) in Figure 4.1) are produced by the same process as the prepulses. Postpulses cause disruptions to the laser-target interaction after the main peak. This can result in changes to the radiation and particle generation in the target, which influences time-integrated diagnostic measurements (see Chapter 3). In this work it is assumed that the target is disintegrated before the postpulses reach the target. This implies that the impact of postpulses to diagnostics measurements are ignored.

4.1.3 Laser contrast

In practice[5,97,103,104] the laser contrast is defined as the fraction of pedestal, prepulses and rising edge to the peak intensity of the main peak. The contrast provides a measure to assess the impact of the features ahead of the main peak on the laser-target interaction. Ideally, the peak intensity of any feature should be below the ionisation threshold of the target material. Targets made of aluminium have a threshold of 3×10^{10} W/cm^2. For silicon and carbon-based materials studied in this thesis, the thresholds are around 9×10^{10} and 2×10^{12} W/cm^2. These are calculated using the NIST database for ionisation energies[52] and Eqn. 2.13, which assumes ionisation to occur due to barrier-suppression (see Subsection 2.2.3). The ionisation threshold for silicon coincides with results by Pronko et al.[100].

For measuring the contrast the shape of the temporal laser profile must be known. On the Vulcan petawatt laser the shape is evaluated over a number of measurements taken with a Sequoia, which is a single-shot third-order cross-correlator.[102] Two such diagnostics are used: one before the CPA, in the so-called 'front end', and after recompressing the pulse. In the method an intensity cross correlation is measured on one shot between both Sequoia. This measurement is a convolution of the temporal pulse shape and a reference pulse used by the diagnostic. The reference is initially a guessed pulse shape with a pulse duration shorter than the actual laser pulse. Using a Fourier transform the measurement is deconvolved by the reference shape to obtain a new reference pulse. Another intensity cross-correlation is measured and deconvolved for the next reference pulse. The measurement and deconvolution are repeated over a sequence of shots until the deconvolved pulse shape resembles the previous

measurements. This is referred to as a contrast scan, and the last deconvolved pulse shape is defined as the temporal laser profile. Robust measurements require a high shot rate.[102] A 2 Hz shot rate is used. Consequently, the amplifiers are not in operation for the cross-correlation because of the 20-minute cooling time.[105] Thermal stabilisation is important to reduce shot-to-shot fluctuations in the pulse shape of the laser. Ideally, a contrast scan should be taken when operating the amplifiers and a full energy shot. This would provide more accurate details of the true temporal intensity profile and understanding the laser interaction on target.

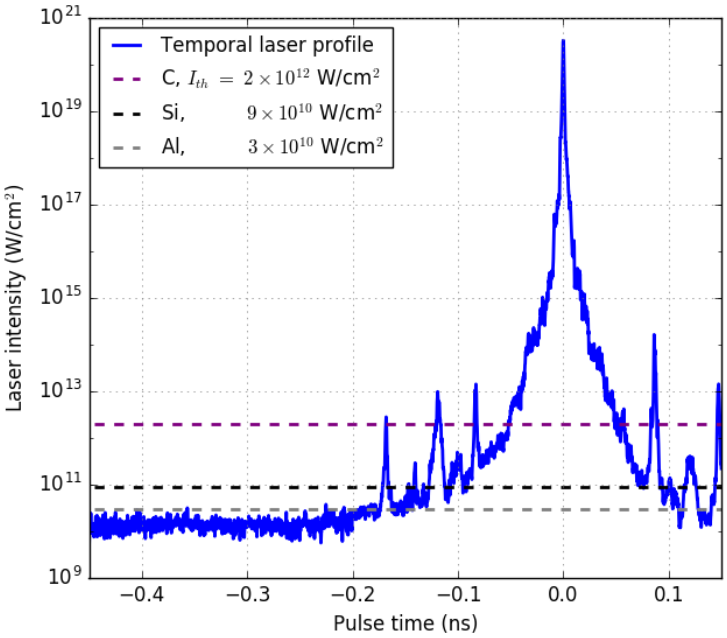

Figure 4.2: Temporal laser profile of the Vulcan petawatt laser from a contrast scan using a Sequoia at optimum performance (courtesy of I. Musgrave). The peak intensity is set to $I_0 = 3.3 \times 10^{20}$ W/cm^2. Ionisation thresholds, I_{th}, for carbon, silicon and aluminium are compared to the profile.

Figure 4.2 shows the temporal intensity profile of the Vulcan petawatt laser using the Sequoia after the recompressing stage. In the contrast scan the laser is at optimum performance with a pulse duration of 1 ps at full-width-half-maximum (FWHM). The main peak is set to 0 ns. Pedestal, prepulses and rising edge are shown at < 0 ns pulse time, and postpulses at > 0 ns. As taken from Figure 4.2, the laser contrast is 10^{-10} at 1 ns for the pedestal, 10^{-8} for the first prepulse at ∼170 ps and 10^{-5} at 10 ps inside the rising edge. Typically a contrast scan is shown with the temporal profile normalised to the maximum intensity of the laser. The profile in Figure 4.2 is multiplied by a peak intensity of $I_0 = 3.3 \times 10^{20}$ W/cm^2, which is the laser intensity used on experiments. This allows comparing the ionisation thresholds, I_{th}, for aluminium, silicon and carbon based targets, which correspond to the dashed lines in Figure 4.2. As seen in Figure 4.2, the pedestal will ionise aluminium, whereas the prepulses

ionise all three materials. The early interaction pose a challenge in preserving the near-solid target integrity before the main peak.

4.2 Contrast cleaning using plasma mirrors

One method for suppressing the intensity structure early in the laser pulse and resulting pre-plasma expansion on a solid target is the use of a contrast cleaning technique, such as using plasma mirrors. The design of these mirrors can vary between anti-reflective coated glass,[5] iron oxide doped polymer tape[106] and suspended, ultra-thin liquid crystal film.[107] Specific to this work, the plasma mirror is a plano-plano fused silica transparent plate with an anti-reflective coating on both front and back surfaces. The anti-reflective coating, which is a material that reduces the reflectivity, is deposited on the surface of the fused silica plates. This coating can reduce the reflectivity by more than one order of magnitude depending on the laser wavelength, λ_0.[8,104]

For high power laser experiments the plasma mirror is used to transmit the low intensity signal before the main peak of the pulse through the mirror. As the induced intensity increases and exceeds the ionisation threshold of the mirror (around 10^{12} W/cm^2), the mirror absorbs laser energy mainly via multiphoton ionisation.[5,108] A plasma forms on the surface that rapidly increases the electron density, n_e, towards critical density, n_{cr}. For $\lambda_0 = 1.054$ μm, $n_{cr} = 1.1 \times 10^{21}$ cm^{-3}. At this point the laser pulse is reflected by the plasma surface. The reflectivity increases as more of the mirror surface ablates with increasing laser intensity. As the intensity approaches $\sim 10^{15}$ W/cm^2 the ionisation begins to saturate and the whole irradiated plasma surface exceeds n_{cr}. Part of the rising edge and remainder of the laser pulse are reflected with an efficiency that may exceed 80 %, resulting in an enhanced contrast on target.[5,6] As the interaction continues the plasma mirror will switch off once hydrodynamic motion of the plasma at the front surface occurs. This can occur within 15 ps.[109] Note that this description assumes that the laser pulse has a good contrast to begin with. A laser with poor contrast may ionise the plasma mirrors early in the pulse, which switches off the mirror due to hydrodynamic motion and can occur before the main peak arrives. Therefore an excellent laser design is necessary to ensure that the early interaction ahead of the main peak is minimised before the plasma mirror.

The laser contrast can be further enhanced by simply combining two or more plasma mirrors. This has the advantage of further suppressing the temporal intensity structure and, as a result, delay pre-plasma formation on a solid-density target front surface with the additional plasma mirror. The design constraints for this double plasma mirror (DPM) are to ensure sufficient intensity on each mirror surface such that the main peak is delivered to the target before the mirror surfaces move. The irradiated target density and topography determines the details of the laser energy coupling. Hence, using a DPM provides a

method of controlling the shot-to-shot variation in the laser-solid interactions. According to previous use of DPM the contrast is expected to improve by more than three orders of magnitude.[109,110]

Plasma mirrors have been previously used on high power laser systems for improving the laser contrast. A single planar plasma mirror has been reported to make the use of sub-micron thin targets possible and increase the proton energies.[111] An increase in proton energies[18,82,112] as well as improvement in X-ray spectroscopy measurements[32,113] was achieved on the Vulcan petawatt laser using a plasma mirror. Proton energies further increased by almost double the energy using an elliptically-shaped concave plasma mirror over a planar mirror surface.[114] A DPM has been used previously for higher order harmonic generation,[109] including the Vulcan petawatt laser.[110] Such studies required control of the plasma density scale length through plasma mirrors, which in turn can provide a method for improving the generation of K_α yield as much as a factor of eight.[115]

4.2.1 Basic double plasma mirror model

The effect of plasma mirrors on the Vulcan petawatt laser is analysed by using the reflectivity model developed by Bagnoud and Wagner[5]. Their work measured the reflectivity R_{PM} at laser intensities on the mirror surface, I_{PM}, between 10^{12} and 10^{15} W/cm^2 shown by the error bars in Figure 4.3. These measurements may be compared to a hyperbolic function of the form

$$R_{PM}(\%) = 35 \arctan(1.8 \log_{10}(I_{PM}) - 24) + 42 \tag{4.1}$$

This is shown as the blue curve in Figure 4.3, which provides a good description of the plasma mirror reflectivity with laser intensity. Above 10^{15} W/cm^2, R_{PM} is assumed to saturate at $\sim$85 %.

Below the ionisation threshold of the plasma mirror ($< 10^{12}$ W/cm^2), R_{PM} depends on λ_0 and laser incidence angle on the mirror surface relative to surface normal, θ_{PM}. Measurements provided by Thorlabs Ltd. Technical Support show these dependencies in Figures 4.4 (a) and (b). The measurements correspond to the Thorlabs N-BK7 Broadband-B anti-reflective coated standard design suitable for reducing R_{PM} when $\lambda_0 = 1.054$ μm. An uncoated N-BK7 (NC (not coated), black dashed line) is compared to the coated mirrors (C (coated), solid lines) in Figure 4.4 (a), whose reflectivity is three times higher than plotted. The reflectivity profiles of the coated mirrors correspond to $\theta_{PM} = 0$, 10, 20, 30 and 45°. At these values of θ_{PM} and $\lambda_0 = 1.054$ μm, R_{PM} is approximated with an exponential in Figure 4.4 (b).

For optimum suppression of the pedestal and prepulses a small θ_{PM} is desired. The anti-reflective coating may improve the contrast by an order of magnitude, inline with measurements by Doumy et al.[104]

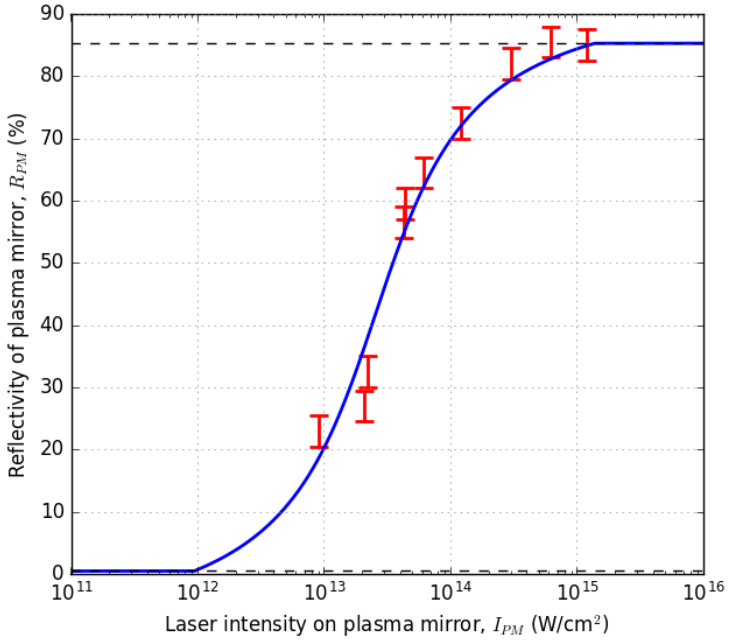

Figure 4.3: Reflectivity, R_{PM}, with laser intensity on a plasma mirror, I_{PM}, following Eqn. 4.1 (blue curve), as interpolated from the measurements (red error bars) from Bagnoud and Wagner [5]. Horizontal dashed lines at $R_{PM} = 0.47$ and 85% indicate the lower and upper limits to R_{PM}.

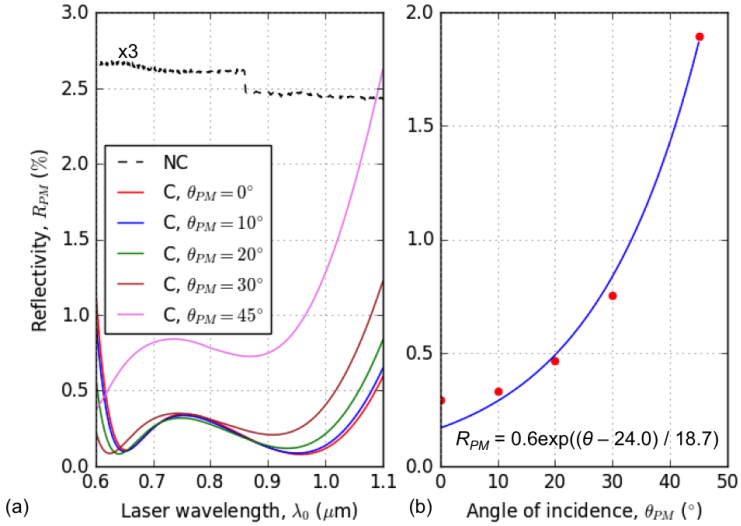

Figure 4.4: (a) Reflectivity, R_{PM}, with respect to wavelength λ_0 for a Thorlabs N-BK7 B-coated plasma mirror at different angles of laser incidence, θ_{PM}. The dashed profile is R_{PM} without anti-reflective coating and scaled down by a factor of three for comparison. (b) R_{PM} at $\lambda_0 = 1.054\mu$m as an exponential function of θ_{PM}. Courtesy of Thorlabs Ltd. Technical Support.

To determine the expected intensity on target after the laser reflects off one or two plasma mirrors, a simple geometric model for the DPM is constructed. A schematic of the model is depicted in Figure 4.5. The first and second mirror are placed a distance s_1 and s_2 from

the target at best focus. The laser has a focal number $f_{\#}$ and spot diameter at best focus d_0. The laser intensity on target is $I_0F(t)$, where I_0 is the peak intensity and $F(t)$ describes the normalised to the peak of the temporal laser profile (see Figure 4.2). The dashed red regions indicate the transmission of the laser through the plasma mirrors before ionising the surface. When the mirrors switch on the laser is incident at angles θ_1 and θ_2 relative to surface normal. The major diameters of the laser spot on the mirrors are d_1 and d_2, and the corresponding laser intensities are I_1 and I_2. Reflectivities R_1 and R_2 both describe the reflectivity curve shown in Figure 4.3, which is a function of laser intensity, wavelength, λ_0, and incidence angle on the mirror surface. Using this geometric model, the final intensity on target, I_f, is derived using the following sets of equations:

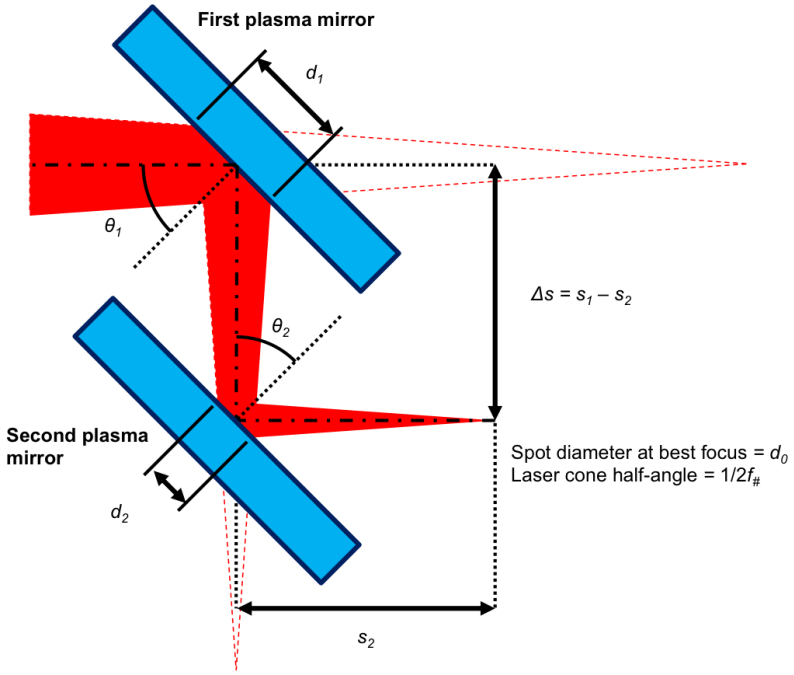

Figure 4.5: Schematic illustration of the DPM geometry. The subscripts identify the first and second plasma mirror (1 and 2) assuming the intensity is spatially constant like a top-hat function.

$$I_f(t) = I_0 F(t) R_1(I_1) R_2(I_2) \tag{4.2}$$

$$I_1 = I_0 F(t) \left(\frac{d_0}{d_1}\right)^2 \tag{4.3}$$

$$I_2 = I_0 F(t) R_1(I_1) \left(\frac{d_0}{d_2}\right)^2 \tag{4.4}$$

$$d_1 = \frac{1}{\cos\theta_1}\left(2s_1 \tan\left(\frac{1}{2f_\#}\right) + d_0\right) \tag{4.5}$$

$$d_2 = \frac{1}{\cos\theta_2}\left(2s_2 \tan\left(\frac{1}{2f_\#}\right) + d_0\right) \tag{4.6}$$

The DPM model is used on the Vulcan petawatt laser using Eqns. 4.2-4.6 to calculate the contrast improvement. In this work the angle of incidence is $\theta_1 = \theta_2 = 20°$ for both plasma mirrors. The reflectivities R_1 and R_2 follow Eqn. 4.1 as represented in Figure 4.3. The lower limit for the reflectivity is 0.47% at intensities below 10^{12} W/cm^2, as taken from Figure 4.4 (b). Upper limit is 85% at 10^{15} W/cm^2. The distances of the first and second mirror from target are $s_1 = 4.7$ cm and $s_2 = 3$ cm. The temporal laser profile at best focus with a peak intensity of $I_0 = 3.3 \times 10^{20}$ W/cm^2 between -0.45 and 0.15 ns is shown in Figure 4.2. The laser is focused on target using the $f/3.1$ off-axis parabolic mirror for $f_\# = 3.1$ and $d_0 = 6$ μm.

For calculating the contrast improvement of a single plasma mirror using Eqns. 4.2-4.6, $R_2 = 1$ and all terms corresponding to the second plasma mirror are removed.

Using Eqns. 4.2-4.6 with the above setups the calculations for one and two plasma mirrors produce the temporal laser profiles shown in green and red in Figure 4.6. The blue profile represents the Vulcan petawatt laser with no plasma mirrors. The calculations predict a suppression for the pedestal and prepulses by a factor of 5×10^{-3} using one mirror and 2×10^{-5} with two mirrors. One mirror delays the early interaction to the prepulses for aluminium and silicon, as inferred from comparing the ionisation thresholds, I_{th}, to the green profile in Figure 4.6. By using two mirrors the ionisation occurs tens of picoseconds before the main peak for all target materials given. This suggests that the impact of the pedestal and prepulses in the laser-target interaction is all but eliminated when using a DPM. Furthermore, the upper reflectivity limit of 85 % for intensities exceeding 10^{15} W/cm^2 reduces the peak intensity on target from 3.3×10^{20} to 1.9×10^{20} W/cm^2 using one mirror. With two mirrors the peak intensity drops to 1.2×10^{20} W/cm^2. In addition, the integrated intensity from -0.45 to 0.15 ns in the temporal laser profile decreases to 44% using one mirror and 24% using two mirrors.

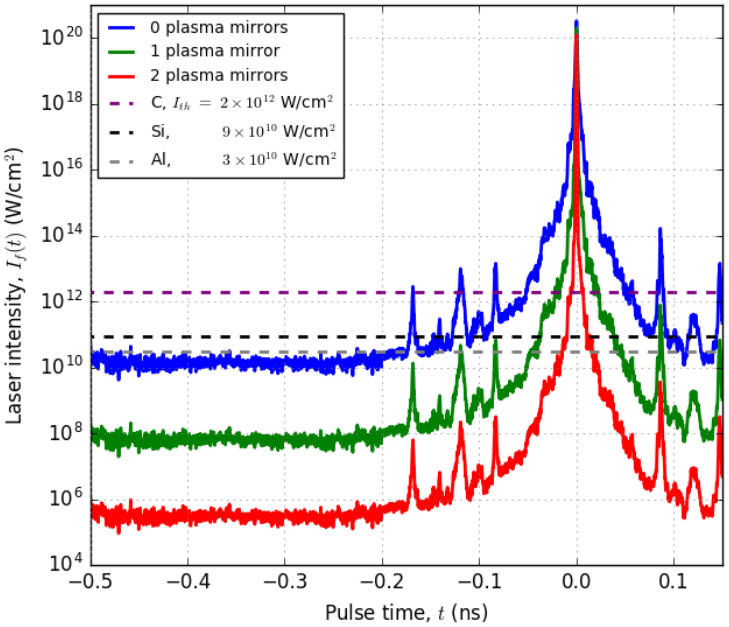

Figure 4.6: Enhancing the contrast of the temporal intensity profile of Vulcan petawatt laser (blue) using one (green) and two (red) plasma mirrors. Ionisation thresholds, I_{th}, for carbon, silicon and aluminium are compared to the profile.

In addition, the calculations also indicate that the onset of hydrodynamic motion on the mirror surfaces start close to the peak. Hydrodynamic motion is assumed to start when the laser exceeds 10^{12} W/cm^2. Using Eqns. 4.3-4.6 the peak intensities on the first and second plasma mirrors are $I_1 = 4.9 \times 10^{13}$ and $I_2 = 6.9 \times 10^{13}$ W/cm^2. Multiplying these on the normalised temporal laser profile, $F(t)$, predicts the onset of hydrodynamic motion at -2 and -1 ps before the main peak. Therefore, the setup for the DPM is chosen appropriately for ensuring a high-contrast and ultra-intense laser pulse interacts with the target.

4.2.2 Radiative-hydrodynamic modelling on contrast cleaning using Helios

With the basic DPM model predicting the suppression of the pedestal and prepulses, it is important to understand when hydrodynamic processes occur. Ideally, the DPM needs to switch on the plasma mirrors less than 10 ps before the main peak of the laser pulse. This ensures that ultra-intense laser interaction with the target is optimised. In turn, the DPM will also define the plasma density scale length, L_{cr}. Recall from Figures **??** that the combination of L_{cr} and laser incidence angle determine the laser-to-target energy coupling. Therefore, interpreting the length of L_{cr} close to the peak of the laser pulse is important.

To determine the onset of hydrodynamic processes and L_{cr} at the target surface one-dimensional (1D) Lagrangian radiation-hydrodynamic calculations were studied using the

Helios code by Prism Computational Sciences Inc.[116].

4.2.2.1 Helios setup

Figure 4.7 illustrates the setup of the 1D Helios calculations. The Vulcan petawatt laser of wavelength $\lambda_0 = 1.054$ μm irradiates the target from -504 to -4 ps before the peak of the pulse. The intensity of the laser pulse starts at 10^{10} W/cm^2. The intensity is reduced by two and four orders of magnitude in subsequent runs inline with the single and double plasma mirrors modelled in Subsection 4.2.1 (see Figure 4.6). The laser irradiates at an incidence angle of $\theta_0 = 20°$ a 15 μm thick planar silicon slab. The initial density is 2.33 g/cm^3. Electrons and ions in the slab are set to follow a two-temperature Maxwellian model starting at room temperature (25 meV). The slab is divided into two regions. The irradiated front side is 0.5 μm containing 200 zones. The rear side is 14.5 μm with 300 zones. Zones are volume elements that conserve mass and show the motion of the plasma as a fluid. Zones are depicted in Figure 4.7 as the sections enclosed by the orange lines. The origin of the simulation space is at the initial position of the slab front surface. The fluid motion driven by the laser conserves momentum and energy across the simulation space. Hence, the fluid motion is calculated using conservation equations (see Eqns. 2.26-2.28 in Subsection 2.2.9). Hydrodynamics processes are calculated in Helios by a set of equation of states and opacities based on the PROPACEOS database.[116] The hydrodynamics assumes a free expansion when the fluid temperature due to the laser exceeds 30 meV (above room temperature).

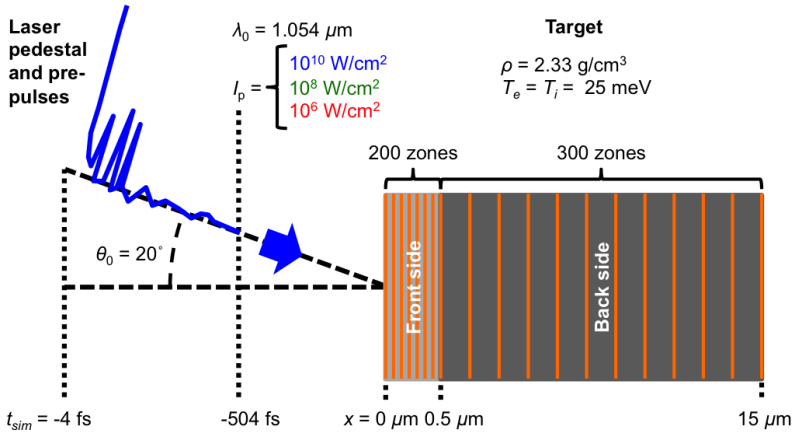

Figure 4.7: Illustration of the setup in the Helios code for modelling the early interaction of the laser pulse with a 15 μm silicon slab.

In Helios the zones are feathered, which means that within a defined fluid region the thinnest zones are close to the outer boundaries. This results in a mass difference between adjacent zones and, in turn, affect numeric consistency. For reliable calculations in the 0.5 μm front side slab, 400 zones/μm are used. This ensures the mass difference between the zones remains close to unity and does not exceed 1.5. The 14.5 μm rear side slab is least

perturbed by the early laser interaction and is assumed not to affect the accuracy of the calculations significantly. Hence, ∼21 zones/μm are used for the rear side. The thickness of the front side is based on test calculations on Helios looking for the amount of target material involved in the early interaction with a laser pedestal at 10^{10} W/cm^2.

Helios models laser absorption using inverse bremsstrahlung (see Subsection 2.2.4). The corresponding absorption efficiency depends on the product $I_0\lambda_0^2$. As $I_0\lambda_0^2$ the absorption efficiency rises because the plasma density increases. As a result the plasma becomes hotter, reducing the electron-ion collision rates. Consequently, laser absorption couples directly into the plasma, which is most efficient at the critical density surface of the plasma. Here the laser frequency is comparable to the plasma frequency, $\omega_0 \approx \omega_{pe}$. The evanescent laser field reaching this point should drive resonance absorption (see Subsection 2.2.5), which is not modelled in Helios. Resonance absorption becomes more important and eventually dominates over inverse bremsstrahlung when $I_0\lambda_2^2 \geq 10^{15}$ W μm^2/cm^2. Therefore, calculations stop when $I_0 > 10^{15}$ W/cm^2.

4.2.2.2 Onset of target hydrodynamics

Figures 4.8 (a)-(c) show the longitudinal position, x, of the critical density surface where $n_e = n_{cr}\cos^2(\theta_0)$ using pedestal intensities of 10^{10}, 10^8 and 10^6 W/cm^2 (marked by the dashed blue, green and red horizontal lines respectively). The dotted lines show the used temporal intensity profiles relative to x with simulation time, t_{sim}. x is normalised to the laser wavelength $\lambda_0 = 1.054$ μm, where $x/\lambda_0 = 0$ is the initial position of the critical surface. The density at the surface is $n_e \approx 8.8 \times 10^{20}$ cm^{-3} at laser incidence angle $\theta_0 = 20°$. The corresponding plasma density scale length at this surface is $L_{cr} = n_e/(dn_e/dx)$, which is shown for different pedestal intensities in Figures 4.8 (d)-(f). L_{cr} is normalised to λ_0 because the laser absorption depends on how laser wavelength compares to the plasma wave[30]. Figures 4.8 (a)-(f) show qualitative differences. For a qualitative comparison it is necessary to notice the changes in the vertical and horizontal axes between figures.

In the case without using plasma mirrors (see Figure 4.8 (a) and (d)) the onset of hydrodynamic motion at time, t_{HD}, occurs at the start of the calculations. This is inferred from x/λ_0 and L_{cr}/λ_0 increasing. Hence, $t_{HD} = -504$ ps. Note that the pedestal intensity at $I_p = 10^{10}$ W/cm^2 is less than the ionisation threshold of silicon at $I_{th} = 9 \times 10^{10}$ W/cm^2. I_{th} is calculated for barrier suppression ionisation. Processes such as multiphoton ionisation[30,100] occur at intensities lower than I_{th} and comparable to I_p, and in turn trigger hydrodynamic motion. The early onset and high laser intensities in the pulse lead to changes in x and L_{cr} of a few laser wavelengths. The calculation finishes at time $t_{end} = -16$ fs where the laser intensity reaches 10^{15} W/cm^2.

The calculations clearly show that the critical density surface remains close to the initial position and plasma density scale length becomes smaller when using one (see Figures 4.8

(b) and (e)) two plasma mirrors (see Figures 4.8 (c) and (f)). Using one mirror the surface position and density scale length at the end of the calculations decrease from $x/\lambda_0 = (7.4 \pm 0.3)$ to (2.0 ± 0.1) and $L_{cr}/\lambda_0 = (7.4 \pm 0.5)$ to (1.5 ± 0.2). Error in x is the zone size and L_{cr} is from interpolating dn_{cr}/dx at the critical density surface. With two mirrors the values are reduced further to $x/\lambda_0 = (0.6 \pm 0.1)$ and $L_{cr}/\lambda_0 = (0.54 \pm 0.05)$. These results are summarised in Table 4.1. The reduced surface displacements are smaller than the 6 μm spot size of the Vulcan petawatt laser at best focus, which indicates that the hydrodynamic expansion is nearly one dimensional. This provides support for using Helios for preplasma calculations. Furthermore, the reduced density scale length implies a steepening of the density gradient at the surface. This indicates that the main peak may interact with a near-solid target. This is important for nano-thin solid targets like graphene (see Chapter 6). On the other hand, the coupling efficiency may drop with a reduced density scale length. Improving the coupling efficiency is studied in Chapter 5 using microstructured targets.

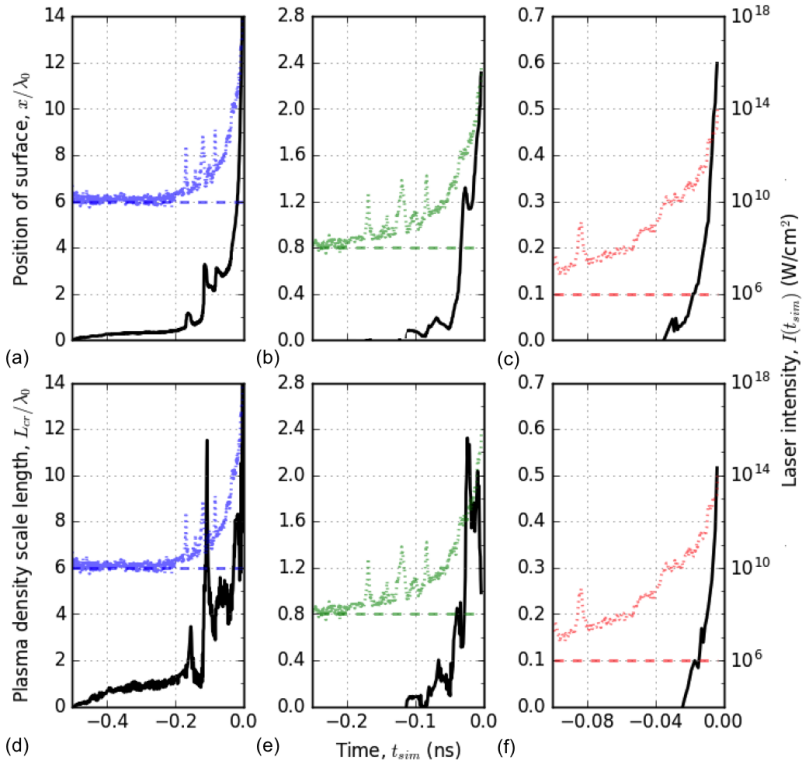

Figure 4.8: Helios calculations of the normalised plasma surface position, x/λ_0, with time t_{sim} using (a) $I_p = 10^{10}$, (b) 10^8 and (c) 10^6 W/cm^2. (d)-(f) show the corresponding normalised plasma density scale lengths, L_{cr}/λ_0.

Table 4.1: Summary of Helios calculations for the used starting intensities, I_0, inferred onset of hydrodynamic motion, t_{HD}, simulation end time, t_{end} and plasma density scale lengths, L_{cr}, at t_{end}.

Number of plasma mirrors	0	1	2
I_0 (W/cm^2)	10^{10}	10^8	10^6
t_{HD} (ps)	-504	-170	-36
t_{end} (ps)	-16	-6	-4
$x/\lambda_0[t_{sim} = t_{end}]$	(7.4 ± 0.4)	(2.0 ± 0.1)	(0.6 ± 0.1)
$L_{cr}/\lambda_0[t_{sim} = t_{end}]$	(7.4 ± 0.5)	(1.5 ± 0.2)	(0.54 ± 0.05)

The timing for hydrodynamic motion to start, t_{HD}, is delayed when using plasma mirrors as summarised in Table 4.1. With one mirror (see Figures 4.8 (b) and (e)) the onset changes from $t_{HD} = -504$ to -170 ps, which coincides with the timing of the first prepulse. This suggests that the interaction of the prepulses with the target triggers hydrodynamic motion. By using two mirrors the calculations predict that the prepulses do not cause hydrodynamic motion, as seen in Figures 4.8 (c) and (f). The onset is delayed to $t_{HD} = -36$ ps, which corresponds to a time within the rising edge and is much closer to the main peak. Therefore, using DPMs provides a solution for suppressing the interaction of the pedestal and prepulses with a solid target. This also suggests uncertainties in the plasma expansion from shot to shot can become small.

4.3 Designs of double plasma mirror assemblies for high power laser experiments

The DPM model and Helios calculations lend support that a DPM ensures high-contrast, ultra-intense laser-solid interaction. The use of a DPM has been previously been achieved. [109,110] The design outlined in this thesis differ by how they are used by two approaches: increasing the rate of data acquisition on the Vulcan petawatt laser with a four-shot cycle DPM assembly; and installing a compact 3D-printed DPM holder on the LFEX laser.

4.3.1 Four-shot cycle double plasma mirror system

The DPM assembly used successfully on the Vulcan petawatt laser is shown in Figure 4.9. The assembly uses custom-designed plasma mirrors manufactured by Manx Precision Optics. The mirrors are a pair of 12 $\times$ 2 cm^2 N-BK7 glass slabs with anti-reflective coating on both front and rear surfaces. The reflectivity is assumed to follow the model described in Subsection 4.2.1. On the front surface the top and bottom of the mirrors are coated with a highly reflective silver coating. The coating covers 2 $\times$ 2 cm^2 and 1 $\times$ 2 cm^2 at top and bottom. In Figure 4.9 (a) the DPM assembly sits close to target chamber centre (TCC) after the large mirror and off-axis parabola. Figures 4.9 (b) and (c) show close-up views at

different angles of the assembly. The separation of the first and second mirror from target are 4.7 and 3 cm. Both mirror surface normals are inclined 20° to the incident laser. Using these parameters in the DPM model and Helios calculations predict a high-contrast, ultra-intense laser interaction with a near-solid target.

The mechanical counterpart of the DPM assembly was designed at Techinsche Universität Darmstadt and developed at Central Laser Facility (CLF, UK). The stage drivers translate the DPM in x, y, z, polar and azimuthal axes. The mirrors slot into the stage and are secured by tightening the grub screws. Over-tightening is avoided to prevent bending the mirrors. The component holding the mirrors detaches from the assembly using a kinematic base, which removes and inserts the DPM quickly. The mirror design provides an approach for using the DPM for four shots in one pump down of the chamber to vacuum. Ensuring four shots with one DPM requires installing metallic plates before the mirrors for on-shot debris protection (not shown in Figure 4.9).

The highly reflective silver coating on the mirrors is useful for target alignment. Two beams are used for alignment to target chamber centre (TCC): An 1.054 μm beam transmitted through the compressor, and a 0.532 μm laser in the target area. The DPM assembly is installed with the desired parameters from the model calculations. Both alignment beams reflect off the silver coating at the mirror top to the new position of TCC at which a reference target is placed. The mirrors are translated up to reflect the beams off the bottom coating. Any offset from the new TCC position is corrected by adjusting the mirror position and angle as needed. This is repeated until both top and bottom coatings direct the beams to TCC.

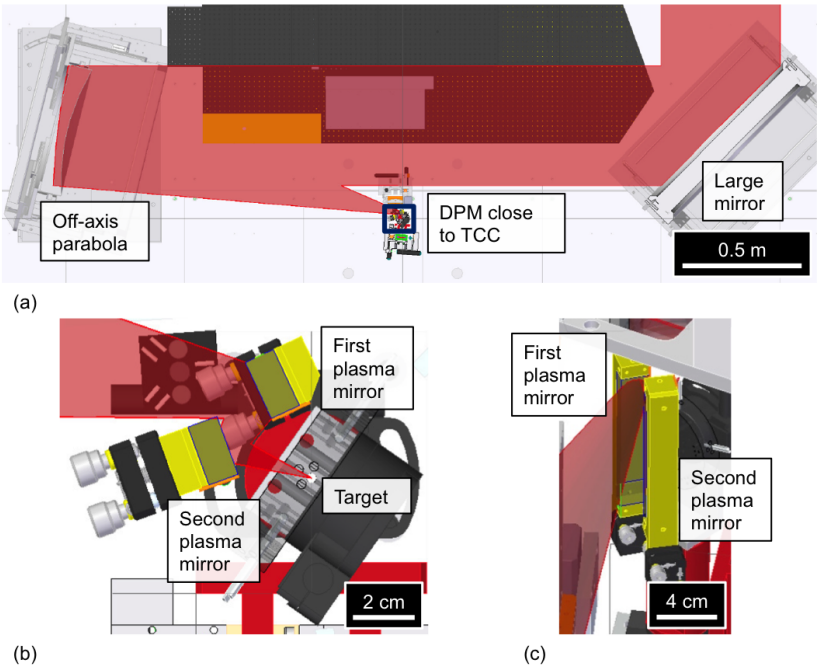

Figure 4.9: 3D CAD diagrams of the DPM assembly (a) inside the Vulcan petawatt target chamber. (b) and (c) are close-up views of the assembly from above and at an angle. Courtesy of N. W. Neumann.

After defining the new TCC, the DPM is taken outside the chamber for constructing a pre-alignment system. Two parallel 0.532 μm laser beams reflect a beam on the top and another on the bottom silver coated surfaces. The beams project onto a wall several metres away from the DPM, which are marked for alignment references. The second mirror is then removed and the references from reflecting the beams off only the first mirror is marked as well. Another pair of references for the beams without any mirrors is taken to fix the position of the pre-alignment beams. The pre-alignment system is used for preparing a new DPM for the next four-shot cycle. New pairs of mirrors are placed and positioned such that the pre-alignment beams irradiate the references. This provides a reproducible DPM alignment to the target.

The total reflectivity of the DPM, which is a measure of the laser energy across the time-integrated pulse, is measured using a calorimeter. The laser defocuses over 80 cm past TCC and then irradiates the 25 cm diameter detector plate. On shots without DPM 90 J of laser energy irradiate the calorimeter. With the DPM assembly 90 and 500 J of laser energy are used. The calorimeter absorbs the energy and transmits the measured signal to an oscilloscope outside the target area. The signal results in a voltage increase up to a peak. Converting this voltage increase to energy provides a measure of the laser energy. By taking the ratio of the recorded energy with and without DPM gives a total reflectivity of $(27 \pm 5)\%$. This is in agreement with the reduced laser energy calculated with the DPM model. The result suggests that the DPM is working as expected. Therefore, it is assumed that the DPM

suppresses the pedestal and prepulses ahead of the main peak of the laser and improved the contrast as predicted by the model.

4.3.2 Compact 3D-printed, single-shot double plasma mirror units

For prospective experiments the DPM used on the Vulcan petawatt laser needs to be adaptable. With the four-shot cycle design this is impossible because the assembly is heavy and large. A high power laser facility, such as the GEKKO-XII chamber of LFEX (Laser for Fast Ignition Experiments) based at the Institute of Laser Engineering (Japan),[95] uses a mechanical 'arm' that holds the target stage on one end. The arm supports a stage up to 13 kg in mass and moves the stage through a tube with a 12.5 cm diameter clearance from above the chamber. This approach for inserting the target remotely is necessary as the target chamber is otherwise inaccessible during experiments. The spherical chamber has a 4.4 m outer diameter and the wall thickness is 0.2 m. The weight and clearance restrictions as well as chamber size prevent the installation of the four-shot cycle DPM assembly. Therefore, a compact, 3D-printed DPM holder is designed for a contrast cleaning solution on LFEX.

LFEX is an OPCPA high power laser system developed for fast ignition experiments and includes the capability for studying laser-driven ion acceleration.[95] In the GEKKO-XII chamber the system delivers four laser pulses on target. Each laser pulse is s-polarised with a 1.5 ps pulse duration, 1.054 μm central wavelength and 400 J nominal laser energy contained within a square-shaped laser spot. The four lasers are separately and spatially configured to a 2 $\times$ 2 square array spanning 80 $\times$ 80 cm in spot size (40 $\times$ 40 cm per beam) when incident on the f/10 off-axis parabola. The parabola focuses the beams to a spot size of 60 μm at best focus. The beams intersect at the best focus and can be temporally synchronised to irradiate the target simultaneously. This delivers a total laser energy of 1.6 kJ on target with a peak intensity reaching 2×10^{19} W/cm^2. Contrast scans on LFEX use a third-order cross-correlator[102] after the pre-amplifier and a photodiode after the compressor. At optimum performance the contrast is $\sim 10^{-10}$ at 3 ns before the main peak for the pedestal.[6,117]

4.3.2.1 Design of the double plasma mirror holder

The compact DPM holder is designed using Autodesk Inventor 2018. A 2D engineering drawing with all physical dimensions is shown in Figure 4.10 (a). The laser enters and exits the holder through the front and rear sides shown. Engraved circles mark the locations for placing the 12.7 mm diameter and 3 mm thick plasma mirrors. The mirrors attach to the holder with 5-minute epoxy adhesive inserted in the 0.2 mm deep recesses on the circles. Two M4 clearance holes on the 'wings' secure the holder to the target stage with a metallic adaptor plate. A 3D illustration of the holder itself and a photograph of a printed holder with mirrors attached are shown in Figures 4.10 (b) and (c). The holder bolts on the adaptor plate attached to the target stage. A custom-made 20 mm high metallic block secures on the

target stage to adjust the DPM height to TCC, as illustrated in Figure 4.10 (d). A fiducial reference for target alignment (explained below) is placed behind the first mirror. An image of the target stage is seen in Figure 4.10 (e). The DPM holder is 3D printed on a nonporous plastic that is vacuum compatible and light weight. Another and important benefit of the compact design is that the holder causes minimum obstruction to diagnostic access to the target.

The DPM holder is tailored for an f/10 OPCPA system such as LFEX with two laser pulses − one on top of the other − moving through the holder. On the experiment two of the four LFEX beams are used, which deliver a laser energy and peak intensity of 800 J and 10^{19} W/cm^2 on target. For the DPM to work with an f/10 system, the first and second plasma mirrors have a separation of $s_1 = 46$ and $s_2 = 24$ mm from the target placed at best focus. The corresponding peak intensities of each beam on the mirror surfaces are $I_1 = 7.8 \times 10^{14}$ and $I_2 = 2.3 \times 10^{15}$ W/cm^2. The mirrors are Thorlabs N-BK7 Broadband-B anti-reflective coated windows with a 12.7 mm diameter and 3 mm thickness. The model in Subsection 4.2.1 is assumed to describe the mirror reflectivity. The laser irradiates both mirror surfaces with an incidence angle of $\theta_1 = \theta_2 = 20°$. The temporal profile of the beams is given as the blue plot in Figure 4.11, which is adapted from Morace et al.[6] Using Eqns. 4.2-4.6 (see Subsection 4.2.1), the DPM model is used to calculate the temporal profile shown in red in Figure 4.11. From the figure it is inferred that the DPM suppresses the pedestal and prepulses well below the ionisation thresholds, I_{th}, of carbon, silicon and aluminium and delay the onset of hydrodynamic motion of the target to ∼10 ps before the peak of the pulse. The model predicts a contrast improvement of 2×10^{-5}. With the two beams spatially coinciding on TCC the peak intensity on target is reduced to 7.2×10^{18} W/cm^2 (3.6×10^{18} W/cm^2 per beam). The total reflectivity of the DPM is 52%, which is greater than the 24% reflectivity calculated for the Vulcan petawatt laser. This is because in the LFEX setup the first and second plasma mirror switch on −10 and −3 ps before the main peak. In comparison in the Vulcan setup the mirrors switch on at −2 and −1 ps. Hence, more laser energy is delivered to target in an LFEX laser.

An important consideration for the DPM design is the target alignment. The plasma mirrors are highly transparent and, hence, may not transmit a detectable signal from the alignment laser inside the chamber to the target. Therefore, a fiducial reference is installed ∼43 mm behind the first plasma mirror along the incident laser axis. The alignment laser is focused to this reference inside the chamber.

The DPM is prepared using a pre-alignment system based outside the target chamber. A 632.8 nm (red) laser is modified to form an f/10 focusing beam by using a combination of three lenses and irises. The laser is sufficiently bright that it reaches target position after reflecting off both anti-reflection coated plasma mirrors. Note that there are no reflecting silver surfaces to aid alignment of the 3D-printed compact DPM in comparison to the design

used on the Vulcan petawatt laser. Therefore, the laser moves through the DPM holder to the fiducial and target, which prepares the target stage assembly before shot. Inside the chamber it must be assumed that the target is positioned correctly when the fiducial is aligned to the laser.

The accuracy of target alignment depends strongly on the laser incidence angle on the plasma mirror surface, θ_{PM}, and mirror size. Table 4.2 summarises the angular tolerance for the laser incidence angle, $\Delta\theta_{PM}$, when $\theta_{PM} = 20°$, $30°$ and $45°$. A holder with $\theta_{PM} = 10°$ requires in a large mirror separation, which would make the holder large and result in a poor DPM performance on LFEX. The angular tolerance improves slightly the smaller θ_{PM} is. Furthermore, a thin plasma mirror provides small tolerances. Therefore, the mirror thicknesses are 3 mm, which are the thinnest commercially available. The mirror diameter is also small to ensure an optimum DPM performance and mechanical robustness. The angular tolerance indicates how reliable the fiducial reference is for target alignment. All other parameters for the DPM setup result in a very small and, hence, negligible impact on the tolerance.

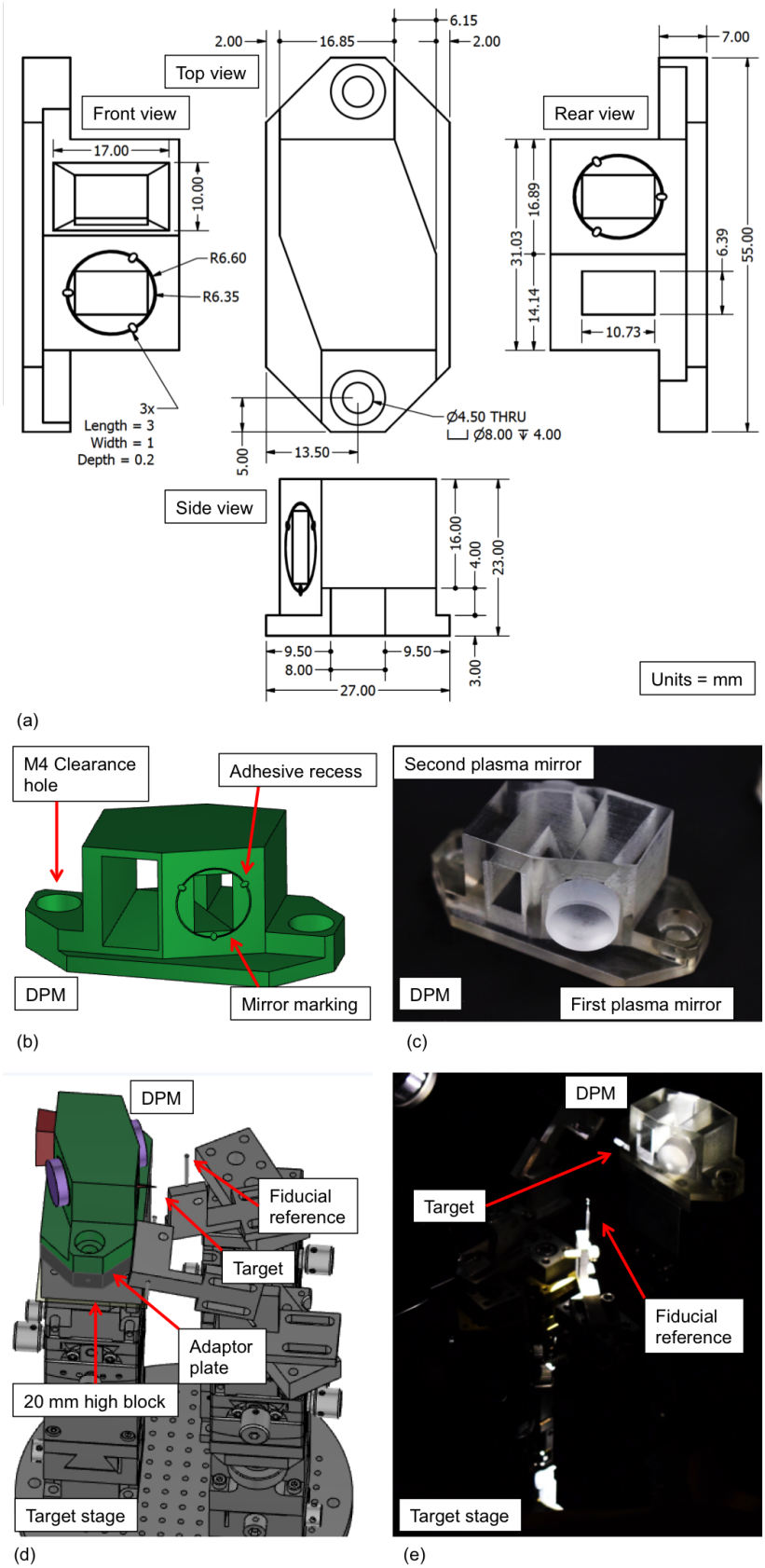

Figure 4.10: (a) 2D drawings of the DPM holder. All dimensions are in mm. (b) A 3D design and (c) picture with plasma mirrors on the holder are shown. The LFEX target stage assembly including the DPM holder is illustrated in (d) and photographed in (e).

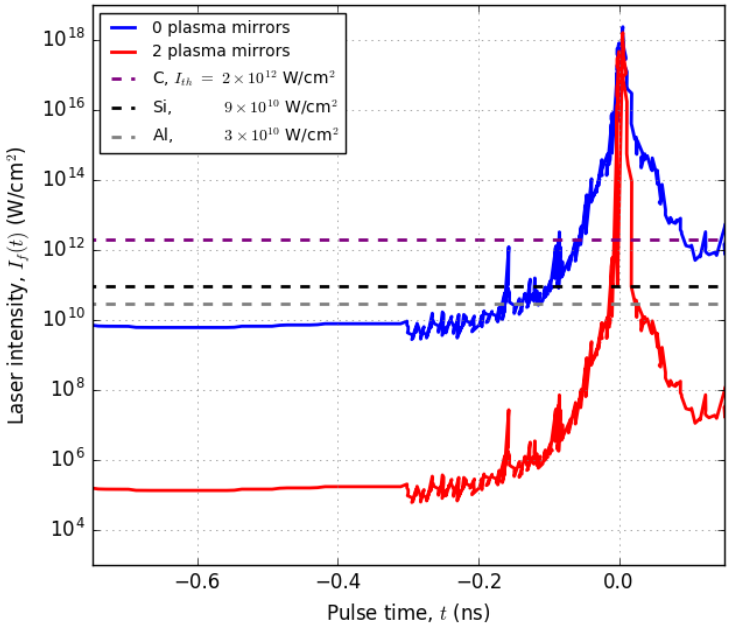

Figure 4.11: Temporal profile of one LFEX laser pulse as given in Morace et al. [6] (blue). The peak intensity is set to $I_0 = 5.0 \times 10^{18}$ W/cm^2. Contrast improvement using the DPM model produce the temporal profile in red with $I_0 = 3.6 \times 10^{18}$ W/cm^2 per beam. Ionisation thresholds, I_{th}, for carbon, silicon and aluminium are compared to the profiles.

Table 4.2: Angular tolerances, $\Delta\theta_{PM}$, using the setup described in the modelling for LFEX at selected laser incidence angles on the plasma mirror, θ_{PM}.

θ_{PM}	20°	30°	45°
$\Delta\theta_{PM}$	±0.17°	±0.16°	±0.15°

An important observation made using pre-alignment is the three laser spots incident on target. These are seen exiting the DPM holder by placing masking tape over the rear side as shown in Figure 4.12 (a). Without the tape, the reference camera monitoring target position along laser axis observes these three spots (see Figure 4.12 (b)). The spots are equally spaced horizontally across ∼3 mm. This observation occurs because the laser reflects partially on the outer and inner mirror surfaces. This is illustrated in Figure 4.12 (c). The far right and dim spot at the DPM exit (1) is the true laser spot on target because the laser reflects on the outer mirror surfaces. Therefore, a target must be aligned to this spot. The central, bright spot (2) consists of two spots that separate upon defocusing the reference camera. These are from one outer and one inner reflection on each mirror. The far left spot (3) comes from two inner reflections. This spot is brighter than the actual laser spot (1), which suggests that the reflectivity inside the mirrors is greater than on the outer surface. This is because of the anti-reflective coating.

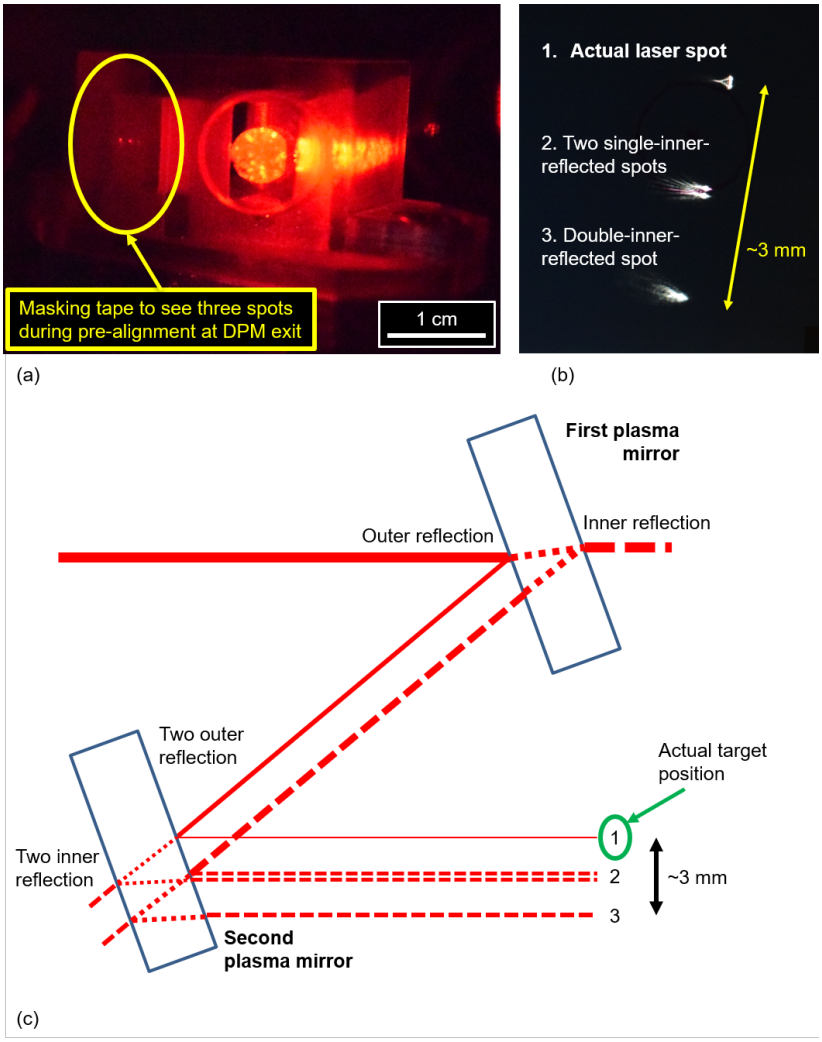

Figure 4.12: (a) Three horizontally displaced laser spots seen at the DPM holder exit using masking tape during pre-alignment. (b) On the reference camera the spots are (1) the actual laser from outer reflections, (2) outer and inner reflections and (3) inner reflections off the mirrors. (c) An illustration showing the formation of the three spots from outer and inner reflections.

4.3.2.2 Test experiment for the double plasma mirror holder

A two-week experiment on the LFEX GEKKO-XII laser system was conducted to test the DPM holder. The results focus on the near field of the laser when using the DPM holder. Shots on targets were in most part unsuccessful because the main laser was vertically misaligned during those shots. This is apparent from the holders breaking. For comparison, a DPM holder before and after a misaligned shot are shown in Figure 4.13. Nevertheless, it was viable to install the 3D-printed DPM holder and gain an insight on using a DPM on LFEX.

Figure 4.14 illustrates the experimental setup on LFEX. The two vertically-displaced lasers project through the DPM onto a polymer plastic plate of polytetrafluoroethylene (PTFE), $(C_2F_4)_n$. The PTFE is 2.4 m from laser focus to spread the laser spots across a

20×10 cm^2 area on the plate and, therefore, irradiate the near field on the PTFE. The top and bottom beams on the PTFE have a vertical cut-off along the middle of the near field from the two segmented gratings in the compressor.[117] Shots are taken without DPM using 150 J of laser energy with both beams, and then with DPM using 170 and 630 J. The corresponding laser energy fluences incident on the PTFE are tabulated in Table 4.3.

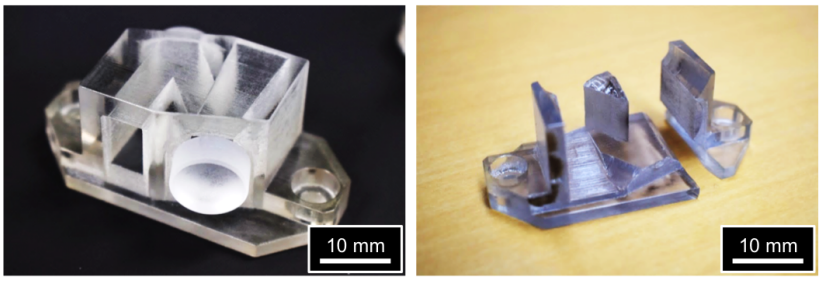

Figure 4.13: DPM holder (a) before and (b) after a vertically misaligned full energy laser shot on LFEX.

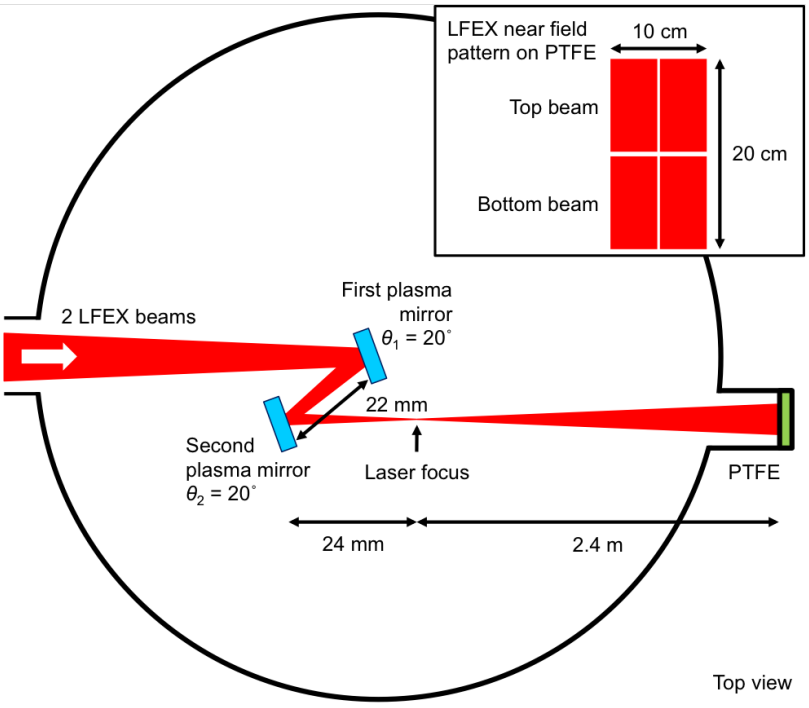

Figure 4.14: Illustration of the LFEX setup using the DPM holder. Two lasers project through the DPM on the PTFE plate. The near field of the two lasers irradiate the PTFE in the configuration shown in the top-right insert featuring a vertical cut-off along the middle.

In the original setup an infrared camera was used to record the near field of the LFEX lasers on the PTFE. Unfortunately, the diagnostic failed on every shot due to electromagnetic pulse (EMP). This may be solved in the future with additional EMP shielding and appropriate target design.[78] Therefore, the data is limited to the near field imprinted on the

PTFE on shot.

Table 4.3: Summary of delivered laser energies, E_0, and energy fluences on the PTFE, E/A. Energy fluences on shots with DPM are reduced by the total reflectivity of 52% predicted by the model.

E_0 (J)	DPM used	E/A (J/cm^2)
150	No	0.8
170	Yes	0.4
630	Yes	1.6

The near field imprinted on the PTFE after each shot are shown in Figures 4.15 (a)-(c). The images are photographed with a Canon D3300 digital single lens reflex camera. Room lights reflect off the PTFE and cause the images to appear artificially brighter at top and bottom and therefore should not be confused with any laser fluence. For the shot without DPM unit (see Figure 4.15 (a)) a dim grid-like pattern is seen. Bright regions in the pattern have high laser fluence. When using the DPM with a lower fluence (see Figure 4.15 (b)), localised 'hot spots' are seen in the near field on the PTFE. On a high energy shot similar features in the near field are seen imprinted across a larger surface area on the PTFE, as seen in Figure 4.15 (c).

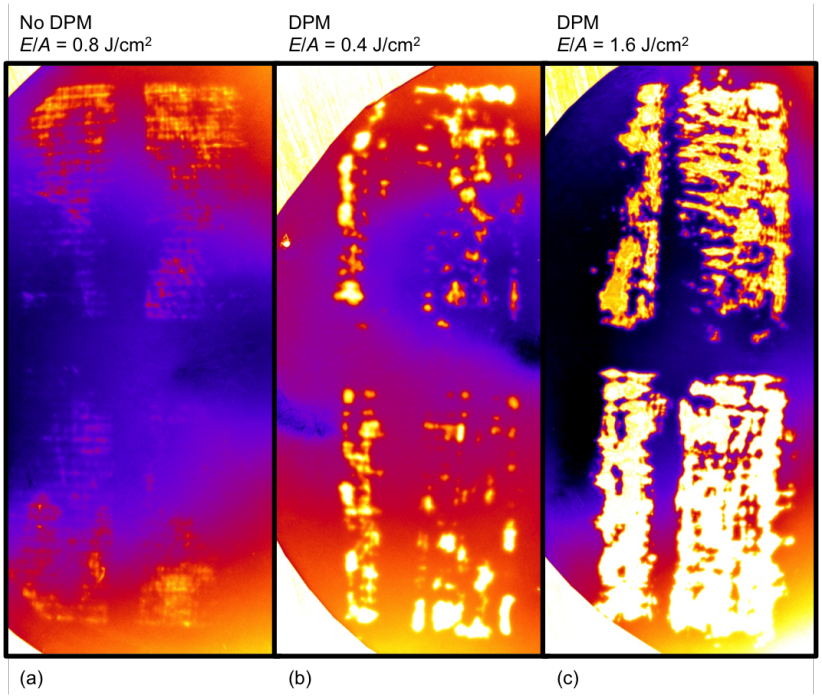

Figure 4.15: Imprinted near field of two LFEX laser beams on shots (a) without the DPM unit at low laser energy, (b) with DPM at low energy and (c) high energy. The estimated energy fluence on the PTFE is indicated above. The compressor grating splits the square-shaped beams vertically.

The pattern on the PTFE forms using the DPM because of the grid-like spatial distribution of the near field without using the DPM (see Figure 4.15 (a)). The laser imprints on

the PTFE when the induced energy fluence exceeds 1.4 J/cm^2.[118] This threshold is greater than the laser energy fluence on both low-energy shots, which suggests that the energy across the near field is not uniformly distributed. Consequently, the inhomogeneity of the energy fluence causes early hydrodynamic motion on the plasma mirror surfaces at localised regions irradiated by the laser. This is evident in Figures 4.16 (a) and (b) which shows the near field imprinted on the mirrors with 170 J of laser energy. On the first mirror the spot looks uniform by first inspection. The spot on the second mirror is slightly deformed. Therefore, it can be expected that the near field forms these 'hot spot' features after the laser moves through the DPM. This is seen in Figure 4.15 (b) as well as for the near field seen in Figure 4.15 (c) with the high 630 J energy on shot.

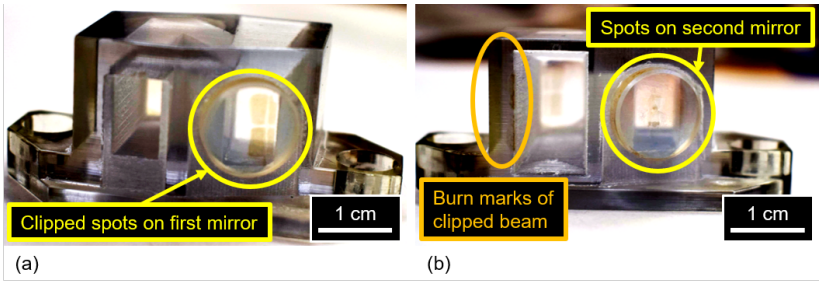

Figure 4.16: Imprinted laser spots (yellow) of the two LFEX beams after the low-energy shot on the DPM. Part of the beams are clipped at the DPM entrance (orange).

Note that the near field in Figures 4.15 (b) and (c) appears thinner on the left side of the vertical central cut-off. This is seen because the DPM holder clips the laser beams at the entrance, which is highlighted in Figure 4.16 (b). The alignment in chamber may have not been fully reproducible. In future, a DPM holder with silver mirrors may be needed to verify target alignment in order to avoid clipping of the beams.

On the high laser energy shots, those exceeding 600 J, the plasma mirrors detach from the holder and shatter. This is because the laser fluence exceeds 30 J/cm^2 on the mirrors.[117] The fragments were not recoverable because the chamber was inaccessible during the experiment. Prospective experiments using this DPM holder need a solution for catching the fragments and keep the chamber clean.

4.4 Summary and future work

Installing a double plasma mirror (DPM) on high power laser experiments is important for suppressing the intense pedestal and prepulses ahead of the main peak, which delays the onset of hydrodynamic motion. Helios calculations show that near solid density interaction with the Vulcan petawatt and LFEX lasers are possible. This method readily extends to other petawatt-class high power laser facilities. These predictions also suggests a method for controlling the plasma expansion with the DPM. The DPM was successfully installed on

experiments using the Vulcan petawatt laser with a four-shot cycle design. The additional advantage with the enhanced laser contrast is that the measurements can be effectively coupled to computational simulations that use an idealised laser pulse without prepulses. The impact of the DPM for ensuring high-contrast, laser pulses interacting with solid targets will be discussed in the results presented in Chapters 5 and 6.

Laser contrast improvements are possible on any system, and a method for achieving this is by using a 3D-printed compact DPM assembly. This was tested preliminarily on LFEX. The experiment was limited to results showing the near field imprinted on PTFE. The near field of LFEX was seen to have a grid-like spatial distribution, which after the laser moves through the DPM resulted in a non-uniform near field with localised regions of high laser fluence. This may not be ideal for methods that laser accelerate ions, but it may provide a solution for mitigating the early interactions on the target. Further work on testing the holder with the laser irradiating targets are needed. This may provide more ideas on advancing and adapting this work for using DPM on other high power laser systems. The DPM holder is a sophisticated design as it is tailored to the laser system, accounts for mechanical compatibility for easy installation and the compactness provides large diagnostic access to the target.

Chapter 5

Engineered microstructured targets for producing a bright K_α source

In this chapter the use of targets with microstructured surfaces for improving the laser-to-target coupling will be discussed. This will include a brief outline of the target properties, followed by the experiment on the Vulcan petawatt laser. The setup includes a double plasma mirror (DPM), and the results of using the DPM will also be discussed as these are of importance to using microstructured targets. The experimental measurements show that using the targets with microstructured surfaces and DPM together produces a bright and reliable K_α source. Finally, spectral analysis using PrismSPECT will provide an insight to the plasma conditions required to produce the K_α emission.

5.1 Targets with microstructured surfaces

The reason for investigating the use of targets with microstructured surfaces is to increase the coupling of the laser to the target. Studies show that using structured targets, such as nanospheres,[119] nanowires,[120] microwires[121,122] and foam[123] generate energetic particle and radiation sources as a result of the improved coupling. In this work the focus was on using silicon microstructured surfaces for improving the generation of X-ray radiation sources. This relates to early studies[15] linked to this thesis on creating radiation fields during ultra-intense laser-solid interaction.

Silicon with needle-like microstructured surfaces have high light absorption because of their topography. For 1.053 μm infrared light the absorption may reach more than 90% efficiency compared to using plane silicon surface with 60%.[124] These microstructured targets were tested on the Vulcan petawatt laser for understanding how the higher absorption efficiency improves the spectrally-resolved X-ray emission.

5.1.1 Target fabrication

Targets with microstructured surfaces are developed at the Technische Universität Darmstadt using a rapid laser ablation technique. This method is described in detail by Ebert et al.[7] and illustrated in Figure 5.1. A 25 μm thick silicon foil is placed on a target holder inside the processing chamber. The foil surface is irradiated by a laser with a spot size adjusted between $d_0 = 65$ and 75 μm after the laser focus and in turn provides laser intensities between $I_0 = 4.4 \times 10^7$ and 6×10^7 W/cm^2. The laser operates at $\lambda_0 = 0.8$ μm wavelength, $t_0 = 100$ fs pulse duration and $R_{rep} = 5$ kHz shot rate. The laser scans across the surface with a speed of $v_{scan} = 0.5 - 2.0$ mm/s using a galvanometric two-mirror optics system. This allows imprinting microstructures across a 1×1 mm^2 surface on the foil. The processing chamber is in ambient air to produce 15 μm high needle-like structures. Shorter structures are made by filling the chamber with an electrically-conducting liquid.

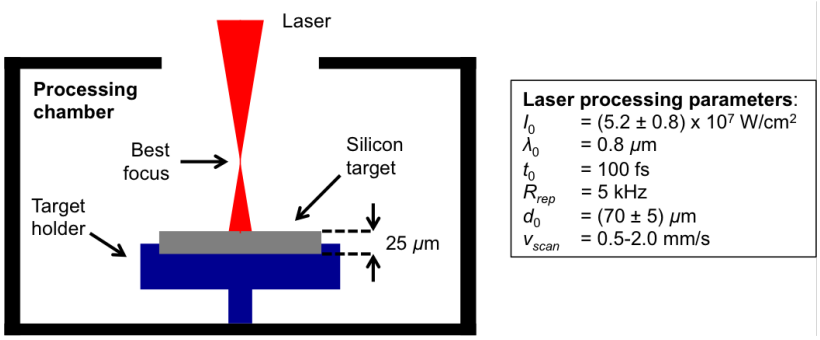

Figure 5.1: Method for fabricating silicon targets with microstructured surfaces. Figure reproduced from Ebert et al.[7].

5.1.2 Scanning electron microscopy imaging

Using a scanning electron microscope a sample silicon target with microstructured surface was imaged as shown in Figure 5.2 (a). The needle-like structures are non-uniformly distributed across the surface. A schematic illustration of the microstructures is depicted in Figure 5.2 (b). The imaged microstructures have a needle height of roughly 15 μm and a spacing of about 5 μm on average. The structures are supported by the silicon base, which is not irradiated by the laser during fabrication.

5.2 Vulcan petawatt experiment

The targets with microstructured surfaces were used on an experiment using the Vulcan petawatt laser based at the Rutherford Appleton Laboratory (UK).[93] The aim was to determine how the laser-to-target coupling improved when switching from conventional flat foils to microstructured targets. This required using a double plasma mirror (DPM) to suppress the early interaction in the laser pulse with the target. This ensured that the microstruc-

tures were preserved close to the peak of the laser. A diagnostic suite for a detailed study on the laser-to-target coupling was used in the experiment. This included measuring the laser reflection from the target surface,[122] ion generation along laser axis and target normal, and spectral X-rays emitted from the front surface. This thesis focuses on the DPM and spectral X-ray measurements.

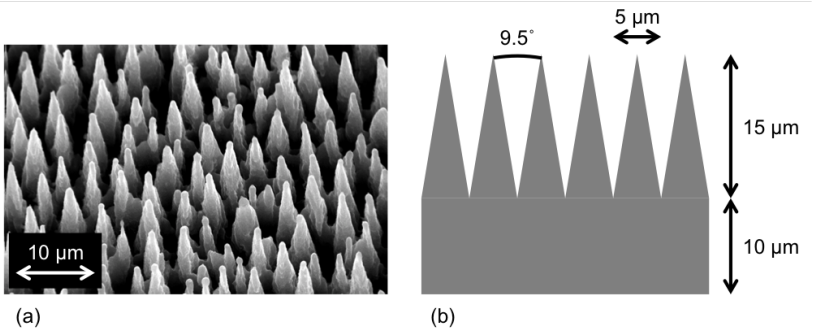

Figure 5.2: (a) Scanning electron microscope image (courtesy of N. W. Neumann.) and (b) schematic design of a target with the microstructured surface.

5.2.1 Double plasma mirror setup

The experimental setup is illustrated in Figure 5.3 (a). This shows the DPM, target and conical crystal spectrometer used. The DPM setup and temporal laser profile of the laser (see blue plot in Figure 5.3 (b)) are used in the basic DPM model described in Chapter 4. This model calculated the suppressed temporal profile shown in Figure 5.3 (b) in red and predicts that the laser energy after the DPM is 24% of the initial laser energy.

For the DPM the first and second plasma mirror were placed 45 and 30 cm from the target. Both mirrors were irradiated by the focusing laser pulse at 40° to their surface normal. Using a calorimeter and transmitting the main laser through the DPM, the total reflectivity of the laser was (27 ± 5) %, which is in agreement with model calculations described in Chapter 4. Hence, it was assumed that the DPM reduced the laser energy to $\mathcal{E}_0$ = (160 ± 30) J. 30 % of that energy was contained within the FWHM of a ∼6 μm spot size at best focus. By using a FWHM pulse duration of t_0 = (1.0 ± 0.1) ps, the peak intensity on target was $I_0 = (1.6 \pm 0.3) \times 10^{20}$ W/cm^2.

For testing the performance of the DPM, the plasma mirrors were substituted with silver-coated mirrors. The silver mirrors reflect the whole laser pulse without suppressing the pedestal and prepulses. Silver has an ionisation energy of 7.58 eV,[52] which by using Eqn. 2.13 provides an ionisation threshold of 6×10^9 W/cm^2. The threshold assumes that the laser ionises via barrier-suppression ionisation (see Subsection 2.2.3). The peak intensity on the first mirror was around 4.9×10^{13} W/cm^2. The DPM model (in Subsection 4.2.1) predicts that hydrodynamic motion starts ∼9 ps before the main peak. This start time ensures that the main peak reaches the target. It is important to note that hydrodynamic motion on

plasma mirrors make the mirrors useless after about 15 ps.[109] After this time, scattering and absorption in the plasma formed at the mirror surface is significant. This means that plasma mirrors, both silver and anti-reflection coated, should only be used with high contrast laser pulses. Hence, a laser pulse without improving the laser contrast was irradiated on target while preserving the experimental setup using this approach.

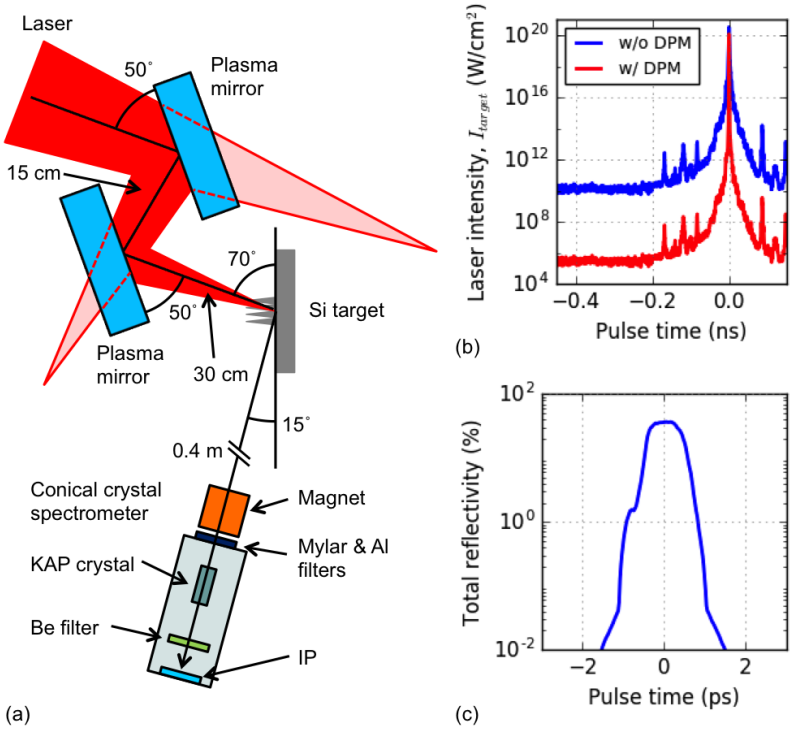

Figure 5.3: (a) Schematic setup of the Vulcan petawatt laser experiment using the microstructured targets, featuring the DPM and conical crystal spectrometer. (b) The temporal intensity profile of the Vulcan petawatt laser (blue) is suppressed by the DPM using the model described in Chapter 4. (c) The total reflected signal by the DPM at the main laser peak is shown.

In addition to the setup, the pulse duration was extended from $t_0 = (1.0 \pm 0.1)$ to ~5 ps for a number of shots on target. This reduced the laser intensity by a factor of five. Changing the intensity by increasing pulse duration provided details on the performance of the microstructured target surface. The pulse duration remains short enough such that the plasma mirrors are effective in reflecting the main peak of the laser.

5.2.2 Target setup

The target was changed between flat and microstructured surfaces. The flat-surfaced foils used were 25 μm thick. These corresponded to the combined base thickness with structure height of the microstructured targets, which were 15 μm high needles on a 10 μm base. The needle separation was about 5 μm. These were the main parameters used for the microstructured targets. In addition, 10 μm high microstructures with a ~4 μm separation

on a 15 μm base were used to compare the impact of short and long microstructures.

After the DPM the laser irradiated the target with a 20° incidence angle relative to target normal. This angle was used to reflect the laser from the target surface to a diagnostic measuring the reflected light signal (see Jarrett et al. [122]). It was also assumed that the laser coupling efficiency to the target was at optimum using this angle of incidence. [124,125]

The targets were irradiated at best focus (spot size of 6 μm) and when defocused to a spot size of ∼50 μm by moving the best focus roughly 80 μm before the target front surface. Defocusing reduced the laser intensity irradiated on the target from $I_0 = (1.6 \pm 0.3) \times 10^{20}$ to $(2.3 \pm 0.4) \times 10^{18}$ W/cm^2, where the changes at the plasma mirror surfaces are relatively small. The purpose for these shots was to investigate the effect of irradiating more of the structured surface with a larger spot size and the same laser energy.

5.2.3 Conical crystal spectrometer

In the experimental setup shown in Figure 5.3 (a), a conical crystal spectrometer recorded the spectral X-ray emission from the target front surface at 75° to target normal on shot. The horizontal distance between the X-ray source and image plate (IP), h, and vertical source to crystal distance, s, were $h = 405$ mm and $s = -60$ mm. A magnet of 0.5 T was installed in front of the spectrometer to deflect electrons irradiated from target away from the crystal and IP. The front of the spectrometer was covered by 6 μm polyethylene terephthalate (PET) and 5 μm mylar with a nm-thin aluminium coating on one side. The filtering attenuated the X-ray irradiated on the crystal, which reduced radiative overheating and fluorescence of the crystal. Thereafter, the X-ray emission was spectrally dispersed by a potassium acid phthalate (KAP) crystal with a spacing between crystal planes of $d = 13.317$ Å (or typically given as $2d = 26.634$ Å). The dispersed X-rays propagated through a 25 μm beryllium filter for further filtering. Lastly, the X-rays were captured on Fujifilm BAS SR-TP 2040 IP. Details to the spectrometer components were provided in Chapter 3.

On the back of the spectrometer a rotating drum contained IPs, which could be moved into position for shot by driving the drum remotely. This allowed recording four spectra in the four-shot cycle setup used on the experiment.

The spectrometer was designed to disperse an X-ray spectrum from 1.65 to 1.84 keV on to an IP, which centralises on Si K_α emission at 1.739 keV. Spectral resolving power was $\mathcal{E}_x/\Delta\mathcal{E}_x = (1200 \pm 100)$ and was estimated from the width of the spectrum at $\mathcal{E}_x = 1.739$ keV along the spatial axis perpendicular to the spectral image. This was estimated from the full width at half maximum, which was (0.101 ± 0.005) mm with standard error. By multiplying the width with the spectral dispersion relation, $d\mathcal{E}_x/dg = (-1.45 \pm 0.01) \times 10^{-2}$ keV/mm (see Section 3.1).

Spectral measurements are a composite of emission over space and time. The plasma conditions vary with space and time, where the spectra is usually dominated by the hottest

and densest plasma. The emission from this plasma is from the irradiated laser spot region, which typically includes He_α and Ly_α lines. K_α emission, on the other hand, provides information about the relativistic electrons interacting with cold matter in the target.

For alignment a micro-balloon was placed at the target position. Irradiating a 532 nm laser on the balloon, the light scattered towards the spectrometer. Without filters on the spectrometer the light was reflected by the conical crystal to the IP. By relying on the human eye, the whole spectrometer was translated towards or away from the balloon until the image cast on the IP was in focus. The image was further focused by adjusting the crystal height with the attached micrometer. After completing the setup the filters and a magnet were installed.

After alignment the spectral image recorded on the IP on the first shot cycle was not fully focused. This was corrected by adjusting the micrometer displacing the crystal in the spectrometer. By looking at the images in the subsequent shots, further changes to the crystal position were made until the spectrum was focused. This was determined from narrowing the image as much as possible.

5.3 Data reduction

The IPs from the spectrometer, after a four-shot cycle, were digitized using a Fujifilm FLA-5000 IP scanner. The data is reduced from digitised images to analysable spectra using the procedure described in Chapter 3. The raw and background spectra were extracted along the image using ImageJ (see Figure 3.6 (a)). The data was converted from quantum level (QL) to photostimulated luminescent (PSL) emission using Eqn. 3.6. The background was then subtracted from the data. Spectra were spectrally calibrated to the position of K_α at $g = 52.5$ mm by using the spectral dispersion profile shown in Figure 3.2. Thereafter, the spectral intensity is corrected from the crystal reflectivity, IP response function and filter attenuation using Eqn. 3.8.

5.4 Results from microstructured targets

The results focus on the performance of the 15 μm long microstructured targets. This is compared to four changes in the experiment: target topography, laser contrast, spot size and pulse duration.

5.4.1 Data reproducibility

Figure 5.4 shows seven individual (grey profiles) and averaged (red profile) X-ray spectra recorded from irradiating the laser on 15 μm microstructured targets. It is noticeable that the data is reproducible with the standard deviation of the average indicated by the red

shaded region. The laser energy on target and pulse duration used are $\mathcal{E}_0 = (160 \pm 10)$ J and $t_0 = (1.8 \pm 0.1)$ ps for the data shown in the figure. All spectra are normalised to the maximum of the average spectrum. K_α emission is seen as the asymmetric peak with its maximum at 1.743 keV and a ~4 eV full-width at half-maximum (FWHM). The energy corresponds to the Si III state, and the FWHM suggest that the K_α peak is composed of Si I-IV emission (from 1.739 to 1.745 keV). Peaks from B-, Be- and Li-like ionisation states of silicon are seen at energies above 1.8 keV.

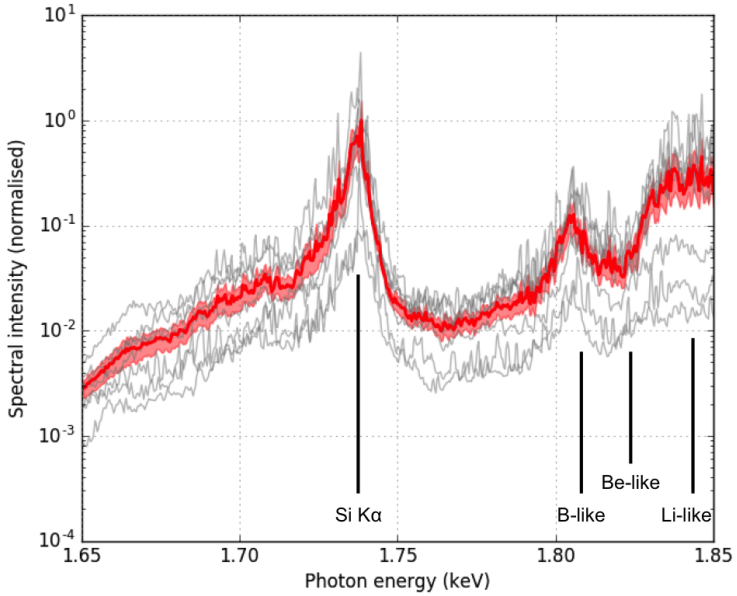

Figure 5.4: X-ray spectra from laser irradiating 15 μm microstructured targets over many shots (grey). The statistical average of the spectra is shown in red with the shaded area showing the standard error. The position of Si K_α and B-, Be- and Li-like ionisation states are annotated on the figure.

An important observation is the high level of shot-to-shot data reproducibility. The deviation of the whole spectral intensity is about 6%. The accuracy of this deviation is mainly affected by the background subtraction and spectral calibration during data reduction. This high data reproducibility was consistent when using the DPM. The observation was not investigated in detail as this was not an objective of the experiment. Therefore, there are not enough data shots without DPM available to justify the result. On the other hand, the Helios simulations shown in Section 4.2.2.2 suggest that suppressing the early interactions in the laser pulse reduces the plasma density scale length and, in turn, may reduce the variability in the laser interaction with the target. It is possible that the DPM is needed for producing the high level of shot-to-shot data reproducibility.

For the following subsections the average spectra are compared instead of evaluating individual shots. The spectra are normalised to the maximum spectral intensity of the data due to the 15 μm long microstructured targets. This provided concise and qualitative data

evaluation.

5.4.2 Target topography

X-ray spectra from flat, 10 and 15 μm microstructured targets were averaged and shown Figure 5.5. Switching the target topography from flat to 10 μm microstructures increases the signal of K_α. The signal further increases when using 15 μm microstructures. In addition, the longer microstructures raise the signal of B-, Be- and Li-like ionisation states seen above 1.8 keV.

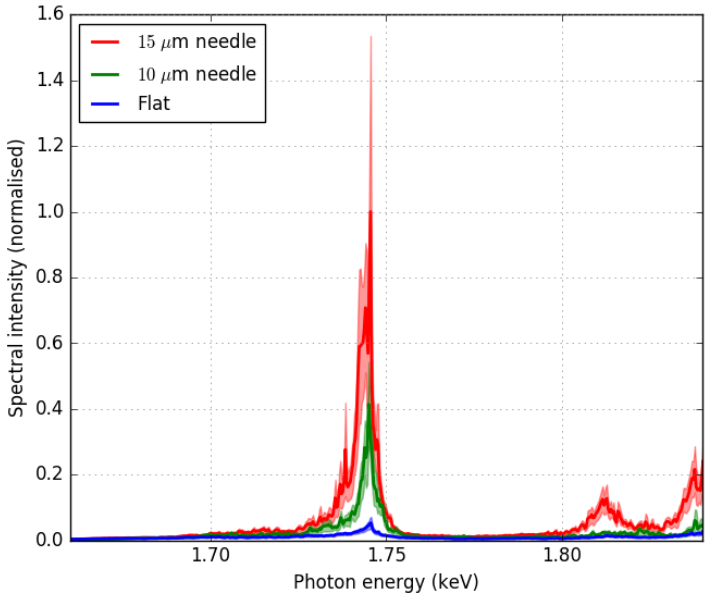

Figure 5.5: X-ray spectra recorded when laser irradiating the 15 μm (red) and 10 μm (green) long microstructured targets and flat surfaced foils (blue).

The K_α integrated intensity is calculated between 1.74 and 1.75 keV for the three target topographies. The results are normalised to the 15 μm microstructures and summarised in Table 5.1. The errors are derived from the standard error shown as the shaded area on the spectra within the integrated range. As deduced from the table and Figure 5.5 by changing from a flat to 10 μm long microstructured targets increases the K_α signal by a factor of (6.9 ± 0.7). Using the 15 μm microstructures over the 10 μm microstructures further increases the signal by a factor of (2.6 ± 0.3) and provides a K_α peak that is (18 ± 2) brighter than from using the flat foils.

Table 5.1: K_α integrated intensities from changing the target topography. The values are normalised to the integrated intensity from using the 15 μm microstructures.

Target topography	K_α integrated intensity (normalised)
15 μm microstructures	(1.00 ± 0.09)
10 μm microstructures	(0.38 ± 0.03)
Flat surface target	(0.055 ± 0.003)

5.4.3 Impact of double plasma mirrors

Results from high- and low-contrast shots, using the DPM and silver mirrors respectively, are shown in Figure 5.6. The spectrum in red is due to the high contrast and blue is from using the low contrast. Both spectra are from irradiating the 15 μm microstructured targets. Relatively few shots with low contrasts were measured because of poor data reproducibility and focusing on collecting more data using DPM in the experiment. As seen in the figure, a high contrast results in large spectral intensities. The K_α integrated intensity rises by a factor of (5.7 ± 0.6). Higher ionisation states are more significant in the high contrast shots. This indicates that the plasma is hotter, suggesting the generation of more relativistic electrons. This result shows that the DPM increases the spectral intensity.

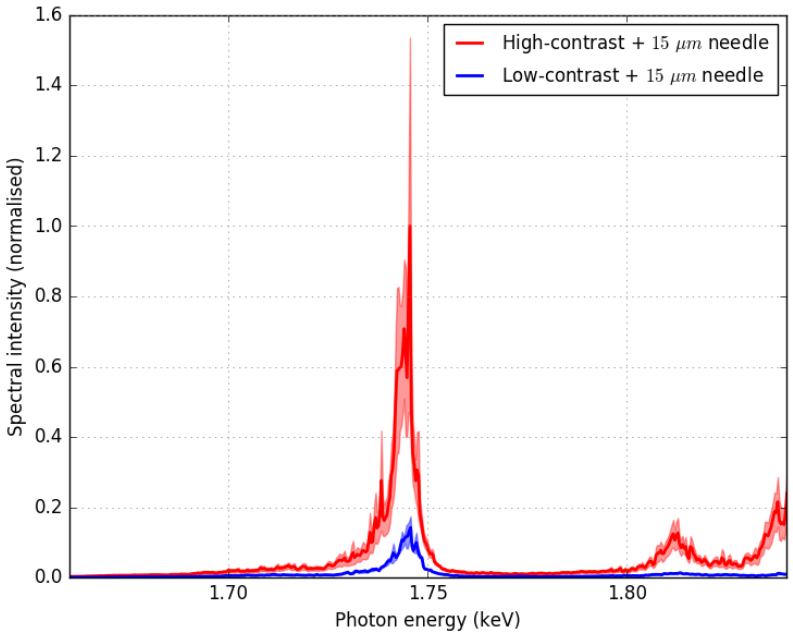

Figure 5.6: X-ray spectra recorded when laser irradiating the 15 μm microstructured targets when using the DPM for a laser with high-contrast (red) and silver mirrors for a low-contrast (blue).

When switching the target topography to a flat-surfaced foil the measurements show a similar result to the microstructured targets. This is shown in Figure 5.7, where the spectra are normalised in spectral intensity to the maximum of the spectrum due to using the microstructured targets and DPM (see the red spectrum in Figure 5.6). Using the DPM

over the silver mirrors for irradiating a high-contrast laser pulse on the target results in a large spectral intensity. The K_α integrated intensity rises by a factor of (6.4 ± 0.4). As explained in this sub-section, relatively few shots without using the DPM were recorded on the experiment.

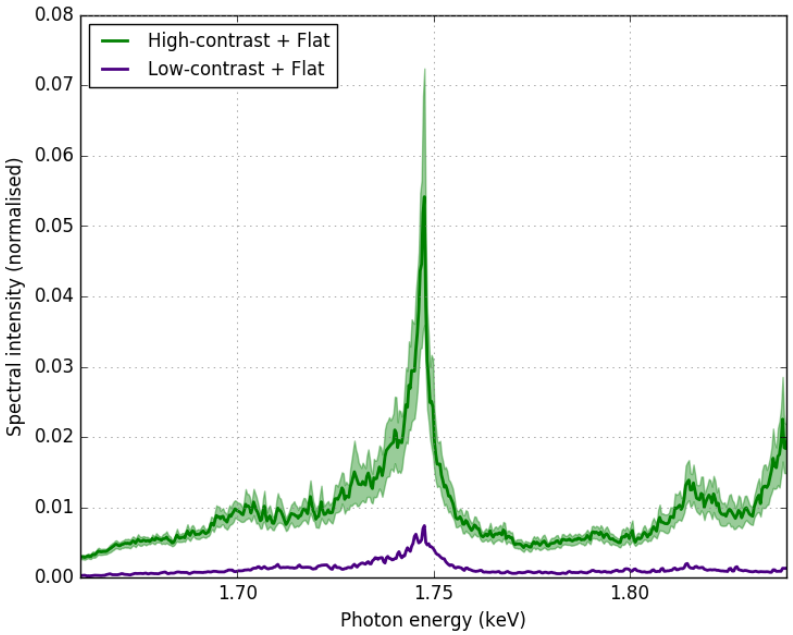

Figure 5.7: X-ray spectra recorded when laser irradiating the flat-surfaced foils when using the DPM for a laser with high-contrast (green) and silver mirrors for a low-contrast (indigo). Note that the spectral intensity is normalised to the spectrum produced by using the 15 μm microstructured targets and DPM.

5.4.4 Laser defocusing

The laser was defocused by moving the parabola away from the target such that the best focus was infront of the target front surface. This results in expanding the spot diameter from $d_0 = 6$ μm at best focus to 50 μm, which reduces the laser intensity from $I_0 = (2.3 \pm 0.4) \times 10^{20}$ to $(1.6 \pm 0.3) \times 10^{18}$ W/cm^2. Figure 5.8 shows the red and blue spectra produced when irradiating with $d_0 = 6$ μm and 50 μm respectively. The result shows that defocusing the laser results in a decrease of spectral intensity. The integrated intensity of K_α drops by a factor of (3.0 ± 0.4). The higher ionisation states are present, yet likewise lower in intensity and these transitions are centred at slightly lower energy.

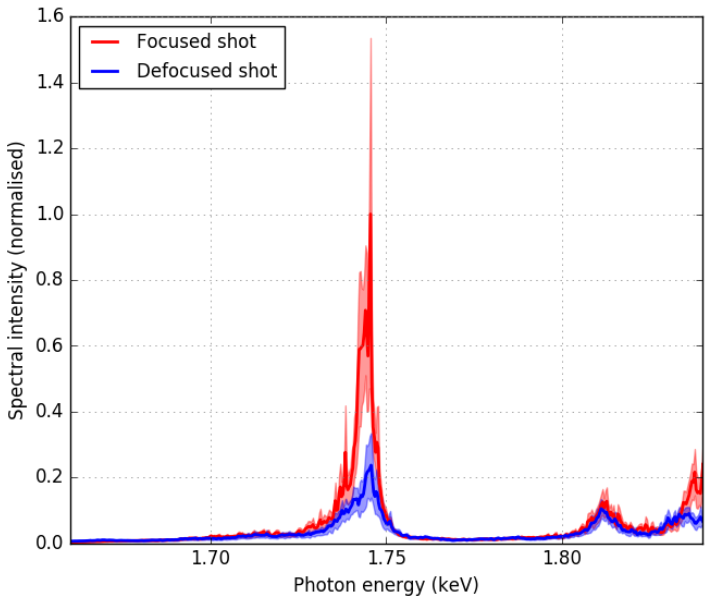

Figure 5.8: X-ray spectra recorded when laser irradiating a 6 μm (red) and 50 μm spot (blue) on 15 μm microstructured targets.

5.4.5 Pulse duration

Figure 5.9 shows the impact of extending the pulse duration, t_0. The red spectrum is produced using $t_0 = (1.0 \pm 0.1)$ ps, which was the shortest and typical pulse duration used in the experiment. Extending the duration to $t_0 \approx 5$ ps results in the blue spectrum seen in the figure and, in turn, leads to a drop in laser intensity from $I_0 = (2.3 \pm 0.4) \times 10^{20}$ to $(4.6 \pm 0.8) \times 10^{19}$ W/cm^2. The outcome is shown as the blue profile in Figure 5.9. The longer pulse duration decreases the K_α integrated intensity by a factor of (1.3 ± 0.1). Signal from higher ionisation states decrease in signal and remain resolvable. Both defocusing and extending the pulse duration of the laser reduce the peak intensity. The main difference between these two approaches is that the pedestal and prepulses drop in intensity when defocusing. A longer pulse duration might not change the pedestal irradiated on target.

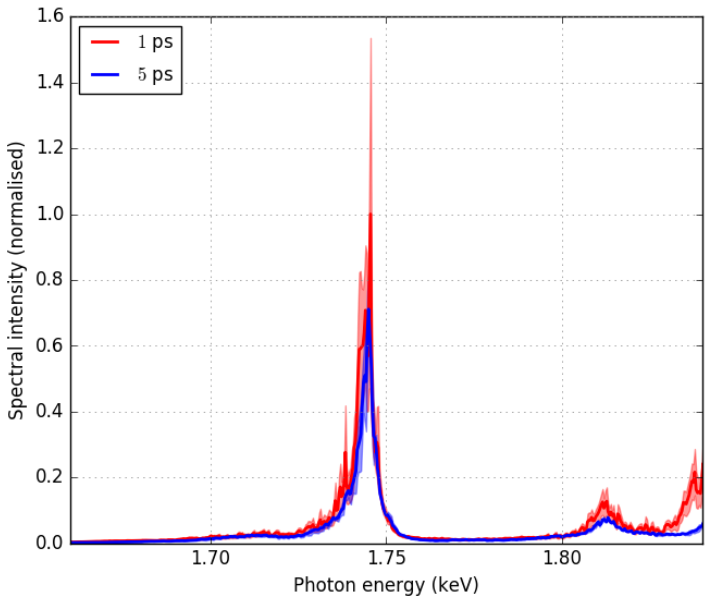

Figure 5.9: X-ray spectra recorded when laser irradiating a laser with a (1.0 ± 0.1) ps (red) and 5 ps (blue) pulse duration on 15 μm microstructured targets.

5.4.6 Summary and discussion of experimental results

The changes in K_α intensity with respect to the 15 μm long microstructured targets are summarised in Table 5.2. Changes in the experiment include changing the target surface to a flat surface and shorter microstructures, laser contrast, spot size and pulse duration. The largest change in K_α occurs when switching the target surface, and the smallest transition happens upon extending the pulse duration.

Table 5.2: Change in K_α integrated intensity by changes in the experimental setup. These are compared to a 15 μm microstructured targets irradiated by a high-contrast, 6 μm spot and (1.0 ± 0.2) ps laser pulse.

Change in experiment	K_α factor change
Flat surface target	(18 ± 2)
10 μm long microstructures	(2.6 ± 0.3)
Low-contrast	(5.7 ± 0.6)
Enlarge spot to 50 μm	(3.0 ± 0.4)
Extend pulse to 5 ps	(1.3 ± 0.1)

The interpretation results in two key observations. The inclusion of the DPM is for suppressing the early interactions closer to the main peak of the laser. This leads to a delay in hydrodynamic expansion on the target and, in turn, decreases the plasma density scale length (see Chapter 4). The suppression of the pedestal and any prepulses is a possible reason for the high level of shot-to-shot data reproducibility. As the suppressed pedestal

and prepulses leads to a shorter density scale length the microstructured surface integrity is preserved. This improves the laser-to-target coupling as the microstructures are designed to engineer a specific plasma length scale and increase the laser absorption. Note that relatively few data shots without using the DPM were acquired in the experiment. To justify the improved shot-to-shot data reproducibility further measurements are needed. Secondly, the K_α integrated intensity produced using the 15 μm long microstructures is significantly higher than that produced from the flat surfaced targets. Therefore, the combination of the DPM and microstructured targets provides a method for producing a bright and reliable K_α source.

A number of studies have observed changes in the K_α integrated intensity using a variety of target designs and approaches. Using the Vulcan petawatt laser, Evans et al.[56] recorded Al K_α emission line when irradiating a 0.2 μm aluminium foil coated with 12 μm and 17 μm CH at laser-irradiated front surface and 4 μm on the back surface. Other thicknesses for the front surface coating produced no significant K_α emission. In another study using a table-top Ti:sapphire laser Purvis et al.[120] irradiated a 60 fs laser pulse of 5×10^{18} W/cm^2 intensity on 55 nm wide and 5 μm long nano-wire nickel targets. The laser contrast was improved by frequency-doubling the laser pulse. Their results showed almost a 50 times increase in the spectral intensity, which is larger than the 18-fold rise in Si K_α signal in this work. On the other hand, the spectrally-resolved background signal does not increase by a comparable factor, and hence the measurements in this thesis shows a better signal-to-noise ratio improvement. Furthermore, Sumeruk et al.[126] used the THOR laser at the University of Texas (USA)[127] for investigating the use of laser-irradiated targets with silicon micro-spheres on a solid foil. Using spheres of 0.25 μm in diameter resulted in the largest rise in Si K_α yield by a factor of 8 from using a flat-surfaced foil. This is less than half of the rise in K_α signal measured in this work, suggesting that needle-like microstructures are more efficient in coupling laser energy to hot electrons compared to micro-spheres.

The use of laser contrast enhancement has been studied in relation to the generation of K_α emission. Fourmaux and Kieffer[128] installed saturable absorber plates in the Advanced Laser Light Source system (see Fourmaux et al.[129] for setup) for improving the contrast. By irradiating molybdenum targets with the contrast-enhanced laser pulse with intensities around 1×10^{18} W/cm^2 resulted in an optimised conversion efficiency from laser energy to K_α yield. The contrast improvement was important for achieving this result. Furthermore, in experiments DPMs have produced reduce plasma density scale-length from suppressing the pedestal,[130] which in turn generated a larger hard X-ray intensity through higher harmonic generation.[110] To the best of our knowledge, there have been no publications reporting a reduction in the shot-to-shot variability using microstructured targets in combination with a DPM.

Defocusing laser spot reduces the K_α integrated intensity by a factor of 3 when defocusing

from 6 μm to 50 μm. Previous work[131] studied the effect of defocusing the laser pulse irradiating a 2 mm thick copper foil using the ASTRA laser based at the Rutherford Appleton Laboratory (UK).[132] The results showed that defocusing the spot size to 50 μm did not change the signal noticeably. By enlarging the spot size to 1.6 mm with the f/2 focusing laser on target reduced the signal by a factor of 2. Using the silicon microstructured target in this work show a larger reduction in K_α integrated intensity. The reason for the drop in the signal may be due to a transition in the laser absorption mechanism to relativistic electrons.

5.5 K_α spectral analysis using PrismSPECT

The K_α peak observed in the experiment emerge from atomic processes driven by the laser-target interaction. To gain an insight on the conditions needed to observe this emission, the measurements are compared to spectral calculations using PrismSPECT.[133] PrismSPECT is a collisional-radiative spectral analysis code. In this thesis the code is used to understand the physics generating the K_α emission from the parameters characterising the plasma.

5.5.1 Calculation setup

The PrismSPECT[133] calculations were configured for studying K_α emission from a plasma. For the atomic model the ATBASE[134] 6.1 data table of silicon was used. The table contains a list of ionisation states, energy level configurations that the bound electrons can have and the corresponding transition probabilities and rates. By selecting the model with the label 'Backlighter K-shell spectroscopy', 12001 number of configurations (out of 14030) were imported. These included ionisation states with 1 to 14 electrons and K-shell vacancies for K_α emission.[32,133,135] The corresponding atomic rate equations were solved using a steady-state plasma in non-local thermodynamic equilibrium (see Subsection 2.3.3).

Four parameters were used in the calculations. The relativistic electron temperature, T_{rel}, was varied between 0 eV and 5 MeV. $T_{rel} = 0$ eV is identical to removing the relativistic electrons from the calculations. The Wilks' (Eqn. 2.20) and Beg's (Eqn. **??**) scalings for a laser of intensity $I_0 = 1.6 \times 10^{20}$ W/cm^2 and wavelength $\lambda_0 = 1.054$ μm respectively predict that the $T_{rel} = 5$ and 1 MeV and, hence, the upper range includes these temperatures in the calculations. The fraction of relativistic electrons from the bulk plasma, f_{rel}, was set to values between 0 and 20%, where the lower limit removed the relativistic electrons in the calculations. T_{rel} and f_{rel} were studied to determine the impact of relativistic electrons on producing K_α emission. As for the bulk plasma the temperature, T_e, was set to values between 0.03 and 3000 eV. The lower limit accounts for matter at room temperature and higher limit exceeds the ionisation energy of the K-shell, which is sufficient for the plasma to be fully ionised. The high T_e was used to verify that a hot plasma produces Ly$_\alpha$, He$_\alpha$ and

Li-like emission and no K_α line at 1.740 keV. Changing T_e provides information about the degree of outer-shell ionisation (see Subsection 2.3.1). The spectral resolving power, $\mathcal{E}_x/\Delta\mathcal{E}_x$, was also studied to infer the impact of instrumental broadening. $\mathcal{E}_x/\Delta\mathcal{E}_x$ was varied between 400 and 1200 for low and high resolving powers. These were used as the values in a normal distribution, N, that convolves the spectrum calculated in PrismSPECT, S_i, to determine the broadened spectrum, S_b,

$$S_b = S_i * N \tag{5.1}$$

$$N = \frac{1}{\sqrt{2\pi\Delta\mathcal{E}_x^2}} \exp\left(-\left(\frac{\mathcal{E}_x}{\Delta\mathcal{E}_x}\right)^2\right) \tag{5.2}$$

The spectral calculations were configured to interpret the basic physics. Therefore, the calculations use a zero-width plasma, which is a system with no opacity. The spectrometer in the experiment recorded x-ray emission from an angle 75° relative to target surface normal at the front side. If assuming that most of the K_α emission is produced near the front surface rather than deep inside the target, the emission is produced from optically thin matter (see Subsection 2.3.2). Therefore, the zero-width approximation in the calculations is assumed reasonable.

The plasma mass density, ρ_e, was set to 1 g/cm^3. This is less than half the solid density of silicon (2.328 g/cm^3).

Recall from Subsection 5.2.3 that the conical crystal spectrometer integrated the emission over space and time. The measurements were a composite of many plasma conditions. PrismSPECT provides spectra using single values of electron temperature, mass density and non-thermal electron fraction and temperature. The calculations are run as steady state. To gain an insight to the possible plasma conditions in the experiment, the measurement from 15 μm microstructured targets was compared to multiple spectra using different values for T_e, ρ_e, f_{rel} and T_{rel}.

5.5.2 Comparison between calculation and experiment

The experimental measurement is compared to the calculated spectrum in Figure 5.10. The measurement is shown as the grey spectrum with the shaded area. For the calculated spectrum plotted in black, $T_{rel} = 1$ MeV, $f_{rel} = 5\%$, $T_e = 7$ eV, $\mathcal{E}_x/\Delta\mathcal{E}_x = 800$ and $\rho_e = 1$ g/cm^3 are used in PrismSPECT. The contributions of silicon ionisation states from I to III are given by the coloured plots in Figure 5.10. The photon energies of these states and Si IV are annotated on the figure. The bumps of emission towards higher photon energies relative to the peaks correspond to satellite emission of each ionisation state.

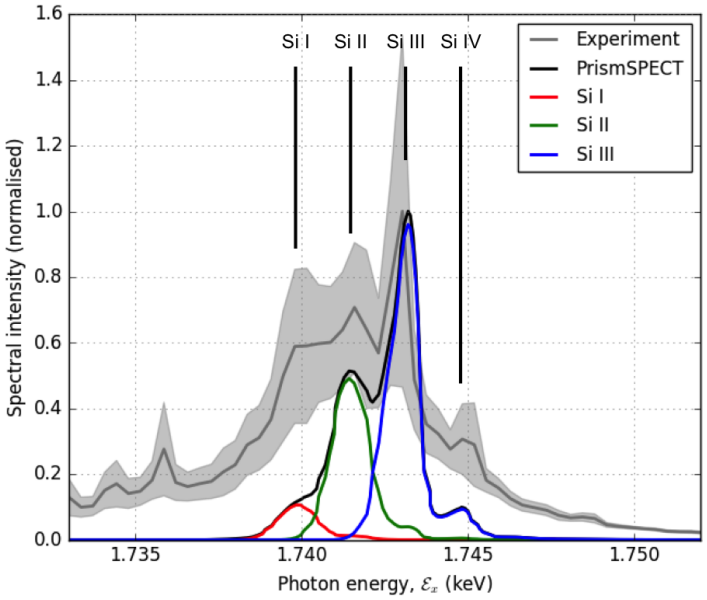

Figure 5.10: Calculated spectrum of K_α using the PrismSPECT code with input parameters $T_{rel} = 1$ MeV, $f_{rel} = 5\%$, $T_e = 7$ eV and $\mathcal{E}_x/\Delta\mathcal{E}_x = 800$ and $\rho_e = 1$ g/cm^3. Spectral emission from Si I-IV ionisation states is shown by the coloured plots, where the peak energies are annotated in the figure. Experimental measurement from using 15 μm microstructured targets is shown in grey.

As seen in Figure 5.10 the shape of the K_α manifold is determined by the ionisation states Si I (1.740 keV), II (1.742 keV), III (1.743 keV) and IV (1.745 keV). The overall peak width at half-maximum for the calculated peak is 6 eV, coinciding closely with the estimated width from experimental measurements. In addition, from comparing multiple spectra to the experimental result suggests that the brightest signal is produced from the Si III state.

5.5.2.1 Relativistic electrons

When the relativistic electron temperature, T_{rel}, and fraction, f_{rel}, are set to zero independent of each other, there is no K_α emission predicted by the calculations. Without relativistic electrons there is no collisional ionisation or excitation that generated K-shell vacancies. The relativistic electrons are important for explaining the experimental observation. Furthermore, the shape of the K_α manifold is nearly independent of T_{rel} and f_{rel}. This is inferred from the calculated spectra upon changing T_{rel} and f_{rel}.

5.5.2.2 Plasma temperature

Calculations varying the plasma temperature, T_e, between 0.03 and 60 eV are shown in Figures 5.11. K_α line emission at different selected values of T_e are seen in Figure 5.11 (a). The relative spectral intensities of the Si I, II, III and IV states changes with rising T_e such that the degree of ionisation increases. Figure 5.11 (b) gives the spectral intensity at the

peak of the Si I-IV states that make up the K_α manifold as a function of T_e. The vertical solid lines correspond to the spectra in Figure 5.11 (a). As seen from the figure the line emission is optimised from the Si I state at $T_e = 4$ eV. From the Si II state, $T_e = 6$ eV, and for Si III and IV state, $T_e = 9$ eV. The brightest signal is produced from the Si III state. The experimental measurement is a composite of different values for T_e, which makes the interpretation more complex.

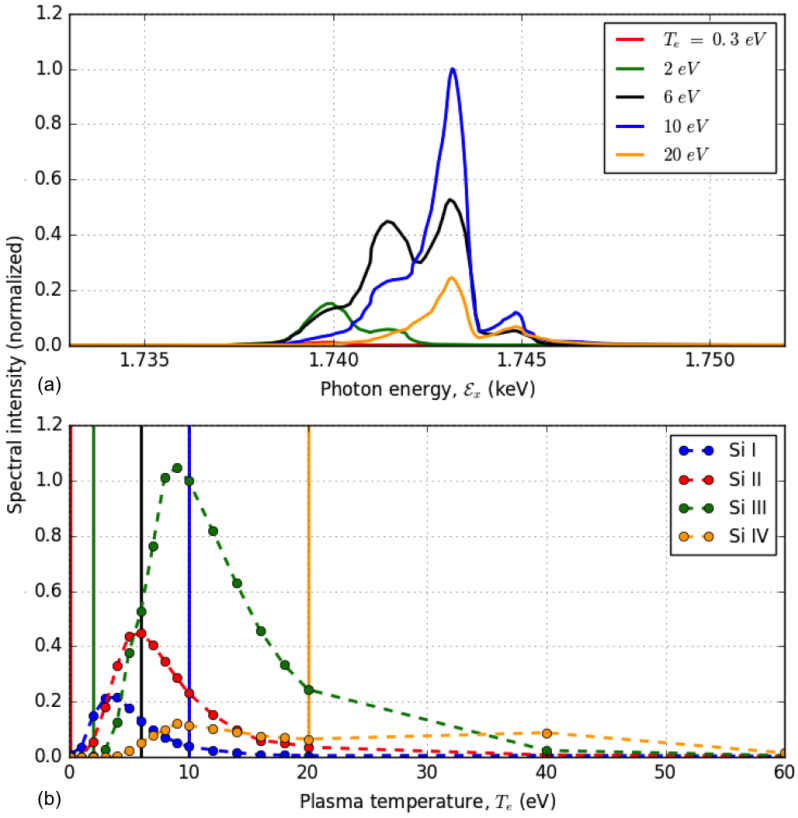

Figure 5.11: (a) Calculated spectra using PrismSPECT by changing the electron temperature between $T_e = 0.1$ (red), 2 (green), 6 (black), 10 (blue) and 20 eV (orange). (b) Spectral intensities from emission due to the Si I (blue dashed), Si II (red dashed), Si III (green dashed) and Si IV (orange dashed) at different T_e. The dots correspond to selected T_e used in the calculations. Solid vertical lines correspond to the spectra and T_e shown in (a)

As seen in Figure 5.11, the K_α signal reduces as T_e increases above 10 eV. When T_e rises higher than 60 eV, the K_α disappears from the spectrum. Instead, He_α and Li-like emission become the prominent signals towards 100 eV and higher. This result is expected because the increase in electron temperature increases the likelihood for outer-shell ionisation to become important.

5.5.2.3 Spectral resolving power

Figure 5.12 shows the change in the calculated spectrum when modifying the spectral resolving power between $\mathcal{E}_x/\Delta\mathcal{E}_x = \infty$, 400, 800 and 1200. $\mathcal{E}_x/\Delta\mathcal{E}_x = \infty$ corresponds to the theoretical case without broadening and represents the spectrum produced in PrismSPECT. The resolving powers are used in the broadening function given by Eqn. 5.2, which convolves the spectrum in red to the broadened spectra using Eqn. 5.1. The higher the resolving power, the narrower and more resolved the peaks. The other parameters were $T_{rel} = 1$ MeV, $f_{rel} = 5\%$, $T_e = 7$ eV and $\rho_e = 1$ g/cm^3.

The black spectrum corresponding to $\mathcal{E}_x/\Delta\mathcal{E}_x = 800$ in Figure 5.12 produced the closest comparison to the experimental measurement. This is smaller than the resolving power of the spectrometer, $\mathcal{E}_x/\Delta\mathcal{E}_x = (1200 \pm 100)$. A plausible reason for this discrepancy may be that the experimental spectrum is a composite spectrum of many plasma conditions, which are influenced by T_e and opacity. Therefore, the calculated spectral resolving power may underestimate the performance of the spectrometer. In addition, due the resolving power and spectral broadening the individual ionisation states in the K_α peak are inseparable.

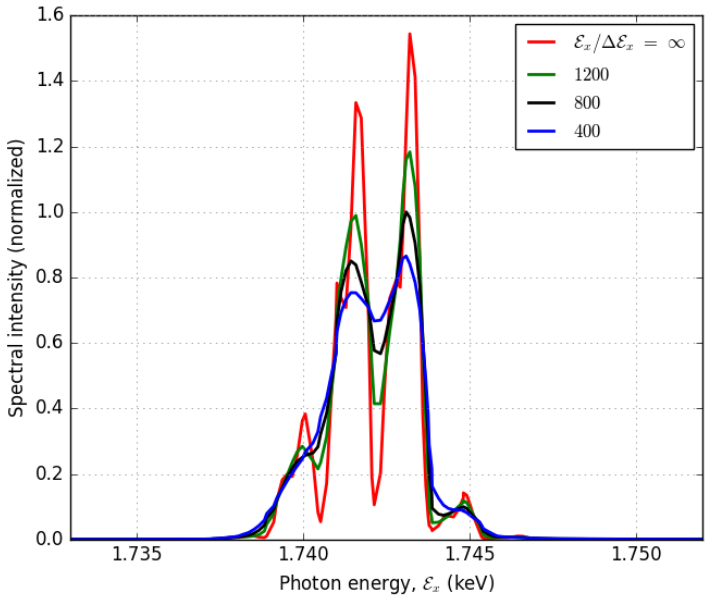

Figure 5.12: Calculated spectra using PrismSPECT using spectral resolving powers of $\mathcal{E}_x/\Delta\mathcal{E}_x = \infty$ (red, no broadening), 1200 (green), 800 (black) and 400 (blue). A normal broadening function is used to broaden the spectra.

5.6 Summary and future work

Irradiating targets with microstructured surfaces with a high-contrast Vulcan petawatt laser pulse shows the production of a very bright K_α signal. The spectral analysis indicates that switching the target topography to long microstructures amplifies the spectral emission by

a factor of 18. Microstructures increase the irradiated surface area, which in turn results in an increase of relativistic electron yield that propagate into the solid target. PrismSPECT calculations complement this observation. Relativistic electron yield determines the spectral intensity, and without relativistic electrons, there is no K_α emission generated. Furthermore, the spectral measurements are of high-quality and show little fluctuation shot-by-shot. The double plasma mirror is key in achieving these measurements. Double plasma mirror suppresses the early interactions in the laser pulse close to the main peak. In turn the solid microstructured surfaces are unperturbed by the pedestal and prepulses, which ensures that high-intensity laser interaction with a overdense microstructured surface is achieved. Therefore, combining the double plasma mirror and targets with microstructured surfaces provides a method for generating a bright and reliable X-ray source.

The spectral measurement and PrismSPECT calculations provide an insight to the laser interaction with the microstructured targets. The details are limited to a region in the plasma below 10 eV temperatures, which surrounds the laser irradiated volume. In order to achieve a broader understanding about the interaction physics a spectral range including higher ionisation states, such as He_α and Ly_α, are needed. This would in turn allow inferring the relativistic electron yield and temperatures required to generate the spectrum by collisional processes. In addition, a broader spectral range may show how important radiative processes are during the laser interaction with the microstructured targets. Prospective work using high-contrast laser pulses and microstructured targets should focus on understanding the nature of the interaction physics and how this changes from conventional approaches using flat-surfaced foils.

Chapter 6

High energy carbon ions using large-area suspended graphene

This chapter focuses on irradiating a high-contrast laser pulse on to a large-area suspended graphene (LSG) target. A brief description of the target and fabrication is followed by measurements on radiochromic film (RCF) and CR-39 showing energetic protons and carbon ions. These results are interpreted with the support of 1D and 2D EPOCH particle-in-cell simulations. In the analysis the onset of relativistic induced transparency (RIT) is seen to be important to explain the high ion energies. From these simulations it is inferred that Coulomb explosion is the most plausible mechanism driving the ions to high energy. Furthermore, 2D simulations are discussed to explain the ion beam pattern observed in the experiment.

6.1 Large-area suspended graphene

The idea for using graphene as a target for laser-driven ion acceleration was initiated at National Central University (Taiwan). The University owns a small 100 TW laser system for high power laser experiments. The system is installed in the fourth floor of the Department of Physics. The floor restricts the weight the building can withstand, which is approaching its limit. As a result, the facility is not well shielded against high energy radiation, which emerge as a consequence of the laser-target interaction. One solution for reducing the high energy radiation is to laser irradiate ultra-thin targets. Hence, graphene is used as the target.[11] From a visit testing the target at the University the motivation of using graphene on a "look-see" experiment on the Vulcan petawatt laser emerged.

Graphene is a peculiar material. Pristine graphene does not have a band gap, which means that electrons flow freely between the valence and conduction band. On the other hand, a high band gap forms when doping the material,[136], when exerting an external electric potential[136,137] or inducing 100-kbar laser shocks.[138] This binds the electrons strongly to

the valence band. Graphene also has a high thermal conductivity along the plane because electrons move at the Fermi velocity between atoms.[137,139] Out of the plane the conductivity is poor. This may lead to spreading the energy along the plane when irradiating within the laser spot across the target plane. Combining the induced band gap and high conductivity can make graphene highly transparent to optical radiation, which potentially ensures that the material survives the early interaction in the laser. This work is the first time graphene interacts with a high contrast laser approaching intensities of 10^{20} W/cm^2, providing an insight into the use of this material in extreme fields.

6.1.1 Target fabrication

Graphene is fabricated at the National Central University using a rapid thermal chemical vapor deposition method. A flow chart of the fabrication method is shown in Figure 6.1, as described by Khasanah et al.[11] A copper sample, which has the same hexagonal surface structure as graphene,[11,140] is cleaned from contaminants and placed inside a H_2 gas furnace. The furnace is radiatively heated to 980°C, which is below the breakdown of H_2 bonds. Methane gas is then injected and broken down for depositing carbon on the copper surface to grow the graphene. After roughly 28 minutes the furnace is quickly cooled to room temperature to remove the sample with graphene on its surface (see step 1 in Figure 6.1). A polymethyl methacrylate (PMMA) is coated on the graphene (step 2). This supports the target as the copper sample is detached from the graphene using electrolysis (step 3). Afterwards the graphene is suspended over holes on a silicon or metal substrate (step 4). The holes are hundreds of microns in diameter, which are five orders of magnitudes larger than the ∼1 nm thickness of a single graphene sheet. The thickness is measured using an atomic force microscope.[11] This is the largest area-to-thickness dimensions ever used for such a thin target on high power laser experiment. Hence, the target is called large-area suspended graphene (LSG). Finally, the PMMA is annealed from the graphene for an ultra-thin and pure-carbon target (step 5).

Following the fabrication method in Figure 6.1 a single graphene sheet is made. Multi-layer LSG targets are produced by repeating the procedure. The only change to the method is to transfer the graphene on a prepared LSG in step 4 (see Figure 6.1). Using this approach multiple layers of graphene can be stacked together. This provides nanometer precision of the target thickness.

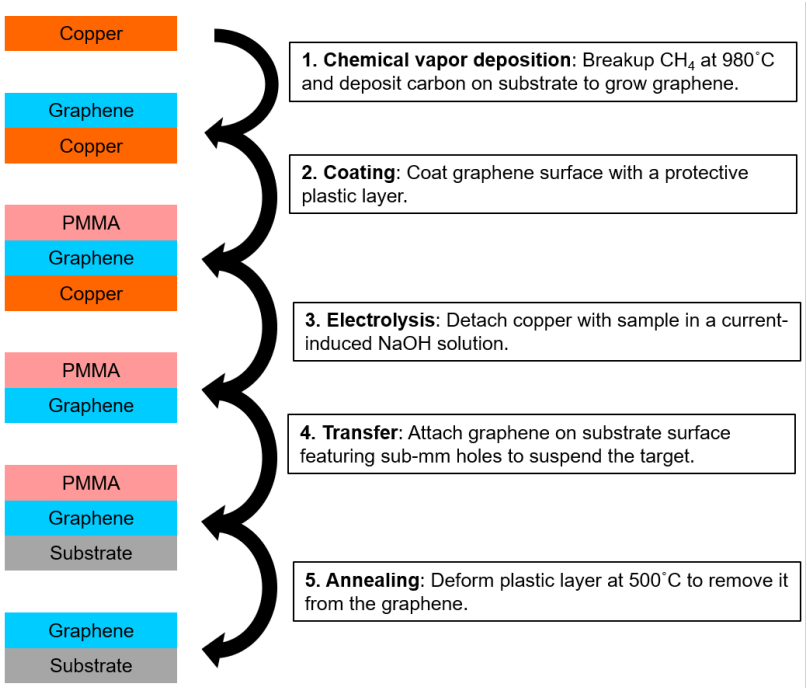

Figure 6.1: Flow chart of the rapid thermal chemical vapor deposition method for making large-area suspended graphene (LSG).

6.1.2 Scanning electron microscopy imaging

Figures 6.2 (a)-(d) show images of the LSG targets taken with a scanning electron microscope. The magnification is changed to look at different details of the targets (see inserted box indicating the image dimensions). The orange circles inserted in (b)-(d) indicate the spot size of the Vulcan petawatt laser at best focus for comparison to the features on the LSG. Figure 6.2 (a) shows a two-layer LSG attached on the back of a substrate with 50, 100 and 200 μm diameter holes. By magnifying into image (a) a hole with a broken LSG is seen in Figure 6.2 (b). The damaged LSG area is larger than the laser spot (see yellow circle in the figures). This occurred during transportation from Taiwan to the UK. Figure 6.2 (c) shows a magnified region on a four-layer LSG target. Debris of plastic and damage on the LSG smaller than the laser spot are seen. When imaging the central region of the four-layer LSG, the surface and interfacing graphene show wrinkles[137] (see Figure 6.2 (d)). The wrinkles are comparable to the laser spot. In summary, the images show microscopic imperfections on the LSG targets comparable to the laser spot size. These may have an impact on driving the carbon ions from the targets with a high power laser pulse.

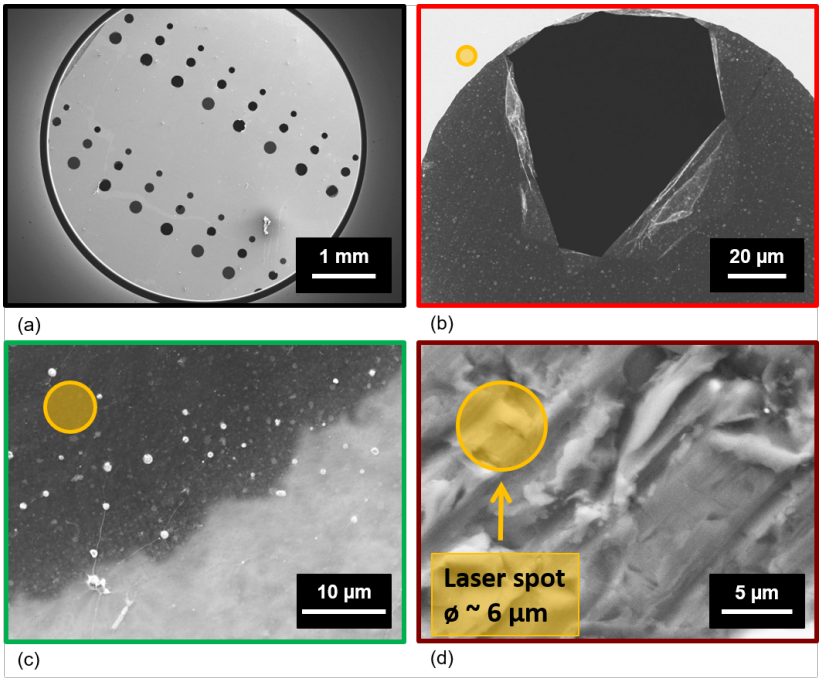

Figure 6.2: Scanning electron microscopic images of a (a) two-layer LSG on the back of the multi-hole substrate. (b) A damaged target on the two-layer LSG is identified. (c) A four-layer LSG on the front of a substrate with plastic debris, damages and (d) wrinkles as shown. Images (b)-(d) are compared to the Vulcan petawatt laser spot at best focus at 6 μm (orange circle). (Courtesy of B. Kuerbanjiang and V. Lazarov).

6.2 Vulcan petawatt laser experiment

The LSG targets were used on an experiment using the Vulcan petawatt laser based at the Rutherford Appleton Laboratory (UK).[93] The objective was to test the targets on laser-driven carbon ion acceleration using a high-contrast, ultra-intense laser pulse for the first time. The experimental platform was adapted from another experiment running in parallel. Therefore, the setup was limited to a double plasma mirror (DPM), an LSG target, spatially-resolved ion energy detector and optical transmission radiation diagnostic. Figure 6.3 shows this setup, which will be explained in the next subsections. The setup was not tailored for a comprehensive ion acceleration experiment. Nonetheless, the observations made were of great interest and demonstrate a potential new use for graphene as a target for laser-driven ion acceleration.

6.2.1 Double plasma mirror setup

In the experiment the DPM was installed to suppress the pedestal and prepulses. This ensured that the laser interaction with the target was delayed close to the peak of the pulse. In the setup the laser was incident at 40° to the normal of both mirrors. The mirrors were 15 mm apart and the second mirror was 30 mm from the target (see Figure 6.3). Using these

parameters resulted in a DPM reflectivity of (27 ± 5) %, which was in agreement with model calculations described in Chapter 4. Therefore it was assumed that the DPM reduced the laser energy to $\mathcal{E}_0 = (160 \pm 30)$ J. 30 % of that energy was contained within the FWHM of a ∼6 μm spot size at best focus. By using a FWHM pulse duration of $t_0 = (0.7 \pm 0.1)$ ps, the peak intensity on target was $I_0 = (1.6 \pm 0.3) \times 10^{20}$ W/cm^2.

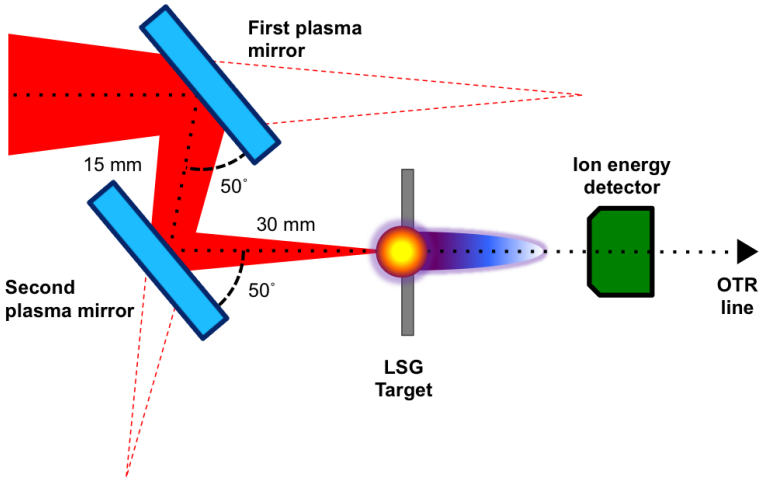

Figure 6.3: Schematic setup of the Vulcan petawatt laser experiment for ion acceleration using LSG targets.

6.2.2 Target setup

After the DPM the laser irradiates the LSG target at normal incidence. This suggests that laser absorption into the target may be dominated by $\mathbf{J} \times \mathbf{B}$ heating[16,29,30] (see Chapter 2). Secondly, irradiating a solid target with a high intensity laser at normal incidence poses a risk for laser back-reflection. This can damage the optics of the high power laser. By including the DPM this risk was circumvented. Laser moves 45 mm from the first plasma mirror to the target taking ∼150 ps. By this time the plasma mirrors will absorb and scatter any back reflected light.

For the target designs a single to two-, four- and eight-layered LSG targets were used. With a single layer as thin as 1 nm, target thicknesses were 1, 2, 4 and 8 nm. The thicknesses are measured using an atomic force microscope.[11] For this experiment all LSG targets were suspended over multi-hole silicon substrates with 50, 100 and 200 μm diameter holes. This was done for ensuring that over a number of holes the LSG remained intact after transportation from Taiwan to the UK (see Figure 6.2 (b) for an example of broken LSG).

Another advantage of suspending the LSG targets over the multi-hole substrates was for target alignment to the main laser pulse. For alignment a 1.053 μm laser beam was used. The beam was transmitted before the compressor of the laser system along the path of the main pulse. A focal spot camera looked at the target from the rear side on which the LSG

was attached. The camera was set to monitor the alignment beam at best focus of the main pulse. The concern was the potential of breaking the LSG with a focused alignment beam. To avoid this during alignment a hole with broken LSG was placed at target position. The target position was adjusted until the broken LSG was resolvable with the alignment beam by the camera. Afterwards, the alignment beam was switched off, and then the substrate was translated to a hole with unbroken LSG. On the camera monitor LSG was confirmed to exist over the hole by scattering a dim HeNe laser on the target. After finishing alignment the camera was moved out to position the on-shot diagnostics.

6.2.3 Spatially-resolved ion energy detector

On shot the laser-produced ions were recorded by a spatially-resolved ion energy detector. The detector was placed 50 mm from the rear of the target along target normal. Size of the detector was 50×25 mm^2. The detector was positioned such that the top of the diagnostic covered half of the laser beam.

The detector was a stack composed of radiochromic film (RCF), TASTRAK CR-39 and attenuator plates. The three stack design used are shown in Figure 6.4 (a)-(c). The RCFs were HDV2 and EBT2. The former had a lower detection sensitivity to particles and therefore was placed in the first few layers of the stacks. EBT2 was placed as the last RCFs for detecting the low flux and high energy ions. The detected proton energies, $\mathcal{E}_p$, are labelled on each RCF in Figure 6.4. The used filter thicknesses, X, are annotated above the attenuator plates. All stacks used a 13 μm aluminium (Al) attenuator to protect the stack from direct laser irradiance. For stack designs 1 and 2, mylar attenuators were placed between interlaying HDV2 for detecting $\mathcal{E}_p$ up to 27.5 MeV with an energy resolution of ~ 3 MeV. For energies above 27.5 MeV iron (Fe) was used for attenuation. Stack designs 1 and 2 detected protons between $\mathcal{E}_p = 1.7$-51.5 and 1.7-73.3 MeV. In case LSG produced protons up to 99.4 MeV stack design 3 was used. Here only Fe was used for attenuation, reducing the energy resolution early in the stack to around 5 MeV. In addition to stack designs 2 and 3, two CR-39 plates were included for distinguishing ions from electrons. For stack design 2 the recorded proton and carbon ion energies ranged between $\mathcal{E}_p = 32.4$-34.7 and $\mathcal{E}_{cb} = 714$-770 MeV for the first CR-39 and $\mathcal{E}_p = 34.7$-36.9 and $\mathcal{E}_{cb} = 770$-815 MeV for the second. For stack design 3, first CR-39 had $\mathcal{E}_p = 31.3$-33.7 and $\mathcal{E}_{cb} = 697$-755 MeV, and for the second $\mathcal{E}_p = 33.7$-36.0 and $\mathcal{E}_{cb} = 755$-802 MeV.

The proton energies given for each RCF corresponded to the peaks at the energy deposition curves. These are shown for the three stack designs in Figure 6.5. Green and blue curves correspond to HDV2 and EBT2 in the stack. The differences in the peak deposition energy, $\Delta\mathcal{E}_p$, were associated with the sensitivities of the RCFs. The deposition curves were calculated by using the ion stopping ranges of the RCF and filters from the SRIM code [12] in the RCF Stack Builder Matlab® code (see Chapter 3).

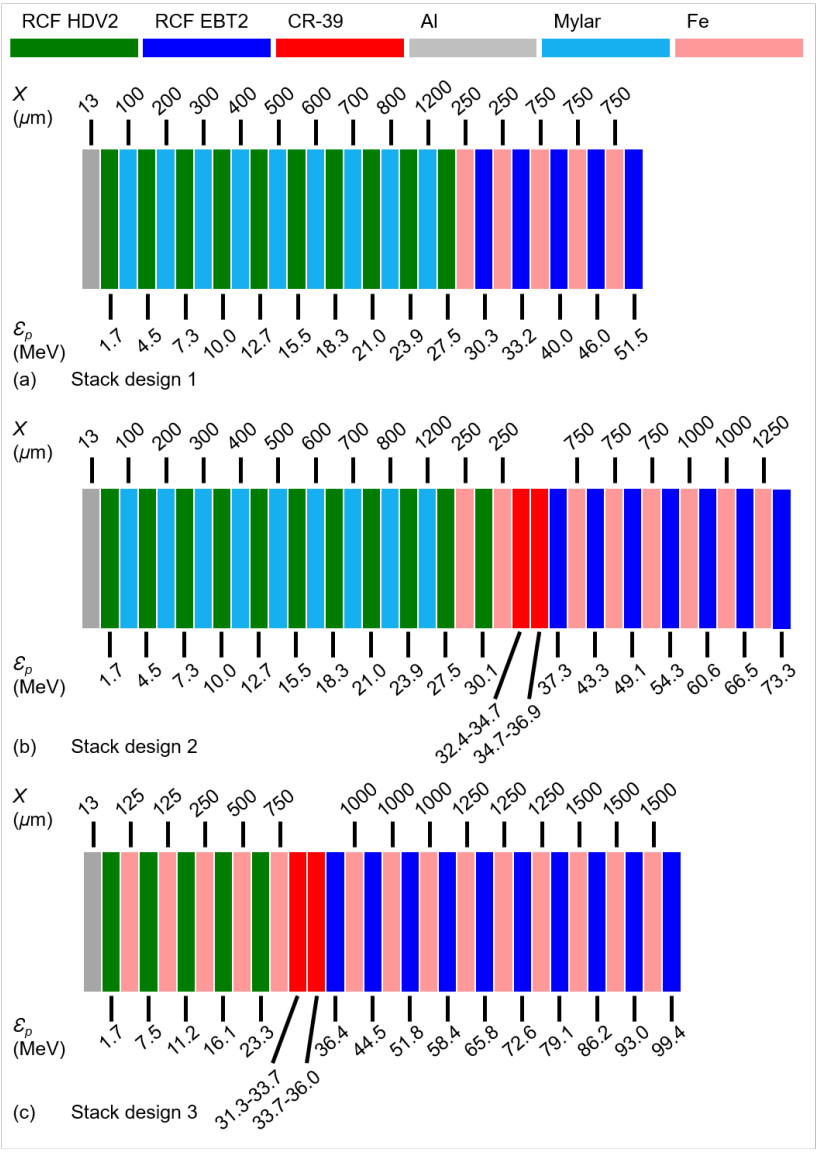

Figure 6.4: Stack designs 1-3 (a)-(c) used for the ion energy detector. The colors identify the RCFs, CR-39 and attenuator plates used with given proton energies, $\mathcal{E}_p$, and attenuator thicknesses, X.

The proton and carbon ion energy ranges detected by the CR-39 were calculated using the SRIM code[12] and measured using the Heavy Ion Medical Accelerator in Chiba (HIMAC, Japan).[42,43] On HIMAC protons of energies between 0.5 and 5 MeV as well as carbon and oxygen ions of 3 and 5 MeV/n directly irradiate unused CR-39 samples. By using the etch pit method and analysis described in Subsection 3.2.3 the detected ion energies are extracted.

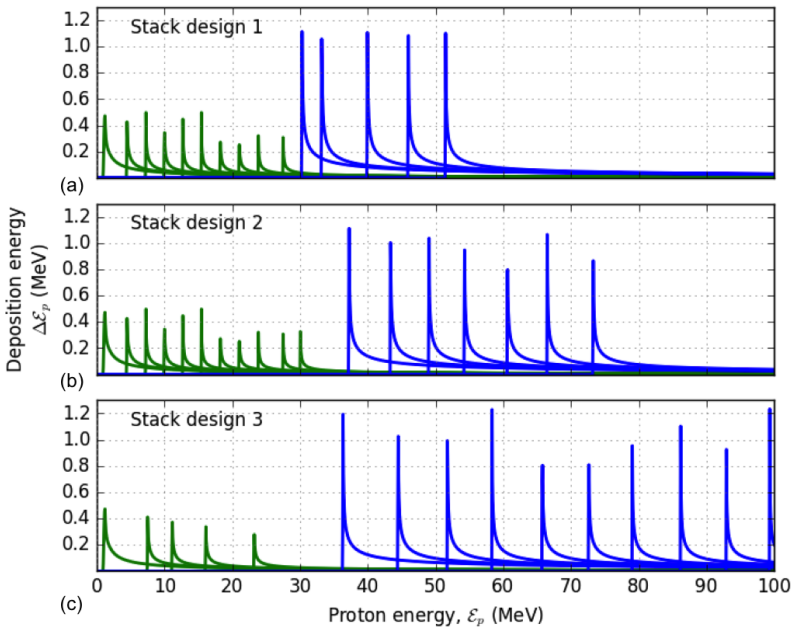

Figure 6.5: Proton energy deposition curves of HDV2 (green) and EBT2 (blue) for stack designs 1-3 (a)-(c) HDV2 (green).

6.2.4 Optical transition radiation

By aligning the top of the ion energy detector to target normal rear provided a line of sight for the optical transition radiation (OTR) diagnostic.[141] The OTR diagnostic recorded the transmitted near- and far-field laser emission from above the ion detector, as shown in Figure 6.3. For this experiment the OTR was used for ensuring that the laser hit the target during a shot. Any shots showing the laser clipping on the edge of the hole on the substrate were discarded from the data set.

6.3 Ion acceleration results

6.3.1 Maximum ion energies

Figure 6.6 (a) and (b) shows the recorded ion beam on the RCFs after a high energy laser shot using, respectively, 1 and 8 nm LSG targets shot. Proton energies, $\mathcal{E}_p$, are indicated on the images. Errors in $\mathcal{E}_p$ correspond to the FWHM of the energy deposition curves. Both measurements used stack design 3 (see Figure 6.4 (c)), which include CR-39 before the RCF recording (36.4 ± 0.2) MeV protons. Notice that the first RCF is fully saturated by absorbed radiation, including ions, whereas the second RCF shows structured features that are close but not fully saturated. The difference between Figure 6.6 (a) and (b) is that the 1 nm LSG produced a randomly shaped beam pattern. The 8 nm LSG generated a structured pattern with a central spot and a ring structure. From the CR-39 data analysis (see Sub-section

6.3.2) protons are identified using the 8 nm LSG. Hence, the highest proton energy recorded is (44.5 ± 0.3) MeV. Protons are not detected on the CR-39 in the case of using the 1 nm LSG. Therefore, it is not possible to confirm what signal corresponds to ions. In the case of Figure 6.6 (a), the highest proton energy from using the 1 nm LSG may be (11.2 ± 0.2) MeV.

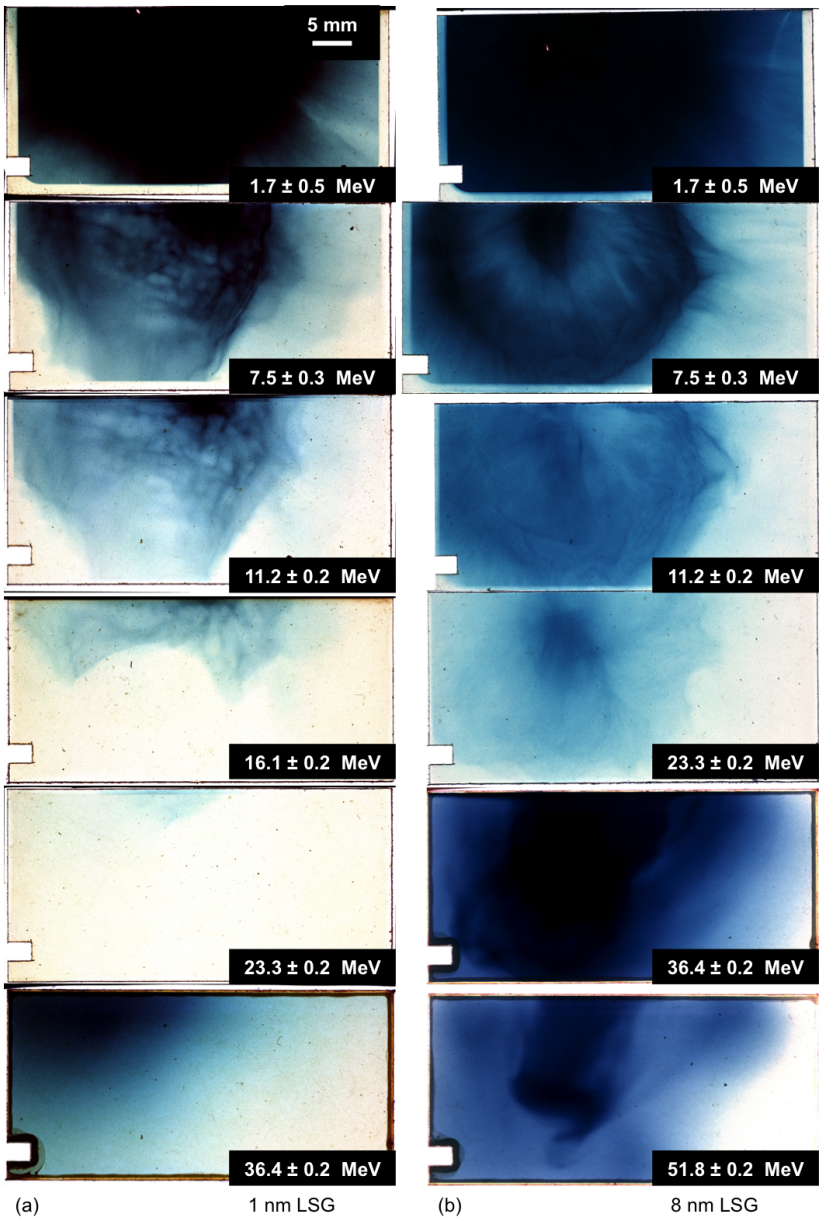

Figure 6.6: RCF images of the captured laser-driven ion beam pattern from LSG targets of thicknesses (a) 1 and (b) 8 nm. The corresponding proton energies are given on the bottom-right corner of every image. Stack design 3 was used for both sets of images shown.

The maximum proton energies, $\mathcal{E}_{p,max}$, for each target thickness, x_0, used are summarised in Figure 6.7. $\mathcal{E}_{p,max}$ is taken from the last RCF showing a distinct structure (see Figure 6.6). Red, blue and green points in the figure identify stack designs 1, 2 and 3 used on shot.

Measurements for each thickness are statistical averaged (white points with standard error) for comparison. The standard error is larger for the 2 nm LSG as this is an average of two shots, whereas three shots are achieved for all other LSGs, as confirmed by the OTR. The 8 nm LSG target produced the most energetic protons, reaching $\mathcal{E}_{p,max} = (26 \pm 9)$ MeV on average and (44.5 ± 0.3) MeV as the highest energy observed. The highest energy is comparable to the proton energies measured by Higginson et al.[18] using a 10 nm plastic where one plasma mirror is used in the setup. The results may have a correlation to these previous measurements.

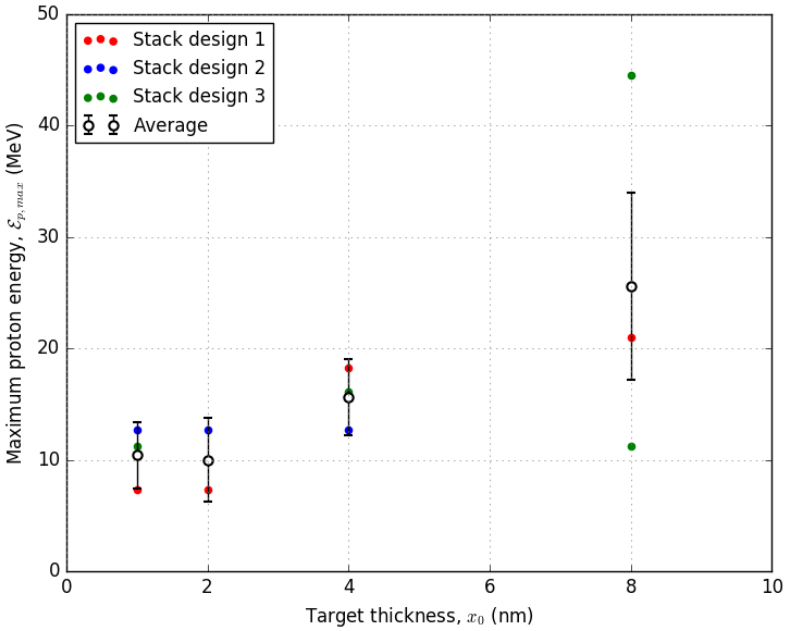

Figure 6.7: Maximum proton energy, $\mathcal{E}_{p,max}$, with respect to target thickness, x_0, where the coloured points identify the stack design and white points are the statistical averages.

On the shot with the highest proton energy the CR-39 was analysed to verify the existence of ions. Chemically etching and data processing of CR-39 is described in Chapter 3. In the analysis a large number of small etch pits and a few large pits due to ions were seen. It was assumed that the small pits corresponded to protons. This observation suggests that the proton energies exceeded 36.0 MeV. These were the maximum energies detected on the back of the second CR-39 in stack design 3. As for the large etch pits, if assuming these are carbon ions, the carbon ion energies surpassed 802 MeV. Further discussions on the identification of ions on the CR-39 will be addressed in Subsection 6.3.2.

With the measurements producing high ion energies, the RCF and CR-39 were analysed further to determine how the LSG targets performed.

6.3.1.1 Ion beam directionality

Figures 6.8 (a)-(d) show the ion beam pattern on specific pieces of the 5×2.5 cm^2 RCF. These results are from laser irradiating the 1, 2, 4 and 8 nm LSG targets repeatedly. Assuming both protons and carbon ions are captured the energies on the RCF are from 4.5 to 7.5 MeV for protons and 100 to 170 MeV for carbon ions. Note that the highly dark features on the RCF show signs of film saturation. This is interpreted from comparing the counts across the scanned film of the shown RCFs and the first RCF in the stack design, which are fully saturated. Using 1 nm LSG the beam pattern shows filament-like structures randomly distributed across the RCF (see Figure 6.8 (a)). Switching to 2 nm LSG in Figure 6.8 (b) a dim ring-like structure extending ~2 cm across the image is observed. With the 4 nm LSG (see Figure 6.8 (c)) this ring becomes enlarged to ~3.5 cm to its outer diameter, as well as sharper and distinct. When using the thick 8 nm LSG the ring structure encloses a dark and distinct central spot in the ion beam. This is shown in Figure 6.8 (d). The ion beam patterns are repeatable for the given target thicknesses. Therefore these observations were thought of being characteristic to the LSG targets used.

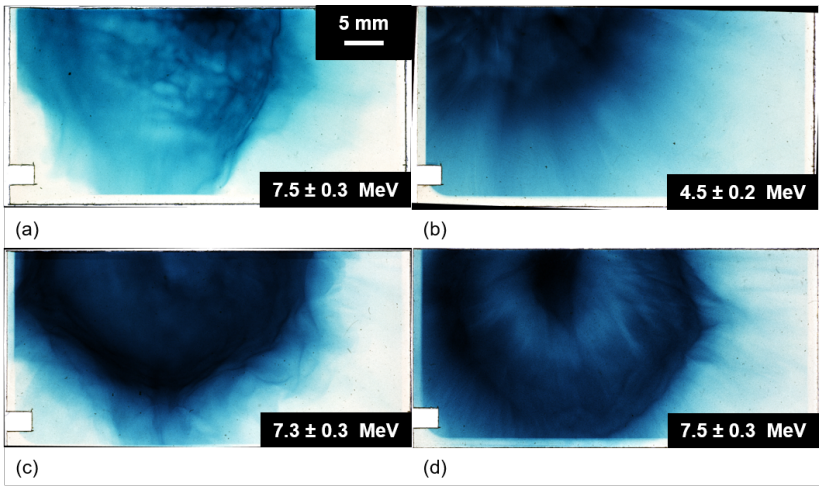

Figure 6.8: Ion beam pattern captured on RCF between 4.5-7.5 MeV protons and 100-170 MeV carbon ions using (a) 1, (b) 2, (c) 4 and (d) 8 nm LSG targets.

The filaments in the ion beam patterns observed may be linked to the wrinkles on the LSG targets. The wrinkles can be considered similar to targets with rough surfaces. Studies [60,142] suggest that the surface roughness, particularly on the rear side of the target, determines how collimated the ion beam is. A rough surface produces filaments in the ion beam, and a smooth surface results in a smooth beam pattern. As the target thickness was increased the beam filamentation was more concentrated in to a ring and a central spot seen on the RCF in Figure 6.8 (d).

The ring structure has been previously studied (see Ref. [62,143]). The low energy ions driven out of target rear via target normal sheath acceleration (TNSA) are subject to a

transverse deflection. This transverse field deflects the ions. Furthermore, those studies[62,143] suggested that a central spot of high energy ions is produced because of the combined acceleration along target normal and onset of relativistically induced transparency. A central spot is observed on the RCF measurements using the 8 nm LSG target (see Figure 6.6 (b)). Later in this chapter it is shown that particle-in-cell simulations reproduce most of the ion beam pattern seen in experiment and predicted in studies.[62,143]

6.3.2 CR-39 results

6.3.2.1 Ion identification

Key reasons for using CR-39 were to include an additional diagnostic to the RCF measurements and, more importantly, separate ions from electrons. Hence, the CR-39 verified the existence of ions on the RCF. Figure 6.9 (a) shows (from top to bottom) the ion beam pattern on the RCF HDV2 before the CR-39, on the first CR-39 in the stack after etching, and RCF EBT2 after the CR-39. Stack design 3 and the 8 nm LSG target are used. Proton energies are indicated on the images. Magnified images of regions A-F on the CR-39 are shown in Figure 6.9 (b). These images are trimmed and enlarged to show the details of the CR-39 surface. Regions A-B are on the front surface of the first CR-39 and C-F are on the back of the second CR-39. Their positions on the CR-39 and RCF are annotated and matched on Figure 6.9 (a). Positions A and B are shown on the RCF immediately before the first CR-39, and C-F are indicated on the RCF immediately after the second CR-39. Small and large etch pits are seen on the CR-39. All CR-39 images are taken using a fully automated optical microscope with a 0.7×0.7 μm^2 image resolution (see Subsection 3.2.3).

From the energy calibration measurements performed using the HIMAC (see Subsection 6.2.3) small etch pits are comparable to irradiating a beam of protons between 0.5 and 5 MeV directly on an unused CR-39 sample. Hence, it is assumed that the small etch pits correspond to protons. Irradiating both carbon and oxygen ions between 3 and 5 MeV/n on CR-39 produced identical and large etch pits. Therefore it is unclear what fraction of large etch pits seen on the CR-39 from the experiment are due to carbon ions from the LSG targets. Measurements on carbon and oxygen flux are referred in the next subsection collectively as heavy-ion flux, and the contribution to this flux due to carbon ions is discussed towards the end of this section.

The etched CR-39 shows the same beam structure as on the RCF in front of and behind the CR-39 (see Figure 6.9 (a)). The sharp and distinct features were due to ions. Hence, this validates the assumption that the beam pattern on the RCF was due to laser-driven ions.

6.3.2.2 Ion beam directionality on CR-39

In Figure 6.9 (b), regions A and C show the ion etch pits within the central spot of the ion beam on the front of the first CR-39 and back of the second CR-39. The central spot (white region in Figure 6.9 (a) (middle)) corresponds to the region with the highest number of etch pits and, in turn, ion flux. The number of small etch pits due to protons seen at those regions is uncountable as the pits are merged to clusters (see Figure 6.9 (b) A and C). Therefore it was assumed that the proton flux exceeds the ion flux resolvable by the optical microscope, which is 10^5 ions/cm^2. The large black pits were assumed to be carbon ions. As for the large etch pits, (5 ± 3) and (20 ± 10) pits are counted across an image size of 0.7×0.7 mm^2. The errors are one standard deviation of the mean pit count, which is 68%. A standard deviation is used for all large pits counted. Hence, the heavy-ion fluxes are around $(1.0 \pm 0.7) \times 10^3$ and $(4 \pm 3) \times 10^3$ ions/cm^2. Comparing these to the proton flux of 10^5 protons/cm^2 the heavy-ion-to-proton flux ratios are (0.010 ± 0.007) and (0.04 ± 0.03) on regions A and C. Note that these and following ratios are overestimates because of the saturated proton flux. These results show that the number of heavy ions stopped by the first CR-39 is a third of those stopped in the second CR-39 within the centre of the ion beam.

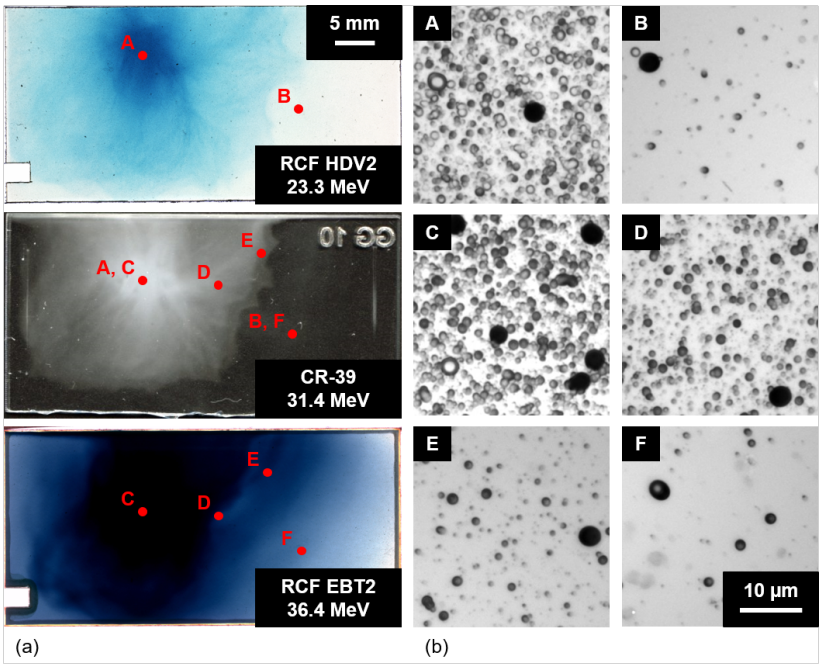

Figure 6.9: (a) Image of the RCF before the CR-39, first CR-39, and RCF after the CR-39. (b) Scanned images at the marked positions A-B on the front surface of the first CR-39 and C-F on the back of the second CR-39. The images were cropped from the original image size to show the small and large etch pits.

Regions B and F in Figure 6.9 (b) are taken from regions outside the ion beam. These regions are used to assess the contribution of background noise from cosmic rays and other sources. Etch pits are distinct and resolvable on the images in regions B and F. Tiny etch

pits of ∼10 nm in size are seen. These pits are not circularly symmetric as inferred from Figure 6.9 (b) B and F. These pits are formed by ions incident at an oblique angle on the CR-39 and not aligned to target normal as in the experimental setup. Therefore, these tiny pits are assumed to be background noise and excluded from the count of laser-driven ions. As the background noise is low at regions B and F it is assumed that the majority of etch pits in regions A, C, D, and E are due to laser accelerated ions.

Regions D is taken from within a filament seen on the back surface of the second CR-39 and the RCF. Only 3 large etch pits are counted. This corresponds to a heavy-ion flux of (600 ± 400) ions/cm^2 and, in turn, a heavy-ion-to-proton flux ratio of (0.006 ± 0.004). Hence, the filamental structures outward from the centre of the beam is assumed to be mainly due to protons. Electric field emerging during the laser-target interaction on target rear surface may deflect protons depending on the surface roughness.[60,142] In addition, the protons can also be deflected more easily by fields because of their high charge-to-mass ratio. Both fields and charge-to-mass ratio may explain why protons form filaments in the RCF.

On the back of the second CR-39 region E shows the etch pits along the edge of the observed ion beam. Tiny, small and large etch pits are resolved. Ignoring all tiny and asymmetric pits due to background noise, the number of large pits counted result in a heavy-ion flux of $(2 \pm 1) \times 10^3$ ion/cm^2 and a heavy-ion-to-proton ratio of (0.02 ± 0.01). This ratio is similar to the ratio in the centre of the beam at region C.

Table 6.1 summarises the estimated heavy-ion-to-proton flux ratios from regions A, C, D and E. As stated previously, these results are overestimates due to the proton flux being saturated for the diagnostic technique used. The errors are one standard deviation of the mean. The estimates suggest that most heavy ions are driven along the centre and edge of the ion beam. The ions along the edge may be influenced by a transverse electric field during the acceleration, and the central beam is possibly driven before a transverse field forms.

Table 6.1: Heavy-ion-to-proton flux ratios, Γ_i/Γ_p, estimated at regions A, C, D and E in Figure 6.9 (b). All values are overestimates due to the saturated proton flux.

Region	A	C	D	E
Γ_i/Γ_p	(0.010 ± 0.007)	(0.04 ± 0.03)	(0.006 ± 0.004)	(0.02 ± 0.01)

The heavy-ion-to-proton flux ratios in Table 6.1 indicate that the abundance of protons on the LSG is larger than carbon and oxygen ions. Therefore the LSG targets are not solely graphene. Plastic residuals from target fabrication[11] and hydrocarbons from the air[29,61] may have contaminated the graphene surfaces. Using an atomic force microscope a single LSG layer has a measured thickness of ∼1 nm.[11] Theoretically, pure graphene is one carbon atom thick, which is 0.3 nm thin.[137,139] This suggests that about 70 % of the individual LSG layers may be proton contaminants.

From the ion energy measurements using the HIMAC, it is not possible to distinguish

large etch pits due to carbon and oxygen ions with the stack designs used. Therefore it is expected that the carbon-to-proton flux ratio is much smaller than the values summarised in Table 6.1. By comparing the results to other studies measuring ion energies and fluxes[18,80,119,144] the carbon ion flux may be at least one order of magnitude below the typical detection threshold of a Thomson parabola and RCF. Furthermore, the protons, carbon and oxygen ions can cause knock-on interactions with atoms in the CR-39. These atoms creates additional etch pits that may not be distinguishable from other etch pits if the interaction pushes the atom in the same direction as the laser driven ions. These are not separated in the analysis.

6.4 Theoretical interpretation of experiment

The experimental results on ion energies and beam patterns observed by using the LSG targets are interesting results. To understand these observation requires knowledge of the laser interaction physics and acceleration mechanisms producing these ions. Both depend on how electrons absorb energy from the laser.[16,145] Here the five acceleration mechanisms described in Section 2.4 will be discussed in the experimental setup. This provides a theoretical insight to the nature of the laser-driven ions from the LSG targets.

6.4.1 Target normal sheath acceleration (TNSA)

Target normal sheath acceleration (TNSA) is the most studied mechanism of laser-driven ion acceleration. TNSA depends on the most energetic component of the relativistic electron flux driven by the laser exiting the target rear surface. The higher the flux, the stronger the electrostatic field accelerating the ions.[29] For the highest electron flux there is an optimum target thickness around tens of micron when not using plasma mirrors[111] and less than a micron with plasma mirrors.[111,146] Thicker targets lead to a low flux as electrons deposit or radiate energy in matter.[29,30,146] On the other hand, the thinner the target, a lower number of electrons may be driven by the laser.[29,111,146] As nano-thin LSG are much thinner than sub-micron thick targets, TNSA is likely to be inefficient. This is due to the low number of available electrons.

6.4.2 Enhanced target normal sheath acceleration (ETNSA)

Enhanced target normal sheath acceleration (ETNSA) is a special case of TNSA where all electrons across the thickness of the target are directly heated by the laser. This results in driving these electrons to high energies, which in turn strengthens the electrostatic field. ETNSA is possible with LSG targets because of their thicknesses being comparable to the skin depth, δ_s, at solid target density.[29,61,63] Assuming that the density of graphene is the same as for graphite at 2.25 g/cm^3 and using Eqns. 2.6 and 2.10, $\delta_s \approx 6$ nm. Target

thicknesses are 1 to 8 nm and are comparable to δ_s. This suggests that the LSG targets are penetrated by the laser, leading to the laser heating the whole target. In turn all electrons couple to the laser and accelerate to relativistic energies. This may contribute to the ion acceleration.

6.4.3 Radiation pressure acceleration in the light-sail regime (RPA-LS)

As the laser intensity peaks at $I_0 = 1.6 \times 10^{20}$ W/cm^2, the laser reaches pressures up to $P_0 = 2I_0/c \approx 500$ Gbar.[16,145] This high pressure suggests that radiation pressure acceleration (RPA) may be important in driving the ions.

The hole-boring speed, v_{hb}, determines how rapid the front surface is pushed through the target.[29,147] Its formula is

$$v_{hb}/c = \frac{a_0\sqrt{n_{cr}m_e/\rho_i}}{1 + a_0\sqrt{n_{cr}m_e/\rho_i}} \tag{6.1}$$

where $a_0 = 0.85\sqrt{I_0[\mathrm{W/cm^2}](\lambda_0[\mu\mathrm{m}])^2/10^{18}}$ is the normalized laser amplitude, c is the speed of light, n_{cr} is the critical density, m_e is the electron mass and ρ_i is the target ion density. The brackets in a_0 denote the units for I_0 and λ_0. Assuming $\rho_i = 2.25$ g/cm^3, $v_{hb} \approx 0.013$c. By dividing the 1 and 8 nm thicknesses by v_{hb} suggests that the target front surface may reach the rear side in 2 and 0.3 fs respectively. This suggests that the laser may directly drive the ions from LSG targets via RPA in the light-sail regime (RPA-LS).

On the other hand, the LSG target thicknesses are comparable to the initial skin depth is $\delta_s \approx 6$ nm. Part of the laser is transmitted through the target rather than absorbed.[29,61] This in turn may reduce the coupling of the laser to the target via RPA-LS. In addition, studies on RPA-LS[147] suggest that if the target is thinner than $ct_0/2$, relativistic electrons reflux and deform the target. Deformation decreases the target densities, which in turn reduces laser to target coupling. For the Vulcan petawatt laser with a pulse duration of $t_0 = 0.7$ ps, $ct_0/2 \approx 0.1$ mm. The target thickness is comparable to δ_s and smaller than $ct_0/2$, suggesting that RPA-LS is unlikely for ion acceleration.

6.4.4 Breakout afterburner (BOA)

The breakout afterburner (BOA) mechanism may accelerate ions because of the LSG thicknesses being comparable to the skin depth, $\delta_s \approx 6$ nm. All electrons are driven to relativistic energies within the laser spot. Maximising the electron energies depends on the laser energy, E_0, pulse duration, t_0, and the time that the plasma becomes transparent to the laser driver. The latter is the onset of relativistically induced transparency (RIT), which is described in Chapter 2. A $E_0 = 160$ J and $t_0 = 0.7$ ps pulse may couple most of its energy to the electrons close to the peak of the laser. Ideally then, the onset of RIT should occur near the peak for the highest electron energies. Assuming that the ions move significantly slower

than the relativistic electrons, a large drift between the electrons and ions may form. The drift may result in a two-stream electron-ion instability, also called a Buneman instability, that amplifies the electrostatic field at the onset of RIT.[63,69–71]

For ion acceleration via BOA, the onset of RIT depends on the initial target thickness and density used. For this onset to coincide closely with the peak of the laser, the target thickness and density need to match. Studies on RIT suggest that a sub-micron to micron thick target of near-critical density[64,70] or, alternatively, tens of nanometer thin targets at solid density[63,69] may be suitable for driving ions via BOA. Whether BOA is important using LSG targets needs to be inferred from computational simulations (as shown in the next section).

6.4.5 Coulomb explosion (CE)

For Coulomb explosion (CE) to drive the ions requires the target thickness to be comparable but smaller than the skin depth, δ_s. This condition implies that piling up the electrons inside the target with the laser is avoided. This is different from RPA-LS where this pile up forms an electron bunch in the target that the laser pushes forward. Preventing the electron pile up ensures that a positive charge can form within the target. This in turn blows out and accelerates the ions.[64,65,148]

The larger the positive charge inside the target, the higher the ion energies. One way this may be achieved with the LSG targets is with the laser driving all electrons out from the irradiated spot. Since the target thicknesses used are comparable to the skin depth at $\delta_s \approx 6$ nm, the laser can penetrate the target and, as a result, heat the whole target.[64,148] This may result in a rapid removal of electrons from the target faster than the ions can move. Hence, it is possible that a large positive charge may form that subsequently blows out the ions from the target.

6.4.6 Summarised overview on ion acceleration mechanisms

In summary, ETNSA and CE are probably the acceleration mechanisms that drive the ions to high energies because of the 1-8 nm thicknesses of the LSG targets. For the same reason, TNSA and RPA-LS are not expected to be significant in driving the most energetic ions. As for BOA it is not clear how important this mechanism may be because, to the best of knowledge, computational studies have not investigated thicknesses as thin as a few nanometers.

It may be that the ions were driven in the experiment under a hybrid acceleration.[18] As in, each mechanism contributes to the electrostatic field, E_x, driving the ions to high energies. Therefore, the acceleration field is considered being the superposition of the fields from each mechanism. Determining and understanding the contribution of the mechanisms to E_x required linking the experimental observations and theoretical interpretation to computational

simulations.

6.5 Simulations of ion acceleration using EPOCH

For the computational simulation study in this work, the Extendable Particle-in-cell Open Collaboration (EPOCH) code[149] was used. Particle-in-cell (PIC) codes were extensively used to understand the laser-driven ion acceleration mechanisms described in the previous section.[18,61,63,64,68,70,147,149,150] Hence, it was appropriate to use EPOCH.

6.5.1 One-dimensional simulation setup

All one-dimensional (1D)-EPOCH simulations were attained using the computing resources provided by STFC Scientific Computing Department's Scientific Computing Application Resource for Facilities (SCARF) cluster.[151] Up to 120 cores and 128 GB memory were used for the simulations. With the 1D setup, the simulations took up to one day to complete without crashing. If a crash occurred, the restart input in EPOCH was used to continue the simulations from the last output file produced.

Figure 6.10 shows the setup of the 1D-EPOCH simulations. The simulation box was 135 μm long containing 36864 cells. The cells size was $\Delta x = 3.7$ nm. An s-polarized laser pulse entered the simulation box from the left boundary at -3 μm. The laser was a Gaussian-shaped pulse with a FWHM pulse duration of $t_0 = 0.7$ ps and a peak intensity of $I_0 = 3\times10^{20}$ W/cm^2. The peak entered the simulation at 700 fs, which meant that the laser started with an intensity of $\sim 2\times10^{19}$ W/cm^2 at the left boundary. The laser wavelength was $\lambda_0 = 1.054$ μm. The laser irradiated the target front surface positioned at 0 μm, which was 3 μm from the left boundary of the simulation box. The target was composed of a fully ionized plasma slab with a total of $N_e = 9.6 \times 10^6$ electrons, $N_p = 1.6 \times 10^5$ protons and $N_{cb} = 1.6 \times 10^6$ carbon ions for all thicknesses used. Slab thicknesses between 1 and 100 nm were used, where the focus was on the 8 nm target as it produced the highest ion energies in the experiment. The density was assumed uniform and to correspond to graphite at 2.25 g/cm^3. Therefore the electron density used was $n_e = 690 n_{cr}$, where $n_{cr} = 1 \times 10^{21}$ cm^{-3}. Exponential density ramps extended 5 and 1 nm from the front and rear sides of the target. The initial plasma temperature used was $T_e = 100$ eV, which corresponded to a Debye length of $\lambda_D \approx 90$ nm.

The Vulcan petawatt laser was modelled as a Gaussian pulse. The temporal Gaussian profile started -0.7 ps before the peak. The simulation start time is chosen from a parameter scan performed using a 80 fs duration Gaussian pulse. The shorter pulse was chosen for computational speed and easy analysis. These simulations used start times at half, one and four times the pulse duration from the peak, which correspond to -40, -80 and -360 fs respectively. It was found that the final ion energies produced were the same for the simulations between -80 and -360 fs, and dropped when using -40 fs. Therefore, the start

time for the main simulations with the 0.7 ps pulse duration was set at one times the pulse duration, as in -0.7 ps before the peak.

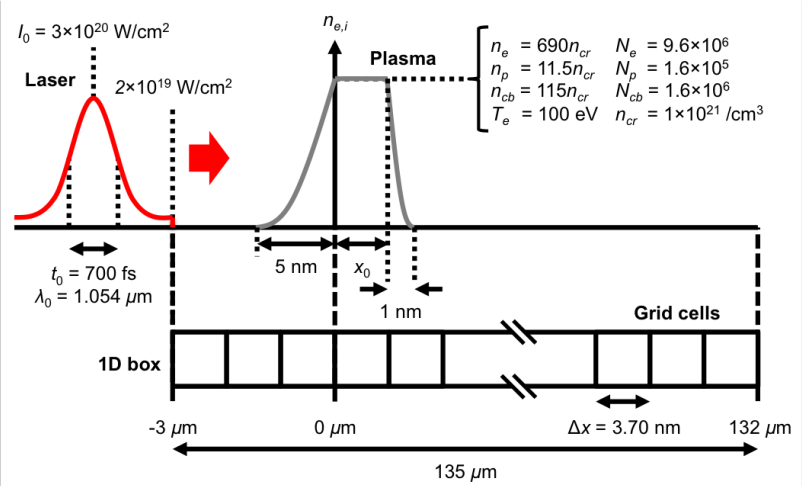

Figure 6.10: Schematic of the 1D-EPOCH simulation setup.

The density ramps at the front and rear target surfaces were included to improve the numerical stability. In PIC simulations, the electromagnetic fields are calculated on computational cell boundaries from interpolation of the particle charge within the neighbouring cells. Density ramps help limit the charge difference between these cells and limit the magnitude of these fields. Large fields on cell boundaries are unphysical and produce noise in the simulations.[149,152] The 5 and 1 nm long density ramps at the front and rear of the target respectively were found to be adequate

$T_e = 100$ eV was used for $\lambda_D \approx 90$ nm. With a cell size of $\Delta x = 3.7$ nm, this satisfied the condition $\pi\lambda_D/\Delta x \geq 1$.[152] The choice of $T_e = 100$ and Δx are based on running reliable simulations, which is discussed in the next subsection.

6.5.1.1 Convergence testing

PIC simulations generate noise through numeric self-heating and electrostatic instability. Managing and reducing sources of noise is a complex task that requires convergence testing. Numeric self-heating occurs when high frequency interactions are not sufficiently resolved. To reduce self-heating it is necessary that the condition $\pi\lambda_D \geq \Delta x$ is satisfied.[152] Notice that the condition is similar to the number of particles in a Debye sphere exceeding unity, $N_D > 1$, where $N_D \propto n_e\lambda_D$ in 1D (see Eqn. 2.3 in Section 2.1). Consequently, if there are not enough number of particles there will be a miscalculation in the electrostatic field. Achieving convergence requires decreasing Δx and increase the number of particles per cell, but this demands more computational resources. Therefore, an optimum choice for a small Δx and large number of particles per cell is chosen for robust and feasible simulations.

A simple approach for convergence testing is to compare the electron densities, n_e, be-

tween successive runs that either reduce the cell size, Δx, (below $\pi\lambda_D$) or increase the number of particles per cell. Electrons are the particles with the highest charge-to-mass ratio and, therefore, can probe for small changes due to numeric noise. n_e is used as it is linked to the number of particles per cell and has been previously used for robust convergence testing.[153]

An example of a convergence test in 1D simulations is illustrated in Figures 6.11 (a) and (b). Here the number of electrons $N_{e,j}$ in run j was increased to the values given in the legend. In this test 24 cores on SCARF are used. The electron density, n_e, is taken at the end of the simulation where the numeric noise is highest. The differences between electron densities across the x-axis in the simulation box are taken between the current $(j+1)$ and previous (j) run. This provides the regression, R_j, with x shown in Figure 6.11 (a). R_j is normalised to the largest absolute value (see violet plot). R_j and the number of grid points, G_j, for run j are used to obtain the convergence term, C_j,

$$R_j = n_{e,j+1} - n_{e,j} \tag{6.2}$$

$$C_j = \frac{\sqrt{\sum_k^{G_j} R_j(x_k)^2}}{G_j} \tag{6.3}$$

The root-mean-square summation adds the regression at each grid point, x_k, as n_e is assigned to these points in EPOCH. As seen in Figures 6.11 (a) and (b), R_j and C_j decrease with increasing $N_{e,j}$ in every successive run. This indicates that the numeric noise is suppressed. With every run improving the robustness, the time for finishing the simulations increases. The last run in Figures 6.11 (a) and (b) ($j = 7$) took nearly 48 hours using 24 cores, which is the runtime limit on the SCARF cluster. With the simulations showing little change at that run and approaching computational constraints, the simulations can be considered converged.

The simulation setup for the key results used a cell size of $\Delta x = 3.7$ nm and 9.6×10^6 electrons. These parameters provided robust simulations using 120 cores up to 72 hours of computation time. Running simulations beyond 48 hours on SCARF required using the restart function in EPOCH to finish the simulations. In principle, larger number of particles and smaller cell sizes could be used. On the other hand, the data size becomes large and unfeasible to store and analyse. The setup parameters of $\Delta x = 3.7$ nm and 9.6×10^6 electrons provided simulations that are converged and computationally manageable.

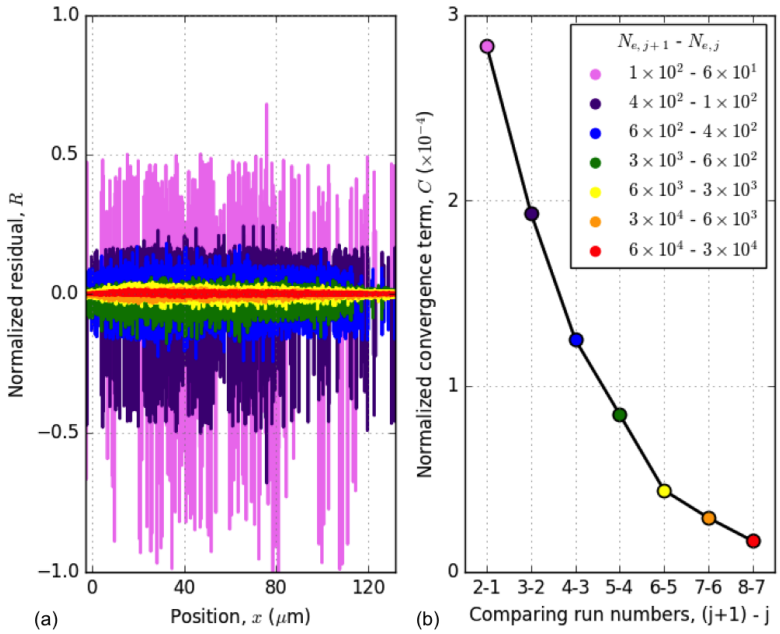

Figure 6.11: (a) Normalised residual, R_j, were taken of n_e between consecutive runs. Each successive run, j, increased the number of particles per cell (given in the legend). (b) The convergence term, C_j, from the root-mean-square averaged R_j show an increasing improvement in the simulation consistency from the variation in n_e.

6.5.1.2 Onset of relativistically induced transparency

The time evolution of the 1D EPOCH simulations using the 8 nm thick is shown for the transverse electric field, E_y, of the laser against the plasma density defined by n_e and relativistic critical density, $\gamma_e n_{cr}$, in Figure 6.12 (a)-(c). Simulation times, t_{sim}, at -665, -420 and -385 fs are shown, where 0 fs corresponds to the laser peak entering the particle grid at position $x = -3$ μm. The horizontal dashed line is $n_{cr} = 1 \times 10^{21}$ cm^{-3}. The vertical dashed line marks the peak of n_e. The origin is at the initial position of the target front surface (see Figure 6.10).

During the early simulation time ($-700 \leq t_{sim} < -385$ fs) the laser interacts with an overdense plasma where $n_e > \gamma_e n_{cr}$. The laser encounters the solid target with an initial intensity of 1.9×10^{19} W/cm^2. The interaction drives electrons out of the target rear by radiation pressure as inferred from $\gamma_e n_{cr}$ in spatial region between 0 and 5 μm in Figure 6.12 (a). As the simulation evolves with time the target is heated by the laser. This is inferred from the periodic peaks in n_e and $\gamma_e n_{cr}$ at both target front and rear sides seen in Figure 6.12 (b) at time $t_{sim} = -420$ fs. At this time the laser intensity is 1.2×10^{20} W/cm^2 on target. Laser heating occurs at the rear side because the laser penetrates the plasma. This occurs due to the skin depth being comparable to the plasma thickness. At $t_{sim} = -420$ fs, $\delta_s \sqrt{\gamma_e} \approx 0.4$ μm. This is calculated at position $x \approx 0.5$ μm where n_e and $\gamma_e n_{cr}$ intersect (see Figure 6.12 (b)). The plasma thickness, which is inferred from the two points where n_e and

$\gamma_e n_{cr}$ intersect (∼0.5 and ∼1.1 μm), is ∼0.6 μm.

As t_{sim} approaches −385 fs the overdense plasma decreases in density below the relativistic critical density where $n_e < \gamma_e n_{cr}$ (see Figure 6.12 (c)). At this time the density is greater than the critical density $n_e > n_{cr}$ between −0.7 and 2.5 μm. Hence, relativistic electron motion causes the plasma to become transparent to the laser. This observation suggests that the laser interaction physics changes from the overdense plasma to where the system is characterised by the relativistically induced transparency (RIT) regime.

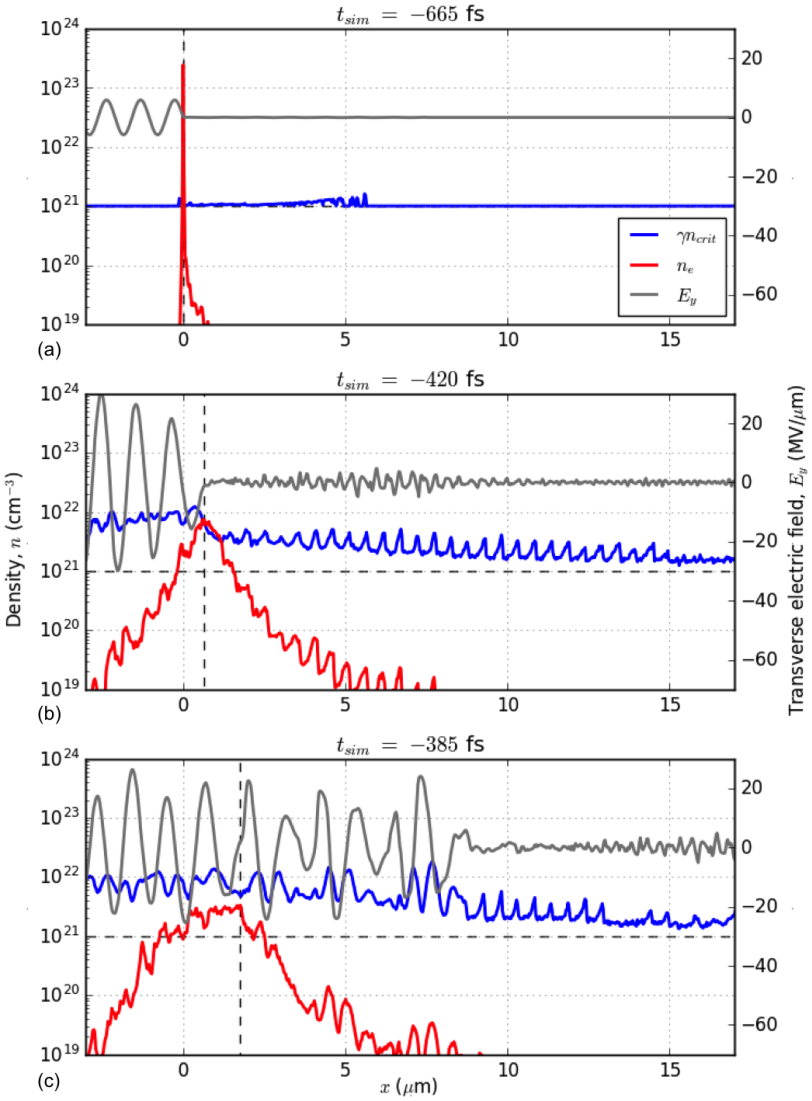

Figure 6.12: 1D EPOCH simulations of n_e and $\gamma_e n_{cr}$ evolving with simulation times (a) $t_{sim} = -665$, (b) −420 and (c) −385 fs relative to the laser field given by E_y.

The onset of RIT is important for determining how ions are accelerated. TNSA, ETNSA, RPA-LS and CE are mechanisms that depend on the laser interaction with the overdense target. This interaction determines the longitudinal electrostatic field that drives the ions

forward. The magnitude of the field depends on the main mechanisms emerging during the laser-plasma interaction. At the onset of RIT the mechanisms switch off and no longer strengthen the electrostatic field. Therefore it was assumed that the acceleration mechanisms may be identified at the time just before the onset of RIT.

In contrast to the other acceleration mechanisms, BOA emerges at the onset of RIT. If BOA is important, the electrostatic field may be amplified due to the Buneman instability. This rapidly drives to high energies. It was assumed that by looking at the electrostatic field and ion motion immediately after the onset of RIT that any effect of BOA may be identified.

6.5.1.3 Ion energies

The ion motion relative to the longitudinal electric field, E_x, determines the proton and carbon ion energies, $\mathcal{E}_p$ and $\mathcal{E}_{cb}$. This is shown in Figure 6.13 (a) from the 1D-EPOCH simulations. The mean position of protons (circles) and carbon ions (crosses) with energies between 80% and 100% of their maximum energy are plotted at each dump time (35 fs per dump) from $t_{sim} = -700$ to 0 fs. E_x is shown in the background of Figure 6.13 (a) for spatial comparison to the ions. The dark red region in E_x accelerates ions forward in the positive x direction. The horizontal dashed line marks the start of RIT. Figures 6.13 (b) and (c) show the maximum $\mathcal{E}_p$ (green line) and $\mathcal{E}_{cb}$ (indigo line) between $t_{sim} = -700$ and 700 fs. Values of E_x that spatially coincide with the protons and carbon ions are taken and then averaged to shown $E_{x,ave}$ (red lines) in Figures 6.13 (b) and (c). For reference, the Gaussian transverse laser field, E_y, is shown as the dotted blue line. The vertical dashed lines indicate the time that RIT starts.

Before the onset of RIT the energetic ions are moving ahead of the acceleration field (see red region in Figure 6.13 (a)). The acceleration field is confined close to the target rear surface and drives the ions forward. The field strength determines the ion energies. As the ions are accelerated away from the field, the ions do not gain more energy. Hence, the highest ion energies are limited to the ion acceleration close to the target before $t_{sim} = -420$ fs. At this time the field reached its largest amplitude of about 6.7 MV/μm.

After the onset of RIT at $t_{RIT} = -420$ fs, the acceleration field in E_x (see red region in Figure 6.13 (a)) detaches from the relativistically transparent plasma and moves rapidly forward. This field catches up with the energetic ions pre-driven by this field before the onset of RIT. This results in continuing acceleration of the ions to higher energies. This is shown by Figures 6.13 (b) and (c). Because of the onset of RIT, the highest energies achieved in the simulations are $\mathcal{E}_p \approx 290$ MeV and $\mathcal{E}_{cb} \approx 1.8$ GeV. How this strong field is generated depends on the emerging acceleration mechanisms.

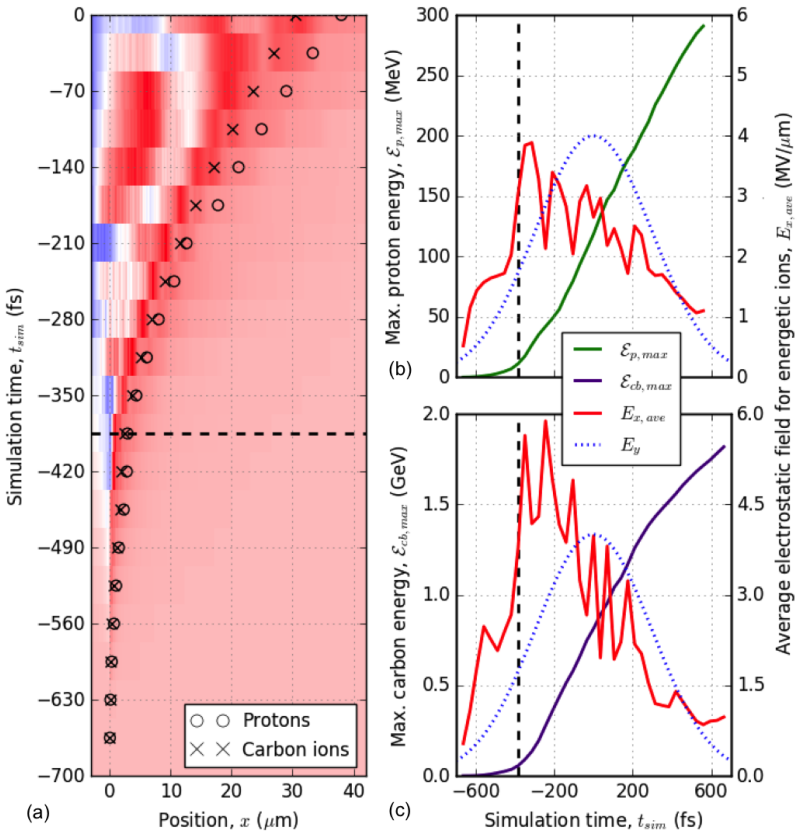

Figure 6.13: (a) Electrostatic field, E_x, at simulation times t_{sim} and mean position x relative to the most energetic protons (circles) and carbon ions (crosses). The average E_x (red line) acting on these ions is compared to the maximum proton and carbon ion energies, $\mathcal{E}_{p,max}$ and $\mathcal{E}_{cb,max}$ (green and indigo lines), in (b) and (c) with t_{sim}. The laser pulse (dotted blue line) is plotted in the background.

Complementing the 1D simulations, Figure 6.14 (a) and (b) shows the proton and carbon ion energy distributions accelerated from target rear side ($x > 0$ μm) at selected simulation times, $t_{sim} = -210$, -140, 0 and 560 fs. t_{sim} are times after the onset of RIT. From this onset onward, the protons are initially accelerated as a bunch of two quasimonoenergetic regions. By 0 fs the energy distribution starts to broaden because of the gradual decrease in the peak amplitude of the acceleration field. This also results in protons behind the acceleration field gaining less energy than the protons co-moving with the peak. As a result, the energy distribution broadens, resulting in the distribution seen at 560 fs (red). As for the carbon ions, the energy distribution has two continuous regions. For times $t_{sim} = -210$, -140 and 0 fs the low-energy region is at energies $\mathcal{E}_{cb} < 260$, 350 and 1100 MeV, and the high-energy region is between 260 and 360 MeV, 640 and 820 MeV and 1250 and 1750 MeV.

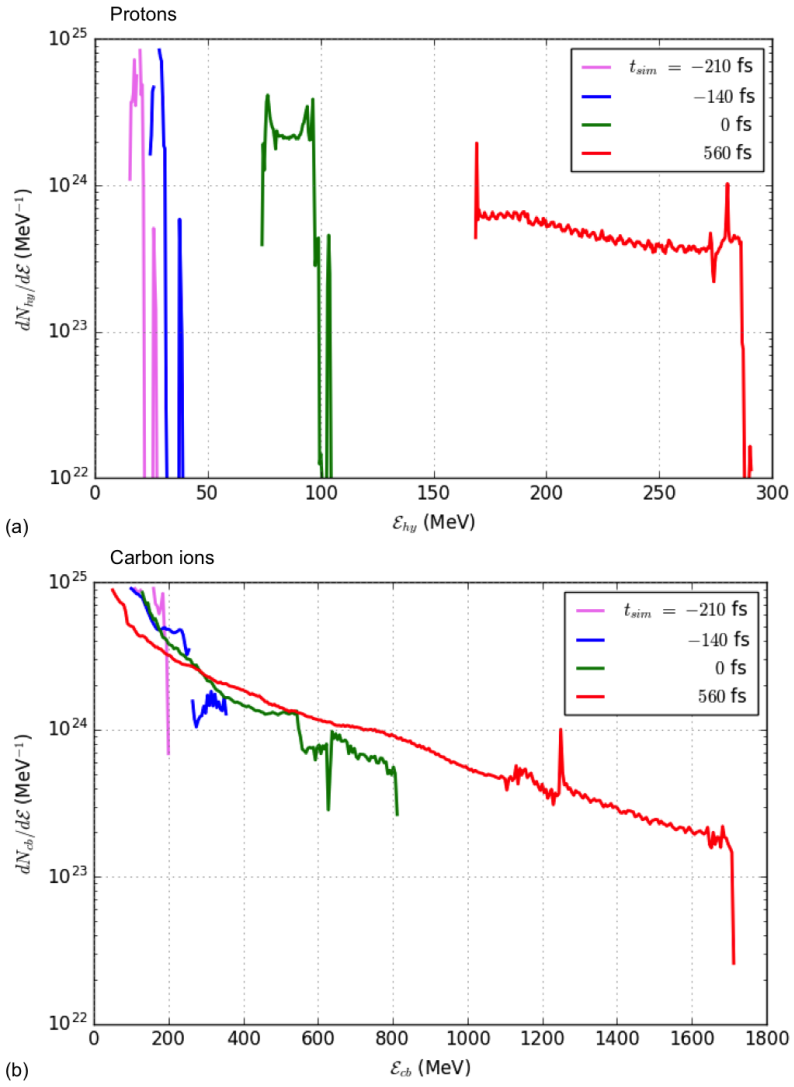

Figure 6.14: Energy distributions of (a) protons and (b) carbon ions in the 1D-EPOCH simulations at $t_{sim} = -210$ (violet), -140 (blue), 0 (green) and 560 fs (red).

6.5.1.4 Inferring for target normal sheath acceleration (TNSA)

The contribution of TNSA to the acceleration field, E_{TNSA}, known as the sheath field, was calculated using the relation $E_{TNSA} = T_{rel}/L_{sh}$.[16,29] $L_{sh} \approx 0.7$ μm is taken as the length of the acceleration field estimated across the red region in Figure 6.13 (a) at $t_{sim} = -455$ fs. The relativistic electron temperature, T_{rel}, was inferred from the average electron kinetic energy within the same region, which was $T_{rel} \approx 1$ MeV. This temperature is nearly equivalent to the mean energy calculated using Beg's scaling (see Eqn. **??**) at 10^{20} W/cm^2 laser intensity. Using $L_{sh} \approx 0.7$ μm and $T_{rel} \approx 1$ MeV from the simulations, $E_{TNSA} \approx 1.4$ MV/μm. Assuming that the ion energy is related to T_{rel} and atomic number, Z, by $\mathcal{E}_i \approx ZT_{rel}$,[29] the corresponding proton and carbon ion energies are respectively $\mathcal{E}_p \approx 1$ and $\mathcal{E}_{cb} \approx 6$ MeV. These estimates are well below the energies of the energy distributions simulated (see Figure

6.14 (a) and (b)) and, hence, TNSA is expected to have no strong contribution to the ion acceleration.

E_{TNSA} was calculated assuming the electrons in the overdense plasma were cold. The assumption is not valid as volumetric coupling of the laser to all electrons occurs across the target.

6.5.1.5 Inferring for enhanced target normal sheath acceleration (ETNSA)

For ETNSA to accelerate ions the target needs to be volumetrically heated by the laser, which is inferred from Figure 6.12. As discussed in Section 6.4.2 this is possible because the 8 nm target thicknesses is comparable to the $\delta_s \approx 6$ nm skin depth. This suggests that TNSA was dominated by ETNSA as all electrons interact with the laser. Hence, both theory and EPOCH simulations suggest that ETNSA may contribute to the ion acceleration. This contribution may be small because of the thinness of the target.

6.5.1.6 Inferring for radiation pressure acceleration in light-sail regime (RPA-LS)

For RPA-LS it was assumed that Eqns. (2.29) and (2.30) may be used directly to determine the ion energy, $\mathcal{E}_i$. Solving the definite integral in Eqn. (2.30) for a Gaussian laser pulse of peak intensity, I_0, and pulse duration, t_0, these equations are rewritten as

$$\mathcal{E}_i = \frac{m_i c^2}{2}\frac{\mathcal{F}}{\mathcal{F}+1} \tag{6.4}$$

$$\mathcal{F} = \frac{2\sqrt{\pi \ln 2} I_0 t_0}{m_i n_i x_0 c^2}\mathrm{erf}\left(\frac{t_{RIT}-t_s}{2\sqrt{\ln 2}t_0}\right) \tag{6.5}$$

The dimensionless laser fluence is $\mathcal{F}$. n_i and m_i are the ion density and mass, x_0 is the initial thickness, t_s is the simulation start time, t_{RIT} is the time for the onset of RIT. Integrating a Gaussian function results in the error function, erf(), in Eqn. 6.5. Between t_s and t_{RIT} the laser interacts with the overdense plasma. Key assumptions for Eqns. 6.4-6.5 are that the target is perfectly reflecting the laser, no laser absorption occurs and the target remains overdense up to the onset of RIT.[29] The first two conditions are not satisfied because of the target thickness is comparable to the skin depth.[29,61]

Using Eqns. 6.4-6.5 for the carbon ions for the $x_0 = 8$ nm thick target gives $\mathcal{E}_{cb} = (2.0 \pm 0.3)$ GeV. From the 1D-EPOCH setup the carbon ions used $n_{cb} = 1.15 \times 10^{23}$ cm^{-3} and $m_{cb} = 12u$ for carbon ions ($u = 1.66 \times 10^{-24}$ g is the atomic mass unit). As for the Gaussian laser pulse, $I_0 = 3 \times 10^{20}$ W/cm^2, $t_0 = 700$ fs and $t_s = -700$ fs. $t_{RIT} = (-410 \pm 35)$ fs from the EPOCH simulations. The standard error in $\mathcal{E}_{cb}$ is calculated from t_{RIT}. Repeating the calculation for the simulated protons where $m_p = u$ and $n_p = 1.15 \times 10^{22}$ cm^{-3} gives $\mathcal{E}_p = (460 \pm 10)$ MeV. The calculated energies are larger than simulations predict.

The key assumptions that perfect reflection and no absorption of the laser occurred are not valid. In the EPOCH simulations at $t_{sim} = -420$ fs before the onset of RIT it was shown that the laser penetrated the target (see Figure 6.12 (b)). A quarter of the laser transmits through the target, which is estimated from comparing the peaks in E_y in Figure 6.12 (b). Furthermore, about 11% of the incident laser energy is absorbed by the target in the simulations. Multiplying the fraction of penetrated and absorbed laser energy on $\mathcal{E}_p$ and $\mathcal{E}_{cb}$ reduces the calculated energies to $\mathcal{E}_p = (12.1 \pm 0.3)$ and $\mathcal{E}_{cb} = (53 \pm 8)$ MeV. These energies are significantly lower than the simulated ion energies shown in Figure 6.14 (a) and (b). Hence, the result suggests that RPA-LS may not be efficient in driving the ions from LSG targets.

6.5.1.7 Inferring breakout afterburner (BOA) acceleration

According to Stark et al.[70] one approach for determining the impact of BOA to the ion acceleration is to infer a rapid growth in ion energies at the onset of RIT. This growth in energy coincides spatially with a longitudinal electric field that rapidly increases within a sub-micron range at target rear. This is inferred in PIC simulations by comparing the ion phase-space to this co-moving electric field.

Figures 6.15 (a)-(b) show the longitudinal and transverse electric fields, E_x and E_y (blue and red profiles), before and after the onset of RIT ($t_{sim} = -420$ and -350 fs). The peak in E_x above 4 MV/μm is defined as the acceleration field. The corresponding energy phase-space of the protons and carbon ions are shown in Figures 6.15 (c)-(d) and (e)-(f). The initial target thicknesses used is 8 nm. The colorbars provide the ion densities n_p and n_{cb}.

By comparing Figures 6.15 (a)-(b) and (c)-(d), the densest proton bunch are inferred to move ahead of the acceleration field. A low density of protons are driven to high energy by this field. At $t_{sim} = -350$ fs, the bunched protons achieve energies of 12 MeV, and the most energetic protons reach up to 17 MeV (see Figure 6.15 (d)).

Comparing E_x to the carbon ion phase-space in Figure 6.15 (e)-(f) the densest carbon ions are spatially coinciding with the acceleration field. At $t_{sim} = -350$ fs a carbon bunch at $\sim$3 μm (see Figure 6.15 (f)) is in co-motion with the field, leading to an increase in their energy from about 30 up to 90 MeV.

A rapid increase in neither E_x nor the ion energies is inferred from the EPOCH simulations using an 8 nm thick plasma. Similar results were achieved for thicknesses down to 1 nm. According to Stark et al.[70] the carbon ion energy phase-space (see Figures 6.15 (e)-(f)) suggests that ETNSA may result in the most energetic ions and may be important.

As explained in Subsection 6.4.4, optimising BOA required the onset of RIT, t_{RIT}, to coincide closely with the peak of the laser pulse interacting with the target. The laser peak is at 0 fs when it enters the simulation box and close to the target. For the 8 nm target, $t_{RIT} = (-410 \pm 35)$ fs. Hence, the onset of RIT occurs too early for BOA to drive the ions.

To determine the target thickness where t_{RIT} is closest to 0 fs a number of 1D-EPOCH simulations for different target thicknesses were computed.

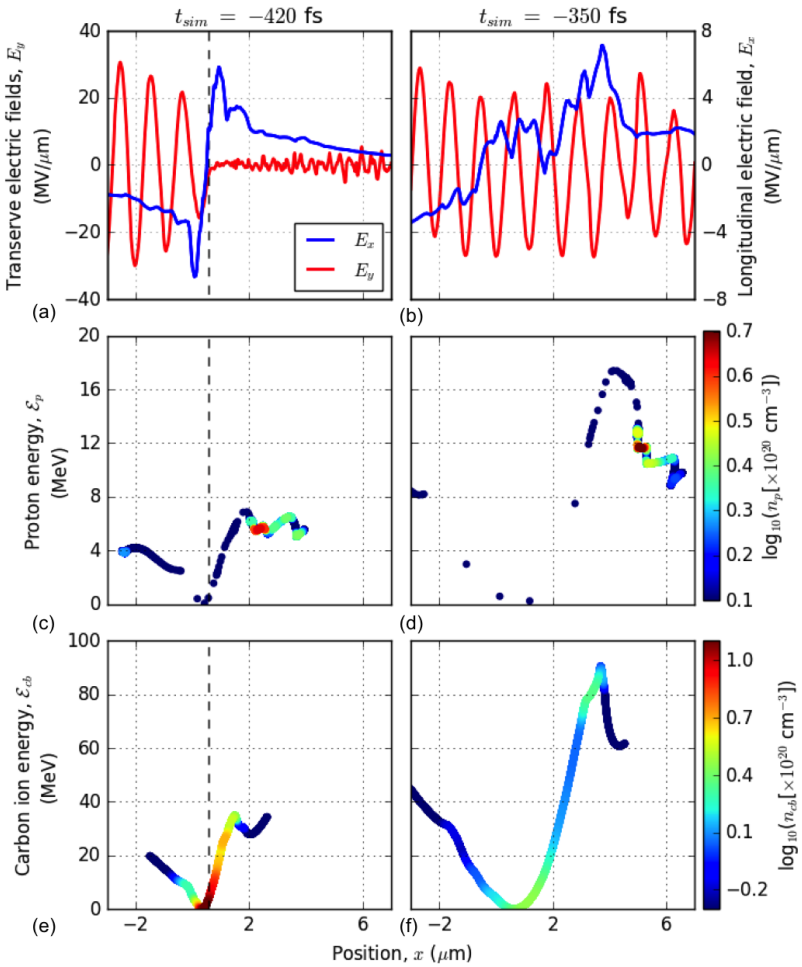

Figure 6.15: 1D-EPOCH simulations using 8 nm target at times before the onset of RIT (−420 fs, left column) and after (−350 fs, right column). The longitudinal and transverse electric fields, E_x and E_y (blue and red), are shown in (a) and (b). The energy phase-spaces of the protons and carbon ions are compared to the fields in (c)-(d) and (e)-(f).

Table 6.2 summarises the times for the onset of RIT, t_{RIT}, for the tabulated target thicknesses, x_0, used in the 1D-EPOCH simulations. For x_0 = 100 nm no onset of RIT is inferred throughout the simulation. The uncertainty in t_{RIT} was ±35 fs for the 8 nm target. For all other targets the uncertainty is ±70 fs. The uncertainty are taking from the time step used between output dumps in the simulations. The focus is on the 8 nm LSG target used in experiment, which used 35 fs time steps for detailed information.

Table 6.2: Onset of RIT, t_{RIT}, inferred in 1D-EPOCH simulations using different initial target thicknesses, x_0. Uncertainty in t_{RIT} is the time step between output data. *Uncertainty for $x_0 = 8$ nm is ± 35 fs.

x_0 (nm)	1	4	8	10	20	40	60	100
$t_{RIT} \pm 70$ (fs)	-490	-420	-385*	-350	-280	-140	0	-

As implied by the information in Table 6.2, the onset of RIT occurs near the main laser peak when the target thickness is 60 nm. Using this thickness produced the electric field and ion energy phase space plots in Figure 6.16. This figure is the same as Figure 6.15 for the 8 nm target. (a)-(b) show the electric fields, E_x and E_y, before and after the onset of RIT ($t_{sim} = -140$ and 0 fs). The proton and carbon ion energy phase-spaces at these simulation times are shown in (c)-(d) and (e)-(f). The colorbars refer to the proton and carbon ion densities.

As seen in Figure 6.16 before the onset of RIT (left column), the protons are ahead of the peak in E_x, whereas a dense carbon bunch is spatially correlated to the acceleration field. This is also observed for the 8 nm target (see Figure 6.15). The amplitude is 2.5 greater when using the 60 nm thick target compared to the 8 nm target. The 1D-EPOCH simulation suggests that the main coupling of the acceleration field is to the carbon ions rather than the protons. It will be shown later that this result is not observed when including the transverse ion motion present in two-dimensional (2D)-EPOCH simulations. The co-motion of carbon ions with the acceleration field may therefore be a special case in one dimension.

After the onset of RIT a sharp increase in the acceleration field at 8.8 μm is seen in Figure 6.16 (b). Simultaneously, the carbon ions accelerate rapidly as inferred from the broad energies from 150 to 600 MeV between 8.5 and 11 μm (see Figure 6.16 (f)). Within this region there is a dense carbon bunch at an energy of $\sim$570 MeV. The carbon ion phase-space shows similar results by Stark et al. [70]. In their work they suggest that the sharp increase in the acceleration field and in turn carbon ion energies is a result of BOA driving the ions. Therefore, the 1D-EPOCH simulations indicate that BOA might becomes important if the target thickness is 60 nm.

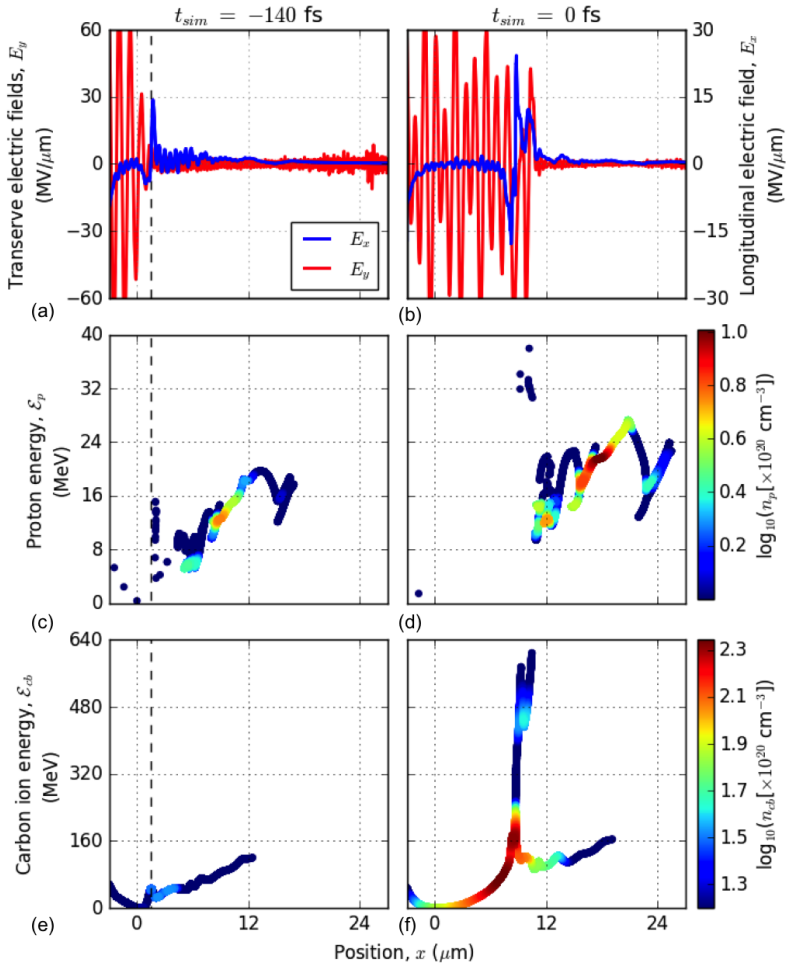

Figure 6.16: 1D-EPOCH simulations using 60 nm target at times before the onset of RIT (−140 fs, left column) and after (0 fs, right column). The longitudinal and transverse electric fields, E_x and E_y (blue and red), are shown in (a) and (b). The energy phase-spaces of the protons and carbon ions are compared to the fields in (c)-(d) and (e)-(f).

6.5.1.8 Inferring for Coulomb explosion (CE)

CE requires the target thickness to be comparable to the relativistic skin depth, $\delta_s\sqrt{\gamma_e}$.[64] The 8 nm target is comparable to the skin depth as well as in the relativistic case until the onset of RIT at −420 fs. At this time the target expands to a thickness of ∼0.6 μm (see Figure 6.12) and $\delta_s\sqrt{\gamma_e} \approx 0.4$ μm. This comparison is important because the laser volumetrically heats the target and, hence, decreases n_e.

With the electrons leaving the target, a positively charged dense plasma forms. This is shown in Figure 6.17 (a) with the charge difference, $\Delta(qn) = e(n_p + 6n_{cb} - n_e)$, within the dense plasma between 0.2 and 0.7 μm. The electron density, n_e, is plotted in the background for reference. The simulation time is $t_{sim} = -455$ fs, which is the time that the positive charge within the overdense plasma is maximised and before the onset of RIT. The longitudinal and transverse electric fields, E_x and E_y, for the same time are shown in Figure 6.17 (b).

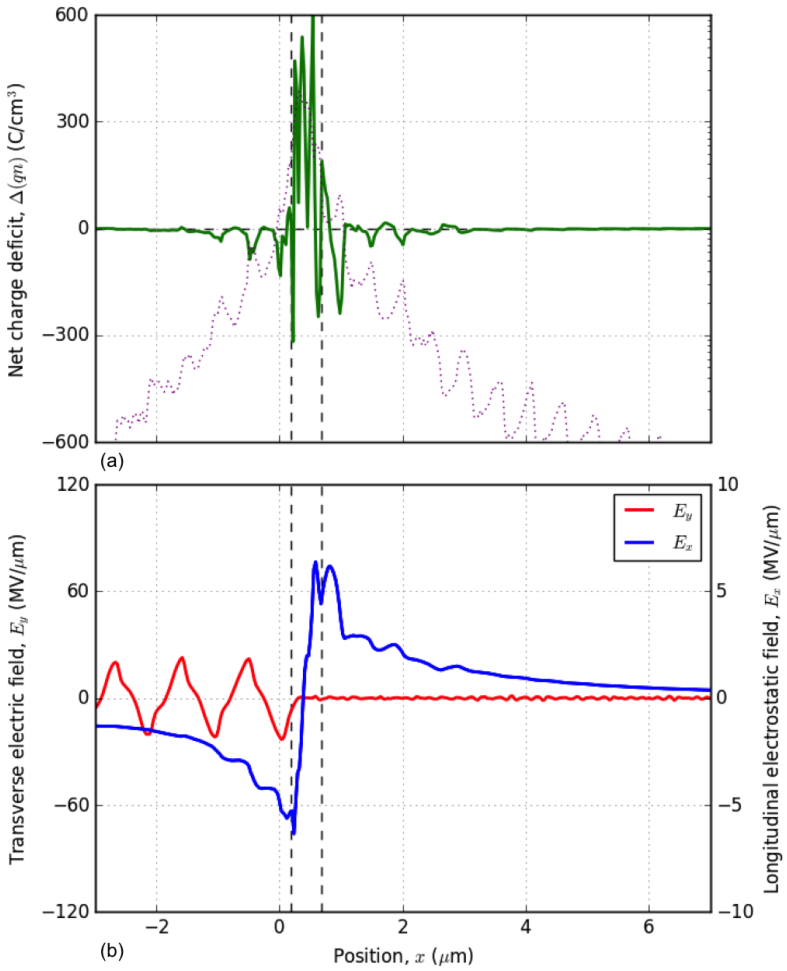

Figure 6.17: 1D EPOCH simulations of the 8 nm thin target comparing the (top) electric fields E_y and E_x against (bottom) the charge difference, $\Delta(qn)$, in the plasma. Enclosed vertical dashed lines mark the region of the overdense plasma. The purple dotted line is the corresponding relative plasma density n_e for reference.

The longitudinal electric field strength E_{CE} inside the overdense plasma was assumed to be due to CE. E_{CE} was derived using Gauss's Flux Law,[30,39,154]

$$E_{CE} = \frac{1}{\varepsilon_0} \int_{x_{front}}^{x_{rear}} \Delta(qn) dx \tag{6.6}$$

where $x_{front} = 0.2$ and $x_{rear} = 0.7$ μm are the front and rear surface positions of the overdense plasma. By integrating $\Delta(qn)$ in Figure 6.17 within this range, $E_{CE} \approx 10$ MV/μm. E_{CE} was 70% of the total E_x enclosed between 0.2 and 0.7 μm in Figure 6.17 (b), which was 14 MV/μm. This result suggests that CE contributed significantly to the ion acceleration in the EPOCH simulations.

6.5.1.9 Summary on 1D EPOCH simulations

To summarise the 1D-EPOCH simulations, CE is the most plausible mechanisms driving the ions to high energy. Volumetric heating results in TNSA being overtaken by ETNSA and reduce the impact of RPA-LS. These occur as a result of the target thicknesses being comparable to the skin depth. The contribution of ETNSA to the ion acceleration is unclear as it may be dominated by CE. At the onset of RIT, BOA is inferred to be insignificant in accelerating ions from 8 nm thick targets and thinner. Instead, a 60 nm thick target may be needed. The onset of RIT is important in order for the acceleration field to continue driving the ions to the high energies simulated.

In the 1D simulations the proton and carbon ion energies reach as high as $\mathcal{E}_p \approx 290$ MeV and $\mathcal{E}_{cb} \approx 1.8$ GeV. These results are greater than $\mathcal{E}_p = (44.5 \pm 0.3)$ and $\mathcal{E}_{cb} = 802$ MeV measured in the experiment, which is unsurprising because the simulations are constrained to 1D.

6.5.2 2-dimensional simulation setup

To understand the limitations of the 1D simulations, and to interpret the ion beam pattern in the experiment, two-dimensional (2D)-EPOCH simulations were conducted. The setup was adapted from the 1D simulations described in Subsection 6.5.1.

The 2D-EPOCH simulations were computationally demanding and therefore larger computational resources were required. These simulations were run using the York Super Advanced Research Computing Cluster called Viking.[155] 1000 CPU cores were used with a RAM limited to 192 GB. To limit the amount of data and storage problems, the time step was increased to 140 fs. This was four times larger than in the 1D case. One simulation took approximately 48 hours.

The simulation box was 80×50 μm^2 containing 10928×6832 square cells. The cell size was $\Delta x = \Delta y = 7.3$ nm. The p-polarised laser pulse entered the simulation box from the left boundary at -3 μm. The laser was Gaussian with a $t_0 = 0.7$ ps FWHM pulse duration and peak intensity of $I_0 = 3 \times 10^{20}$ W/cm^2. The transverse spatial laser profile was also Gaussian with a FWHM spot diameter of $w_0 = 6$ μm. The peak entered the simulation box at -700 fs from the left hand side boundary. The laser wavelength was $\lambda_0 = 1.054$ μm. The laser irradiated the target front surface at normal incidence and 0 μm, which was 3 μm from the left boundary. The target was a fully ionised plasma slab with 480 electrons, 8 protons and 80 carbon ions per cell. Target thickness was 8 nm with a uniform density of $n_e = 690 n_{cr}$ ($n_{cr} = 1 \times 10^{21}$ cm^{-3}). Exponential density ramps extending 5 and 1 nm from the front and rear sides of the target were used. Initial plasma temperature used was $T_e = 1$ keV for a Debye length of $\lambda_D \approx 280$ nm.

The 80 μm longitudinal length of the simulation box was chosen because of computational runtime and it is smaller than the Rayleigh length, $R_x = \pi w_0^2 / \lambda_0$. Therefore it is assumed

in the 2D simulations that focusing and defocusing effects are unimportant.

Even though Viking is a larger computing cluster, compromises between the resources and numeric stability were taken. This ensured that it was feasible to do the 2D simulations. The cell size is 7.3 nm cell size and double from that used in 1D-EPOCH simulations, and the number of particles were reduced to 3.0×10^6 electrons, 5.1×10^4 protons and 5.1×10^5 carbon ions in the simulation box. These were selected accordingly from 1D convergence testing assuming the test is transferrable to the 2D platform.

6.5.2.1 Onset of relativistically induced transparency

Figure 6.18 (a) shows the electron density, n_e, normalised to the critical density, n_{cr}, against the transverse electric field, E_y, at simulation time $t_{sim} = -560$ fs. The colorbars indicate the order of magnitude for n_e and field strength and sign of E_y. This is one time step into the 2D-EPOCH simulation. In the region enclosed by the horizontal dashed lines, n_e, relativistic critical density, $\gamma_e n_{cr}$, and E_y are averaged along the transverse axis. These averages are shown in Figure 6.18 (b) as the red, blue and grey profiles respectively.

As inferred from Figure 6.18 the onset of RIT occurs at (-560 ± 140) fs in the 2D-EPOCH simulations. The uncertainty is the time step used. This time occurs earlier in the laser pulse compared to the 1D simulation at (-420 ± 35) fs. This is the result of the plasma expanding in both the longitudinal the transverse axes. n_e decreases rapidly when accounting for the transverse expansion in 2D. Consequently, due to the early onset of RIT, the amplitude of the acceleration field reaches 1.7 MV/μm, which is nearly four times lower than in the 1D simulations. Hence, in the 2D case the proton and carbon ion energies drop from $\mathcal{E}_p = 290$ to 50 MeV and $\mathcal{E}_{cb} = 1.8$ to 0.4 GeV.

6.5.2.2 Simulated ion beam directionality

An insight to the ion beam pattern is obtained from the ion motion inferred in the 2D-EPOCH simulations. In Figure 6.19 (a) the divergence angle of the protons and carbon ions from target rear, θ, is compared to the corresponding ion energies, $\mathcal{E}_p$ and $\mathcal{E}_{cb}$. Note that the energy units are in MeV/n instead of MeV to compare the ions. Both target normal and laser direction are at $\theta = 0°$. The simulation time is $t_{sim} = 560$ fs, which is after the main peak interacts with the target and before the protons leave the simulation box. The 'fire' and 'jet' colorbars give, respectively, the densities of protons and carbon ions, n_p and n_{cb}, normalised to their maximum. 10% of the ions are protons. Another simulation without protons (see Figure 6.19 (b)) produces carbon ions with the same divergence seen in Figure 6.19 (a) and ~2 MeV/n more energy.

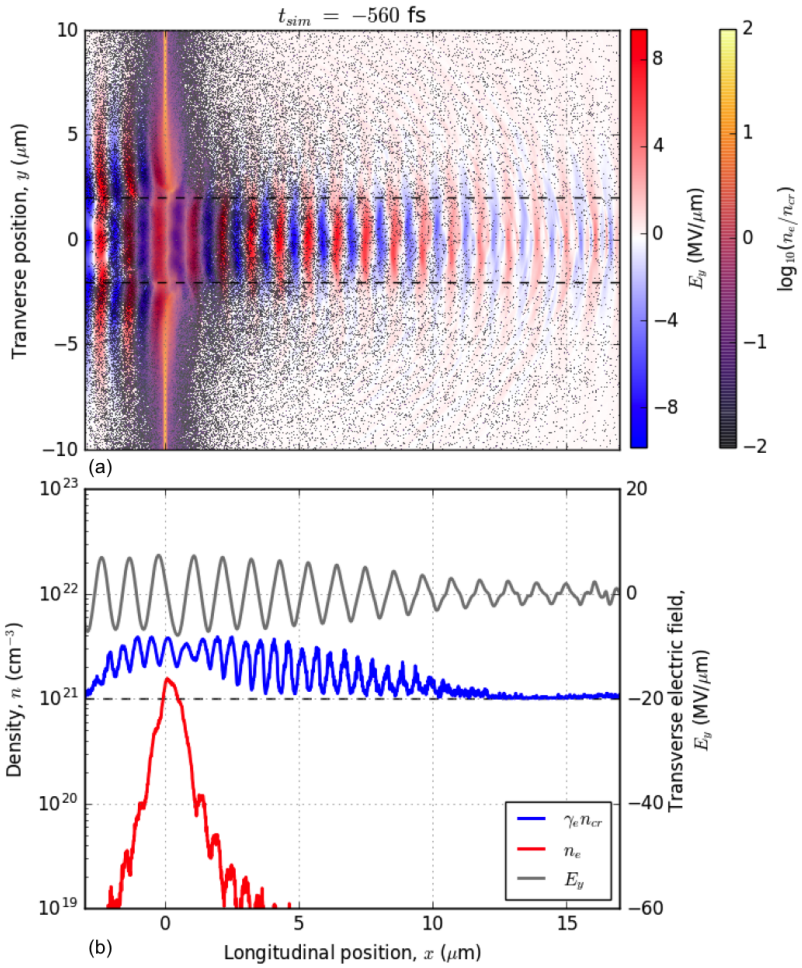

Figure 6.18: (a) 2D EPOCH simulations of electron density n_e and transverse electric field, E_y, at simulation time $t_{sim} = -560$ fs. The dashed region is averaged along transverse position for n_e, $\gamma_e n_{cr}$ and E_y shown in (b).

Protons produce the divergence-to-energy distribution shown with the 'fire' colormap, and the carbon ions describe the distribution with the 'jet' colormap in Figures 6.19 (a) and (b). These ions produce different distributions. As seen in Figure 6.19 (a), the carbon ions preferentially propagate away from target normal and between $\theta \approx 8°$ and 20°. The carbon ion energies span from $\mathcal{E}_{cb} \approx 15$ MeV/n ($\sim$ 180 MeV) at highest density to $\sim$ 22 MeV/n ($\sim$ 260 MeV) where n_{cb} is 0.4 of the maximum density. The most energetic carbon ions reach nearly 25 MeV/n (300 MeV) with a tenth of the maximum n_{cb} between $\theta \approx -10°$ and 10°. The protons propagate with a high density between $\theta = 15$ and 25° and energies from $\mathcal{E}_{cb} = 15$ to 24 MeV, which are close to the directionality and energies of the carbon ions.

In Figure 6.19 (a) a second dense bunch of protons is seen between $\theta = 4$ and 16° and $\mathcal{E}_p = 36$ and 45 MeV, which is similarly inferred in another study using a PIC code.[156]

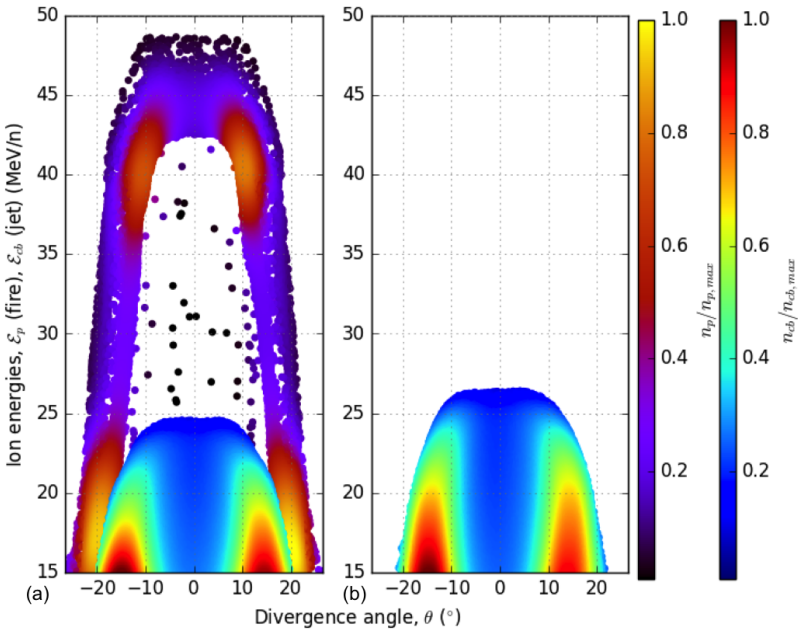

Figure 6.19: 2D EPOCH simulations of ion beam directionality with energies $\mathcal{E}_p$ and $\mathcal{E}_{cb}$ against divergence angle, θ, at target rear side. Colorbars indicate the normalised densities. Simulations (a) with and (b) without protons are shown.

Another important observation inferred from Figure 6.19 (a) is the generation of monoenergetic protons. Within a divergence of $\theta = -5$ and 5° the protons span in energies between 42 and 49 MeV. The proton density in this region reaches up to 20% of the maximum. This is not seen for the carbon ions. Instead, carbon ions are more absent within the central region near $\theta = 0°$ as inferred in Figure 6.19 (a).

When omitting the protons in the 2D-EPOCH simulations (see Figure 6.19 (b)), the carbon ion directionality remains qualitatively unchanged. The maximum energy of carbon ions propagating between $\theta = 8$ and 20° increases from 22 to 24 MeV/n (260 to 290 MeV). The most energetic carbon ions in the centre of the beam at $\theta = 0°$ also increases from 25 to 27 MeV/n (300 to 320 MeV). The energy rise is due to the absence of protons in the simulations, as seen previously by Jung et al. [68].

The proton and carbon ion directionality shown in Figure 6.19 depends on the longitudinal and transverse electric fields, E_x and E_y. This is shown in Figure 6.20 (a) and (b) respectively. $\langle E_x \rangle$ and $\langle E_y \rangle$ are E_x and E_y time-averaged over the laser period. The averaged fields are squared to show the regions in the fields that influence the average ion motion. $\langle E_x \rangle$ features an arc-shaped field between $x = 35$ and 55 μm. $\langle E_y \rangle$ shows two distinct channels in the region between $x = 0$ and 35 μm and $|y| = 5$ and 20 μm. The quiver points correspond to the protons (see Figure 6.20 (a)) and carbon ions (see Figure 6.20 (b)) and indicate their direction of motion and energy. The number of closely packed quiver points correlates to the normalised densities in Figure 6.19. Protons are compared to $\langle E_x \rangle$ and carbon ions to $\langle E_y \rangle$. The colorbars indicate the field strengths and ion energies. The simulation time is

$t_{sim} = 420$ fs.

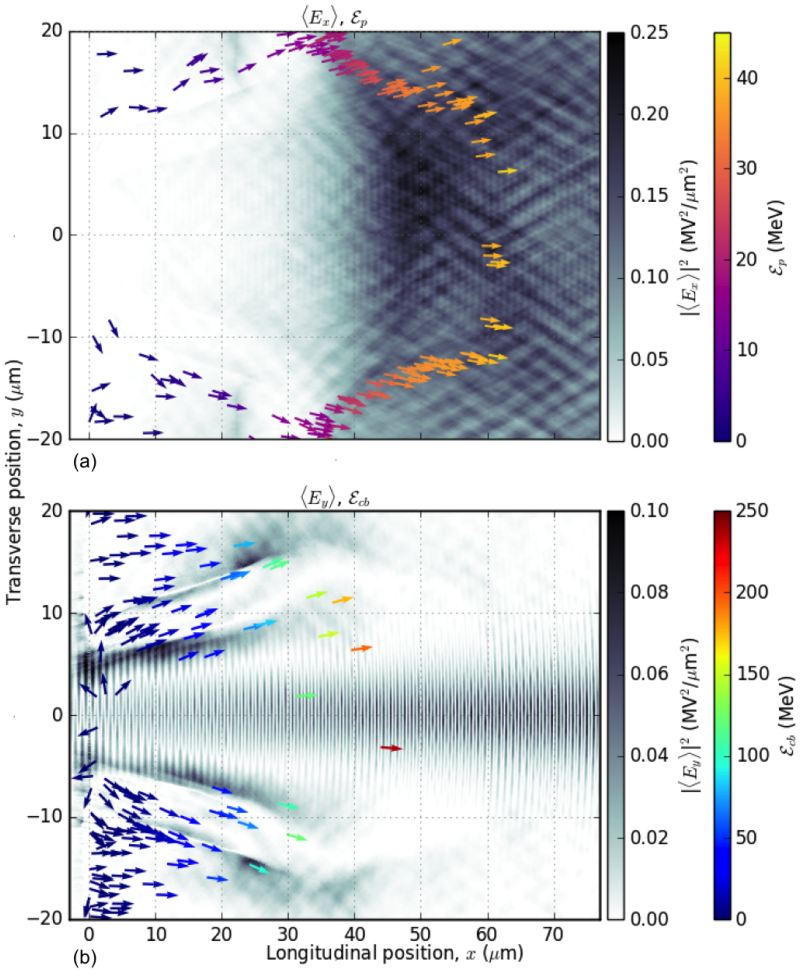

Figure 6.20: 2D EPOCH simulations of the (a) longitudinal and (b) transverse electric fields, $\langle E_x \rangle$ and $\langle E_y \rangle$, time-averaged over the laser period. The quiver points show the direction of the (a) proton and (b) carbon ion motion relative to these fields. The quiver colors indicate the relative $\mathcal{E}_p$ and $\mathcal{E}_{cb}$ values.

The ions are plotted to the compared fields because their motion depends strongly on those field. Protons at $x = 60$ μm are the monoenergetic proton bunch, which move ahead of the acceleration field centred around $x = 48$ μm (see Figure 6.20 (a)). The protons are closest to the field around $x = 50$ and $|y| > 10$ μm, which have energies between 36 and 45 MeV. These protons correspond to the high-energy bunches seen in Figure 6.19 (a).

The acceleration of carbon ions is different to the protons. A sparse number of the carbon ions propagate close to the acceleration field between $x = 30$ and 50 μm. This is interpreted from comparing $\langle E_x \rangle$ in Figure 6.20 (a) to the quiver points in Figure 6.20 (b). These carbon ions are of low density and have energies between 100 and 250 MeV (about 8 and 20 MeV/n), which correspond to the ions seen in Figure 6.19 between $\theta = -10$ and 10°. The energies are much lower per nucleon than protons, which suggests that the carbon ions are not strongly

driven by the acceleration field. Figure 6.20 (b) shows that carbon ions are mainly moving along the channels in $\langle E_y \rangle$ at an angle of $\sim 13^\circ$ relative to the laser axis, which correlates to the dense low-energy carbon ions inferred from Figures 6.19. This result suggests that carbon ions may be strongly driven by the transverse electric field.

By comparing Figures 6.19 (a) and (b), a number of low-energy protons are inferred to propagate along the transverse field at $x < 35$ and $|y| > 10$ μm. These are not driven by the acceleration field to high energy. Low-energy protons move along the channel in the transverse field, which also drives the carbon ions.

From the 2D simulation results it may be suggested that the acceleration field in the longitudinal direction drives the ions to high energies. The transverse electric field is mainly important in determining the divergence of the ion beam and beam shape. What may have led to the difference in the ion motion between the protons and carbon ions is their charge-to-mass ratio.[157] Protons have a high charge-to-mass ratio, enabling them to react more readily to the growth in the longitudinal field. The carbon ions with a low charge-to-mass ratio cannot keep up with the strong acceleration field and, in turn, are not driven to high energies. The transverse field diverges the carbon ions away, which prevents the ions from gaining energy from the acceleration field, as inferred from the 1D-EPOCH simulations. This in turn may have led to the reduction in carbon ion energies in the 2D simulations compared to 1D.

6.5.2.3 Ion acceleration in 2-dimensional simulations

As described in Subsection 6.5.2.1, the onset of RIT occurs rapidly because the transverse component of the laser drives electrons out of the initially overdense plasma. This occurs within a plasma region twice the size of the FWHM of the Gaussian laser pulse and 140 fs into the simulations, which is -560 fs before the main peak. Because of this early onset of RIT, and referring to the 1D simulation results in Subsection 6.5.1.7, BOA is expected to have no significant contribution to the ion acceleration. A much thicker target thickness may be needed for BOA to be important. A plausible mechanism generating the acceleration field driving the protons is CE because the laser rapidly vacates the electrons from the irradiated plasma region.

The channels between 14° and 24° from laser incidence along which protons and carbon ions move (see Figure 6.20 (b)) were previously shown to be generated by a combination of TNSA, RPA and the formation of the transverse electric field.[62,143] The impact of CE for those ions may be unimportant due to the electrons moving slower outside the FWHM width of the laser pulse.

6.5.2.4 Summary on 2D-EPOCH simulations

Comparing the 1D to 2D simulations, the onset of RIT occurs changes from -385 fs to -560 fs. This results in a lower amplitude in the acceleration field reducing the maximum proton and carbon ion energies from $\mathcal{E}_p = 290$ to 50 MeV and $\mathcal{E}_{cb} = 1.8$ to 0.4 GeV. $\mathcal{E}_p$ is closer to the experimental measurements, which is $\mathcal{E}_p = (44.5 \pm 0.3)$ MeV. $\mathcal{E}_{cb}$ is underestimated by a factor of two.

The proton and carbon ion directionality inferred in simulations show features comparable to the experimental observations. In the experiment a ring-like structure is seen at the lower ion energies on the RCF when using the 8 layer LSG target. The ring diameter is ~ 3.5 cm, which at a 5 cm distance from the target corresponds to a $\sim 19^\circ$ divergence angle from laser axis. This angle is comparable to the channels in the transverse electric field that the low energy protons and carbon ions move along. This suggests that these ions may be driven by TNSA, RPA and the transverse field. Furthermore, high energy protons and carbon ions along laser axis are seen on the CR-39 measurements. From the simulations, these ions are driven by the acceleration field, which may be generated via CE.

6.6 Summary and future work

The first measurements using graphene are robust and fascinating even though the ion flux is low. The analysis suggests that the most prominent mechanism driving the ions is Coulomb explosion (CE). This is supported by EPOCH particle-in-cell simulations indicating that the targets are comparable to the skin depth. The results are achieved due to the unusual experimental setup using the double plasma mirror and normal laser incidence with ultra-thin graphene targets. Close to the peak the target is heated completely by the laser. This heating rapidly vacates electrons out of the target, resulting in turn to a strong Coulomb explosion. Furthermore, EPOCH simulations show that the most energetic protons are contained within a central beam within a $\sim 10^\circ$ divergence angle. Carbon ions from low to high energies are concentrated in a cone of around 30° divergence. This matches our RCF and CR-39 analysis. EPOCH simulations indicate that the ion beam divergence emerges due to the high charge-to-mass ratio protons closely co-moving with the longitudinal electrostatic field, screening carbon ions from this field, whereas the carbon ions are strongly influenced by a transverse electric field. Interestingly, this has not been observed before possibly because of the ion flux being at least one order of magnitude below the detection threshold of commonly used diagnostics such as a Thomson parabola and RCF.

This work is new to the area of laser-driven ion acceleration. The observations using graphene as a target of thickness never used before on a "look-and-see" experiment are of great interest primarily due to the measurement of highly energetic protons and heavy ions. The heavy ions are a mix of carbon and oxygen ions that need separation in future exper-

imental studies on laser-driven ion acceleration. Secondly, the unusual material properties that graphene exhibits in combination with the experimental setup may enable the target to survive the prepulses. The material interaction with highly intense laser pulses needs to be studied to demonstrate this and understand how. Thirdly, the experimental measurements and EPOCH simulations indicate that carbon ions are not driven efficiently to high energies and in a central beam. To realise the potential of carbon ions for applications such as cancer treatment, a clearer understanding of the material properties and target design integrating graphene is needed. EPOCH simulations show that by increasing the target thickness to a point that the material turns relativistically transparent near the peak of the laser can increase the ion energies and coupling efficiency. Further studies should investigate the use of tens of femtosecond pulse duration with the nano-thin targets. This work may open further interesting investigations exploring the feasibility of using graphene as a target for compact carbon ion accelerators.

Chapter 7

Conclusion

In this thesis I present research on understanding and advancing the coupling of a high intensity laser with engineered targets. This required the use of a double plasma mirror (DPM) to further improve the contrast of the high-contrast Vulcan petawatt laser. Improving the contrast with the DPM ensured that reliable and reproducible measurements of X-rays from microstructured surface silicon and high energy ions from ultra-thin large-area suspended graphene (LSG) targets. The results suggest that the DPM provided an approach for preserving the target structural integrity to times closer to the peak of the laser pulse. Detailed measurements of the pulse structure after the DPM are not available. Therefore, a model was developed for determining how the pulse structure changes due to the DPM. Using this model on existing high fidelity Vulcan petawatt pulse shape measurements predicts that the DPM significantly improves the laser contrast. This contrast improvement was sufficient to reduce the pedestal and prepulses in the laser to intensities below the material ionisation thresholds. This is important as the energy in the pedestal and prepulses can fluctuate shot-to-shot due to small gain variations in the laser amplifiers. Suppressing these fluctuations in the pulse provides smaller variations in the laser-target interaction, resulting in more reproducible and reliable data.

The impact of the Vulcan petawatt pedestal and prepulses, as well as the DPM suppressing these features in the laser pulse, was assessed using the one-dimensional radiation-hydrodynamic calculations. These show that hydrodynamic motion of the target due to the laser is delayed closer to the main peak of the pulse when reducing the pedestal and prepulse signals. As a result the plasma density scale length becomes very small and, hence, reduce uncertainties in its size. From these calculations it is predicted that the DPM 'cleans up' the pulse shape, suggesting that the high intensity laser peak interacts with an overdense, possibly close to solid density, target with steep density gradients.

Highly reproducible and bright spectral X-rays were observed by irradiating the Vulcan petawatt laser through a DPM on to a surface microstructured silicon target. The DPM 'cleans' the pulse and ensures the target integrity is preserved, which reduces the density

scale length. By using the microstructures the scale length is enlarged to a controllable size, which optimises the laser-to-target coupling. This is evident from the measurements showing a significant rise in K_α brightness. The combined setup using the DPM and microstructured surface targets provides a method for engineering density scale lengths that generate a reliable and reproducible K_α source. Experiments and applications requiring reliable measurements can benefit from using this setup.

The DPM is key to enabling the use of ultra-thin large-area suspended graphene (LSG) as targets. Irradiating the Vulcan petawatt laser, after improving the contrast with the DPM, at near-normal incidence on single- and multi-layer LSGs. Using an octuple-layer LSG target produced (44.5 ± 0.3) MeV protons and $\sim$800 MeV carbon ions. It is noted that the flux of carbon ions is very low. The observations are intriguing as this is the first time that targets as thin as a few 1 nm are used for laser-driven ion acceleration. Linking these observations to EPOCH particle-in-cell simulations suggest that the most prominent mechanism driving the ions to high energies is Coulomb explosion (CE). The LSG targets are comparable to the skin depth, which is key for CE to generate strong electric fields across the thickness of the target. In addition, the onset of relativistically induced transparency, which is inferred from simulations, is found to be important as this results in the electric fields that co-move with the ions. The co-moving fields accelerate the ions for a longer time enabling them to gain high energies. 2D-EPOCH simulations predicted protons reaching 50 MeV and 400 MeV for carbon ions, where the former is comparable to the experimental measurements. This work provides new insight in to the interaction of a laser pulse approaching intensities of 10^{20} W/cm^2 with an ultra-thin target using a material, made of carbon, that is of interest for the treatment of certain cancers. These are the first ion acceleration measurements using graphene as a target, which are not fully understood yet. Future studies should focus on investigating the material properties of graphene in very strong electromagnetic fields to provide a deeper understanding to this material as ion acceleration targets.

For prospective experiments to benefit from the DPM, the setup used on the Vulcan petawatt laser needs to be transferrable to other high intensity laser facilities. These was tested by installing a compact 3D-printed DPM unit on the LFEX laser. Preliminary results showed that this DPM is easy to use and may raise the laser fluence. The measurements were limited yet suggest that similar experimental setups on the Vulcan petawatt laser can be accomplished on laser facilities worldwide.

Appendix A

Appendix

A.1 Contribution to this and other research

Over the period of the PhD the author has contributed to a number of collaborations and publications, including projects that are not mentioned in this thesis. These are the following:

1. E. Oks, E. Dalimier, A. Faenov, P. Angelo, S. Pikuz, T. Pikuz, I. Skobelev, S. Ryazanzev, P. Durey, L. Doehl, D. Farley, C. Baird, K. Lancaster, C. Murphy, N. Booth, C. Spindloe, P. McKenna, N. Neumann, M. Roth, R. Kodama and N. Woolsey, *In-depth study of intra-Stark spectroscopy in the x-ray range in relativistic laser-plasma interactions*, Journal of Physics B: Atomic, Molecular and Optical Physics **50**, 245006 (2017).

2. M. T. Oliver, T. G. White, P. Mabey, M. Kühn-Kauffeldt, L. Döhl, R. Bingham, R. Clarke, P. Graham, R. Heathcote, M. Koenig, Y. Kuramitsu, D. Q. Lamb, J. Meinecke, T. Michel. F. Miniati, M. Notley, B. Reville, S. Sarkar, Y. Sakawa, A. A. Schekochihin, P. Tzeferacos, N. Woolsey, H.-S. Park and G. Gregori, *Magneto-optic probe measurements in low density-supersonic jets*, JINST **12**, P12001 (2017).

3. I. Yu. Skobelev, S. N. Ryazantsev, D. D. Arich, P. S. Bratchenko, A. Ya. Faenov, T. A. Pikuz, P. Durey, L. Doehl, D. Farley, C. Baird, K. Lancaster, C. Murphy, N. Booth, C. Spindloe, P. McKenna, S. B. Hansen, J. Colgan, R. Kodama, N. Woolsey and S. A. Pikuz, *X-ray absorption spectroscopy study of energy transport in foil targets heated by petawatt laser pulses*, Photonics Research **6**, 4 (2018).

4. J. J. Jarrett, M. King, N. Neumann, L. Döhl, C. D. Baird, T. Ebert, M. Hesse, A. Tebartz, D. R. Rusby, N. C. Woolsey, D. Neely, M. Roth and P. McKenna, *Reflection of intense laser light from microstructured targets as a potential diagnostic of laser focus and plasma temperature*, High Power Laser Science and Engineering **7**, e2 (2019).

5. T. G. White, M. T. Oliver, P. Mabey, M. Kühn-Kauffeldt, A. Bott, L. Dóhl, A. Bell, R. Bingham, R. Clarke, J. Foster, G. Giancinti, P. Graham, R. Heathcote, M. Koenig, Y.

Kuramitsu, D. Q. Lamb, J. Meinecke, T. Michel. F. Miniati, M. Notley, B. Reville, D. Ryu, S. Sarkar, Y. Sakawa, M. Selwood, J., Squire, R. Scott, P. Tzeferacos, N. Woolsey, A. A. Schekochihin and G. Gregori, *Supersonic plasma turbulence in the laboratory*, Nature Communications 10, 1758 (2019).

6. R. Kumar, Y. Sakawa, L. N. K. Döhl, N. Woolsey and A. Morace, *Enhancement of collisionless shock ion acceleration by electrostatic ion two-stream instability in the upstream plasma*, Physical Review Accelerator and Beam **22**, 043401 (2019).

7. M. V. Sedov, A. Ya. Faenov, A. A. Andreev, I. Yu. Skobelev, S. N. Ryazantsev, T. A. Pikuz, P. Durey, L. Doehl, D. Farley, C. D. Baird, K. L. Lancaster, C. D. Murphy, N. Booth, C. Spindloe, K. Yu. Platonov, P. McKenna, R. Kodama, N. Woolsey and S. A. Pikuz, *Features of the generation of fast particles from microstructured targets irradiated by high intensity, picosecond laser pulses*, Laser Particle Beam **10**, 1017 (2019).

8. L. N. K. Döhl, R. Alraddadi, N. Booth, Y. Fukuda, Y. Kuramitsu, C. Ridgers and N. Woolsey, *Modeling ion acceleration from ultra-thin graphene using the Vulcan petawatt laser*, SCARF Annual Report 2017-2018, 47-48 (2019).

A.2 Conferences presented this work

The author has presented the work in this thesis at a number of international conferences and internal seminar. These include the following:

1. L. Döhl, C. Ridgers, P. Durey, D. Farley, C. Baird, C. Murphy, K. Lancaster, J. Green, N. Booth, C. Spindloe, S. Pikuz, A. Faenov, S. Ryazantsev, L. Gizzi, P. Köster, L. Labate, N. Neumann and N. C. Woolsey, *In-situ hollow ion spectroscopy of strong X-ray fields from ultra-intense laser-solid interactions*, poster, Joint 2017 ICTP-IAEA School on Atomic Processes in Plasmas, ICTP, Miramare, Trieste, Italy, 27 February - 3 March 2017.

2. L. Döhl, C. Ridgers, and N. C. Woolsey, *Interpreting radiation processes in ultra-intense laser-solid interactions*, internal seminar, Institute for Laser Engineering, Osaka University, Osaka, Japan, 26 April 2017.

3. L. Döhl, N. Neumann, C. Baird, T. Ebert, R. Heathcote, M. Hesse, J. Jarrett, P. McKenna, D. Neely, D. Rusby, C. Spindloe, A. Tebartz, M. Roth and N. Woolsey, *X-ray and electron spectroscopic observations of micro-structured Si targets during high-contrast ultra-intense laser-solid interactions*, talk, 10th International Conference on Inertial Fusion Sciences and Applications, St. Malo, France, 11-15 September 2017.

4. L. Döhl, N. Neumann, C. Baird, T. Ebert, R. Heathcote, M. Hesse, J. Jarrett, P. McKenna, D. Neely, D. Rusby, C. Spindloe, A. Tebartz, M. Roth and N. Woolsey, *Enhancing X-ray and electron sources solid micro-structured Si targets in high-contrast ultra-intense laser experiments*, internal seminar, Department of Engineering, Osaka University, Osaka, Japan, 15 November 2017.

5. L. Döhl, N. Booth, Y. Fukuda, Y. Kuramitsu, C. Ridgers W.-Y. Woon and N. Woolsey, *Studying atom-thick graphene film for laser-driven ion acceleration*, poster, Institute of Physics Computational Plasma Physics Conference, York, UK, 20-22 November 2017.

6. L. Döhl, N. Neumann, C. Baird, T. Ebert, R. Heathcote, M. Hesse, A. Hughes, J. Jarrett, P. McKenna, D. Neely, D. Rusby, C. Spindloe, A. Tebartz, M. Roth and N. Woolsey, *X-ray and electron spectroscopy of ultra-intense laser interaction with micro-structured Si targets*, poster, Christmas High Power Laser Science Community Meeting, Abingdon, UK, 19-21 December 2017.

7. L. Döhl, N. Neumann, C. Baird, T. Ebert, R. Heathcote, M. Hesse, A. Hughes, J. Jarrett, P. McKenna, D. Neely, D. Rusby, C. Spindloe, A. Tebartz, M. Roth and N. Woolsey, *X-ray and electron spectroscopy of ultra-intense laser interaction with micro-structured Si targets*, poster, NIF/JLF User Meeting, 5-7 February 2018.

8. L. N. K. Döhl, R. Alraddadi, C. D. Baird, N. Booth, D. Farley, Y. Fukuda, R. S.-M. He, Heathcote, M. Kanasaki, Y. Kuramitsu, K. Lancaster, C. D. Murphy, C. Ridgers. W. Trickey, W.-Y. Woon and N. Woolsey, *Laser-driven carbon ion acceleration using ultra-thin graphene*, poster and talk, Christmas High Power Laser Science Community Meeting, Abingdon, UK, 18-20 December 2018.

9. L. Döhl, R. Alraddadi, C. D. Baird, N. Booth, D. Farley, Y. Fukuda, S.-M. He, R. Heathcote, M. Kanasaki, Y. Kuramitsu, K. Lancaster, C. D. Murphy, C. P. Ridgers, C.-Y. Su, W. Trickey, W.-Y. Woon and N. Woolsey, *Laser-driven ion acceleration using sub-picosecond intense laser pulses and nano-thin solid targets*, poster, 11th International Conference on Inertial Fusion Sciences and Applications, Osaka, France, 23-27 September 2019.

10. L. Döhl, N. Booth, R. Clarke, T. Ebert, Y. Fukuda, M. Hesse, J. Jarrett, M. Kanasaki, K. Sakai, Y. Kuramitsu, Y.-Z. Liao, P. McKenna, A. Morace, D. Neely, N. Neumann, M. Ota, S. Pikuz, M. Roth, D. Rusby, Y. Sakawa, C. Spindloe, T. Hihara, T. Minami, A. Tebartz, W.-Y. Woon and N. Woolsey, *Double plasma mirror systems for high-contrast laser-solid interactions*, talk, 11th International Conference on Inertial Fusion Sciences and Applications, Osaka, France, 23-27 September 2019.

List of References

[1] T Bonnet, M Comet, D Denis-Petit, F Gobet, F Hannachi, M Tarisien, M Versteegen, and M M Aleonard. Response functions of fuji imaging plates to monoenergetic protons in the energy range 0.6–3.2 mev. *Review of Scientific Instruments*, 84(1):013508, 2013.

[2] C T Chantler, K Olsen, R A Dragoset, J Chang, A R Kishore, S A Kotochigova, and D S Zucker. X-ray form factor, attenuation, and scattering tables, 2001. URL https://www.nist.gov/pml/x-ray-form-factor-attenuation-and-scattering-tables.

[3] Garchromic hd-v2 dosimetry film, 2019. URL http://www.gafchromic.com/documents/gafchromic-hdv2.pdf.

[4] Garchromic ebt2 dosimetry film, 2019. URL https://www.gotopeo.com/images/stories/pdf/rt/isp_ebt2productspec_09_peo.pdf.

[5] V Bagnoud and F Wagner. Ultrahigh temporal contrast performance of the phelix petawatt facility. *High Power Laser Science and Engineering*, 4, 2016.

[6] A Morace, S Kojima, Y Arikawa, S Fujioka, A Yogo, S Tosaki, S Sakata, Y Abe, SH Lee, K Matsuo, A Sagisaka, K Kondo, A S Pirozhkov, T Norimatsu, T Jitsuno, N Miyanaga, H Shiraga, M Nakai, H Nishimura, and H Azechi. Plasma mirror implementation on lfex laser for ion and fast electron fast ignition. *Nuclear Fusion*, 57(12):126018, 2017.

[7] Tina Ebert, Nico W Neumann, Torsten Abel, Gabriel Schaumann, and Markus Roth. Laser-induced microstructures on silicon for laser-driven acceleration experiments. *High Power Laser Science and Engineering*, 5, 2017.

[8] N-bk7 high precision windows, 2019. URL https://www.thorlabs.com/newgrouppage9.cfm?objectgroup_id=1117.

[9] Burton L Henke, Eric M Gullikson, and John C Davis. X-ray interactions: photoabsorption, scattering, transmission, and reflection at e= 50-30,000 ev, z= 1-92. *Atomic data and nuclear data tables*, 54(2): 181–342, 1993.

[10] Michael J Haugh, Joshua Lee, Edward Romano, and Marilyn Schneider. Calibrating image plate sensitivity in the 700 to 5000 ev spectral energy range. In *Target Diagnostics Physics and Engineering for Inertial Confinement Fusion II*, volume 8850, page 885007. International Society for Optics and Photonics, 2013.

[11] Nur Khasanah, Nima Bolouki, Tzu-Yao Huang, Yi-Zhe Hong, Wen-Liang Chung, Wei-Yen Woon, Ching-Yuan Su, and Yasuhiro Kuramitsu. Large-area suspended graphene as a laser target to produce an energetic ion beam. *High Power Laser Science and Engineering*, 5, 2017.

[12] James F Ziegler, Matthias D Ziegler, and Jochen P Biersack. Srim–the stopping and range of ions in matter (2010). *Nuclear Instruments and Methods in Physics Research Section B: Beam Interactions with Materials and Atoms*, 268(11-12):1818–1823, 2010.

[13] Donna Strickland and Gerard Mourou. Compression of amplified chirped optical pulses. *Optics communications*, 55(6):447–449, 1985.

[14] F N Beg, A R Bell, A E Dangor, C N Danson, A P Fews, M E Glinsky, B A Hammel, P Lee, P A Norreys, and Ma Tatarakis. A study of picosecond laser–solid interactions up to 1019 w cm- 2. *Physics of plasmas*, 4(2):447–457, 1997.

[15] J Colgan, J Abdallah Jr, A Ya Faenov, S A Pikuz, E Wagenaars, N Booth, O Culfa, R J Dance, R G Evans, R J Gray, J Hoarty, T Kaempfer, K L Lancaster, P McKenna, A L Rossall, I Yu Skobelev, K S Schulze, I Uschmann, A G Zhidkov, and N C Woolsey. Exotic dense-matter states pumped by a relativistic laser plasma in the radiation-dominated regime. *Physical review letters*, 110(12):125001, 2013.

[16] S C Wilks, W L Kruer, M Tabak, and A B Langdon. Absorption of ultra-intense laser pulses. *Physical review letters*, 69(9):1383, 1992.

[17] R A Snavely, M H Key, S P Hatchett, T E Cowan, M Roth, T W Phillips, M A Stoyer, E A Henry, T C Sangster, M S Singh, S C Wilks, A MacKinnon, A Offenberger, D M Pennington, K Yasuike, A B Langdon, B F Lasinski, J Johnson, M D Perry, and E M Campbell. Intense high-energy proton beams from petawatt-laser irradiation of solids. *Physical review letters*, 85(14):2945, 2000.

[18] A Higginson, R J Gray, M King, R J Dance, S D R Williamson, N M H Butler, R Wilson, R Capdessus, C Armstrong, J S Green, S J Hawkes, P Martin, W Q Wei, S R Mirfayzi, X H Yuan, S Kar, M Borghesi, R J Clarke, D Neely, and P McKenna. Near-100 mev protons via a laser-driven transparency-enhanced hybrid acceleration scheme. *Nature communications*, 9(1):724, 2018.

[19] U Feldman, G A Doschek, and R W Kreplin. High-resolution x-ray spectra of the 1979 march 25 solar flare. *The Astrophysical Journal*, 238:365–374, 1980.

[20] Peter Beiersdorfer. Laboratory x-ray astrophysics. *Annual Review of Astronomy and Astrophysics*, 41 (1):343–390, 2003.

[21] H Koyama, Kand Tsunemi, T Dotani, M W Bautz, K Hayashida, T G Tsuru, H Matsumoto, Y Ogawara, G R Ricker, J Doty, S E Kissel, R Foster, H Nakajima, H Yamaguchi, H Mori, M Sakano, K Hamaguchi, M Nishiuchi, E Miyata, K Torii, M Namiki, S Katsuda, D Matsuura, T Miyauchi, N Anabuki, N Tawa, M Ozaki, H Murakami, Y Maeda, Y Ichikawa, G Y Prigozhin, E A Boughan, B LaMarr, E D Miller, B E Burke, J A Gregory, A Pillsbury, A Bamba, J S Hiraga, A Senda, H Katayama, S Kitamoto, M Tsujimoto, T Kohmura, Y Tsuboi, and H Awaki. X-ray imaging spectrometer (xis) on board suzaku. *Publications of the Astronomical Society of Japan*, 59(sp1):S23–S33, 2007.

[22] A Mančić, J Fuchs, P Antici, S A Gaillard, and P Audebert. Absolute calibration of photostimulable image plate detectors used as (0.5–20 mev) high-energy proton detectors. *Review of Scientific Instruments*, 79(7):073301, 2008.

[23] Dongxing Yang, Aruna Velamakanni, Gülay Bozoklu, Sungjin Park, Meryl Stoller, Richard D Piner, Sasha Stankovich, Inhwa Jung, Daniel A Field, Carl A Ventrice Jr, and Rodney S Ruoff. Chemical analysis of graphene oxide films after heat and chemical treatments by x-ray photoelectron and micro-raman spectroscopy. *Carbon*, 47(1):145–152, 2009.

[24] S V Bulanov and V S Khoroshkov. Feasibility of using laser ion accelerators in proton therapy. *Plasma Physics Reports*, 28(5):453–456, 2002.

[25] Ugo Amaldi and Gerhard Kraft. Radiotherapy with beams of carbon ions. *Reports on progress in physics*, 68(8):1861, 2005.

[26] Wayne D Newhauser and Rui Zhang. The physics of proton therapy. *Physics in Medicine & Biology*, 60(8):R155, 2015.

[27] M Roth, T E Cowan, M H Key, S P Hatchett, C Brown, W Fountain, J Johnson, D M Pennington, R A Snavely, S C Wilks, K Yasuike, H Ruhl, F Pegoraro, V Bulanov, S, E M Campbell, M D Perry, and H Powell. Fast ignition by intense laser-accelerated proton beams. *Physical Review Letters*, 86(3): 436, 2001.

[28] Juan C Fernández, J J Honrubia, Brian J Albright, Kirk A Flippo, D Cort Gautier, Björn M Hegelich, Mark J Schmitt, M Temporal, and Lin Yin. Progress and prospects of ion-driven fast ignition. *Nuclear fusion*, 49(6):065004, 2009.

[29] Andrea Macchi, Marco Borghesi, and Matteo Passoni. Ion acceleration by superintense laser-plasma interaction. *Reviews of Modern Physics*, 85(2):751, 2013.

[30] Paul Gibbon. *Short pulse laser interactions with matter*. World Scientific Publishing Company Singapore, 2004.

[31] D Salzmann, Ch Reich, I Uschmann, E Förster, and Paul Gibbon. Theory of k α generation by femtosecond laser-produced hot electrons in thin foils. *Physical Review E*, 65(3):036402, 2002.

[32] I Yu Skobelev, S N Ryazantsev, D D Arich, P S Bratchenko, A Ya Faenov, T A Pikuz, P Durey, L Doehl, D Farley, C D Baird, K L Lancaster, C D Murphy, N Booth, C Spindloe, P McKenna, S B Hansen, J Colgan, R Kodama, and N Woolsey. X-ray absorption spectroscopy study of energy transport in foil targets heated by petawatt laser pulses. *Photonics Research*, 6(4):234–237, 2018.

[33] James H Scofield. Radiative decay rates of vacancies in the k and l shells. *Physical Review*, 179(1):9, 1969.

[34] James H Scofield. Relativistic hartree-slater values for k and l x-ray emission rates. *Atom. Data Nucl. Data Tabl.*, 14:121–137, 1974.

[35] Albert C Thompson, David Attwood, Eric Gullikson, Malcolm Howells, Kwang-Je Kim, Janos Kirz, Jeffrey Kortright, Ingolf Lindau, Yanwei Liu, Arthur Robinson, James Scofield, James Underwood, Gwyn Williams, and Herman Winick. *X-ray data booklet*, volume 8. Lawrence Berkeley National Laboratory, University of California Berkeley, CA, 2001.

[36] Ch Reich, P Gibbon, I Uschmann, and E Förster. Yield optimization and time structure of femtosecond laser plasma k α sources. *Physical Review Letters*, 84(21):4846, 2000.

[37] S J Gitomer, R D Jones, F Begay, A W Ehler, J F Kephart, and R Kristal. Fast ions and hot electrons in the laser–plasma interaction. *The Physics of fluids*, 29(8):2679–2688, 1986.

[38] S C Wilks, A B Langdon, T E Cowan, M Roth, M Singh, S Hatchett, M H Key, D Pennington, A MacKinnon, and R A Snavely. Energetic proton generation in ultra-intense laser–solid interactions. *Physics of plasmas*, 8(2):542–549, 2001.

[39] Francis F Chen. *Introduction to plasma physics and controlled fusion*, volume 1. Springer, 1984.

[40] Stefano Atzeni and Jürgen Meyer-ter Vehn. *The physics of inertial fusion: beam plasma interaction, hydrodynamics, hot dense matter*, volume 125. OUP Oxford, 2004.

[41] M Tabak, D S Clark, S P Hatchett, M H Key, B F Lasinski, R A Snavely, S C Wilks, R P J Town, R Stephens, E M Campbell, R Kodama, K Mima, K A Tanaka, S Atzeni, and R Freeman. Review of progress in fast ignition. *Physics of Plasmas*, 12(5):057305, 2005.

[42] Osama Mohamad, Brock Sishc, Janapriya Saha, Arnold Pompos, Asal Rahimi, Michael Story, Anthony Davis, and D W Kim. Carbon ion radiotherapy: a review of clinical experiences and preclinical research, with an emphasis on dna damage/repair. *Cancers*, 9(6):66, 2017.

[43] Tatsuaki Kanai, Masahiro Endo, Shinichi Minohara, Nobuyuki Miyahara, Hiroko Koyama-Ito, Hiromi Tomura, Naruhiro Matsufuji, Yasuyuki Futami, Akifumi Fukumura, Takeshi Hiraoka, Yoshiya Fukusawa, Koichi Ando, Masao Suzuki, Fuminori Soga, and Kiyomitsu Kawachi. Biophysical characteristics of himac clinical irradiation system for heavy-ion radiation therapy. *International Journal of Radiation Oncology Biology Physics*, 44(1):201–210, 1999.

[44] Joseph D Huba. Nrl plasma formulary. Technical report, NAVAL RESEARCH LAB WASHINGTON DC PLASMA PHYSICS DIV, 2006.

[45] Shalom Eliezer. *The interaction of high-power lasers with plasmas*. CRC press, 2002.

[46] Lev Davidovich Landau and Evgenii Mikhailovich Lifshitz. The classical theory of fields. 1971.

[47] G Malka and J L Miquel. Experimental confirmation of ponderomotive-force electrons produced by an ultrarelativistic laser pulse on a solid target. *Physical review letters*, 77(1):75, 1996.

[48] W L Kruer and K Estabrook. J× b heating by very intense laser light. *The Physics of fluids*, 28(1): 430–432, 1985.

[49] R A B Alraddadi. *Modelling fast electron transport in solids and with application to Rayleigh-Taylor instability studies*. PhD thesis, University of York, 2015.

[50] A P L Robinson, D J Strozzi, J R Davies, L Gremillet, J J Honrubia, T Johzaki, R J Kingham, M Sherlock, and A A Solodov. Theory of fast electron transport for fast ignition. *Nuclear Fusion*, 54 (5):054003, 2014.

[51] R Paul Drake. High-energy-density physics. *Phys. Today*, 63(6):28, 2010.

[52] A. Kramida, Yu. Ralchenko, J. Reader, and and NIST ASD Team. NIST Atomic Spectra Database (ver. 5.6.1), [Online]. Available: `https://physics.nist.gov/asd` [2019, May 9]. National Institute of Standards and Technology, Gaithersburg, MD., 2018.

[53] Günter H Zschornack. *Handbook of X-ray Data*. Springer Science & Business Media, 2007.

[54] Jonathan Tennyson. *Astronomical spectroscopy: an introduction to the atomic and molecular physics of astronomical spectra*. World Scientific, 2010.

[55] S A Pikuz, A Ya Faenov, J Colgan, R J Dance, J Abdallah, E Wagenaars, N Booth, O Culfa, R G Evans, R J Gray, T Kaempfer, K L Lancaster, P McKenna, A L Rossall, I Yu Skobelev, K S Schulze, I Uschmann, A G Zhidkov, and N C Woolsey. Measurement and simulations of hollow atom x-ray spectra of solid-density relativistic plasma created by high-contrast pw optical laser pulses. *High energy density physics*, 9(3):560–567, 2013.

[56] R G Evans, E L Clark, R T Eagleton, A M Dunne, R D Edwards, W J Garbett, T J Goldsack, S James, C C Smith, B R Thomas, R Clarke, D J Neely, and S J Rose. Rapid heating of solid density material by a petawatt laser. *Applied Physics Letters*, 86(19):191505, 2005.

[57] Robert D Cowan. *The theory of atomic structure and spectra*. Number 3. Univ of California Press, 1981.

[58] Hans-Joachim Kunze. *Introduction to plasma spectroscopy*, volume 56. Springer Science & Business Media, 2009.

[59] J J MacFarlane, I E Golovkin, and P R Woodruff. Modeling of inner–shell(kα, kβ) line emission from cu targets heated by short pulse lasers. *Prism Computational Sciences, Inc., Madison, WI*, 2010.

[60] M Roth, A Blazevic, M Geissel, T Schlegel, TE Cowan, M Allen, J-C Gauthier, P Audebert, J Fuchs, J Meyer-ter Vehn, M Hegelich, S Karsch, and A Pukhov. Energetic ions generated by laser pulses: A detailed study on target properties. *Physical Review Special Topics-Accelerators and Beams*, 5(6): 061301, 2002.

[61] Daniel Jung, L Yin, D C Gautier, H-C Wu, S Letzring, B Dromey, R Shah, S Palaniyappan, T Shimada, R P Johnson, J Schreiber, D Habs, J C Fernández, B M Hegelich, and B J Albright. Laser-driven 1 gev carbon ions from preheated diamond targets in the break-out afterburner regime. *Physics of plasmas*, 20(8):083103, 2013.

[62] G A Becker, S Tietze, S Keppler, J Reislöhner, J H Bin, L Bock, F E Brack, J Hein, M Hellwing, P Hilz, M Hornung, A Kessler, S D Kraft, S Kuschel, H Liebetrau, W Ma, J Polz, H-P Schlenvoigt, F Schorcht, M B Schwab, A Seidel, K Zeil, U Schramm, M Zepf, J Schreiber, S Rykovanov, and M C Kaluza. Ring-like spatial distribution of laser accelerated protons in the ultra-high-contrast tnsa-regime. *Plasma Physics and Controlled Fusion*, 60(5):055010, 2018.

[63] Lin Yin, B J Albright, B M Hegelich, and J C Fernández. Gev laser ion acceleration from ultrathin targets: The laser break-out afterburner. *Laser and Particle Beams*, 24(2):291–298, 2006.

[64] Ryutaro Matsui, Yuji Fukuda, and Yasuaki Kishimoto. Quasimonoenergetic proton bunch acceleration driven by hemispherically converging collisionless shock in a hydrogen cluster coupled with relativistically induced transparency. *Physical Review Letters*, 122(1):014804, 2019.

[65] M Murakami and K Mima. Efficient generation of quasimonoenergetic ions by coulomb explosions of optimized nanostructured clusters. *Physics of Plasmas*, 16(10):103108, 2009.

[66] J Zweiback, R A Smith, T E Cowan, G Hays, K B Wharton, V P Yanovsky, and T Ditmire. Nuclear fusion driven by coulomb explosions of large deuterium clusters. *Physical review letters*, 84(12):2634, 2000.

[67] R P Feynman. *Feynman lectures on physics. Volume 2: Mainly electromagnetism and matter*. Addison-Wesley, 1963.

[68] D Jung, L Yin, B J Albright, D C Gautier, S Letzring, B Dromey, M Yeung, R Hörlein, R Shah, S Palaniyappan, K Allinger, J Schreiber, K J Bowers, H-C Wu, J C Fernandez, D Habs, and B M Hegelich. Efficient carbon ion beam generation from laser-driven volume acceleration. *New Journal of Physics*, 15(2):023007, 2013.

[69] B J Albright, L Yin, Kevin J Bowers, B M Hegelich, K A Flippo, T J T Kwan, and J C Fernandez. Relativistic buneman instability in the laser breakout afterburner. *Physics of Plasmas*, 14(9):094502, 2007.

[70] David J Stark, Lin Yin, Brian J Albright, William Nystrom, and Robert Bird. A detailed examination of laser-ion acceleration mechanisms in the relativistic transparency regime using tracers. *Physics of Plasmas*, 25(4):043114, 2018.

[71] David James Stark, Lin Yin, and Brian James Albright. Harnessing the relativistic buneman instability for laser-ion acceleration in the transparency regime. *Physics of Plasmas*, 25(6):062107, 2018.

[72] E Martinolli, M Koenig, J M Boudenne, E Perelli, D Batani, and T A Hall. Conical crystal spectrograph for high brightness x-ray kα spectroscopy in subpicosecond laser–solid interaction. *Review of scientific instruments*, 75(6):2024–2028, 2004.

[73] Charles Kittel, Paul McEuen, and Paul McEuen. *Introduction to solid state physics*, volume 8. Wiley New York, 1976.

[74] L N Koppel and J D Eckels. High resolution x-ray crystal spectrographs. Technical report, California Univ., 1977.

[75] Yasuo Iwabuchi, Nobufumi Mori, Kenji Takahashi, Terumi Matsuda, and Shigeo Shionoya. Mechanism of photostimulated luminescence process in bafbr: Eu2+ phosphors. *Japanese journal of applied physics*, 33(1R):178, 1994.

[76] Image format description bas2500 system, 2003. URL beamline.harima.riken.jp/bl45xu/web_old/Info/BAS2500imgSpec.pdf.

[77] A L Meadowcroft, C D Bentley, and E N Stott. Evaluation of the sensitivity and fading characteristics of an image plate system for x-ray diagnostics. *Review of Scientific Instruments*, 79(11):113102, 2008.

[78] P Bradford, N C Woolsey, G G Scott, G Liao, H Liu, Y Zhang, B Zhu, C Armstrong, S Astbury, C Brenner, P Brummitt, F Consoli, I East, R Gray, D Haddock, P Huggard, P J R Jones, E Montgomery, I Musgrave, P Oliveira, D R Rusby, C Spindloe, B Summers, E Zemaityte, Z Zhang, Y Li, P McKenna, and D Neely. Emp control and characterization on high-power laser systems. *High Power Laser Science and Engineering*, 6, 2018.

[79] F Nürnberg, M Schollmeier, E Brambrink, A Blažević, D C Carroll, K Flippo, D C Gautier, M Geissel, K Harres, B M Hegelich, O Lundh, K Markey, P McKenna, D Neely, J Schreiber, and Roth M. Radiochromic film imaging spectroscopy of laser-accelerated proton beams. *Review of scientific instruments*, 80(3):033301, 2009.

[80] Marius Schollmeier, Matthias Geissel, Adam B Sefkow, and K A Flippo. Improved spectral data unfolding for radiochromic film imaging spectroscopy of laser-accelerated proton beams. *Review of Scientific Instruments*, 85(4):043305, 2014.

[81] P L Poole, L Obst, G E Cochran, J Metzkes, H P Schlenvoigt, I Prencipe, T Kluge, T Cowan, U Schramm, D W Schumacher, and K Zeil. Laser-driven ion acceleration via target normal sheath acceleration in the relativistic transparency regime. *New Journal of Physics*, 20(1):013019, 2018.

[82] M V Sedov, A Ya Faenov, A A Andreev, I Yu Skobelev, S N Ryazantsev, T A Pikuz, P Durey, L Doehl, D Farley, C D Baird, K L Lancaster, C D Murphy, N Booth, C Spindloe, K Yu Platonov, P McKenna,

R Kodama, N Woolsey, and S Pikuz. Features of the generation of fast particles from microstructured targets irradiated by high intensity, picosecond laser pulses. *Laser and Particle Beams*, pages 1–8, 2019.

[83] N L Kugland, D D Ryutov, P Y Chang, R P Drake, G Fiksel, D H Froula, S H Glenzer, G Gregori, M Grosskopf, M Koenig, Y Kuramitsu, C Kuranz, M C Levy, E Liang, J Meinecke, F Miniati, T Morita, A Pelka, C Plechaty, R Presura, A Ravasio, B A Remington, B Reville, J S Ross, Y Sakawa, A Spitkovsky, H Takabe, and H-S Park. Self-organized electromagnetic field structures in laser-produced counter-streaming plasmas. *Nature Physics*, 8(11):809, 2012.

[84] Will Fox, G Fiksel, Amitava Bhattacharjee, P-Y Chang, K Germaschewski, S X Hu, and P M Nilson. Filamentation instability of counterstreaming laser-driven plasmas. *Physical review letters*, 111(22): 225002, 2013.

[85] M Kanasaki, S Jinno, H Sakaki, K Kondo, K Oda, T Yamauchi, and Y Fukuda. The precise energy spectra measurement of laser-accelerated mev/n-class high-z ions and protons using cr-39 detectors. *Plasma Physics and Controlled Fusion*, 58(3):034013, 2016.

[86] Barry Van Gemert. The commercialization of plastic photochromic lenses: A tribute to john crano. *Molecular Crystals and Liquid Crystals Science and Technology. Section A. Molecular Crystals and Liquid Crystals*, 344(1):57–62, 2000.

[87] Masato Kanasaki, Atsuto Hattori, Keiji Oda, Tomoya Yamauchi, Yuji Fukuda, Hironao Sakaki, Mamiko Nishiuchi, Kiminori Kondo, Satoshi Kurashima, and Tomihiro Kamiya. Applications of cr-39 solid state nuclear track detector to ion beam diagnosis. *Purazuma, Kaku Yugo Gakkai-Shi*, 88(5):261–274, 2012.

[88] B Dörschel, D Hermsdorf, U Reichelt, S Starke, and Y Wang. 3d computation of the shape of etched tracks in cr-39 for oblique particle incidence and comparison with experimental results. *Radiation measurements*, 37(6):563–571, 2003.

[89] D Hermsdorf and M Hunger. Determination of track etch rates from wall profiles of particle tracks etched in direct and reversed direction in padc cr-39 ssntds. *Radiation Measurements*, 44(9-10):766–774, 2009.

[90] P C Kalsi, A Ramaswami, and V K Manchanda. Solid state nuclear track detectors and their applications. *Radiochemistry Division*, 2005.

[91] N Yasuda, K Namiki, Y Honma, Y Umeshima, Y Marumo, H Ishii, and E R Benton. Development of a high speed imaging microscope and new software for nuclear track detector analysis. *Radiation Measurements*, 40(2-6):311–315, 2005.

[92] Colin Danson, David Hillier, Nicholas Hopps, and David Neely. Petawatt class lasers worldwide. *High Power Laser Science and Engineering*, 3, 2015.

[93] C N Danson, P A Brummitt, R J Clarke, J L Collier, B Fell, A J Frackiewicz, S Hancock, S Hawkes, C Hernandez-Gomez, P Holligan, M H R Hutchinson, A Kidd, W J Lester, I O Musgrave, D Neely, D R Neville, P A Norreys, D A Pepler, C J Reason, W Shaikh, T B Winstone, R W W Wyatt, and B E Wyborn. Vulcan petawatt—an ultra-high-intensity interaction facility. *Nuclear Fusion*, 44(12): S239, 2004.

[94] Alexander S Pirozhkov, Yuji Fukuda, Mamiko Nishiuchi, Hiromitsu Kiriyama, Akito Sagisaka, Koichi Ogura, Michiaki Mori, Maki Kishimoto, Hironao Sakaki, Nicholas P Dover, Kotaro Kondo, Nobuhiko Nakanii, Kai Huang, Masato Kanasaki, Kiminori Kondo, and Masaki Kando. Approaching the diffraction-limited, bandwidth-limited petawatt. *Optics express*, 25(17):20486–20501, 2017.

[95] N Miyanaga, H Azechi, K A Tanaka, T Kanabe, T Jitsuno, J Kawanaka, Y Fujimoto, R Kodama, H Shiraga, K Knodo, K Tsubakimoto, H Habara, J Lu, G Xu, N Morio, S Matsuo, E Miyaji, Y Kawakami, Y Izawa, and K Mima. 10-kj pw laser for the firex-i program. In *Journal de Physique IV (Proceedings)*, volume 133, pages 81–87. EDP sciences, 2006.

[96] S Gales, K A Tanaka, D L Balabanski, F Negoita, D Stutman, O Tesileanu, C A Ur, D Ursescu, I Andrei, S Ataman, M O Cernaianu, L D'Alessi, I Dancus, B Diaconescu, N Djourelov, D Filipescu, P Ghenuche, D G Ghita, C Matei, K Seto, M Zeng, and N V Zamfir. The extreme light infrastructure–nuclear physics (eli-np) facility: New horizons in physics with 10 pw ultra-intense lasers and 20 mev brilliant gamma beams. *Reports on Progress in Physics*, 81(9):094301, 2018.

[97] I N Ross, P Matousek, M Towrie, A J Langley, and J L Collier. The prospects for ultrashort pulse duration and ultrahigh intensity using optical parametric chirped pulse amplifiers. *Optics Communications*, 144(1-3):125–133, 1997.

[98] Donna Strickland. Nobel lecture: Generating high-intensity ultrashort optical pulses. *Reviews of Modern Physics*, 91(3):030502, 2019.

[99] Gerard Mourou. Nobel lecture: Extreme light physics and application. *Reviews of Modern Physics*, 91 (3):030501, 2019.

[100] P P Pronko, P A VanRompay, C Horvath, F Loesel, T Juhasz, X Liu, and G Mourou. Avalanche ionization and dielectric breakdown in silicon with ultrafast laser pulses. *Physical Review B*, 58(5): 2387, 1998.

[101] Chris Densham. High power laser amplifier research and development. URL https://www.technologysi.stfc.ac.uk/Pages/ASD_HPT_High_Power_Laser_Amplifier.aspx.

[102] Jean-Claude Diels and Wolfgang Rudolph. *Ultrashort laser pulse phenomena*. Elsevier, 2006.

[103] Yoneyoshi Kitagawa, Hisanori Fujita, Ryosuke Kodama, Hidetsugu Yoshida, Satoshi Matsuo, Takahisa Jitsuno, Tetsuji Kawasaki, Hisao Kitamura, Tadashi Kanabe, Shuji Sakabe, Keisuke Shigemori, Noriaki Miyanaga, and Yasukazu Izawa. Prepulse-free petawatt laser for a fast ignitor. *IEEE Journal of Quantum Electronics*, 40(3):281–293, 2004.

[104] G Doumy, F Quéré, O Gobert, M Perdrix, Ph Martin, P Audebert, J C Gauthier, J-P Geindre, and T Wittmann. Complete characterization of a plasma mirror for the production of high-contrast ultraintense laser pulses. *Physical Review E*, 69(2):026402, 2004.

[105] T B Winstone, C Hernandez-Gomez, S Hancock, and I O Musgrave. A dedicated beamline for the petawatt facility. *CLF Annual Report*, 5, 2004.

[106] B H Shaw, S Steinke, J Van Tilborg, and W P Leemans. Reflectance characterization of tape-based plasma mirrors. *Physics of Plasmas*, 23(6):063118, 2016.

[107] PL Poole, A Krygier, GE Cochran, PS Foster, GG Scott, LA Wilson, J Bailey, N Bourgeois, C Hernandez-Gomez, D Neely, P P Rajeev, R R Freeman, and D W Schumacher. Experiment and simulation of novel liquid crystal plasma mirrors for high contrast, intense laser pulses. *Scientific reports*, 6:32041, 2016.

[108] Thomas Lippert and J Thomas Dickinson. Chemical and spectroscopic aspects of polymer ablation: special features and novel directions. *Chemical Reviews*, 103(2):453–486, 2003.

[109] Cédric Thaury, F Quéré, J-P Geindre, A Levy, T Ceccotti, P Monot, M Bougeard, F Réau, P d'Oliveira, P Audebert, R Marjoribanks, and Ph Martin. Plasma mirrors for ultrahigh-intensity optics. *Nature Physics*, 3(6):424, 2007.

[110] B Dromey, S Kar, C Bellei, D C Carroll, R J Clarke, J S Green, S Kneip, K Markey, S R Nagel, P T Simpson, L Willingale, P McKenna, D Neely, Z Najmudin, K Krushelnick, P A Norreys, and M Zepf. Bright multi-kev harmonic generation from relativistically oscillating plasma surfaces. *Physical Review Letters*, 99(8):085001, 2007.

[111] T Ceccotti, A Lévy, H Popescu, F Réau, P d'Oliveira, P Monot, JP Geindre, E Lefebvre, and Ph Martin. Proton acceleration with high-intensity ultrahigh-contrast laser pulses. *Physical review letters*, 99(18): 185002, 2007.

[112] J Fuchs, P Antici, E D'09Humières, E Lefebvre, M Borghesi, E Brambrink, C A Cecchetti, M Kaluza, V Malka, M Manclossi, S Meyroneinc, P Mora, J Schreiber, T Toncian, H Pépin, and P Audebert. Laser-driven proton scaling laws and new paths towards energy increase. *Nature physics*, 2(1):48, 2006.

[113] E Oks, E Dalimier, A Ya Faenov, P Angelo, S A Pikuz, T A Pikuz, I Yu Skobelev, S N Ryazanzev, P Durey, L Doehl, D Farley, C D Baird, K L Lancaster, C D Murphy, N Booth, C Spindloe, P McKenna, N Neumann, M Roth, R Kodama, and N Woolsey. In-depth study of intra-stark spectroscopy in the x-ray range in relativistic laser–plasma interactions. *Journal of Physics B: Atomic, Molecular and Optical Physics*, 50(24):245006, 2017.

[114] R Wilson, M King, RJ Gray, DC Carroll, RJ Dance, C Armstrong, SJ Hawkes, RJ Clarke, DJ Robertson, D Neely, et al. Ellipsoidal plasma mirror focusing of high power laser pulses to ultra-high intensities. *Physics of Plasmas*, 23(3):033106, 2016.

[115] R J Gray, D C Carroll, X H Yuan, C M Brenner, M Burza, M Coury, K L Lancaster, X X Lin, Y T Li, D Neely, M N Quinn, O Tresca, C G Wahlström, and P McKenna. Laser pulse propagation and enhanced energy coupling to fast electrons in dense plasma gradients. *New Journal of Physics*, 16(11): 113075, 2014.

[116] J J MacFarlane, I E Golovkin, and P R Woodruff. Helios-cr–a 1-d radiation-magnetohydrodynamics code with inline atomic kinetics modeling. *Journal of Quantitative Spectroscopy and Radiative Transfer*, 99(1-3):381–397, 2006.

[117] Y Arikawa, S Kojima, A Morace, S Sakata, T Gawa, Y Taguchi, Y Abe, Z Zhang, X Vaisseau, S H Lee, K Matsuo, S Tosaki, M Hata, K Kawabata, Y Kawakami, M Ishida, K Tsuji, S Matsuo, N Morio, T Kawasaki, S Tokita, Y Nakata, T Jitsuno, N Miyanaga, J Kawanaka, H Nagatomo, A Yogo, M Nakai, H Nishimura, H Shiraga, S Fujioka, FIREX Group, LFEX Group, H Azechi, A Sunahara, T Johzaki, T Ozaki, H Sakagami, A Sagisaka, K Ogura, A S Pirozhkov, M Nishikino, K Kondo, S Inoue, K Teramoto, M Hashida, and S Sakabe. Ultrahigh-contrast kilojoule-class petawatt lfex laser using a plasma mirror. *Applied Optics*, 55(25):6850–6857, 2016.

[118] M Hashida, H Mishima, S Tokita, and S Sakabe. Non-thermal ablation of expanded polytetrafluoroethylene with an intense femtosecond-pulse laser. *Optics express*, 17(15):13116–13121, 2009.

[119] D Margarone, O Klimo, I J Kim, J Prokpek, J Limpouch, T M Jeong, T Mocek, J Pšikal, H T Kim, J Proška, I W Choi, S K Lee, J H Sung, T J Yu, and G Korn. Laser-driven proton acceleration enhancement by nanostructured foils. *Physical review letters*, 109(23):234801, 2012.

[120] Michael A Purvis, Vyacheslav N Shlyaptsev, Reed Hollinger, Clayton Bargsten, Alexander Pukhov, Amy Prieto, Yong Wang, Bradley M Luther, Liang Yin, Shoujun Wang, and Jorge J Rocca. Relativistic plasma nanophotonics for ultrahigh energy density physics. *Nature Photonics*, 7(10):796, 2013.

[121] S Jiang, L L Ji, H Audesirk, K M George, J Snyder, A Krygier, P Poole, C Willis, R Daskalova, E Chowdhury, N S Lewis, D W Schumacher, A Pukhov, R R Freeman, and K U Akli. Microengineering laser plasma interactions at relativistic intensities. *Physical review letters*, 116(8):085002, 2016.

[122] J Jarrett, M King, R J Gray, N Neumann, L Döhl, C D Baird, T Ebert, M Hesse, A Tebartz, D R Rusby, N C Woolsey, D Neely, M Roth, and P McKenna. Reflection of intense laser light from microstructured targets as a potential diagnostic of laser focus and plasma temperature. *High Power Laser Science and Engineering*, 7, 2019.

[123] Irene Prencipe, A Sgattoni, David Dellasega, Luca Fedeli, Lorenzo Cialfi, Il Woo Choi, I Jong Kim, Karol Adam Janulewicz, KF Kakolee, Hwang Woon Lee, Jae Hee Sung, Seong Ku Lee, Chang Hee Nam, and M Passoni. Development of foam-based layered targets for laser-driven ion beam production. *Plasma Physics and Controlled Fusion*, 58(3):034019, 2016.

[124] Xiaogang Liu, Paul R Coxon, Marius Peters, Bram Hoex, Jacqueline M Cole, and Derek J Fray. Black silicon: fabrication methods, properties and solar energy applications. *Energy & Environmental Science*, 7(10):3223–3263, 2014.

[125] Hele Savin, Päivikki Repo, Guillaume Von Gastrow, Pablo Ortega, Eric Calle, Moises Garín, and Ramon Alcubilla. Black silicon solar cells with interdigitated back-contacts achieve 22.1% efficiency. *Nature nanotechnology*, 10(7):624, 2015.

[126] H A Sumeruk, S Kneip, D R Symes, I V Churina, A V Belolipetski, Thomas D Donnelly, and T Ditmire. Control of strong-laser-field coupling to electrons in solid targets with wavelength-scale spheres. *Physical review letters*, 98(4):045001, 2007.

[127] A M Helal. *Explosion dynamics of van der Waals clusters using 38 nm XUV laser pulses*. PhD thesis, 2016.

[128] S Fourmaux and J C Kieffer. Laser-based k α x-ray emission characterization using a high contrast ratio and high-power laser system. *Applied Physics B*, 122(6):162, 2016.

[129] S Fourmaux, S Payeur, S Buffechoux, P Lassonde, C St-Pierre, F Martin, and J C Kieffer. Pedestal cleaning for high laser pulse contrast ratio with a 100 tw class laser system. *Optics express*, 19(9): 8486–8497, 2011.

[130] P McKenna, D C Carroll, O Lundh, F Nürnberg, K Markey, S Bandyopadhyay, D Batani, R G Evans, R Jafer, S Kar, D Neely, D Pepler, M N Quinn, R Redaelli, M Roth, C G Wahlström, X H Yuan, and M Zepf. Effects of front surface plasma expansion on proton acceleration in ultraintense laser irradiation of foil targets. *Laser and Particle Beams*, 26(4):591–596, 2008.

[131] F Y Khattak, E Garcia Saiz, T Dzelzainis, D Riley, and Z Zhai. Scale-length optimizing of short pulse cu k α laser-plasma sources. *Applied physics letters*, 90(8):081502, 2007.

[132] C J Hooker, J L Collier, O Chekhlov, R Clarke, E Divall, K Ertel, B Fell, P Foster, S Hancock, A Langley, D Neely, and J Smith. The astra gemini project–a dual-beam petawatt ti: Sapphire laser system. In *Journal de Physique IV (Proceedings)*, volume 133, pages 673–677. EDP sciences, 2006.

[133] J J MacFarlane, I E Golovkin, P R Woodruff, D R Welch, B V Oliver, T A Mehlhorn, and R B Campbell. Simulation of the ionization dynamics of aluminum irradiated by intense short-pulse lasers. In *Proc. Inertial Fusion and Sciences Applications*, volume 457, 2003.

[134] P Wang. Atbase user?s guide. *Fusion Power Associates Report FPA-93-7 (December 1993)*, 1993.

[135] H Sawada, Y Sentoku, T Yabuuchi, U Zastrau, E Förster, F N Beg, H Chen, A J Kemp, H S McLean, P K Patel, and Y Ping. Monochromatic 2d k α emission images revealing short-pulse laser isochoric heating mechanism. *Physical review letters*, 122(15):155002, 2019.

[136] Taisuke Ohta, Aaron Bostwick, Thomas Seyller, Karsten Horn, and Eli Rotenberg. Controlling the electronic structure of bilayer graphene. *Science*, 313(5789):951–954, 2006.

[137] A H Castro Neto, Francisco Guinea, Nuno M R Peres, Kostya S Novoselov, and Andre K Geim. The electronic properties of graphene. *Reviews of modern physics*, 81(1):109, 2009.

[138] Maithilee Motlag, Prashant Kumar, Kevin Y Hu, Shengyu Jin, Ji Li, Jiayi Shao, Xuan Yi, Yen-Hsiang Lin, Jenna C Walrath, Lei Tong, Xinyu Huang, Rachel S Goldman, Lei Ye, and Gary J Cheng. Asymmetric 3d elastic–plastic strain-modulated electron energy structure in monolayer graphene by laser shocking. *Advanced Materials*, 31(19):1900597, 2019.

[139] L A Falkovsky. Optical properties of graphene. In *Journal of Physics: Conference Series*, volume 129, page 012004. IOP Publishing, 2008.

[140] Yufeng Hao, MS Bharathi, Lei Wang, Yuanyue Liu, Hua Chen, Shu Nie, Xiaohan Wang, Harry Chou, Cheng Tan, Babak Fallahazad, H Ramanarayan, Carl W Magnuson, Emanuel Tutuc, Boris I Yakobson, Kevin F McCarty, Yong-Wei Zhang, Philip Kim, James Hone, Luigi Colombo, and Rodney S Ruoff. The role of surface oxygen in the growth of large single-crystal graphene on copper. *Science*, 342(6159): 720–723, 2013.

[141] D W Rule. Transition radiation diagnostics for intense charged particle beams. *Nuclear Instruments and Methods in Physics Research Section B: Beam Interactions with Materials and Atoms*, 24:901–904, 1987.

[142] T E Cowan, J Fuchs, H Ruhl, A Kemp, P Audebert, M Roth, R Stephens, I Barton, A Blazevic, E Brambrink, J Cobble, J Fernández, J-C Gauthier, M Geissel, M Hegelich, J Kaae, S Karsch, G P Le Sage, S Letzring, M Manclossi, S Meyroneinc, A Newkirk, H Pépin, and N Renard-LeGalloudec. Ultralow emittance, multi-mev proton beams from a laser virtual-cathode plasma accelerator.

[143] Bruno Gonzalez-Izquierdo, Martin King, Ross J Gray, Robbie Wilson, Rachel J Dance, Haydn Powell, David A Maclellan, John McCreadie, Nicholas M H Butler, Steve Hawkes, James S Green, Chris D Murphy, Luca C Stockhausen, David C Carroll, Nicola Booth, Graeme G Scott, Marco Borghesi, David Neely, and Paul McKenna. Towards optical polarization control of laser-driven proton acceleration in foils undergoing relativistic transparency. *Nature communications*, 7:12891, 2016.

[144] PR Bolton, M Borghesi, C Brenner, DC Carroll, C De Martinis, Francesca Fiorini, A Flacco, V Floquet, J Fuchs, Pablo Gallegos, et al. Instrumentation for diagnostics and control of laser-accelerated proton (ion) beams. *Physica Medica*, 30(3):255–270, 2014.

[145] J Denavit. Absorption of high-intensity subpicosecond lasers on solid density targets. *Physical review letters*, 69(21):3052, 1992.

[146] D Neely, P Foster, A Robinson, F Lindau, O Lundh, A Persson, C-G Wahlström, and P McKenna. Enhanced proton beams from ultrathin targets driven by high contrast laser pulses. *Applied Physics Letters*, 89(2):021502, 2006.

[147] B Qiao, S Kar, M Geissler, Paul Gibbon, M Zepf, and M Borghesi. Dominance of radiation pressure in ion acceleration with linearly polarized pulses at intensities of 10 21 w cm- 2. *Physical review letters*, 108(11):115002, 2012.

[148] B Qiao, M Zepf, M Borghesi, B Dromey, M Geissler, A Karmakar, and Paul Gibbon. Radiation-pressure acceleration of ion beams from nanofoil targets: The leaky light-sail regime. *Physical review letters*, 105(15):155002, 2010.

[149] T D Arber, Keith Bennett, C S Brady, A Lawrence-Douglas, M G Ramsay, N J Sircombe, P Gillies, R G Evans, Holger Schmitz, A R Bell, and C P Ridgers. Contemporary particle-in-cell approach to laser-plasma modelling. *Plasma Physics and Controlled Fusion*, 57(11):113001, 2015.

[150] C Scullion, D Doria, L Romagnani, A Sgattoni, K Naughton, D R Symes, P McKenna, A Macchi, M Zepf, S Kar, and M Borghesi. Polarization dependence of bulk ion acceleration from ultrathin foils irradiated by high-intensity ultrashort laser pulses. *Physical review letters*, 119(5):054801, 2017.

[151] N Hill, D Ross, and J Roddom. Scarf scientific computing application resource for facilities, 2019. URL https://www.scarf.rl.ac.uk/home.

[152] B A Shadwick and C B Schroeder. Physical fidelity in particle-in-cell modeling of small debye-length plasmas. In *AIP Conference Proceedings*, volume 1086, pages 321–327. AIP, 2009.

[153] Dixon T K Kwok. A hybrid boltzmann electrons and pic ions model for simulating transient state of partially ionized plasma. *Journal of Computational Physics*, 227(11):5758–5777, 2008.

[154] George B Rybicki and Alan P Lightman. *Radiative processes in astrophysics*. John Wiley & Sons, 2008.

[155] Viking - the york super advanced research computing cluster, 2019. URL https://wiki.york.ac.uk/display/RHPC/Viking+-+The+York+Super+Advanced+Research+Computing+Cluster.

[156] L Yin, B J Albright, K J Bowers, D Jung, J C Fernández, and B M Hegelich. Three-dimensional dynamics of breakout afterburner ion acceleration using high-contrast short-pulse laser and nanoscale targets. *Physical review letters*, 107(4):045003, 2011.

[157] Rajesh Kumar, Youichi Sakawa, Leonard NK Döhl, Nigel Woolsey, and Alessio Morace. Enhancement of collisionless shock ion acceleration by electrostatic ion two-stream instability in the upstream plasma. *Physical Review Accelerators and Beams*, 22(4):043401, 2019.